12-1-2022

Mesozoic Sevier Thrusts Overprinted by Miocene-Quaternary Left-Lateral Deformation: Structures and Tectonism of the Kane Springs Wash Region, Nevada

Andrew Reid

MESOZOIC SEVIER THRUSTS OVERPRINTED BY MIOCENE-QUATERNARY LEFT-LATERAL DEFORMATION: STRUCTURES AND TECTONISM OF THE KANE SPRINGS WASH REGION, NEVADA

By

Andrew Reid

Bachelor of Arts – Psychology
University of Nevada, Las Vegas
2013

Bachelor of Science – Geology
University of Nevada, Las Vegas
2018

A thesis submitted in partial fulfillment
of the requirements for the

Master of Science – Geoscience

Department of Geoscience
College of Sciences
Graduate College

University of Nevada, Las Vegas
December 2022

UNLV | GRADUATE COLLEGE

Thesis Approval

The Graduate College
The University of Nevada, Las Vegas

July 22, 2022

This thesis prepared by

Andrew Reid

entitled

Mesozoic Sevier Thrusts Overprinted by Miocene-Quaternary Left-Lateral Deformation: Structures and Tectonism of the Kane Springs Wash Region, Nevada

is approved in partial fulfillment of the requirements for the degree of

Master of Science – Geoscience
Department of Geoscience

Wanda Taylor, Ph.D.
Examination Committee Chair

Michael Wells, Ph.D.
Examination Committee Member

Simon Jowitt, Ph.D.
Examination Committee Member

David Lee, Ph.D.
Graduate College Faculty Representative

Alyssa Crittenden, Ph.D.
Vice Provost for Graduate Education & Dean of the Graduate College

Abstract

Recognizing how rifts develop through space and time is vital to enrich our understanding of continental breakup. Rifts are commonly segmented by transfer or accommodations zones that form as the rift develops due to differences in the onset, direction, magnitude, or rates of extension on either side of the transfer or accommodation zone. The Basin and Range province is a wide rift where Cenozoic extension overprints and exposes earlier Mesozoic Sevier fold-thrust belt shortening structures. This exposure allows Sevier thrust correlations between individual mountain ranges and use of these shortening structures to study rift segmentation by strike-slip transfer faults. The purpose of this study is to further develop our understanding of regional tectonism by unraveling the tectonic history of the Kane Springs Wash area, Nevada, from Sevier shortening and hinterland highland development, through highland erosion, and finally to overprinting by Miocene-Quaternary strike-slip and normal faults associated with rift segmentation. Focus is placed on clarifying (1) long term issues in the reconstruction of Sevier-related thrusts and the former Sevier hinterland; and (2) the development of a boundary zone within the Basin and Range province that contains strike-slip faults and whether it may be a rift segment boundary. Sevier thrusts exposed in the Delamar and Meadow Valley mountains are offset by a major Cenozoic left-lateral fault, the Kane Springs Wash fault that lies at the southern reach of the boundary zone between the Northern and Central Basin and Range subprovinces. This boundary zone is spatially coincident with the southern Nevada seismic belt where distinct changes in topography, style of deformation, rock exposures, and gravity anomalies occur/ These changes and the structures, together, suggest that the zone may operate as a rift segment boundary.

Using new geologic mapping, detrital zircon ages, and structural analyses, I illustrate several key findings. (1) The left-lateral Kane Springs Wash fault is a transfer fault that separates two distinct domains of extension on either side. (2) The Kane Springs Wash fault zone lies at the southern reach of the boundary zone between the Northern and Central Basin and Range subprovinces, helping to accommodate differences in slip across the broad boundary zone in conjunction with other ~E-W striking structures. (3) The newly dated Eocene conglomeratic sediments, ~39 Ma, that overlie Sevier-related thrusts, show that the earlier Sevier hinterland highland lies to the North and West of the Kane Springs Wash area. (4) The Delamar and Meadow Valley thrusts are distinct faults and the Dry Lake thrust is the southward lateral equivalent of the Delamar thrust. That correlation provides southward continuity to a major regional thrust sheet and requires it to be placed in regional reconstructions where it has rarely been included.

Two major findings are drawn from this work. (1) The classification of the NBR-CBR boundary zone as a segment boundary within the Basin and Range is novel yet needed to better understand how the rift developed though time. (2) The southward correlation of the Delamar-Wah-Wah system to the Dry Lake system is new and furthers our understating of the architecture of the Sevier retroarc-fold-thrust-belt particularly because this large thrust system has been inappropriately minimized in regional reconstructions.

Acknowledgements

This document is dedicated:

To my advisor, Wanda J. Taylor, without whom I would never have been able to do any of this.

To my thesis committee, who provided valuable time, thoughts and input.

I also want to extend thanks to the Clark County Building Department for funding portions of my research through a grant to C.M. dePolo and W.J. Taylor.

To all those that helped in completing this research. The long days of fieldwork were worth it all the more because you were there.

To all the wonderful friends I have met along the way! Without you none of this would be bearable.

To anyone who ever doubted my capacity to do anything worthwhile. I perhaps owe you the most.

Thank you all.

Table of Contents

List of Figures – Figures Located at End of Document

1. Introduction

Overprinted or superposed deformations commonly modify the geometry of earlier structures, proving research opportunities because those early structures may become exposed and can be used to analyze the younger structures. Consequently, despite the tendency for structural geometries to be complex in areas of overprinted deformation, these areas provide valuable insights into each deformation individually and deformation through time. A prime example of an area of overprinted deformation is the Basin and Range province (BRP) where Cenozoic extensional structures overprint a variety of ages of shortening structures (Figs. 1, 2; Wernicke et al. 1988; Snow and Wernicke, 2000; Taylor et al., 2000; Friedrich and Bartley; 2003; DeCelles, 2004; Bidgoli, 2005; Dickinson, 2006; Long 2012; Greene, 2014).

A fundamental aspect of rifts, like the BRP, is that they are commonly segmented by strike-slip faults and/or by dip-slip fault terminations in transfer and accommodation zones that strike at high-angles to the tectonic and structural grain of the rift (Faulds and Varga, 1998; Rowley, 1998; Thenhaus and Barnhard, 1998; Pérouse and Wernicke, 2017). Transfer and accommodation zones can be discrete and spatially limited or broad with a much greater spatial extent (Faulds and Varga, 1998; Rowley, 1998; Thenhaus and Barnhard, 1998; Pérouse and Wernicke, 2017). These zones form as the rift develops and are generated by differences in timing of onset, direction, magnitude, or rates of extension along the length of the rift, transmitting slip from either side and linking the rift segments (Faulds and Varga, 1998; Rowley, 1998; Thenhaus and Barnhard, 1998; Pérouse and Wernicke, 2017). The BRP can be divided subprovinces that may represent different rift segments (e.g., Bidgoli, 2005): the Northwestern, Northern (NBR), Central (CBR), and Southern Basin and Range subprovinces (Fig. 3). The onset of extension within the CBR is younger, has a different magnitude and a higher rate of extension

than that of the Northern and Southern Basin and Range. A major BRP boundary that lies between the NBR and CBR subprovinces (Fig. 3) is considered in this study in light of general rift segmentation concepts.

Decades of work in the BRP on areas that are structurally complex due to extensional deformation overprinting shortening structures draws attention to several important problems that remain unsolved (Tschanz and Pampeyan, 1970; Pampeyan, 1993; Swadley et al., 1994; Snow and Wernicke, 2000; Friedrich and Bartley, 2003; Cassel et al., 2018; Giallorenzo et al., 2018). Regarding Cenozoic extension, the youngest deformation in the BRP, an important issue is the kinematic and regional tectonic role of many E-W to NE-SW-striking structures that cut across the primary structural grain of the BRP and their relation to other local and regional structures. Is the NBR-CBR subprovince boundary zone, a rift segment boundary, how does the ~NE-striking KSW fault zone relate to the segmentation of the BRP as a whole (Figs. 3, 4)? What are the accurate geometries and histories of faults that segment the BRP and do they act as slip transfer zones between the NBR and CBR subprovinces? Because rift segment boundary zones contain different structures and have different structural and earthquake histories than the surrounding rift segments, documenting them is critical to developing structural and regional tectonic models. In parts of the BRP, the Cenozoic structures overprint the Jurassic to Eocene retroarc Sevier fold-thrust belt and the associated hinterland highland or plateau (Figs. 1, 2, 5; Plate 1). Additional structural issues surround that older deformation. The following are addressed here. (1) What are the structural geometries and styles where extensional structures overprinted and disrupted the geometry and configuration of the Sevier fold-thrust belt and the Sevier hinterland at the southern edge of the NBR-CBR boundary zone? (2) What are the distinguishing characteristics of the DT and MVT thrusts of the Sevier fold-thrust belt and how

do they relate to other regionally important Sevier-related structures? This information is used to determine structural style and correlate thrusts along strike as well as the ascertain the location of the Sevier hinterland within space and time. (3) What process(es), tectonic or erosional denudation, resulted in the demise of the Sevier hinterland highland and where do the DT and MVT sit in relation to the Sevier hinterland highland? When did the processes that resulted in the demise of the Sevier hinterland highland occur? The magnitude and configuration of the paleorelief present in the time interval between Sevier orogenesis and extension reflects on thrust geometry as well as depositional systems.

This work addresses these issues in an understudied area with substantial structural overprinting, the Kane Springs Wash (KSW) area, southern Nevada, where Miocene-Quaternary strike-slip and normal faults overprint older Sevier-related shortening structures (Figs. 1, 2; Plate 1 – Appendix A). This area supplies an opportunity to use older Sevier structures to study younger extensional structures and vice versa. The Sevier thrusts are chiefly the Delamar (DT) and Meadow Valley (MVT) thrusts, located in the Delmar and Meadow Valley mountains. The major Cenozoic structure is the KSW fault zone which is ~41 km long and has apparent left-lateral offset estimates ranging between ~8 and 12 km (Anderson, 1999). The KSW area also provides an opportunity to study the evolution of a major Sevier thrust system and the breakdown of the Sevier hinterland highland at a latitude where the hinterland and frontal thrusts diverge to the north. This case study allows us to address these issues and apply the information gleaned to the BRP province and Sevier fold-thrust belt in a broader context.

I use new field mapping, structural analyses, and detrital zircon maximum depositional ages and provenance data to track the evolution in the KSW area from Sevier thrusts and hinterland highland development through demise of the highland and finally to the overprinting of thrusts

by Miocene-Quaternary extension with strike-slip and normal faults involved in developing rift segmentation. From these analyses, I suggest the following. (1) The KSW fault zone operates as a Miocene and Quaternary transfer zone between two domains of extension, here called the NW and SE domains, which have differing extensional styles, distribution and magnitudes on either side of the KSW fault zone. In addition, the KSW fault zone forms part of the southern limit of the NBR-CBR boundary zone, which is considered a rift segment boundary dominated by left-lateral transfer faults. (2) The location of part of the eastern slope of the Sevier hinterland highland lies in and near the KSW area. (3) A major thrust, the Delamar thrust (DT), continues southward and correlates with the Dry Lake thrust. This correlation suggests a larger regional distribution of this structure that is often overlooked in reconstructions of the Sevier retroarc fold-thrust belt at the latitude of southern Nevada.

2. Tectonic and Depositional Settings

Six broad groups of rocks and periods of tectonism are relevant to this study: (1) early Paleozoic, carbonate-dominated passive margin sedimentation disrupted during the Antler orogeny; (2) mid to late Paleozoic tectonism from the Antler through the Sonoma orogenies, with intervening tectonic events and the dominantly shallow marine sedimentary rocks deposited during that time interval; (3) Sevier orogenesis associated with subduction of the Farallon plate and sedimentation in piggyback and foreland basins; (4) post-Sevier but pre-Oligocene volcanic and sedimentary deposition – chiefly, the local Eocene conglomeratic sediments (Ecs); (5) Oligocene to Miocene extension, including strike-slip faulting, and ash-flow tuff emplacement attributed to the ignimbrite flare-up associated with roll-back of the Farallon slab; and (6) lastly, the late Pliocene(?) to Quaternary extension with basin-fill deposits and alluvium deposited into the lows created by the faults.

Early to Late Paleozoic History

In the southwestern U.S., the early to late Paleozoic is dominated by passive margin sedimentation along the western Laurentia margin (Dickinson, 2004; Dickinson, 2006; Yonkee and Weil, 2015). This period of passive margin sedimentation leads to the development of a sedimentary prism dominated by marine carbonates. This westward thickening sedimentary wedge was draped atop basement rocks from the Mojave, Yavapai, Mazatzal, and Wyoming provinces as well as the Farmington zone and the Grouse Creek block (Dickinson, 2004; Dickinson, 2006; Yonkee and Weil, 2015). The KSW area lies approximately within a thinner portion of the sedimentary prism. The area lies E of the initial $^{87}Sr/^{86}Sr$ ratio 0.706 line on continental crust and in the region of shallow and relatively thin deposits (Figs. 1, 2; Wooden et al., 1998; Yonkee and Weil, 2015). The units of this sedimentary prism typically make up the

Sevier thrust plates exposed in the KSW area (Yonkee and Weil, 2015; Swanson and Wernicke, 2017).

The middle to lower Cambrian up into Devonian rocks exposed within the study area range from the passive margin carbonate-dominated Cambrian Highland Peak Formation to Devonian Guilmette Formation (Fig. 6; Plate 1; Longwell, et al., 1965; Tschanz and Pampeyan, 1970; Pampeyan, 1993; Scott et al., 1995; Swanson and Wernicke, 2017). The lateral equivalent of the Cambrian Highland Peak Formation is the Cambrian Bonanza King Formation that commonly occurs in the upper plate of Sevier belt thrusts such as the Keystone thrust (Figs. 1, 2, 6; Longwell, et al., 1965; Tschanz and Pampeyan, 1970; Burchfiel et al., 1982; Long, 2012). The Ordovician Pogonip Group, Ordovician Eureka Quartzite, Ordovician Ely Springs Dolomite and Silurian Laketown Dolomite are not exposed in the thinner cratonal sections east of the Sevier front further demonstrating passive margin sedimentation at the time of deposition (e.g., Tschanz and Pampeyan, 1970; Garrity and Soller, 2009).

During late Devonian to early Triassic time the southwestern Laurentian margin underwent a series of events with southeastward-directed shortening and transpression along generally NE-SW trending structures, oblique to the western Laurentian margin, with synconvergent sedimentation in foreland and successor basins (Cashman et al., 2000; Lawton et al., 2017). Consequently, the passive margin sedimentation was replaced by shallow marine deposition in new foreland and successor basins associated with the Antler and Sonoma orogenies and the intervening Late Paleozoic transpressive deformation (Cashman et al., 2000; Dickinson, 2004; Dickinson, 2006; Lawton et al., 2017; Yonkee and Weil; 2017; Sturmer et al. 2018). This deformation occurred northwest of the study area but influenced the basins and sedimentation within the KSW area, particularly the late Mississippian to early Permian Bird Spring Formation

which typically occurs in the lower plate of the DT and MVT (Sturmer et al., 2018; Cashman and Sturmer, 2021).

Mesozoic History

The Sevier retroarc fold-and-thrust belt and its hinterland highland developed in the late Jurassic to mid-Cretaceous and into the Eocene, in the north, in response to the subduction of the Farallon oceanic plate eastward underneath western Laurentia (DeCelles, 2004; Dickinson, 2004; DeCelles et al., 2006; Dickinson, 2006; Busby and Putrika, 2009; Greene, 2014, Yonkee and Weil, 2015; Cassel et al., 2018; Giallorenzo et al., 2018). The Sevier hinterland highland has modest internal relief, locally documented in this study, and is commonly called the Nevadaplano (DeCelles, 2004; DeCelles et al., 2006; Druschke et al., 2011; Long, 2012; Greene, 2014; Long, et al., 2015; Erdman, et al., 2016). This highland reached elevations that may have been as much as ~8 km or greater, but more likely was 2-3 km high (DeCelles, 2004; DeCelles et al., 2006; Long, 2012; Snell, et al., 2014; Long, et al., 2015; Erdman, et al., 2016). The highland contained that regional topographic maximum and included a major ~N-S drainage divide in the Intermountain West during its lifetime (Figs. 1, 2; DeCelles et al., 2004; Henry and Faulds, 2010; Long, 2012; Henry et al., 2012; Best et al., 2013b; Snell et al., 2014; Long et al., 2015). The Cordilleran magmatic arc and accreted terrains at the western margin of Laurentia developed from mid-Triassic to mid-Jurassic time also in response to subduction of the Farallon plate (Dickinson, 2004; Dickinson, 2006; Greene, 2014; DeCelles and Graham, 2015; Yonkee and Weil, 2015). The KSW area sits E of the Cordilleran magmatic arc and W of the Sevier frontal thrusts, within the Sevier retroarc fold-thrust belt where drainage would be eastward off the highland.

Several regional structures are important to understanding the spatial extent of the former Sevier hinterland and the role the KSW fault plays in later deformation. Important and well-known thrusts include the Gass Peak thrust, Valley thrust, Dry Lake thrust, and the Muddy Mountain-Mormon thrust (Keystone thrust correlatives), from structurally highest to structurally lowest. These thrusts are exposed near the map area and must be considered relative to the DT and MVT in the KSW area. Those thrusts, their along-strike correlatives, and the typical stratigraphic separation in the Spring Mountains, and Sheep and Las Vegas ranges area are as follows (Fig. 1). The Gass Peak-Wheeler Pass thrust system is correlative to faults and folds in the central Nevada thrust belt and places Late Precambrian and Cambrian rocks atop Pennsylvanian-Permian footwall rocks in the south with decreasing stratigraphic separation northward (Taylor et al., 2000; Long, 2012; Giallorenzo et al., 2018). Structurally below that thrust system, the Lee Canyon thrust places Cambrian Bonanza King and Nopah formations atop Pennsylvanian and Permian rock in its footwall (Burchfiel et al., 1974; Lundstrom et al., 1998; Pavlis et al., 2014). The Lee Canyon and Deer Creek thrusts, together, have differing northward along-strike correlatives in different interpretations; one suggested correlative is the Valley thrust and another is the Dry Lake thrust (Pavlis et al., 2014). The Valley thrust lies in the footwall of the Gass Peak thrust and places Pennsylvanian-Permian rock atop Pennsylvanian-Permian rock in its footwall, which is inconsistent with the Lee Canyon thrust (Lundstrom et al., 1998; Page et al., 2005). The Dry Lake thrust place Cambrian and Devonian rock atop the Pennsylvanian-Permian Bird Spring Formation.

During late Cretaceous time, in response to flattening of the Farallon slab dip, the arc migrated eastward, the eastern Sevier retroarc thrusts were active, and basement-cored uplifts initiated and continued to develop in the foreland until ~50 Ma (DeCelles, et al., 2004; Dickinson, 2004;

Dickinson, 2006; Yonkee and Weil, 2015; Best et al., 2016). This switch to a flat-slab style of subduction is coupled with the inboard migration of both arc magmatism and the initiation of basement-cored uplifts to the east of the Sevier belt, called the Laramide orogeny (Dickinson, 2004; Dickinson, 2006; Best et al., 2009; Smith et al., 2014; Best et al., 2016; Yonkee and Weil, 2015). Farallon flat-slab subduction lasted from the latest Cretaceous until slab foundering and rollback primarily during Eocene to Miocene time (Dickinson, 2004; Dickinson, 2006; Best et al., 2009; Smith et al., 2014; Best et al., 2016; Yonkee and Weil, 2015).

Eocene History

Near KSW and the surrounding areas, a period of relative tectonic quiescence occurred from ~40 until ~23 Ma during which the former Sevier hinterland remained a prominent topographic high (DeCelles et al., 2004; Cassel et al., 2014; Best et al., 2016). This hinterland highland or plateau was suggested to be destroyed through various means such as gravitational collapse and erosional denudation (Cassel et al., 2018). Detritus from the Sevier hinterland was transported and deposited eastward and westward from a N-S drainage divide in central Nevada, leaving both lacustrine and fluvial sediments perched atop the hinterland plateau and Sevier thrusts at the base of the topographic slope from the divide to the east (Fig. 1; Henry, 2008; Henry and Faulds, 2010; Smith et al., 2017; Cassel et al., 2018). This erosional denudation, eastward off the hinterland, is of particular importance for the KSW area because it lies E of the former topographic maximum (Taylor et al., 2000; Long, 2012). Eastward erosional denudation off the hinterland plateau led to (1) the development of drainages that are now in disconnected exposures and (2) the deposition of alluvial, fluvial, and lacustrine sediments locally atop deformed Paleozoic and Mesozoic rocks of the Sevier frontal thrusts and foreland basins (Goldstrand, 1994; Henry et al., 2008; Greene, 2014; Smith et al., 2017; Cassel et al., 2018). This

time interval is represented within the KSW area by the Ecs (Eocene conglomeratic sediments) unit, previously mapped as TKc by Tschanz and Pampeyan (1970) and Tc and Tl by Swadley et al. (1994). The Ecs unit sits in a stratigraphic and structural position vital to unraveling the final configuration and paleogeomorphology of the Sevier belt and hinterland plateau after local shortening-related deformation has ended.

New observations indicate that Ecs comprises interbedded medium-coarse sandstone beds and conglomerate with pebble to large boulder-sized clasts, commonly capped by a fresh-water limestone. Graded bedding commonly is exposed throughout the conglomeratic sections. The section of graded beds is commonly capped by medium-fine to medium-coarse calcite cemented sandstone. The clasts are typically limestone, dolostone, and quartzite similar to rocks exposed in both the upper and lower plates of both the DT and the MVT as well as structurally higher plates such as the Gass Peak thrust plate. Although not exposed in all sections within the study area, calcite-cemented sandstone beds are typically deposited atop of a sequence of fining-upward carbonate and quartzite clast-dominated conglomeratic beds. In several locations, paleochannels are distinguished by cut-and-fill structures, but no distinct paleodrainage direction was definitively determined from clast imbrications or other paleoflow indicators.

The Ecs and similar deposits In the region previously were mapped as ranging in age anywhere from Cretaceous to Miocene; to restrict the age range, new detrital zircon provenance analysis was performed by T.S. Bidgoli (2020), on the Ecs unit in the KSW area. The new data suggest a maximum depositional age of ~39 Ma (Appendix B). Bidgoli's analysis indicates that detrital zircon grains within the Ecs unit are sourced primarily from Precambrian and Cambrian quartzites that are not exposed within the KSW area but are exposed in thrust plate structurally higher than the DT and MVT such as the Gass Peak thrust (Figs. 8, 9, 10, 11, Appendix B,

modified from T. Bidgoli; Longwell et al., 1965; Tschanz and Pampeyan, 1970; Page et al., 2005a, 2005b; Felger and Beard, 2010). Bidgoli notes that there are zircon grains from Ordovician quartzite but the unit lacks zircons from units such as the Devonian Oxyoke Canyon Sandstone and Mississippian Scotty Wash Quartzite, common to the upper plates of the local thrusts (DT and MVT). This provenance is a strong indication that a highland in the Sevier hinterland existed to the N and W of the KSW area before Cenozoic extension and drained generally east from ~39 Ma until its final demise by mid-Cenozoic and later extension and emplacement of tuffs by pyroclastic flows.

The rock types of the Ecs are consistent with alluvial or fluvial sedimentation that transitions to a lacustrine setting with the deposition of limestone. This sequence is typical for a drainage system off a proximal highland. I interpret the Ecs unit to represent the erosional denudation of a portion of the Sevier hinterland plateau across much of the orogenic wedge. In the Meadow Valley Mountains, the Ecs unit is composed of conglomerate and sandstone capped by a limestone unit that overlies or, completely composes the Ecs unit where former topography was high enough to preclude the lower clastic lithology. Exposures within the Delamar Mountains are composed of gravel to boulder-sized clasts weathering from beneath the tuffs with little to no limestone capping beds. The limestone generally thickens to the SE (Meadow Valley Mountains) where it is exposed in every section, while the lower conglomerate thins southeastward. This observation in conjunction with the detrital zircon analysis suggests that local drainage was to the south and east further supporting the interpretation that the former Sevier hinterland was a highland that laid to the west or northwest.

Oligocene to Miocene History

The Farallon slab began foundering at ~50 Ma in early Eocene time, supplying an influx of hot asthenospheric material to the lower crust and causing southwestward migrating pyroclastic volcanism – peaking from ~38 Ma in northern Nevada until ~18 Ma just north of the KSW area (Fig. 2; DeCelles, et al., 2004; Dickinson, 2006; Busby and Putrika, 2009; Best et al., 2013b; Best et al., 2016, Yonkee and Weil, 2015). This post-orogenic volcanism is called the ignimbrite flare-up (Best et al., 2016). In addition, plate reconstructions indicate that the southern part of the region of the ignimbrite flare-up, the CBR, may be influenced by a window in the Farallon slab that formed beneath the Mojave region during the 26-19 Ma time interval (Atwater and Stock, 2010). These reconstructions suggest that the early Miocene ignimbrite eruptions and extension in that area may be the result of asthenospheric upwelling into a sub-lithospheric slab window (Atwater and Stock, 2010). East of and across the former or remnant Sevier hinterland highland, the ignimbrites typically were erupted from caldera complexes (Figs. 1, 2; Busby and Putrika, 2009; Best et al., 2013, Best et al., 2016). Exposed within the KSW area are ash-flow tuffs erupted from both the Indian Peak and Caliente caldera complexes as well as the ~15 Ma KSW caldera (Longwell, et al., 1965; Tschanz and Pampeyan, 1970; Scott et al., 1994, Best et al., 2013). These rocks range in age from ~ 23 to ~15 Ma, but ash-flow tuffs as old as ~26 Ma may occur at depth at least in the NW domain of the KSW area (Figs. 6, 7; Plate 1; Best et al., 2013; Best et al., 2016). Paleomagnetic data across the KSW fault zone suggest that there has been no discernable vertical-axis rotation of the tuffs since deposition (Hudson et al., 1998). BRP extension as a result of NNE-striking faults and segmentation by ~E-W structures striking perpendicular to the primary tectonic grain as a whole are necessary to accommodate differences in the timing, magnitude and direction of extension within the NBR and CBR subprovinces (Wernicke et al., 1982; Wernicke, 1992; Dickinson, 2002; Colgan et al., 2006; Pérouse and

Wernicke, 2018; Long, 2019). Extension within the NBR began earlier in Oligocene to early Miocene time, whereas extension within the CBR began in middle Miocene time while extension continued in the NBR (Wernicke, 1992). Extension within the NBR is more west to west-northwest directed than the extension direction of west to west-southwest directed extension of the CBR (Wernicke, 1992). High magnitude extension associated with low-angle normal faulting – such as the Mormon Peak detachment –- is greater and younger in the CBR than in the NBR (Figs. 1, 2, 3, 4; Wernicke, 1992). At the boundary between the NBR and CBR subprovinces strike-slip and transfer faults are noted with a slip history as early as Oligocene time (Abdelhaleem et al., 2020). These faults include faults of the Timpahute Lineament and Pahranagat shear zone as well as the KSW fault zone (Figs. 1, 2, 3, 4).

Late Pliocene to Quaternary History

By late Pliocene time, the modern Basin and Range physiographic province was marked by a lack of volcanism from the ignimbrite flare-up and little low-angle normal faulting as are typically associated with the earlier Cenozoic extension (Dickinson, 2004; Dickinson, 2006; Dickinson, 2010). At this time, the BRP deformation was generally E-W directed extension along high-angle, ~N-S-striking normal faults with basin fill sediments sitting atop hanging-wall blocks, generating the modern topography (Dickinson and Gehrels, 2010; Ellis et al., 2015). Quaternary faults in the northern and central BRP are generally NNE-striking and high-angle. Modern seismic studies combined with horizontal GPS measurements demonstrate that in the southern NBR and northern CBR subprovinces active deformation is focused along the eastern margin, the Intermountain Seismic belt; the western margin of the subprovince, which includes the Eastern California and Walker Lane seismic belts; and in the ENE-WSW trending southern Nevada seismic belt connecting the two rift shoulders (Kreemer et al., 2010). Major E-W to

ENE-WSW striking faults that lie within the southern Nevada seismic belt and spatially coincide with the NBR-CBR boundary zone are faults of the Timpahute Lineament, Pahranagat shear zone, Caliente-Enterprise zone, and the KSW fault zone (Fig. 2; Tschanz and Pampeyan, 1970; Ekren, 1976; Axen, 1998; Hudson et al., 1998; Price, 2017; Ely and Taylor, 2018; Evans; 2018; Peck, 2018; Reed, 2019; Abdelhaleem et al., 2020; Reid et al., 2020; Taylor et al., 2022).

3. Methods

I employed standard geologic mapping techniques using both a GPS enabled tablet with the software FieldMOVE and a Brunton geologic compass to collect attitudes of bedding, compaction foliations, faults, and folds to generate a highly accurate geologic map at a scale of 1:24000 of the KSW area. Measurements and data collected via mapping and NAIP (National Agricultural Imagery Program) imagery were used to create geologic and fault maps on a USGS topographic base map, geologic cross sections and stereograms of collected field measurements (EROS, 2018). Fault scarp heights were collected as part of a guided undergraduate research project in which surveys were performed using a TopCon total station (Reed et al., 2019)

4. Results

The results, which are largely based on the new map data (Plate 1; Appendix C), are presented in reverse chronological order for four different time intervals. Reverse chronology is used to illuminate the impact of the younger structures on older structures and unit deposition. The four times intervals are (1) Quaternary, (2) ~15 Ma to Pliocene, (3) Eocene to Miocene, and (4) Mesozoic time. (1) The youngest deformation within the study area is represented by the Quaternary fault scarps and related offsets along parts of the KSW fault zone. (2) Some fault strands of the ~NE-striking KSW fault zone and faults to both the NW and SE cut the Kane Wash Tuff providing a lower age bracket of middle Miocene, ~15 Ma; however, the upper age bracket is poorly constrained but is provided by the angular unconformity at the base of the Quaternary deposits. These Miocene-Pliocene faults lack scarps, cut the Oligoene to Miocene tuffs and older units, and are covered by the youngest Quaternary fluvial and alluvial sediments. (3) Before the inception of the KSW fault zone a period of erosion and deposition of both sedimentary rocks (the Ecs unit, Plate 1) and ash-flow tuffs occurred. (4) Those deposits unconformably overlie Paleozoic rocks which were shortened in the Jurassic-Cretaceous Sevier fold-thrust belt deformation. This shortening is represented by the DT and MVT and associated folds in the Delamar and Meadow Valley mountains, respectively (Plate 1; Figs. 1, 2).

Two domains of Miocene-Pliocene extensional faults are defined here, the NW domain and SE domain, which lie on opposite sides of the KSW fault (Plate 1; Figs. 1, 2, 12). The NW domain lies generally in the southern Delamar Mountains and the SE domain lies in the Meadow Valley Mountains. The major faults in the SE domain have strikes and displacements that are similar to – but not the same as – the major faults in the NW domain. The number of faults, their style of termination, offset stratigraphy, amount of total extension, and the general extension direction

are different between the two domains, as detailed below. The map data show fault terminations at the KSW fault with no indication that these faults are older faults that were offset by the KSW fault zone (Plate 1; Fig. 12). Some of the larger faults in both the NW and SE domains are buried by the youngest Quaternary alluvium or fluvial deposits or are exposed cutting only bedrock which gives no indication of a Quaternary slip history, but does not exclude Quaternary deformation. These faults cut the youngest ash-flow tuffs, the Ecs, and the Paleozoic rocks shortened in Sevier-related deformation with the youngest ash-flow tuffs down-dropped more than ~300 m (1000 ft) as measured from stratigraphic separation. The large offsets of these faults, which are consistent with their slip history, can be as old as latest Miocene, post KSW caldera eruption, and coeval with the KSW fault zone.

KSW fault zone

Displacement along the Cenozoic KSW fault zone is both down-to-the-NW normal dip-slip and left-lateral strike-slip along multiple strands that offset and capture the pre-existing tectonostratigraphy (Figs. 1, 2; Plate 1). Across the KSW fault zone normal vertical ranges from ~100 to 400 m at a minimum, as measured from exposures of tuffs in the Meadow Valley Mountains – the footwall of the KSW fault zone – to exposures of the same tuffs in the hanging-wall of the KSW fault and KSW-related faults. The left-lateral offset of the KSW fault is more difficult to quantify within the map area because no piercing points are directly observed, but the eastward extent of Cambrian exposures above the DT in the Delamar Mountains and the most northeastern exposures of Cambrian rock in the Meadow Valley Mountains are offset left-laterally ~13 km along strike of the KSW fault zone.

The KSW fault has a long-lived Quaternary and Miocene-Pliocene slip history because some strands offset Quaternary deposits and others are covered by them. Some strands that are

overlain by Quaternary deposits were active during or after the middle-to-late Miocene time (<15 Ma), because they cut ash-flow tuffs of that age, which are members of the Kane Wash Tuff. Thus, the KSW fault may have been active for as much as ~15 m.y.

Quaternary deformation along the KSW fault zone is demonstrated by fault scarps that strike NE-SW along the KSW valley floor (Plate 1; Figs. 1, 2, 12; Reed et al., 2019). Most of the scarps face NW, show left-laterally offset washes and down-to-the-NW displacement of Quaternary surfaces. The exception is fault KSW2, which faces SE, indicating a down-to-the-SE component of offset along this strand of the KSW fault zone (Plate 1; Fig. 12). Quaternary fault scarps along the KSW fault zone measure from ~8-13 m in height (Reed et al., 2019) and exposures near the Meadow Valley Mountains place rocks as old as Cambrian next to Quaternary alluvium. Even though the apparent offset of the along-strike Cambrian exposures – exposed only as hanging-wall rock of the DT – is left-lateral, the presence of these scarps suggests that a nontrivial component of the total slip along the KSW fault is normal.

The KSW fault zone is ~5 km wide, separates the NW and SE domains, and controls the morphology of the KSW Valley, which drains southwestward and into the Coyote Springs Valley (Fig. 2). This drainage pattern is notable because the southwestern tip of the KSW fault zone, the southern Coyote Spring fault, and the northern Wildcat Wash fault spatially coincide with the intersection of KSW and Coyote Spring valleys (Fig. 2; Page and Pampeyan, 1996; Abdelhaleem, 2022).

The boundary between the NW domain and the KSW fault zone proper is the previously documented and named Willow Springs fault (Plate 1; Figs. 1, 2, 12; Tschanz and Pampeyan, 1970; Page et al., 1994). The Willow Springs fault is not well exposed within the study area but generally strikes ~035° and bends to ~045° northeast of the study area (Swadley et al., 1994).

Upon visual inspection the Willow Springs fault does not have Quaternary fault scarps, but this may be due to scarp erosion. Because other faults with NE-strikes are left lateral, the Willow Springs fault may have left-lateral offset and if so, it is part of the KSW fault zone. Where this fault can be accurately located it has a minimum vertical stratigraphic separation of ~200 m based on unit thicknesses and the juxtaposition of the Harmony Hills Tuff and Pennsylvanian Bird Spring Formation. Along the southwestern portion of the trace of the Willow Springs fault, it appears that the fault either steps over to another nearby structure or bends and splays southward, but the relations are obscured by Quaternary deposits.

The boundary fault between the SE domain and the KSW fault zone is fault MV1, the southeasternmost fault in the KSW fault zone. Fault MV1 strikes subparallel to the Willow Springs fault. In general, fault MV1 has an attitude of ~220°/57° NE – however, some subsidiary surfaces can dip as much as 88°. Strikes range from NE to ENE. Fault MV1 or faults that abut it cut older and middle Quaternary alluvium as evidenced by the along-strike Quaternary fault scarps and offset Quaternary units. At least two sets of slickenlines exposed within the damage zone of MV1 indicate both strike-slip and dip-slip displacement at different elevations along the fault surface. The dip-slip set measures ~ 53°/278°, while the strike-slip set, where measured along the northward bend of the lenses, has an attitude of ~ 02°/005° or nearly horizontal. The latter typically occurs higher in elevation along the slip wall. The presence of two distinct slip directions strongly suggests that slip along the KSW fault has varied through time. Along the northern trace of MV1, the fault abuts or splays with another strand of the KSW fault zone and places the youngest Miocene ash-flow tuffs in its hanging wall adjacent to Silurian and Devonian rocks in its footwall.

Near the center of the map area, fault MV1 captures a lens of tilted tectonostratigraphy including a previously existing low-angle normal fault within its hanging wall (Plate 1; Fig. 12). The low-angle fault juxtaposes Ordovician Ely Springs Dolomite and Devonian units such that it omits at minimum the Ordovician Eureka Quartzite and at maximum part of the earliest Ely Springs Dolomite as well (Plate 1; Figs. 2, 12). This low-angle normal fault is cut by high-angle faults genetically linked to the KSW fault zone. This pre-existing low-angle normal fault is offset a minimum of ~400 meters down-to-the-NW, when compared with the elevation of the same low-angle normal fault to the south in the Meadow Valley Mountains. The low-angle normal fault is documented in previous work (Scott et al., 1994). The exposed low-angle normal fault(s) is cut, and potentially reactivated, by the active and/or abandoned Miocene strands of the KSW fault zone. However, no ash-flow tuffs are exposed within the same fault block to provide a timing bracket. In addition, a higher low-angle normal fault in this lens places lower Devonian units atop the Ordovician Ely Springs Dolomite, omitting a portion up to the entirety of the Ely Springs Dolomite (Map Plate, Fault Map). Southwestward within the Meadow Valley Mountains, another low-angle normal fault places youngest Ordovician to Silurian and oldest Devonian rock atop rocks of the Ordovician Pogonip Group (Plate 1; Figs. 2, 12). This fault is used as a marker to determine offset along several faults within the SE domain (Plate 1). These low-angle normal faults, where exposed, have small stratigraphic omission and cannot be linked causally to a larger detachment event such as the Mormon Peak detachment to the east or the Seaman breakaway and Stampede detachment to the north.

NW domain

The structural style of the NW domain is marked by a network of NNE-SSW to NNW-SSE, ~E-W- and NE-SW-striking faults that are interconnected and apparently synchronous as indicated

by various abutting or branching relationships (Fig. 12, Plate 1 – Appendix A). In this network, faults with the smallest offset reach their topological termination against or into larger faults as is typical of a fault network (Plate 1; Fig. 12; Peacock et al., 2016). Extension within the NW domain is primarily directed ENE-WNW, or to ~307°, with overall down-to-the-WNW displacement via the large high-angle faults that form the primary tectonic grain within the NW domain (Fig. 12). The large faults, such as GB and DM1, typically strike from ~N10°W to ~N20°E, sub-parallel to each other (Plate 1; Figs. 1, 2, 12). Measured from map data, vertical stratigraphic separation on the relatively large faults ranges from ~100–300 m. The small faults strike orthogonal to sub-orthogonal to and abut the large faults. These orthogonal faults are one of the defining features of the fault network of the NW domain and are virtually absent within the SE domain. Typically, these smaller faults within the NW domain fault network have down-to-the-SE or down-to-the-NW vertical stratigraphic separation of ~1-3 m though a few have vertical separation on the order of ~10-15 m. Some of the smaller faults in the NW domain fault network have intersections that are x-nodes which indicate that the faults with different strikes are coeval and that the faults operated as a network to transfer strain among the faults (cf., Peackock et al., 2016). The larger faults control this deformation and I will present data on the major faults of the NW domain from east to west below.

Fault GB is ~30 km long and strikes N-S, subparallel to the range-bounding Coyote Spring fault to the west (Plate 1; Figs. 2, 12; Page, et al., 1990; Scott, et al., 1990; Page and Pampeyan, 1996; Anderson, 1999). To the north of the map area, fault GB appears to terminate against either a strand of the left-lateral Maynard Lake fault of the Pahranagat shear zone or a NE-SW striking strand of the Coyote Spring fault (Fig. 2; Scott et al., 1990; Scott et al., 1995). Within the map area, the low dip of the Tertiary ash-flow tuffs on either side of fault GB and the relatively

straight map trace suggest that this fault is high angle. Minimum vertical stratigraphic separation along fault GB is measured from offset ash-flow tuffs (Plate 1) and is ~200 m. Fault GB places Cambrian Highland Peak Formation of the hanging wall of the DT and overlying tuffs (Harmony Hills Tuff, Hiko Tuff, and Delamar Lake Tuff) on the W down against Devonian and Pennsylvanian-Permian rock of the lower imbricates of the DT and overlying tuffs (Harmony Hills Tuff, Condor Canyon Formation, Leach Canyon Formation). The older rocks are in the hanging wall of the normal fault indicating that within the study area fault GB cuts or reactivates the DT. Normal slip along fault GB was less than the thrust displacement along the DT because the older-over-younger relationship of the Cambrian hanging-wall rock and younger footwall rock is maintained. The southernmost trace of fault GB is buried under alluvium, where its trace apparently abuts the KSW fault zone. Cross-cutting relationships constrain the age of fault GB to be younger than the middle Miocene tuffs and older than the Quaternary alluvium at the surface.

Fault DM1 is a down-to-the-NE fault that places the Cambrian Highland Peak Formation in its hanging wall against ash-flow tuffs and Cambrian rock of the same formation in its footwall block with a vertical stratigraphic separation that cannot be readily determined from available map data but is likely less than 100 m (Plate 1, Fig. 12). To the S, the trace of fault DM1 abuts fault GB where it either truncates against or transfers slip onto fault GB. To the NW, fault DM1 appears to die out; along its tip, there are small step-overs and truncations (Plate 1, Fig. 12). Several of the NE-SW striking small faults of the network abut or transfer their slip onto fault DM1 and abut another fault of the primary fault set, DM2.

Fault DM2 strikes N-S and has down-to-the-W displacement with a minimum vertical stratigraphic separation of ~100 m estimated from the difference in average elevation of a Tertiary ash-flow tuff, the Condor Canyon Formation, in its hanging-wall and footwall blocks

(Plate 1; Figs. 2, 12). The offset of fault DM2 could be significantly higher due to differences in elevations of tuff deposition related to paleorelief and the lack of an overlying tuff unit in both the hanging-wall and footwall blocks directly adjacent to fault DM2. A series of NNE-SSW striking normal faults either splay off or transfer slip onto fault DM2; two of the major splays, DM3 and DM4, branch from fault DM2 (Plate 1; Fig. 12). DM3 has down-to-the-NW displacement and DM4 has down-to-the-southeast. The map patterns and dip directions of both DM3 and DM4 suggest that they are coeval and operate simultaneously with fault DM2. All three faults, DM2, DM3, and DM4, are buried by the youngest Quaternary fluvial deposits and alluvium where not exposed in bedrock.

SE Domain

The SE domain is exposed in the Meadow Valley Mountains and is more extended in the WNW-ESE direction, directed ~289°, than the NW domain (Fig. 12). The SE domain is characterized by NNE-SSW-striking high-angle normal faults that abut and either transfer slip from or terminate into fault MV1 and its along-strike correlatives. These strands have down-to-the-WNW or down-to-the-W displacement. Many of the extension-related faults in the northern Meadow Valley Mountains are exposed in only bedrock, limiting our ability to constrain their youngest age. This means that it is impossible to exclude Quaternary slip even though scarps are not exposed, but these faults do not cut the youngest Quaternary sediments. All faults within the SE domain terminate where they abut fault MV1 on their northern end. Overall, the prominent extension-related faults in the SE domain have a westward bend in their strike to become sub-parallel to the KSW fault zone as one follows their strike to the S (Plate 1; Fig. 12). I will discuss the major SE domain faults from E to W.

Faults MV2a, b, and c (map plate) strike N-S and have down-to-the-W displacements. Notably MV2 faults strike similarly to faults exposed within an active lens of the KSW fault zone along most of their strike, but when their map trace is followed north along strike these faults bend northwards to terminate against fault MV1. Southward, along strike, fault MV2 transverses the Meadow Valley Mountains to eventually abut to a southward bending branch of the KSW fault zone or the Wildcat Wash fault. The dips of the Tertiary ash-flow tuffs are different on either side of the main branch of fault MV2 such that the youngest Tertiary ash-flow tuffs in the hanging-wall dip WNW, while the older ash-flow tuffs located within the footwall dip to the E. Faults MV3a, MV3b, and MV3c strike parallel to fault MV2, and also have down-to-the-NNW displacement, as determined from offset Cambrian stratigraphy. Upon visual inspection of satellite imagery, faults MV3a, b and c continue southward from the study area in the Meadow Valley Mountains where they appear on satellite imagery to transverse through Wildcat Wash and interact with the Wildcat Wash fault (Figs. 2, 12). The total slip of these faults changes along strike, but the primary strand of this fault has portions where vertical stratigraphic separation is a minimum of ~200 m based on the vertical positions of rocks in the Cambrian Highland Peak Formation, the Ordovician Pogonip Group, and the previously existing tectonostratigraphy that was generated by the low-angle normal faults. Faults MV3a, b, and c also strike N-S and abut the KSW fault zone at fault MV1 similar to the MV2 faults. Southward along strike, these faults bend to strike NE-SW with down-to-the-northwest displacement. The southern ends of the MV3 faults are buried under alluvium, but project southwestward to intersect with either the southern part of the KSW fault zone (where the KSW fault zone bends southward and splays) or with the Wildcat Wash fault (Pampeyan, 1993).

Faults MV4a and b strike ENE-WSW and abut or splay from the KSW fault zone. Fault MV4a has down-to-the-NNW displacement, while the antithetic splay, fault MV4b, has apparent down-to-the-SSE displacement. Both faults MV4a and MV4b cut the low-angle normal fault in the KSW fault lens and place the hanging-wall late Ordovician-Silurian stratigraphy against the Ordovician rock of the footwall of that same low-angle normal fault. Offset along fault MV4a cannot be determined definitively because of a lack of clear stratigraphic markers but can be assumed to be hundreds of meters at the northern tip and as low as 10s of meters after the splay into the antithetic strands based on stratigraphic separation. The western antithetic splay MV4b also cuts the same tectonostratigraphy, both of which bound a block that only exposes the upper plate of the low-angle normal fault. Faults MV4a and MV4b interact with a part of the KSW fault zone to the south or are buried by Quaternary sediments where they either remain parallel to or abut the KSW fault zone along fault MV1. From cross-cutting and abutting relationships the age brackets on these faults can be assumed to be the age of the Miocene tuffs or younger and older than late Quaternary as they do not cut the latest Quaternary sediments or the KSW fault zone itself.

Timing of the Eocene Conglomeratic Sediments in Relation to Structures

Map relations of the Ecs in the Delamar and Meadow Valley mountains show that it was deposited after Sevier-related deformation and before KSW-fault-zone-related deformation. Where exposed in the Delamar Mountains, the Ecs unit overlies the lowest imbricate of the MVT. Within the Meadow Valley Mountains, the Ecs unit overlies both Devonian rocks of the MVT hanging wall and MVT footwall rocks of the upper Mississippian Chainman Shale and Scotty Wash Quartzite, and lower Pennsylvanian-Permian unit. The Ecs thickens and thins with changes in paleorelief in both the Delamar and Meadow Valley mountains.

Preliminary detrital zircon analysis was performed on Ecs samples to better determine the age and provenance (Appendix B). Samples were taken at several locations from sandstones within the conglomeratic portion of the Ecs unit in the Delamar Mountains where the unit overlies an imbricate thrust and underlies the tuffs (Plate 1). These preliminary analyses reveal that the maximum age of deposition is 39.0 ± 0.3 Ma (Plate 1; Appendix B; T.S. Bidgoli, 2020, personal commun.; Moore et al., 2020). Consistent with the Ecs overlying this Sevier-belt thrust, detrital zircon grains from the new analyses match DZ age distributions from units in Sevier thrust plates (Fig. 11). These units are chiefly Precambrian to Cambrian quartzites – the Wood Canyon Formation, the Zabriskie/Prospect Mountain Quartzite, the Stirling Quartzite, or the Johnny Formation – and the Ordovician Eureka Quartzite which are not exposed in the nearby upper plate of the DT. An additional subset of Mesozoic zircon grains was likely sourced from a granitic stock in the Grant Range. Bidgoli (pers. comm. 2020) notes that grains from late Paleozoic quartzites like the Devonian Oxyoke Canyon Sandstone and the Mississippian Scotty Wash Quartzite, commonly sourced from upper plates of local thrusts, are lacking in the Ecs but occur in Cretaceous-Eocene sediments northwards such as the Newark Canyon, Elko, and Sheep Pass formations (Druschke et al., 2011; Canada et al., 2019). There are no exposures as deep as the Cambrian quartzites like the Prospect Mountain Quartzite within the Delamar or Meadow Valley mountains that could supply the basin in which the Ecs is deposited, and the Ecs unit overlies the Mississippian quartzite and shales. Consequently, the grains are likely sourced from the former hinterland plateau to the northwest because the appropriate Cambrian and Precambrian quartzites are exposed in the upper plate of the Gass Peak thrust.

The Ecs underlies the Tertiary ash-flow tuff section, and faults of both the NW and SE domains as well as the KSW fault zone cut the Ecs. These relations make it relatively older than those units and structures, consistent with the 39 Ma detrital zircon age.

Sevier Thrusts – Delamar and Meadow Valley Thrusts

The Delamar and Meadow Valley thrusts are exposed in the Delamar and Meadow Valley mountains, respectively (Plate 1; Figs. 1, 2, 12). The DT generally strikes 195°, whereas the MVT strikes ~180°; both dip W. The DT juxtaposes middle-late Cambrian Highland Peak Formation strata against Devonian units along the main thrust (main imbricate), Devonian atop Mississippian along a lower (the upper middle) imbricate, Mississippian atop Pennsylvanian (the lower middle imbricate), and Pennsylvanian atop Pennsylvanian rock along the lowest imbricate. The MVT places Silurian and middle-to-late Devonian strata against late Mississippian and early Pennsylvanian rocks in its footwall. Portions of both the hanging wall and footwall strata of the MVT are overlain by the Ecs unit. The DT, DT imbricates and MVT are all overlain locally by the Tertiary ash-flow tuffs (Plate 1; Figs. 2, 12; Longwell et al., 1965; Tschanz and Pampeyan, 1970).

Fault GB dips west and places older Paleozoic rocks of the DT thrust plate over younger Paleozoic rocks of the footwall and is demonstrably a normal fault where it cuts ash-flow tuffs to the north, juxtaposing younger tuffs in the hanging wall and older tuffs in the footwall. These map relationships indicate that fault GB must either cut out the DT or reactivate it. Most of the Paleozoic hanging-wall rocks of the DT dip gently. Whereas, to the east of fault GB, the Paleozoic DT footwall rocks dip relatively steeply and lie in thin thrust imbricates that overlie shallowly dipping Pennsylvanian-Permian rock (Fig. 12). The ash-flow tuffs that overlie both the DT plate as well as the footwall imbricate plates also dip gently, but the ash-flow tuffs that

overlie the Paleozoic rocks in the hanging-wall block of fault GB dip more steeply than those in the footwall of fault GB. This geometry indicates a small amount of differential tilting across fault GB after tuff emplacement.

NNE-SSW trending, gently plunging folds are exposed within the southern Delamar Mountains (Plate 1). These folds include a previously documented range-scale anticline in the DT thrust plate that trends sub-parallel to the strike of the lower imbricates of the DT (Plate 1; Fig. 12; Scott et al., 1995). Within the eastern limb of this range-scale fold, I documented a smaller parallel syncline-anticline pair that are restricted to the upper plate of the DT (Plate 1). The fold pair trends subparallel to the large range-scale hanging-wall anticline. The range-scale anticline is dissected by the NW domain fault network (Page et al., 1990). The western limb of the range-scale anticline continues to young westward until the strata are truncated across-strike by the Coyote Spring fault (Plate 1; Figs. 2, 12).

In the Meadow Valley Mountains, late Cambrian Nopah Formation strata that are the same as the DT upper-plate strata in the Delamar Mountains are exposed in a fault-bounded block. The DT itself is not exposed in the Meadow Valley Mountains because NW-dipping fault MV4 drops it down-to-the-NW. The Ordovician Pogonip Group exposed in the Meadow Valley Mountains is here considered a stratigraphically higher part of the DT plate.

Both the MVT and DT continue beyond the map area along strike. From where the DT is cut by the KSW fault on the S, the thrust continues northward in the Delamar Mountains for about 70 km (~43.5 mi) and is correlated to additional thrusts discussed below (Fig. 1; Pampeyan, 1993; Felger and Beard, 2010). The northern end of the MVT is cut by the KSW fault zone, but to the south, out of the study area, the MVT appears to die out along or into the Bunker Hills folds (Fig. 2; Pampeyan, 1993; Beard et al., 2009; Felger and Beard, 2010). Upon visual inspection of aerial

and satellite imagery along strike of the MVT, the same hanging-wall-footwall stratigraphic relationship appears to continue south on the SE side of the Meadow Valley Mountains for more than 25 km.

5. Discussion

KSW fault zone

The main component of offset along the KSW fault zone, strike-slip, varies in magnitude along strike. The apparent left-lateral offset of the DT in the Delamar Mountains and upper plate exposures of the DT in the Meadow Valley mountains is ~14 km. This amount is ~2-5 km greater than that of the apparent left-lateral displacement of the KSW caldera wall (cf., Harding et al., 1991). This relation suggests greatest offset occurs nearer to the thrust fault exposures and along the central or west-central portion of the KSW fault zone.

Relative to the primary tectonic grain of the BRP (~N-S), the NE-strike and large strike slip of the KSW fault and structural differences across it are consistent with it being a transfer fault zone. Transfer fault zones are essential components of rift systems at which primary rift structures terminate forming abutting geometries. Transfer fault zones also accomplish the compartmentalization of rifts into subprovinces via strike-slip and oblique-slip faults that strike at a high angle to the rift trend (Plate 1; Figs. 1, 2). This case study suggests that the KSW fault transfers strain between faults in the SE and NW domains accommodating differences in fault geometries, extension direction and distribution of extension. In the SE domain extension is WNW-ESE, ~289°, directed along a few steeply dipping normal faults (Plate 1; Figs. 12, 13). In contrast, NW domain extension is more NW-SE, ~307°, directed along a fault network conducting overall more NE-SW directed extension than the E-W extension of the SE domain. Differences in distribution of extension across the KSW fault zone are evidenced by a concentration of faults in the NW domain along the southwestern KSW fault when compared with the SE domain, with fewer faults that are more evenly distributed and generally parallel (Plate 1; Fig. 12). A disparity in amounts of extension across the KSW fault is due to the

differences in extension in the NW and SE domains. These differences are exemplified by the distance between the DT and MVT, however this disparity cannot be measured with confidence because the DT exists at depth (Plate 1).

The Miocene-Pliocene directions of extension north and south of the KSW fault zone are different when compared to previously suggested directions of Quaternary extension within BRP. Geodetic data show that contemporary extension is predominantly E-W within the BRP (Hammond and Thatcher, 2004; Kreemer et al., 2010). To the SW of the KSW fault zone the Wildcat Wash fault, and to the NW, the Coyote Spring fault both accommodate E-W directed Quaternary extension (Fig. 2; Page et al., 1990; Page and Pampeyan, 1996). In comparison, the Miocene-Pliocene extension in the SE domain is WNW-ESE, ~289º, and the Miocene-Pliocene NW domain extension is more NW-SE, ~307°. These new map data demonstrate that extension direction has changed through time.

The new map data also show that extension, including strike-slip and normal faulting, began in middle Miocene time or later; in particular many faults cut the ~15 Ma Kane Wash ash-flow tuff and are overlain by Quaternary alluvium. This timing is consistent with other faults in the NBR-CBR boundary zone. The left-lateral Maynard Lake fault to the north is shown to have both Quaternary and Miocene or later offset (Fig. 2; Muhammad, 2016). The eastern boundary fault for the NW domain – fault GB – abuts to the north against the Maynard Lake fault indicating that the NW domain has deformation that can be as old as Miocene. In addition, no extensional faults that cut only Paleozoic rocks or Paleozoic rocks and only part of the tuff section were identified. This lack suggests that extension did not begin until after the deposition of the youngest tuff cut, the ~15 Ma Kane Wash Tuff. This timing of onset of extension is similar to that in the CBR and

consistent with a major extensional period in the NBR (e,g., Taylor et al., 1989; Bidgoli et al., 2015).

Kane Springs Wash Fault Zone and the NBR-CBR boundary Zone

When considered within the context of the larger BRP rift, the boundary between the NBR and CBR is interpreted to be an E-W to NE-SW oriented long-lived zone of transfer faults defined by the KSW fault zone, Pahranagat shear zone, structures within the Timpahute lineament, and the Caliente-Enterprise zone (Figs. 1, 2, 3, 4; Taylor et al., 2022). These fault zones all strike at a relatively high angle to the Basin and Range rift boundaries (Figs.1, 2, 3) and have been interpreted as transfer zones (Fig. 2; Tschanz and Pampeyan, 1970; Faulds and Varga, 1998; Rowley, 1998; Bidgoli, 2005; Price, 2017; Evans, 2018; Peck, 2018; Gomes et al., 2018; Ely and Taylor 2018; Reed, 2019; Abdelhaleem et al., 2020; Reid et al., 2020; Taylor et al., 2022). Here, these structures are interpreted, all together, to form a major, broad tectonic and geomorphic boundary zone in the Miocene to Quaternary that separates the NBR subprovince from the CBR subprovince. This boundary zone is evident in structures active as old as Miocene , modern seismicity in the southern Nevada seismic belt, modern topography, gravity data, and the terminations of ~N-S striking normal faults against the E-W to NE-SW left-lateral faults (Figs. 1, 2, 3, 4; Ekren et al., 1976; Jayko, 1990, 2007; Dohrenwend, et al., 1996; dePolo, 1998; Kucks, 1999; Kucks et al., 2006; Kreemer et al., 2010; dePolo and dePolo, 2012). The boundary zone, thus, has the characteristics of and appears to be a rift segment boundary. Notably, the width of the NBR-CBR boundary changes along the trend of this zone, which is consistent with slip transfer among faults (Figs. 1, 3, 4). From these data, I interpret the KSW fault zone as the southernmost fault within the NBR-CBR boundary zone in its widest part.

During the Miocene-Quaternary, the NBR-CBR boundary zone has likely performed as a transfer zone and rift segment boundary in which different structures may have been active through time. Within the NBR-CBR boundary zone, the most recent faulting youngs southward, suggesting that deformation is focused southward towards the KSW fault zone through time. All of the structures were active in Miocene-Pliocene time, but the northern-most structures were abandoned by Quaternary time. Faults of the Timpahute lineament, at the northernmost edge of the NBR-CBR boundary zone, do not have any indication of Quaternary displacement along these E-W-striking structures. Much of the motion on faults of the Timpahute lineament post-dates the ~18.5 Ma Hiko Tuff and the faults are overlain by Quaternary deposits – that is, most deformation occurred during Miocene or Pliocene time (Tschanz and Pampeyan, 1970; Taylor et al., 2000; Bidgoli, 2005, Abdelhaleem et al., 2020; Reid et al., 2020). However, some evidence, such as the southern limit of the Oligocene Seaman breakaway-Stampede detachment system, suggests that the Timpahute lineament may have been active during Oligocene time (Fig. 2; Taylor and Bartley, 1992; Axen et al., 1993). Map data within the PSZ provides evidence of post ~15 Ma Miocene-Pliocene offset along all faults and Quaternary offset along its boundary faults on the northwest and southeast but does not have Quaternary fault scarps within its interior (Muhammad, 2016; Price, 2017; Evans, 2018; Peck, 2018; Ely and Taylor, 2018). The KSW fault zone has evidence of both post~15 Ma Miocene-Pliocene and active Quaternary deformation (Plate 1; Figs. 5, 6, 13; Pampeyan, 1993; Swadley et al., 1994; Anderson, 1999; Abdelhaleem et al., 2020; Reid et al., 2020). These age relations suggest that the NBR-CBR boundary zone has either migrated slightly southward through time or the zone initiated as a wide zone and the Miocene and Quaternary fault activity has been focused in the southern portion with time.

Kane Springs Wash Fault and the Mormon Peak Detachment

The Mormon Peak detachment is a Miocene regional low-angle normal fault exposed ~25 km to the SE of the KSW fault zone in the CBR (Fig. 2; Wernicke et al., 1985; Wernicke et al, 1990; Axen, et al., 1990; Swanson and Wernicke, 2017). The Mormon Peak detachment was active at ~14-13 Ma based on structural relationships and low-temperature apatite and detrital zircon thermochronology (Bidgoli et al., 2015; Swanson and Wernicke, 2017). The ~15 Ma KSW caldera is post-dated by both the KSW fault zone and the Mormon Peak detachment, thus, the age brackets allow the possibility that they operated synchronously. The E-W to NE-SW (~275º) extension direction of the Mormon Peak detachment is similar to the slip direction of the KSW fault zone proper and the direction of extension across it. (Figs. 2, 5; Wernicke et al., 1985; Wernicke et al., 1990; Axen et al., 1990). To assess whether it is possible that the Mormon Peak detachment underlies the study area in the Meadow Valley Mountains, estimates of the depth of the Mormon Peak detachment zone were made. The estimates are based on projecting it from the nearest exposures using a dip of ~20°-25° to the NW which suggests that the detachment exists at a depth of ~ 9 km beneath the Meadow Valley Mountains (cf., Stockli et al., 2002; Bidgoli et al., 2015; Swanson and Wernicke, 2017). The average depth to the brittle-ductile transition zone in the BRP is ~10-15 km, a slightly greater depth. Based on the similarity in age, onset, overall extension direction, and spatial proximity, a genetic relationship between the KSW fault zone and the Mormon Peak detachment is possible. However, map relationships in this study cannot resolve that relationship. The data presented in this study allow the possibilities that the KSW fault (1) operates only within the upper plate of the Mormon Peak detachment, (2) that the KSW fault zone acted as a lateral termination of the Mormon Peak detachment and slip was transferred between them, (3) the KSW fault cuts the Mormon Peak detachment in the brittle realm, or (4)

the KSW fault zone is genetically linked in Miocene time to the Mormon Peak detachment, but has continued slip into the Quaternary independent of the detachment because no evidence has been presented that the Mormon Peak detachment has a Quaternary slip history. For reasons of timing of onset, spatial proximity, overall extension direction across both faults, and the interpretation that the KSW fault zone is a transfer fault that is part of the NBR-CBR boundary zone, the favored options are that the KSWF either cuts the Mormon Peak detachment or is the lateral boundary for it during the Miocene.

3-Dimensional Deformation

The KSW fault zone separates the generally 2-dimensional deformation of the SE domain from the fault network of the NW domain, which is suggested to accommodate 3-dimensional deformation. In Andersonian fault theory, conjugate normal faults develop with strikes perpendicular to the direction of the principal extension – this assumes no strike slip component along the faults. Such conjugate faults occur in plane strain, 2-dimensional deformation (Collanega et al., 2020). However, many models and examples of extensional fault networks are orthorhombic in map view and have faults that are not perpendicular to the primary extension direction (Krantz, 1989; Miller et al., 2007). These faults can develop stepwise through time or the faulting may be synchronous (Reches, 1983; Henza et al., 2010; Collanega et al., 2020). Fault networks, particularly orthorhombic normal faults, are oriented such that they accommodate overall extension in localities with complex strain fields and are documented in rift segment intersections such as in the Dead Sea basin or the East African rift system (Reches, 1983; Henza et al., 2010; Collanega et al., 2020). The suggestion of 3-dimensional deformation in the NW domain is based on (1) the non-parallel boundaries of the network and (2) the geometries, abutting fault terminations, and timing of faults within the network of synchronous N-S long

faults with two sets of cross faults (Plate 1; Figs. 2, 12; Reches, 1983; Wilkins and Schultz, 2003; Henza et al., 2010; Peacock, 2016; Collanega et al., 2020). The NW domain extensional network is contained within the hanging wall of the NNE-striking fault GB and the footwall of the N-striking Coyote Spring fault, forming a trapezoid-shaped block between them. A change in shape of the volume of rocks in the NW domain is required as faults move blocks with non-uniform shapes within the trapezoid. Thus, the deformation is likely 3-dimensional and achieves overall E-W extension between the non-parallel boundary faults, fault GB and the Coyote Spring fault. The NW domain fault x-nodes geometries have differing amounts of offset but do not offset each other, and thus, also suggest that deformation within the NW domain is 3-dimensional (Plate 1; Figs. 2, 12; Reches, 1983; Wilkins and Schultz, 2003; Henza et al., 2010; Peacock, 2016; Collanega et al., 2020).

Ecs and Eocene Drainages

The relatively immature texture of the clasts and the DZ grain analyses provided by T.S. Bidgoli and K. Moore (personnel communication) suggest that the sediment source for the Ecs unit is not solely the hanging-wall rocks of the DT because it includes zircons from Precambrian and Cambrian quartzite units not exposed in the DT plate. Given (1) our current understanding of the paleogeomorphology of the Sevier fold-thrust belt with a highland to the W and N of KSW (Taylor et al., 2000; Henry et al., 2008; Busby and Putrika, 2009; Long, 2012; Smith et al., 2014; Erdman et al., 2016; Smith et al., 2017; Cassel et al., 2018) and (2) that Precambrian and Cambrian quartzites are exposed in the Gass Peak thrust sheet just to the west (Plate 1; Figs. 2, 6, 11, 12), I suggest that the source for the Ecs unit lies to the current N and W of the Delamar Mountains in the Sevier hinterland highlands, which include the Gass Peak plate (Plate 1; Figs. 1, 2). In addition, the detrital zircon analyses (Appendix B) require that ~39 Ma source rocks or

pyroclastic air fall provide sediment to the basin. Rocks of that age in the region lie to the north and are primarily pyroclastic units of the ignimbrite flare-up (Best et al., 2013a, b). Thus, the ~39 Ma grains could have been delivered via ~N-S streams or could be from air fall. The Ecs streams and lakes, may have collected air fall, and occurred near the DT. The position of the DT relative to this highland strongly implies that DT was not a hinterland thrust and that the DT lies in an intermediate structural position, structurally lower than the hinterland thrusts and higher than the frontal thrust. Using these data, I interpret that Ecs represents the erosional denudation of the former Sevier hinterland during Eocene time and that it was deposited along a slope between the hinterland highland and the frontal thrusts.

Although the Eocene topographic maximum existed to the N and W of the Ecs unit (Figs. 1, 2, 5), the stratigraphic and structural relationships show that the Ecs unit was deposited in a setting with pre-existing paleorelief (Plate 1; Figs., 1, 13, 14, ;Busby and Putrika, 2009; Long, 2012; Best et al., 2013; Smith et al., 2014; Cassel et al., 2014; Erdman et al., 2016; Smith et al. 2017). The DT is not presently directly overlain by the Ecs unit in the Delamar Mountains, however, given that the lower imbrications of the DT are covered by the Ecs unit in the Delamar Mountains, it is likely that the DT plate made a local high at the base of which was the depositional basin for the Ecs unit (Fig. 13). Within the Meadow Valley Mountains, the new map data show that the Ecs unit unconformably overlies both hanging-wall and footwall rocks of the MVT. The conglomerate facies of the Ecs is thickest in the Delamar Mountains, while the limestone facies is thickest in the Meadow Valley Mountains. This change from proximal clastic sediments to freshwater carbonates is an indication that the Ecs drained S and E, and that the environment shifted to a low energy setting during the latter stages of deposition. In summary, the changes in relative thickness of the two different facies of the Ecs unit suggest that the thick

conglomerate package was proximally located to the highland earlier in Ecs deposition and that a topographic sink existed farther to the SE or E of the KSW area, such as the basin in which the Claron Formation was deposited (Taylor, 1993; Goldstrand, 1994). This drainage direction is consistent with the position of the Sevier hinterland to the N and W.

Because of the limited thickness and distribution of the Ecs, it is unlikely that the Ecs strata were deposited in a primary Eocene drainage but existed as a part of a potentially interconnected fluvial system that would be common to a slope from a hinterland highland to a basin nearer to or in the foreland. While the new data cannot show that the Ecs was part of a series of connected or isolated drainages, deposits that are of similar age, composition, and spatial position relative to the Sevier hinterland are exposed in the region. Such rocks exist nearby within the Pahranagat shear zone, Mount Irish, the Timpahute Range, the Wah Wah Mountains, the North Pahroc Range, and other mountain ranges (Tschanz and Pampeyan 1970; Taylor et al., 2000; Jayko, 2007; Davis et al., 2010; Muhammad, 2016; Price, 2017; Smith et al., 2017; Evans, 2018). These deposits could represent other portion(s) of the same drainage system. Several sedimentary rocks that represent eastward drainages off the Sevier hinterland farther north in the northern NBR are well documented (Smith et al., 2017). These drainages terminate in lakes – such as Lake Uinta, Claron, and Gosiute – that were proximally located to Sevier frontal thrusts and primarily deposited atop the footwalls of these thrusts (Smith et al., 2017). The Claron Formation, which is exposed to the E and N of KSW primarily in southern Utah, overlaps in age with the Ecs unit and sits above the conglomeratic Grand Castle Formation or Triassic to Cretaceous units (Bowers, 1972; Taylor, 1993; Goldstrand, 1994; Eaton et al., 2018; Sanjuan et al., 2020). These units could represent the generation of accommodation space, in the east, in response the topographic relief generated by Sevier-related deformation and to southwestward migrating dynamic

subsidence from slab rollback. The new data presented here, when taken in conjunction with the Eocene drainages suggest that a series of lakes and basins existed to the E of the Sevier hinterland highland and that the Sevier hinterland plateau was in part destroyed through erosion during Eocene time. Local reduction of the highland in the Miocene and later was increased by extension.

Sevier Thrusts

The stratigraphy, lithology and bedding attitudes across the DT in the Delamar Mountains are similar to that in separate Miocene fault blocks within the western Meadow Valley Mountains. These relations suggest that the DT occurs at shallow depth within the western Meadow Valley Mountains and is offset or reactivated by Miocene or later faulting. The gentle dip, stratal characteristics and facies of Cambrian strata exposed in both the Meadow Valley and Delamar mountains are similar and characteristic of the upper plate of the DT. Across faults MV1 and MV3, these strata are juxtaposed with Miocene ash-flow tuffs to the N and E, and Ordovician and Devonian rocks to the S and W (Plate 1; Figs.12, 14). These relations suggest that the DT occurs at shallow depth below the Ordovician and Cambrian units and was dropped down to the W by the Miocene faults MV1 and MV3. Fault MV3 locally places older over younger rocks because it cuts this thrust and has less offset than the thrust. Fault MV3 cannot be a reverse fault, because along strike it cuts and normally offsets both Miocene ash-flow tuff and Eocene paleorelief, and has the synthetic splay MV2 that cuts Miocene units. These relations also suggest that the Ordovician rocks in the hanging-wall block of fault MV4 – that exposes the low-angle normal fault –are part of the upper plate of the DT (Plate 1; Fig. 12).

The new map data lead to the suggestion that the DT and MVT are not the same thrust repeated by normal faults but part of the same imbricate stack with the DT being the highest and the MVT

being a lower imbricate. This interpretation is based on the bedding geometries, stratigraphic separation, and the close fault spacing of the DT and MVT within the KSW area. The stratigraphic separation of the DT is much greater than the stratigraphic separation of the MVT. The DT places Cambrian hanging-wall rock on top of Devonian footwall rock, while the MVT places Devonian rock in its hanging wall over Pennsylvanian rock (Map Plate). Miocene-Pliocene high-angle fault GB juxtaposes the uppermost and shallowly dipping plate of the DT adjacent to the lower imbricates, offsetting or reactivating the thrusts. The spatial and offset relations of the thrusts are characteristic of imbricate thrusts that functioned together and performed different roles in accommodating the along-strike changes in the Sevier belt at this latitude.

The Dry Lake thrust – exposed ~65 km to the south of the KSW – has a similar structural style, geometry, structural position within the Sevier belt, stratigraphic separation, and geometry as the DT and MVT imbricate system. The Dry Lake thrust sits in an intermediate structural position between the Sevier hinterland thrusts such as the Gass Peak thrust and the Sevier frontal thrusts like the Mormon and Muddy Mountain thrusts (Fig. 2). The Dry Lake thrust places Cambrian rock atop Devonian rock and has a structurally lower imbricate placing Devonian rock atop Pennsylvanian-Permian rock. The same pattern as our interpretations for the DT and the structurally lower MVT. Following the trace of the Dry Lake thrust along-strike northwards leads to the Bunker Hills folds which lie in the footwall of both the Dry Lake thrust and MVT or the MVT dies out southward into the Bunker Hills fold (Fig. 2). Thus, the Dry Lake and Delamar thrusts appear to be correlative.

Regional correlation of the Delamar and Dry Lake thrusts southwestward across the right-lateral Las Vegas Valley shear zone to thrusts that lay between the Wheeler Pass thrust, a Gass Peak

correlative, on the W and the frontal thrusts on the E are debatable (Figs. 1, 2). Both the Dry Lake and Valley thrusts previously were correlated to the SW to the Lee Canyon thrust and the Deer Creek thrust (Wernicke et al., 1988; Lundstrom et al., 1998; Page et al., 2005a, b). Both the Lee Canyon and Deer Creek thrusts contain lower Paleozoic rocks (Cambrian and Ordovician) in their hanging walls and upper Paleozoic and Mesozoic rocks in their footwalls (Fig. 2). The Lee Canyon thrust was previously suggested to be correlative to the Valley thrust across the Las Vegas Valley Shear zone, but the stratigraphic separation across the Lee Canyon thrust is more consistent with the Dry Lake thrust and DT (Fig. 2; Page et al., 2005a). The Lee Canyon thrust places Cambrian and Ordovician rocks atop Pennsylvanian-Permian rock, like the Dry Lake thrust and the DT but dissimilar to the Valley thrust which places Mississippian rocks atop Pennsylvanian-Permian rocks (Page et al., 2005b). The Deer Creek thrust also places Cambrian rocks atop Pennsylvanian rocks, similar to the Dry Lake and Lee Canyon thrusts. When taking into account the structural position, the relative stratigraphic separation, and the location of the Lee Canyon or the Deer Creek thrust when compared to the Valley thrust across the Las Vegas Valley shear zone it is difficult to support the conclusion that either the Lee Canyon or Deer Creek thrusts are laterally equivalent to the Valley thrust. It is far more likely that the Lee Canyon thrust is laterally equivalent to the Dry Lake thrust, and according to the interpretations proposed here, the DT.

The Wah Wah thrust, exposed ~160 km to the NE of KSW, is interpreted by this work, and others, to be the northward lateral equivalent of the DT (Taylor et al., 2000; Long, 2012). I concur and further interpret the DT correlative, the Dry Lake thrust, to be the southward lateral equivalent of Wah Wah thrust (Friedrich and Bartley, 2003; DeCelles, 2004; Yonkee and Weil, 2015). While the DT and MVT thrusts are not often considered in reconstructions of the Sevier

belt at this latitude, where typically only hinterland and frontal thrusts are considered, they play an important role in the final configuration in the Sevier belt.

Overprinted Deformation

Although it is common in overprinted terranes that younger deformation either obfuscates or exposes the older deformation, in the KSW area overprinting has done both. Overprinted deformation allowed for the exposure of older rocks used to complete the thrust correlation. The recognition of the DT in the Meadow Valley Mountains and this thrust correlation allowed for a more in-depth analysis of the slip of the KSW fault zone. Locally, older deformation related to the DT is such that it may have controlled some of the orientation expressed in Cenozoic extension from Miocene time such as fault GB but is unlikely to have controlled the youngest extension (Fig. 13). Although the DT is not well exposed at the surface its lower imbricates including the MVT are well exposed, both due to younger KSW-fault-zone-related deformation. The Miocene and younger faults offset and slightly obscure the former rugged highland constructed during Sevier-related deformation which built the basins for the deposition the Ecs rocks and subsequent ignimbrite-flareup-related tuffs. In general, Cenozoic extension created and/or exposed the many structures and stratigraphy vital to increasing our understanding in the KSW area and the BRP as a whole.

6. Conclusions

The KSW area exposes overprinted deformation in which Miocene-Quaternary faulting, including the Kane Springs Wash transfer fault zone and an associated rift segment boundary, overprinted a portion of the earlier Jurassic-Eocene Sevier fold-thrust belt. This part of the Sevier belt lies between the frontal thrusts and the hinterland highland. It includes the DT which is correlated to regional thrusts to the north and south.

The KSW Fault Zone

The KSW fault zone operates as a transfer zone with differing magnitudes, directions, and styles of extension in the NW and SE domains, which lie on opposite sides of it. The NW domain comprises a dense fault network with fault geometries and intersection relations that can only be accomplished through 3-dimensional deformation and slip transfer between the KSW fault zone and the fault network. In contrast, the SE domain includes faults that are relatively evenly spaced and transmit slip to or from the Wildcat Wash fault and the KSW fault zone. Slip from both the NW and SE domains is transferred to the KSW fault zone as strike slip. Left-lateral displacement along the KSW fault zone is ~14 km, ~2-5 km greater than that of the apparent left-lateral displacement of the KSW caldera wall that lies to the northeast of the map area. The disparity in amounts of left slip may be due to the differences in extension in the NW and SE domains and along-strike slip variations.

The KSW fault zone either operates independently from or is the lateral termination of the Mormon Peak detachment. Estimates of the depth of the Mormon Peak detachment beneath the Meadow Valley Mountains place it above the brittle-ductile transition zone indicating that the Mormon Peak detachment and the KSW fault zone could interact within the brittle zone at depth.

In addition, the two faults have similar slip directions. However, no direct or causal relationship can be determined from the new data.

The NBR-CBR boundary is a wide zone with significant left slip faults that spatially coincides with the Southern Nevada seismic belt and contains transfer faults: the KSW fault zone, the PSZ, and the faults of the Timpahute lineament. Gravity data, structures at a high angle to the rift boundaries, strike-slip faults, and a topographic ramp taken in combination with the spatially coincident Southern Nevada seismic belt suggest that the NBR-CBR boundary is broad and composed of transfer faults that segment the BRP. The NBR-CBR boundary zone accommodates the differences in extension between the NBR and CBR subprovinces from Miocene through Quaternary time. Thus, the NBR and CBR subprovinces are considered distinct rift segments, even though more work needs to be done on additional structures that compose the NBR-CBR boundary zone.

Eocene Conglomeratic Sediments

U-Pb analyses of detrital zircon grains from the Ecs show that at ~39 Ma sediment was sourced from Cambrian and older quartzites. These quartzites are not exposed in the upper plate of the DT but are well documented in the upper plate of the Gass Peak thrust and others that have equivalent structural positions in the Sevier retroarc fold-thrust-belt. Thus, those thrust plates, exposed to the north and west, are the likely sediment source area. These relations suggests that in the Eocene part of the Sevier hinterland highland was proximally located.

The Ecs was deposited atop the lowest imbricate of the DT stack and in a paleo-low showing paleorelief and that Sevier-related deformation had ceased in the KSW area at the time of deposition. The spatial distribution and sediment source area of the Ecs unit suggests that the paleorelief of the Sevier hinterland is a rugged highland whose topographic maxima existed to

the N and W of the KSW area. The Ecs unit was deposited on the DT footwall suggesting that the DT plate formed a local high. The structural position of the DT suggests that the Ecs unit was deposited atop the wedge of the Sevier fold-thrust belt.

Locally, the Ecs is representative of an eastward-draining fluvial and lacustrine system and was likely part of a larger system of potentially interconnected drainages across the Sevier wedge. Other lithologically similar deposits in similar structural and stratigraphic positions exist within the region. These rocks document an Eocene period of Sevier wedge and hinterland erosional denudation and tectonic quiescence prior to the ignimbrite flare-up.

Sevier thrusts: Delamar and Meadow Valley Thrusts

The DT and MVT are not the same thrust but part of the same imbricate stack with the DT being the highest thrust, the MVT being the middle imbricate of an imbricate stack, and an unnamed thrust being the lowest of the imbricate stack. The DT places Cambrian rock atop Devonian, the MVT places that same Devonian unit atop Pennsylvanian-Permian rock, with that Pennsylvanian-Permian rock being placed atop more Pennsylvanian-Permian rock

The DT occurs in the ranges on both sides of the KSW fault zone. In the Meadow Valley Mountains, latest Cambrian rock correlates to the DT plate in the Delamar Mountains; however, the thrust is not exposed because the DT was down-dropped along a normal fault. In the Delamar Mountains, the DT similarly is either cut out and down-dropped or reactivated by Miocene and later high-angle normal faults.

The DT is considered to be the southward equivalent to the Wah Wah system and is interpreted here to be the northward equivalent of the Dry Lake and Lee Canyon or Deer Creek thrust systems. The structural and stratigraphic relationships of the DT and MVT are consistent with thrusts southward in the Dry Lake thrust system and the Lee Canyon thrust system, all of which

occupy the structural position between major hinterland thrusts like the Wheeler Pass - Gass Peak thrusts and frontal thrusts like the Keystone and Mormon thrusts.

Overprinted deformation

Overprinted deformation provides the ability to use one deformation event to study the other, providing a more complete picture of the tectonic and deformation history of the area. In the KSW area the younger Cenozoic structures, the KSW fault zone and associated normal faults, exposed lower imbricates of the DT and obscured both the DT and MVT, but these relations provided the opportunity to use the thrust offsets to quantify the total left slip of the KSW fault zone as ~14 km. In addition, the map data revealed that Cenozoic overprinting of the Sevier-related structures did not lead to the earlier structures controlling the orientation of the majority of the younger ones.

In summary, detailed map data were used to suggest that the Cenozoic KSW fault zone is a left-lateral transfer fault that (1) separates distinct normal fault domains, (2) forms part of a broad strike-slip rift segment boundary between the NBR and CBR, and (3) offsets the DT of the Sevier belt as well as post-thrusting paleorelief and sedimentary deposits, the Ecs. The DT correlates regionally to the Wah Wah and Dry Lake thrusts which developed within the Sevier wedge. Rocks of this wedge were unconformably overlain by the Ecs, which has a maximum depositional age of ~39 Ma based on detrital zircon grains in a paleo-low adjacent to the main DT.

Appendix A: Plate 1–- Geologic Map of the Southwestern Kane Springs Wash Area

Plate is located in attachment one of supplemental material in ProQuest

Appendix B: Figures

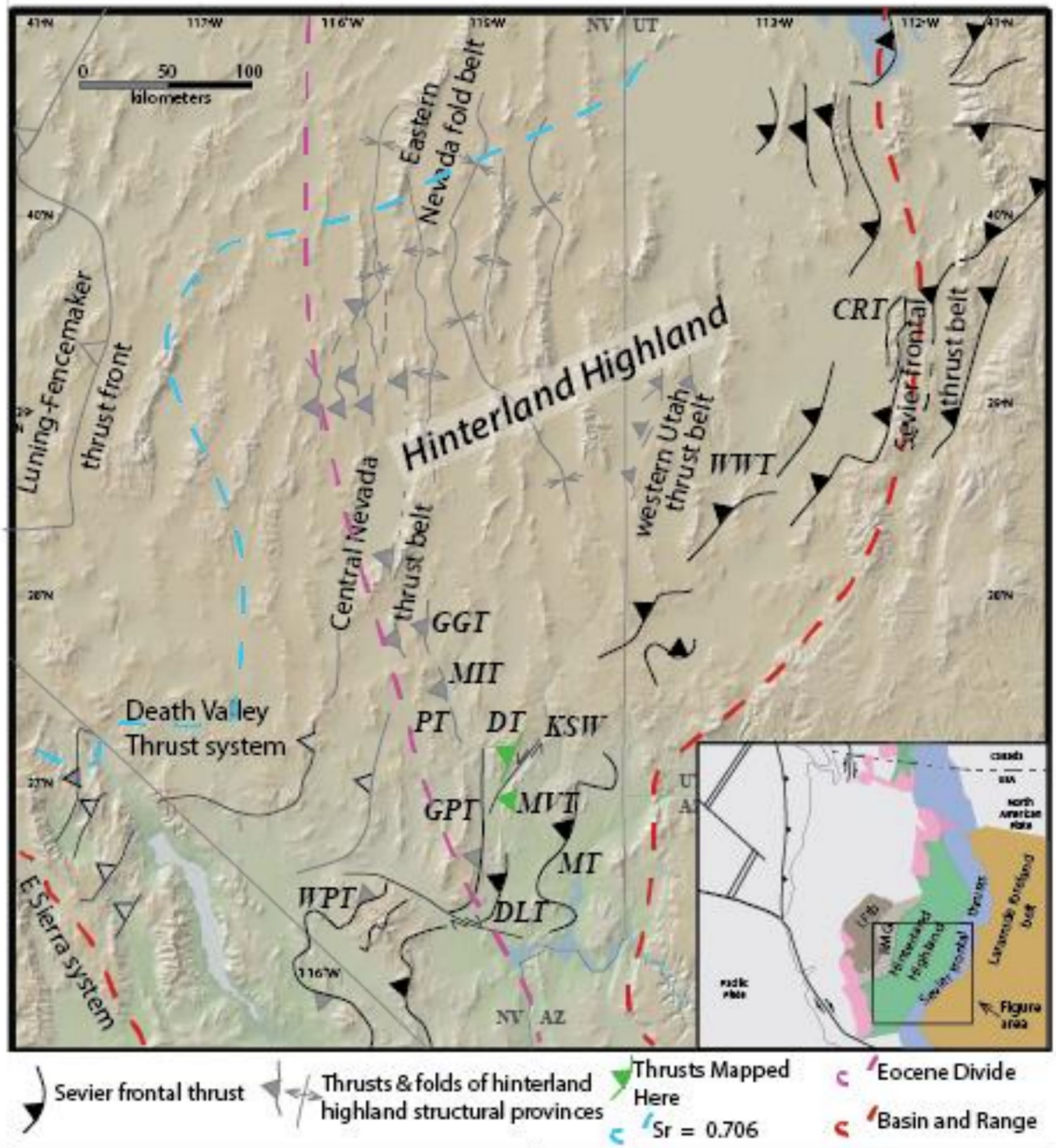

Figure 1: Regional structure and tectonic map. Map shows part of the Basin and Range province boundaries as red dashed lines. Sevier frontal thrusts are shown in dark black lines and hinterland thrusts shown in grey lines. Major thrusts are the Canyon Range thrust (CRT), Delamar thrust (DT, this study), Dry Lake thrust (DLT), Gass Peak thrust (GPT), Golden Gate thrust (GGT), Meadow Valley thrust (MVT, this study), Mormon thrust (MT), Mount Irish thrust (MIT), Pahranagat thrust (PT), Wah Wah thrust (WWT) and Wheeler Pass thrust (WPT). The Kane Springs Wash fault zone (KSW) is a Miocene-Quaternary left-lateral fault that cuts Sevier belt structures. The Eocene drainage divide (purple dashed line) separates drainages that draine ~E and ~W during Eocene time subparallel to the Sevier hinterland topographic maximum. The 0.706 $87^{Sr}/86^{Sr}$ inital ratio line (dashed blue line) shows the boundary between the continental lithosphere to the south and east and accreted rocks. Figure compiled from Taylor et al. (2000), Long (2012), Henry and John (2013), Arehart et al. (2013), Greene (2014), and Giallorenzo et al. (2018).

Figure 1: Regional structure and tectonic map

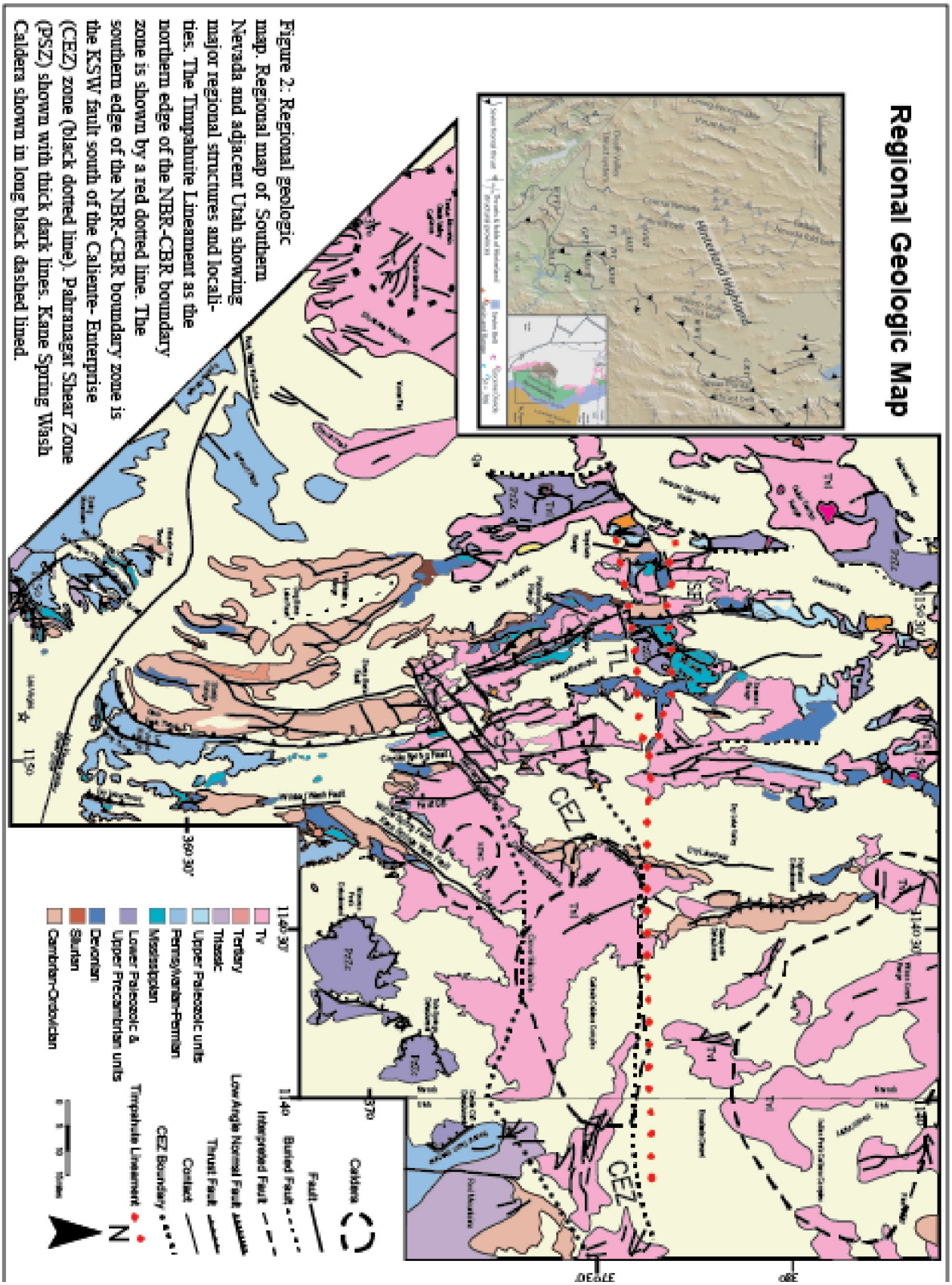

Figure 2: Regional geologic map

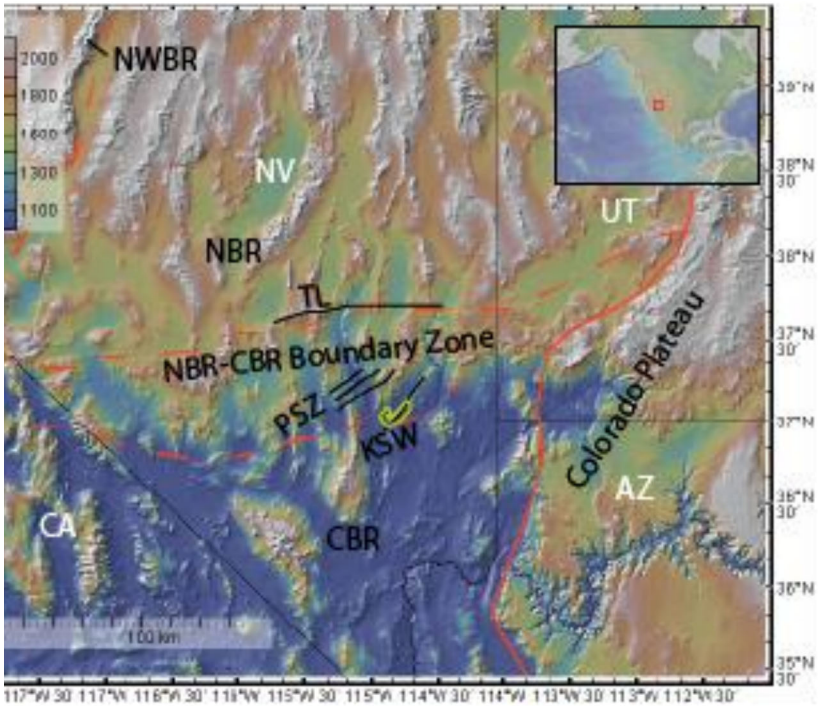

ure 3: Elevations of the Basin and Range province. Figure modified
m GeoMapApp (www.geomapapp.org; Ryan et al., 2009). Elevations of
NBR-CBR boundary zone showing an increase in average basin
vation across this zone. Basin elevations of ~1100 m (blue) are
mmon in the CBR, while elevations of ~1600 m (tan-green) are typical
he NBR. The states NV, CA, UT, and AZ are outlined in thin black
es. The Basin and Range is outlined in thick red lines. The NBR-CBR
ndary zone is outlined in a thick dashed red line where areas of E-W to
-SW topographic grain aid in defining the NBR-CBR boundary zone
ally. The Kane Spring Wash (KSW) fault zone study area outline in
low. The KSW fault zone, the Pahranagat shear zone (PSZ) and the
npahute lineament (TL) are shown by thick black lines (Ekren et al.,
76).

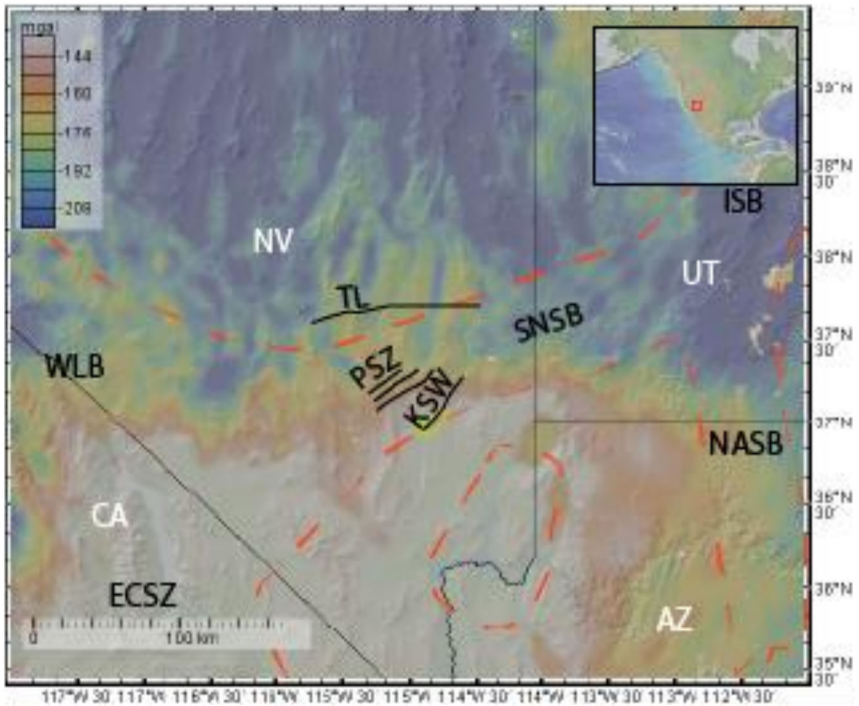

Fig. 4: Bouguer gravity anomaly map of the Basin and Range. Figure modified from GeoMapApp (www.geomapapp.org; Ryan et al., 2009). Bouguer gravity anomoly map overlaying topography (Kucks, 1999). The gravity anomaly near ~37 degrees N helps define the NBR-CBR boundary zone. The areas of significant seismic activity are outlined by a thick dashed red line; these areas include the Southern Nevada seismic belt (SNSB), the Walker Lane belt (WLB), the Eastern California Shear Zone (ESCZ), the Intermountain Seismic Belt (ISB) and the Northern Arizona Seismic Belt (NASB) (Kreemer et al., 2010). The Kane Spring Wash (KSW) fault zone study area is outlined in yellow. The KSW fault zone, the Pahranagat shear zone (PSZ), the Timpahute lineament (TL) - listed from south to north - are shown by thick black lines.

Figure 3: Elevations of the Basin and Range province

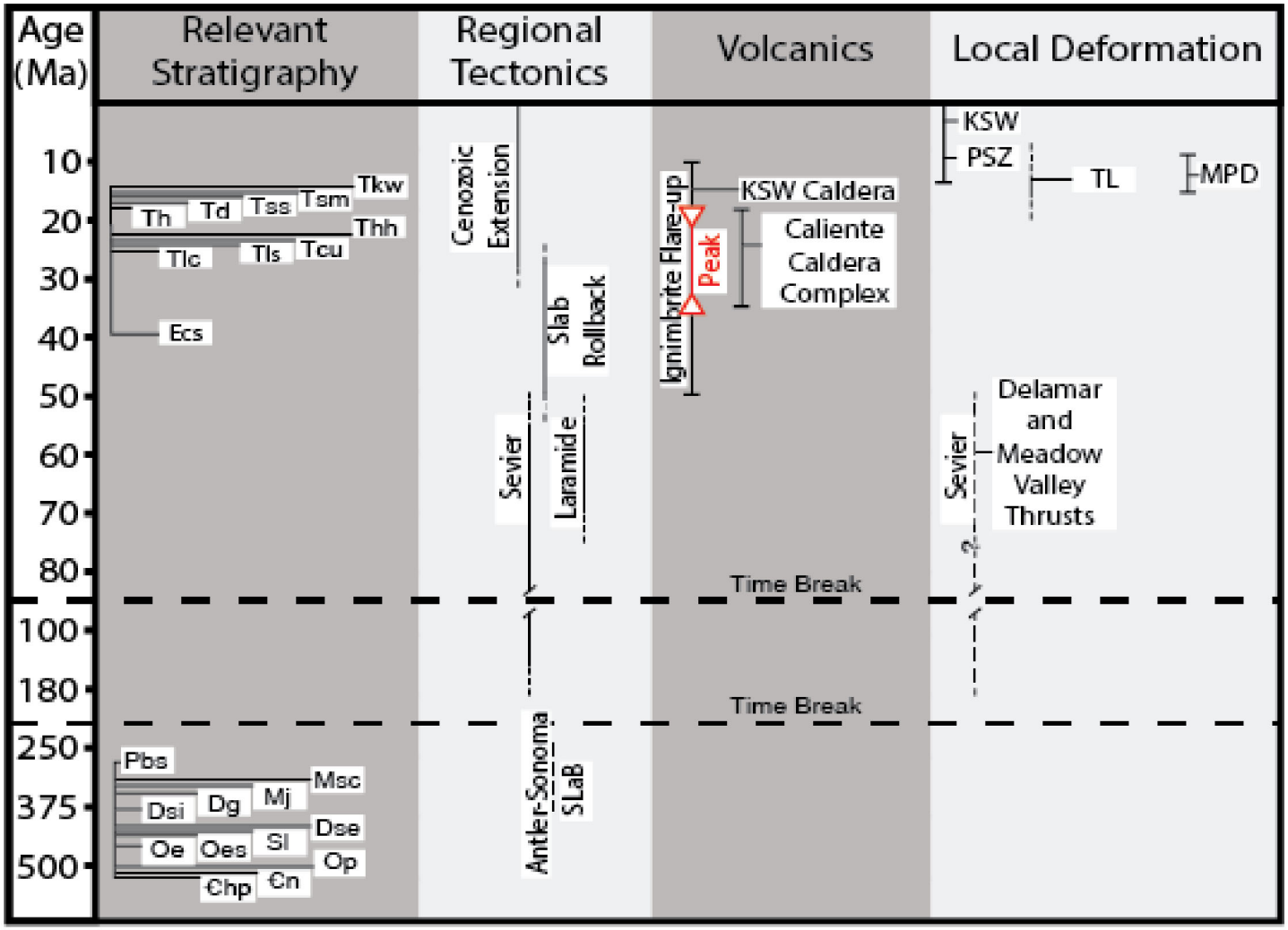

Figure 5: Timing chart. A timing chart showing the timing of major depositional and tectonic events relevant to the history of the KSW area. Unit abbreviatio are the same as Plate 1, and stratrigraphic columns Figure 6 and Figure 7. The peak of the ignimbrite flare-up is shown in red (Best et al., 2009; Best et al., 201 2013b, 2016). The timing of the Kane Springs Wash fault zone (KSW), Pahranagat shear zone (PSZ), Timpahute lineament (TL), and the Moromon Peak detachment (MPD) relative to each other is shown (Pampeyan, 1993; Anderson, 1999, Felger and Beard, 2010; Bidgoli et al., 2015; Giallorenzo et al., 2018; Bidgoli, 2020 personal commun.). Note deposition of the Eocoene conglomeratic sediments (Ecs), relative to the Delamar and Meadow Valley thrusts.

Figure 5: Timing chart

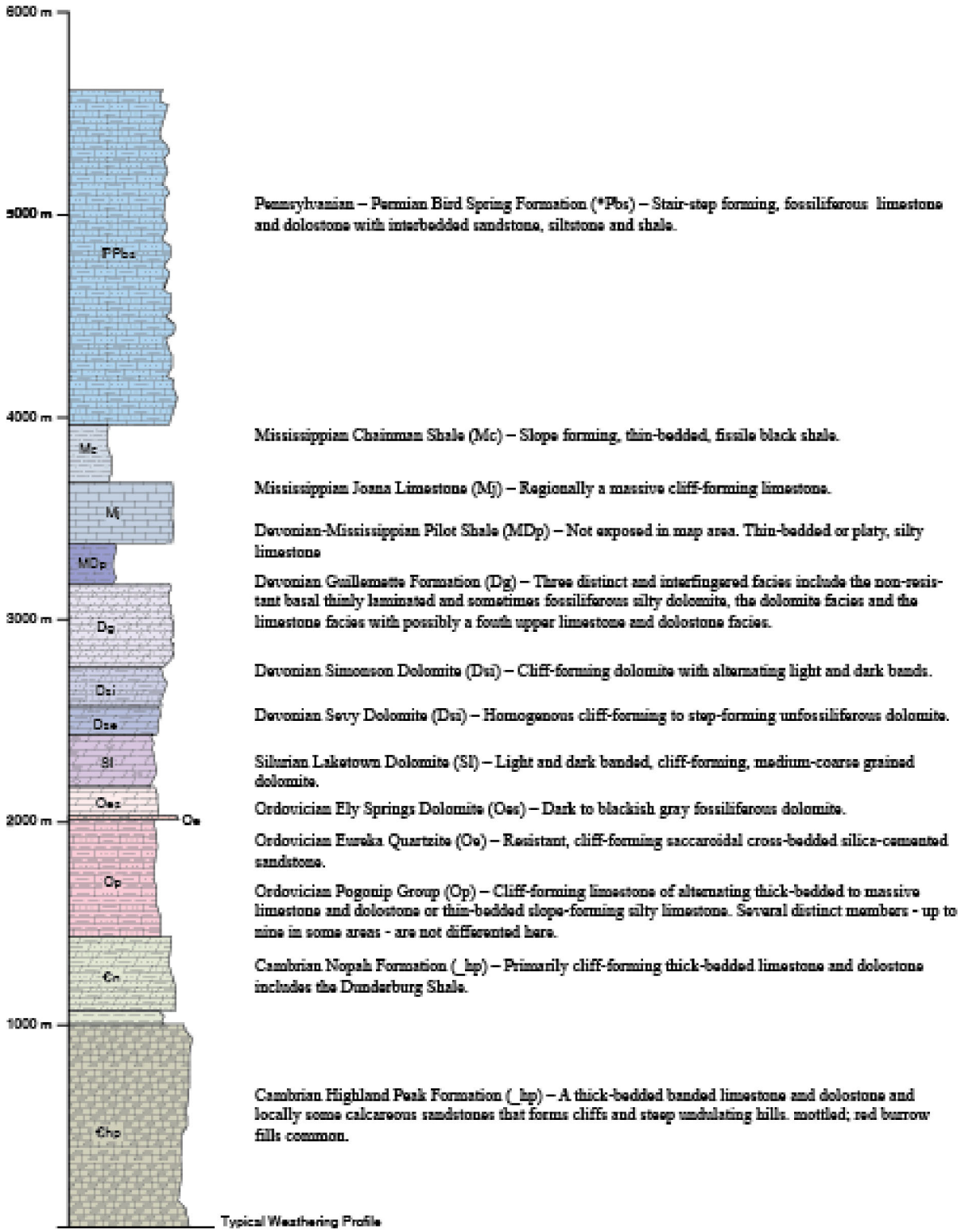

Figure 6: Paleozoic stratigraphic column. Paleozoic stratigraphy relevant to the Kane Springs Wash area. Right side of the the stratigraphic column shows the typical weathering profile. The unit thicknesses are derived from Tschanz and Pampeyan (1970), Page et al. (1990), Scott et al. (1990), Scott et al. (1993), Pampeyan (1993), and Swadley et al. (1994).

Figure 6: Paleozoic stratigraphic column

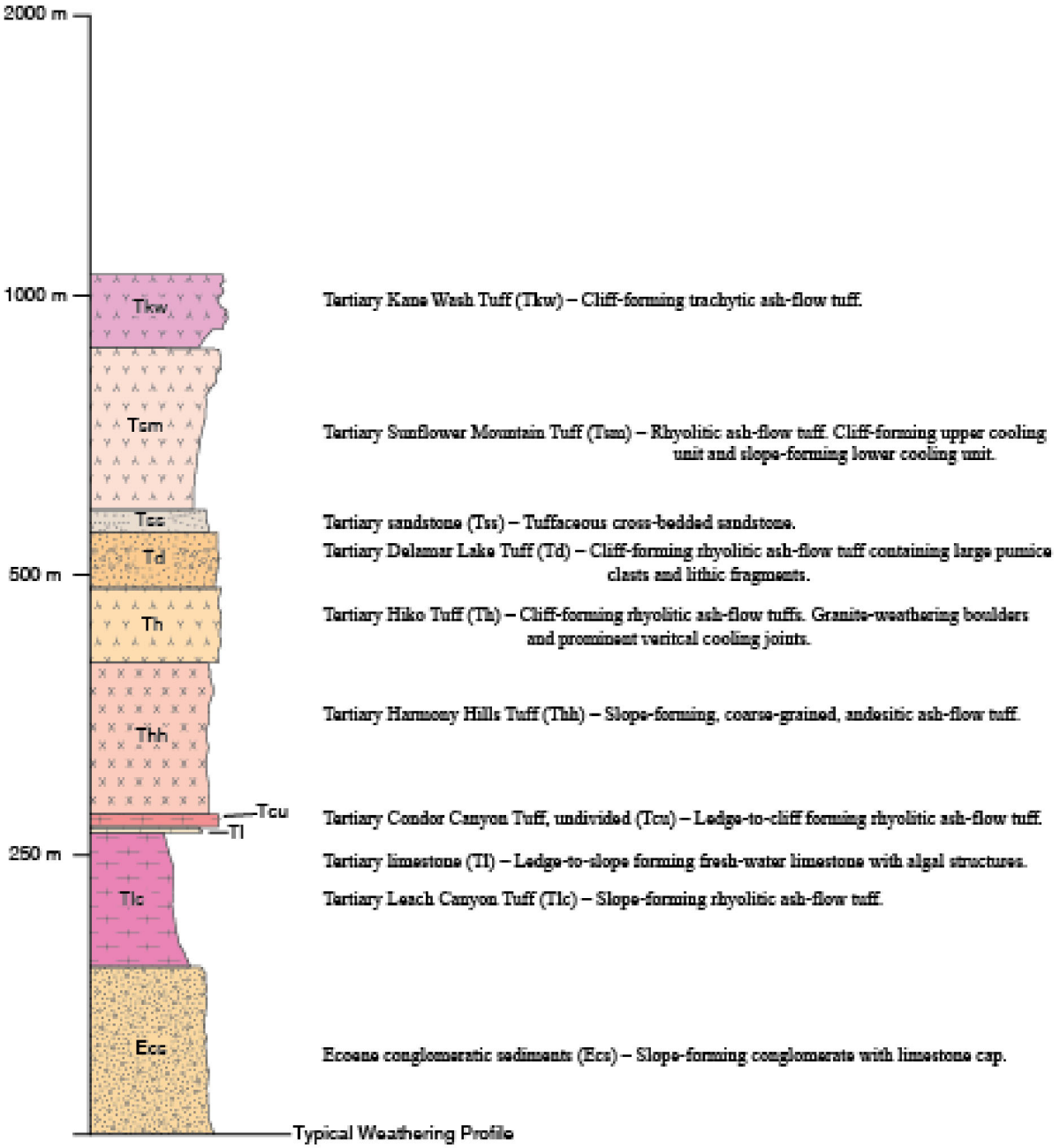

Figure 7: Tertiary stratigraphic column. Right hand side of the stratigraphic column shows the typical weathering profile. The unit thicknesses are derived from Page et al. (1990), Scott et al. (1990), Scott et al. (1993), Pampeyan (1993), Swadley et al. (1994), Best et al. (2006), Best et al. (2013a) Best et al. (2013b), and Page et al. (1990).

Figure 7: Tertiary stratigraphic column

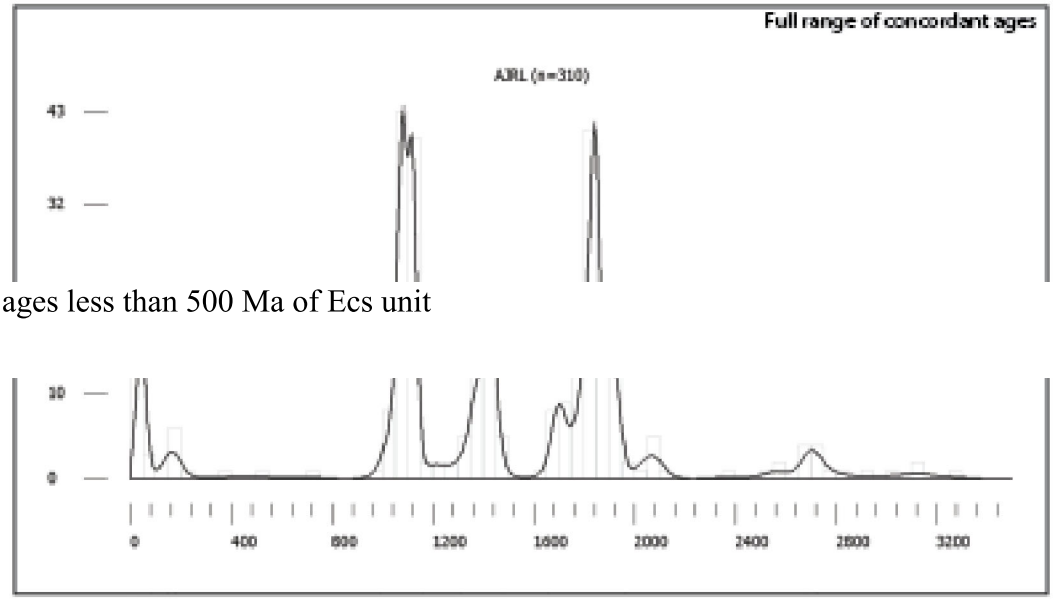

Figure 9: Concordant ages less than 500 Ma of Ecs unit

Figure 8 : Full range of concordant ages of Ecs unit. Full range of condorant ages from zircon grain samples taken from upper Eocene conglomeratic sediment unit (Ecs). Figure and data provided by T. Bidgoli (personal commun., 2020). Sample locations shown on Plate 1.

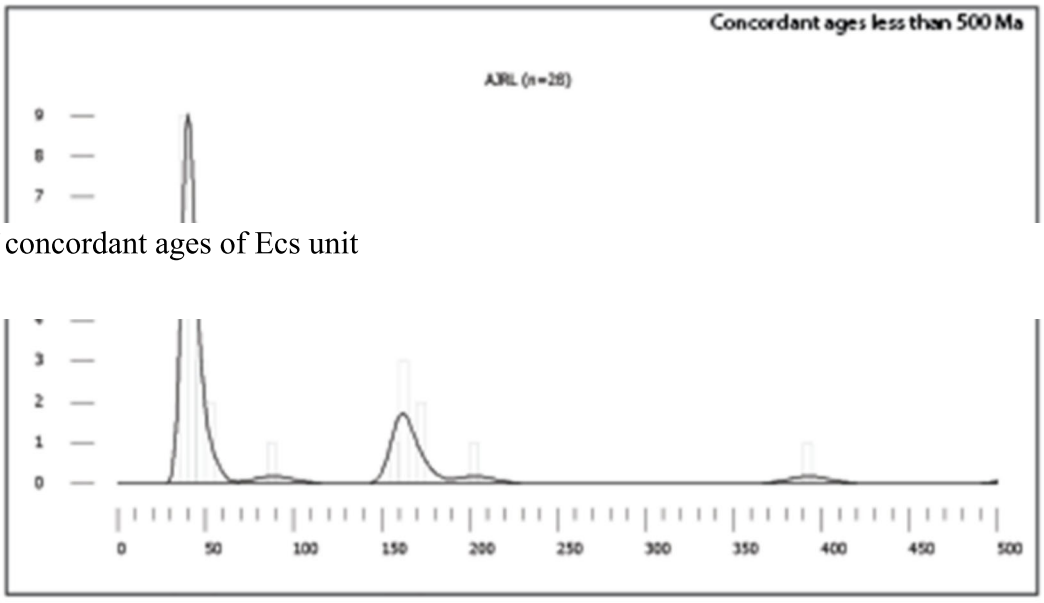

Figure 8: Full range of concordant ages of Ecs unit

Figure 9: Concordant ages less than 500 Ma of Ecs unit. Range of condorant ages from detrital zircon grain samples taken from upper Eocene conglomeratic sediment unit (Ecs) that are less than 500 Ma. Figure and data provided by T. Bidgoli (Appendix B; personal commun., 2020). Sample locations shown on Plate 1. Note late population at 39 Ma.

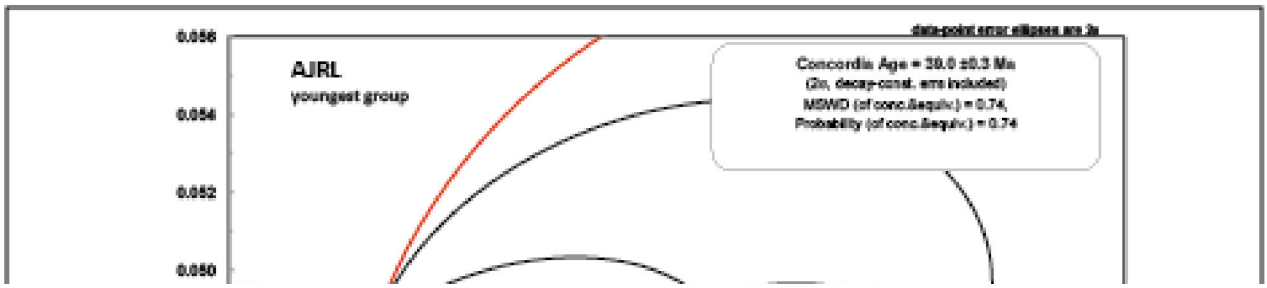

Figure 11: Detrital kernel density estimation

Figure 10: Detrital zircon concordant age plot

Figure 10: Detrital zircon concordant age plot. Concordia diagram that shows the maximum depositional age (39.0 +/- 0.3 Ma) of detrital zircon grain samples taken from upper Eocene conglomeratic sediment unit (Ecs). Figure and data provided by T. Bidgoli (personal commun., 2020). Sample locations shown on Plate 1.

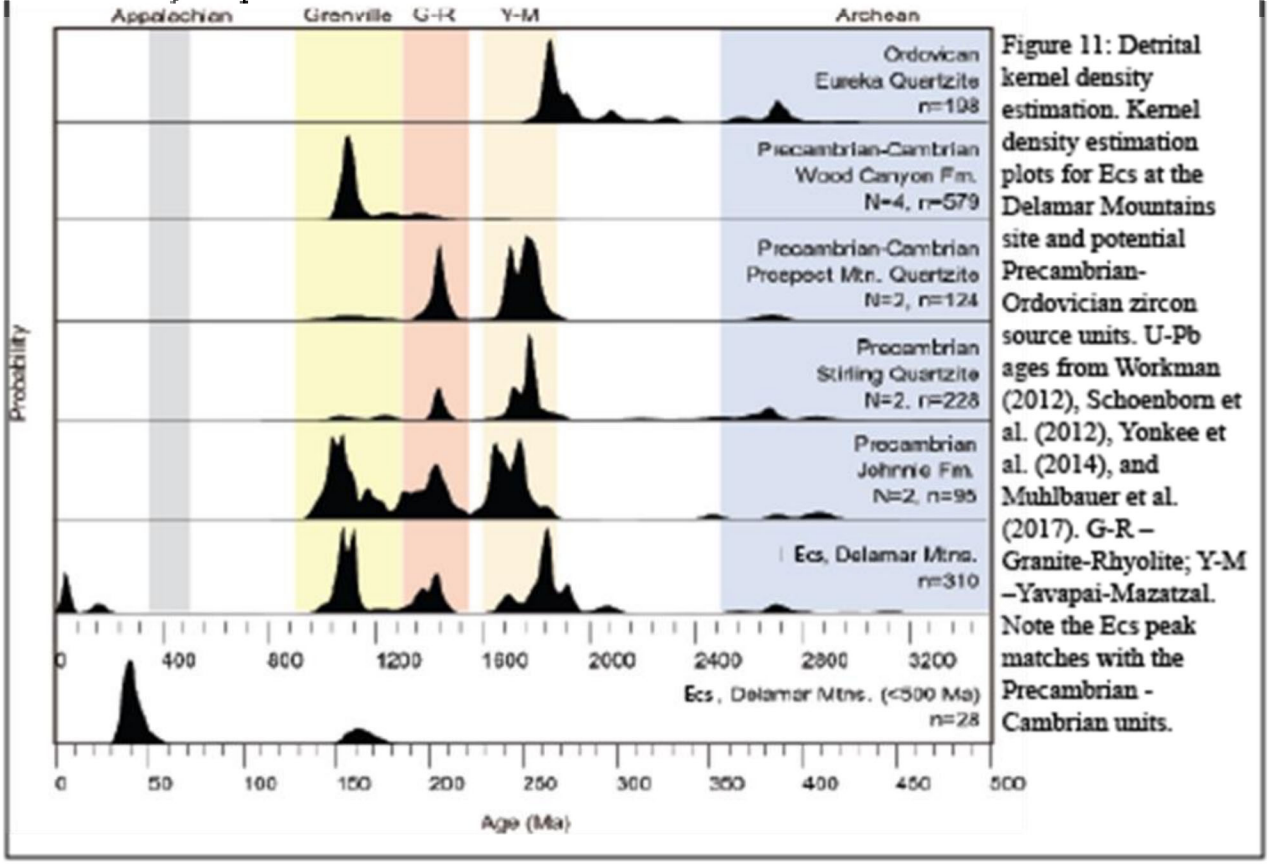

Figure 11: Detrital kernel density estimation. Kernel density estimation plots for Ecs at the Delamar Mountains site and potential Precambrian-Ordovician zircon source units. U-Pb ages from Workman (2012), Schoenborn et al. (2012), Yonkee et al. (2014), and Muhlbauer et al. (2017). G-R – Granite-Rhyolite; Y-M –Yavapai-Mazatzal. Note the Ecs peak matches with the Precambrian - Cambrian units.

Figure 12: Fault map, rose diagrams and stereographs

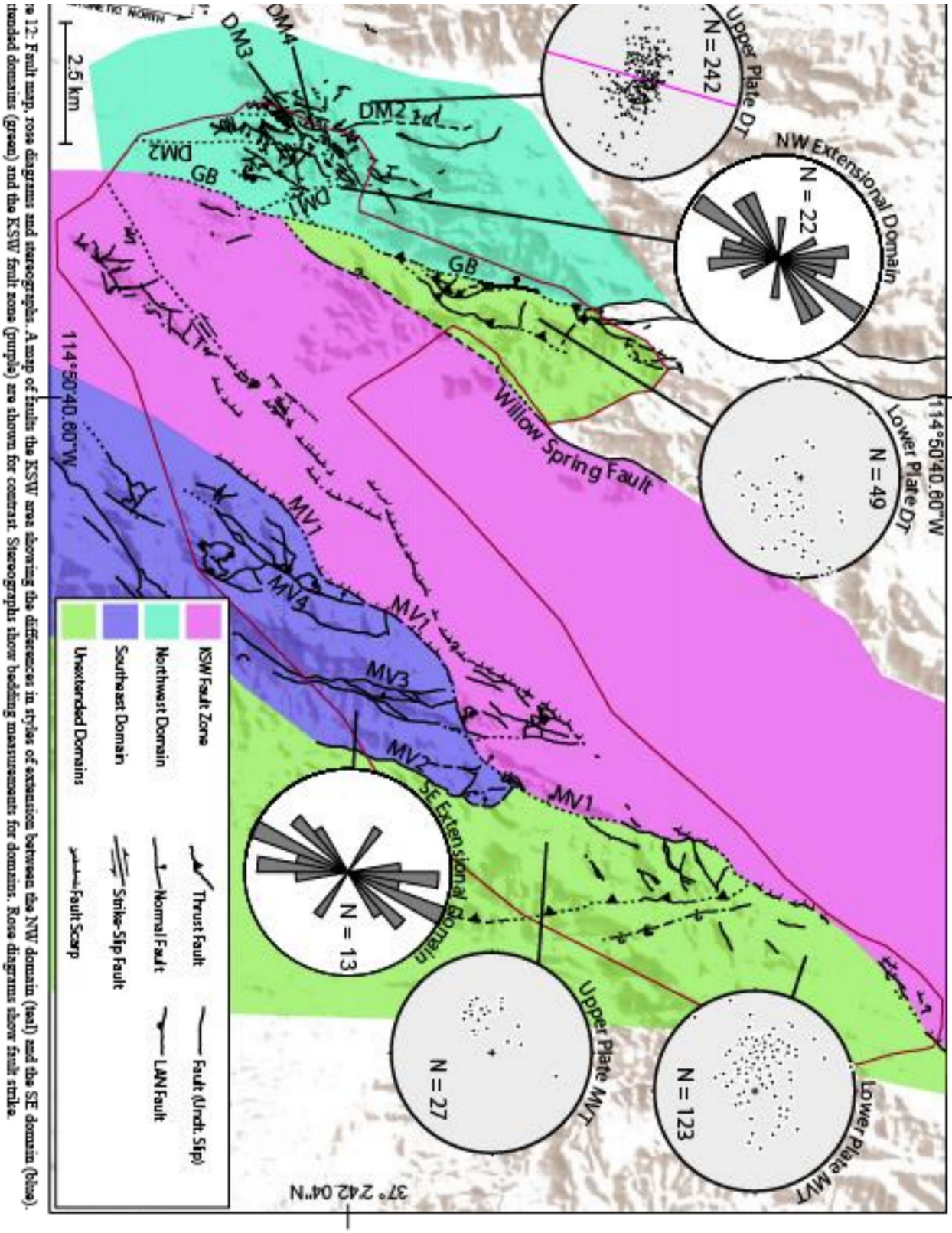

re 12: Fault map, rose diagrams and stereographs. A map of faults the KSW area showing the differences in styles of extension between the NW domain (teal) and the SE domain (blue). tended domains (green) and the KSW fault zone (purple) are shown for contrast. Stereographs show bedding measurements for domains. Rose diagrams show fault strike.

Figure 13: Diagrammatic maps of development through time

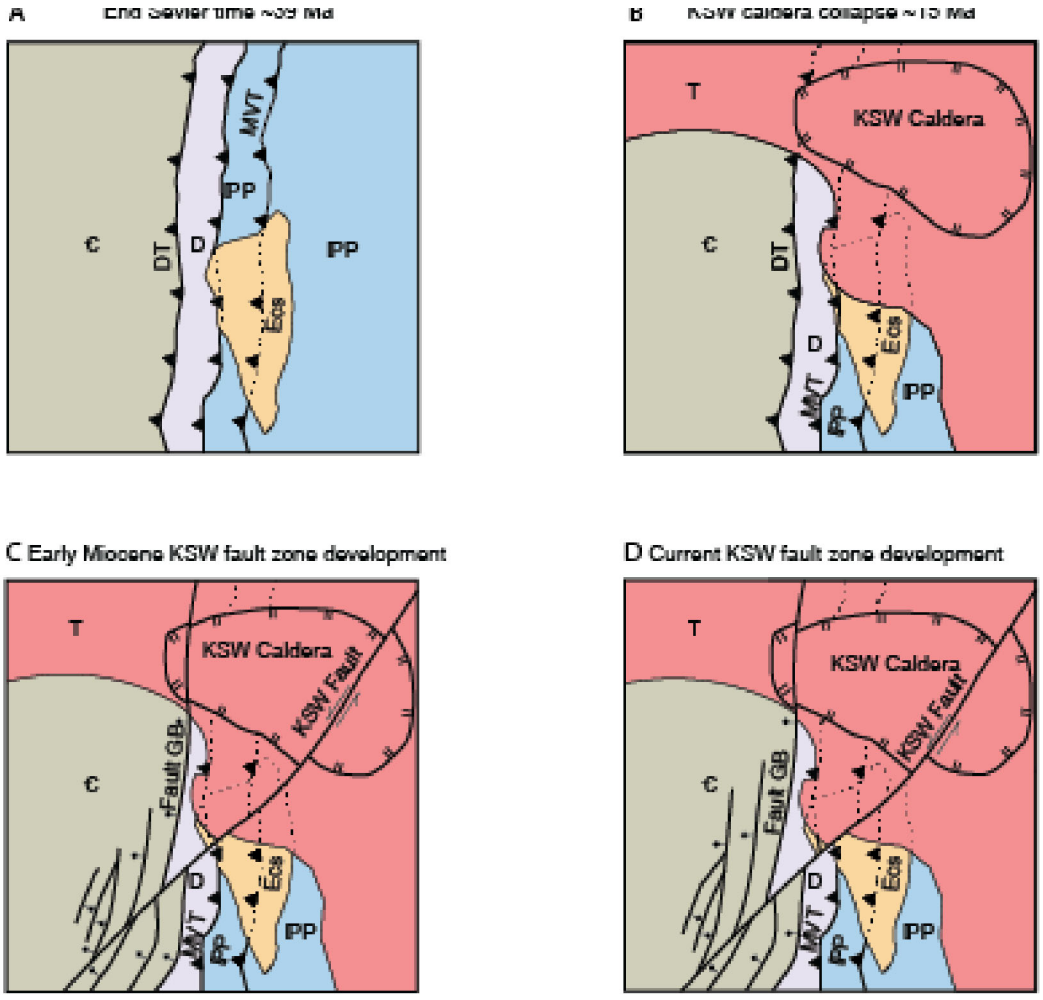

Figure 13: Diagrammatic maps of development through time.The stepwise block diagram showing a diagrammatic progression of the development of the Kane Springs Wash (KSW) area from the end of Sevier time after the depostition of the Eocene conglomeratic sediments (Ecs) unit. At ~39 Ma (A) the map shows, the Cambrian (C) upper plate of the Delamar thrust (DT) over the Devonian (D) upper plate of the Meadow Valley thrust (MVT) and the lowest Pennsylvanian-Permian lower plate overlain by the Ecs. Second (B) is showing the KSW fault area after the collapse of the KSW Caldera in which the caldera wall is shown in a thick dark line as a fault with hachures on the interior of the KSW caldera. Thirdly (C), The early development of the KSW fault zone, shown with diagramatic structural relationships developing, such as Fault GB, note the DT is no longer exposed at the surface but likely exists at depth with the development of the KSW fault zone. Finally (D), the current development of the KSW fault zone, with greater slip than in C, is shown with faults that transfer slip onto it and with quaternary valley fill omitted to clarify the diagramatic structural relationships.

Figure 14: Paleotopography illustrated from map relationships

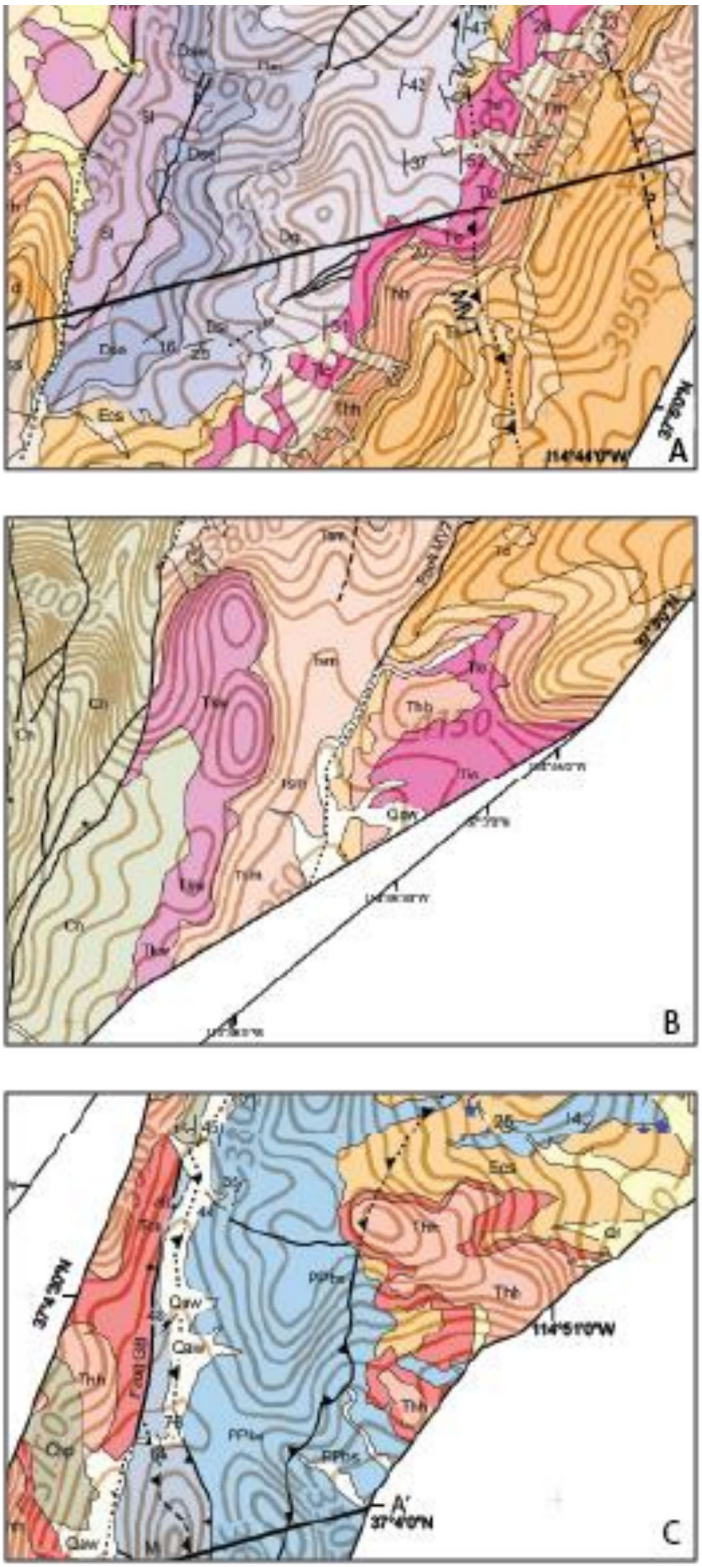

Figure 14: Paleotopography illustrated from map relationships. Figures show critical stratigraphic relationships illustrating former paleotopography as onlapping or buttressing of the Eocene conglomeratic sediments (Ecs) and ash-flow tuffs over the Meadow Valley thrust (MVT) and Paleozoic rocks. Note the Delamar thrust (DT) is not overlain by the Ecs. These relations suggest significant paleorelief along the sub-Tertiary unconformity. Unit labels are the same as in Figures 6 and 7

A. In the Meadow Valley Mountains the Ecs unit is overlain by ash-flow tuffs that together drape over the upper and lower plate of the MVT. Note that the Ecs unit does not completely overlie the upper plate of the MVT such that the Dg formed the upper part of a paleohill.

B. In the Meadow Valley Mountains, the uppermost and youngest ash-flow tuff (Tkw) banks against former topographic highs of the upper plate of the DT composed of Cn and are down-dropped along a normal fault adjacent to lower tuffs.

C. In the Delamar Mountains, the Ecs unit and overlying ash-flow tuffs overlie the lowest imbrication of the MVT and buttress against its upper plate. Note the draping of the ash-flow tuffs over the Cambrian rocks in the upper plate of the DT on the left side of map.

Appendix C: Detrital Zircon Data Tables from T. Bidgoli (2020)

The detrital zircon grains analyzed are double-dated using the U-Pb and (U-Th)/He methods to determine depositional age and provenance (Campbell et al., 2005; Reiners et al., 2005; Dickinson & Gehrels, 2009, 2010; Saylor et al., 2012). A total of 347 grains were picked from samples collected from deposits that overlie the lowest imbricate of the MVT for U-Pb laser ablation inductively coupled plasma mass spectrometry analysis at the University of Kansas, Isotope Geochemistry Laboratory. Analysis of this large number (~300) of grains ensures that the entire range of zircon age populations are captured and can undergo statistical tests required to provide robust data (Sircombe, 2000; Fedo et al., 2003; Jackson et al., 2004; Vermeesch, 2004; Andersen, 2005; Pullen et al., 2014; Saylor & Sundell, 2016).

Sample Name:	AJRL_22	AJRL_86	AJRL_171	AJRL_99	AJRL_158	AJRL_204
Grain #	22	86	171	99	158	204
[U] ppm	84.458	341.5595	386.053	400.9305	379.1315	155.463
U/Th	1.776	6.03	6.14	5.19	5.43	2.127
Pb207_U235	0.0388	0.0383	0.0385	0.0377	0.0384	0.0403
2σ error	0.0074	0.002	0.0021	0.0023	0.002	0.0041
Pb206_U238	0.00596	0.00599	0.00602	0.00602	0.00603	0.00606
2σ error	0.00027	0.00013	0.00012	0.00011	0.00012	0.00019
206_238:207_235 error	0.045436	0.018743	0.026814	0.03368	0.06932	0.078938
Final207_206	0.0492	0.0471	0.0463	0.0457	0.046	0.05
Final207_206_Prop2SE	0.0097	0.0028	0.0025	0.003	0.0025	0.0052
Age Ma	38.3	38.1	38.3	37.6	38.3	40.5
2σ error	7.2	2	2.1	2.2	2	3.9
Age (Ma)	38.3	38.52	38.67	38.71	38.78	38.9
2σ error	1.7	0.82	0.74	0.73	0.79	1.2
Age (Ma)	150	70	60	10	40	170
2σ error	320	110	100	120	100	190
(Ma)	38.3	38.52	38.67	38.71	38.78	38.9
2σ error	1.7	0.82	0.74	0.73	0.79	1.2
% Discordance*	101.6	100.8	107	106.4	105.9	103.7
%error	2.7	3.6	13	6.8	6.9	4.9

%error	7.2	7	7.5	8.2	5.5	6.2	5.1	5.1	4.1	6.6
% Discordance*	103.6	107.1	105.9	99.4	99.7	104.9	102.8	100	100.7	99.2
2σ error	0.64	0.7	0.74	0.69	0.7	0.9	0.82	1.1	1.1	1.5
(Ma)	39.2	39.24	39.65	40.79	41.48	41.59	41.62	44	45.8	45.9
2σ error	68	76	99	81	81	83	80	130	130	250
Age (Ma)	30	83	117	18	73	29	1	140	110	-70
2σ error	0.64	0.7	0.74	0.69	0.7	0.9	0.82	1.1	1.1	1.5
Age (Ma)	39.2	39.24	39.65	40.79	41.48	41.59	41.62	44	45.8	45.9
2σ error	1.4	1.5	2	1.6	1.6	1.8	1.7	2.6	2.8	6.5
Age Ma	38.8	39.2	40	40	41.7	40.9	40.6	44.8	45.9	43.8
Final207_206_Prop2SE	0.0016	0.0018	0.0024	0.0019	0.0019	0.002	0.002	0.0032	0.0032	0.007
Final207_206	0.0462	0.0473	0.0481	0.0461	0.0472	0.0461	0.0455	0.0488	0.0481	0.0448
206_238:207_235 error	0.2854	0.19237	0.13639	0.031568	0.021523	0.29003	0.19411	0.16238	0.19032	0.1
2σ error	0.0001	0.00011	0.00012	0.00011	0.00011	0.00014	0.00013	0.00017	0.00018	0.00024
Pb206_U238	0.006099	0.006106	0.00617	0.006348	0.006456	0.00647	0.00648	0.00684	0.00714	0.00714
2σ error	0.0014	0.0015	0.0021	0.0016	0.0016	0.0018	0.0017	0.0026	0.0028	0.0066
Pb207_U235	0.039	0.0394	0.0402	0.0402	0.042	0.0412	0.0408	0.0452	0.0463	0.0437
U/Th	4.78	5.467	5.91	2.013	2.021	4.91	4.111	1.959	1.284	1.975
[U] ppm	604.388	461.317	378.5935	450.1035	496.17	549.7795	572.9965	488.755	449.675	72.955
Grain #	95	37	2	49	1	176	82	15	194	78
Sample Name:	AJRL_95	AJRL_37	AJRL_2	AJRL_49	AJRL_1	AJRL_176	AJRL_82	AJRL_15	AJRL_194	AJRL_78

%error	10	19	28	25	22	28	38	32	18	71
% Discordance*	96	81	93	86	94	104	107	98	52	40
2σ error	1.1	2.3	1.7	1.5	3.2	2.8	2.4	3.9	3.8	2.5
(Ma)	46.2	51.7	52	88.8	159.9	160.8	161.2	162	170.1	171.2
2σ error	110	300	140	79	120	85	68	160	69	61
Age (Ma)	-20	-120	140	100	100	165	124	230	216	175
2σ error	1.1	2.3	1.7	1.5	3.2	2.8	2.4	3.9	3.8	2.5
Age (Ma)	46.2	51.7	52	88.8	159.9	160.8	161.2	162	170.1	171.2
2σ error	2.8	8	4.4	3.8	8.4	6.6	4.8	12	6	4.6
Age Ma	45.9	46.1	52.1	88.8	158.3	161.9	158.8	166	171.5	172.4
Final207_206_Prop2SE	0.0028	0.0076	0.0035	0.0019	0.0028	0.0021	0.0016	0.0042	0.0016	0.0014
Final207_206	0.045	0.0425	0.0492	0.0476	0.0475	0.0492	0.0483	0.0514	0.0506	0.0496
206_238:207_235 error	0.12875	0.22637	0.56776	0.30639	0.053479	0.24474	0.067445	0.1	0.55982	0.18844
2σ error	0.00018	0.00036	0.00027	0.00024	0.00051	0.00045	0.00039	0.00061	0.0006	0.0004
Pb206_U238	0.00719	0.00805	0.0081	0.01386	0.02511	0.02526	0.02533	0.02545	0.02674	0.02691
2σ error	0.0028	0.0083	0.0046	0.0041	0.0097	0.0076	0.0055	0.014	0.0071	0.0053
Pb207_U235	0.0463	0.0465	0.0528	0.0915	0.1694	0.1735	0.1695	0.179	0.1834	0.1846
U/Th	1.28	2.2	1.82	3.356	1.575	2.501	0.904	1.505	5.7	1.927
[U] ppm	270.3	223.445	619.9	337.972	103.4475	138.4915	257.8575	48.6236	559.85	568.33
Grain #	135	23	16	9	79	175	219	24	66	282
Sample Name:	AJRL_135	AJRL_23	AJRL_16	AJRL_9	AJRL_79	AJRL_175	AJRL_219	AJRL_24	AJRL_66	AJRL_282

%error	45	21	24	22	2.3	4.6	32	2.5	8.3	7
% Discordance*	8	-2	-20	-15	0.9	0	-39	-1.2	-3	-3.2
2σ error	3.6	7.5	8.3	11	10	15	19	14	18	14
(Ma)	202.9	393.1	517.8	702.8	990.3	991	999	1024	1031	1052
2σ error	42	61	62	76	30	41	79	34	68	56
Age (Ma)	223	472	530	721	1009	1007	982	1022	1079	1097
2σ error	3.6	7.5	8.3	11	10	15	19	14	18	14
Age (Ma)	202.9	393.1	517.8	702.8	990.3	991	999	1024	1031	1052
2σ error	3.8	9.9	12	17	9.9	11	24	11	20	17
Age Ma	203.7	402.8	518	703	996.3	991.6	998	1022.5	1039	1066
Final207_206_Prop2SE	0.0009	0.0016	0.0016	0.0022	0.0011	0.0015	0.0029	0.0012	0.0026	0.0021
Final207_206	0.05063	0.0559	0.0579	0.0634	0.07284	0.073	0.0708	0.07318	0.0756	0.0759
206_238:207_235 error	0.59367	0.34144	0.34759	0.11708	0.43354	0.17684	0.068755	0.6368	0.23541	0.10908
2σ error	0.00058	0.0012	0.0014	0.0019	0.0019	0.0027	0.0034	0.0025	0.0032	0.0026
Pb206_U238	0.03198	0.0629	0.0835	0.1152	0.1659	0.1661	0.1677	0.1722	0.1731	0.177
2σ error	0.0046	0.015	0.019	0.035	0.026	0.029	0.065	0.031	0.056	0.049
Pb207_U235	0.2222	0.487	0.666	0.996	1.665	1.657	1.677	1.738	1.79	1.857
U/Th	3.27	3.457	1.904	2.1	4.76	14.41	2.699	9.87	2.571	1.778
[U] ppm	1057.795	320.351	86.723	38.1258	201.93	181.5576	23.15005	378.93	32.4918	53.298
Grain #	170	166	328	157	240	294	222	238	142	299
Sample Name:	AJRL_170	AJRL_166	AJRL_328	AJRL_157	AJRL_240	AJRL_294	AJRL_222	AJRL_238	AJRL_142	AJRL_299

%error	4.3	5.8	1.7	4.6	14	2.4	5.3	2.4	12	4.3
% Discordance*	-0.3	-6.7	2.2	0.7	-11	2.1	-0.2	0.9	-16	-1.2
2σ error	14	15	11	16	21	13	14	12	16	22
(Ma)	1054	1055	1060.4	1063	1063	1063.7	1065	1065.5	1066	1066
2σ error	44	48	26	49	77	33	55	31	73	40
Age (Ma)	1073	1030	1085	1080	1020	1079	1076	1081	1059	1062
2σ error	14	15	11	16	21	13	14	12	16	22
Age (Ma)	1054	1055	1060.4	1063	1063	1063.7	1065	1065.5	1066	1066
2σ error	14	17	8.8	14	24	11	19	11	23	17
Age Ma	1055	1043	1068.6	1081	1043	1067	1069	1073.6	1061	1062
Final207_206_Prop2SE	0.0017	0.0018	0.001	0.0019	0.0028	0.0012	0.0021	0.0012	0.0025	0.0014
Final207_206	0.0752	0.0738	0.07562	0.0753	0.0739	0.0754	0.0753	0.07558	0.0744	0.0747
206_238:207_235 error	0.26278	0.29513	0.52354	0.31104	0.10447	0.48078	0.28616	0.43328	0.27488	0.71544
2σ error	0.0026	0.0026	0.0021	0.0029	0.0039	0.0024	0.0026	0.0022	0.0029	0.0041
Pb206_U238	0.1777	0.1775	0.1788	0.1793	0.1793	0.1794	0.1796	0.1797	0.1799	0.18
2σ error	0.041	0.047	0.025	0.039	0.065	0.03	0.054	0.03	0.065	0.049
Pb207_U235	1.828	1.796	1.865	1.896	1.807	1.862	1.869	1.881	1.856	1.845
U/Th	3.298	1.793	8.88	2.53	2.71	4.45	2.387	2.532	2.211	3.47
[U] ppm	53.9955	39.0308	739.1185	99.2955	16.8489	189.605	43.88925	189.8445	25.3675	167.7215
Grain #	121	122	256	51	195	19	335	201	62	235
Sample Name:	AJRL_121	AJRL_122	AJRL_256	AJRL_51	AJRL_195	AJRL_19	AJRL_335	AJRL_201	AJRL_62	AJRL_235

%error	27	2.8	2.9	4.2	8.9	2.6	3.1	2.8	3.1	2.8
% Discordance*	-34	2.6	2.9	-1.2	-9.7	0.4	-0.9	0.3	-1.1	1.5
2σ error	17	12	14	13	16	12	13	13	13	12
(Ma)	1067	1067.1	1069	1069.8	1071	1072.4	1072.5	1073.7	1074.3	1074.9
2σ error	79	36	36	42	57	32	35	32	35	36
Age (Ma)	1053	1089	1100	1082	1037	1088	1072	1084	1074	1100
2σ error	17	12	14	13	16	12	13	13	13	12
Age (Ma)	1067	1067.1	1069	1069.8	1071	1072.4	1072.5	1073.7	1074.3	1074.9
2σ error	25	12	13	13	20	9.6	11	9.5	11	11
Age Ma	1060	1084	1079	1073	1057	1073	1068.9	1078.6	1070.6	1076.4
Final207_206_Prop2SE	0.0028	0.0013	0.0013	0.0015	0.002	0.0012	0.0013	0.0012	0.0013	0.0014
Final207_206	0.0742	0.076	0.0761	0.0754	0.0745	0.07548	0.0754	0.07556	0.075	0.0761
206_238:207_235 error	0.084016	0.28619	0.49514	0.036759	0.22648	0.19801	0.34497	0.34396	0.32157	0.18558
2σ error	0.0031	0.0022	0.0025	0.0024	0.0029	0.0022	0.0024	0.0023	0.0023	0.0022
Pb206_U238	0.18	0.18	0.1804	0.1805	0.1809	0.181	0.181	0.1813	0.1814	0.1815
2σ error	0.07	0.034	0.036	0.036	0.053	0.027	0.032	0.027	0.032	0.031
Pb207_U235	1.827	1.909	1.894	1.881	1.828	1.878	1.865	1.894	1.872	1.889
U/Th	2.775	3.052	2.47	3.394	2.94	3.24	2.19	3.014	3.16	2.001
[U] ppm	21.15205	95.3915	248.3615	104.1915	31.45	228.57	161.993	183.395	102.7205	217.855
Grain #	199	200	61	93	34	35	87	286	3	164
Sample Name:	AJRL_199	AJRL_200	AJRL_61	AJRL_93	AJRL_34	AJRL_35	AJRL_87	AJRL_286	AJRL_3	AJRL_164

%error	2.9	3.5	1.8	3.2	5	9.5	21	6.3	3.5	2.1
% Discordance*	0.1	1.2	0.1	-2.8	1.6	-14.5	-14	-2.4	-1	-0.3
2σ error	14	13	11	14	15	18	21	17	14	11
(Ma)	1076	1076.7	1078	1078	1078	1079	1081	1082	1082	1082
2σ error	33	42	27	35	52	69	100	62	39	28
Age (Ma)	1087	1106	1093	1058	1121	1054	1070	1069	1069	1076
2σ error	14	13	11	14	15	18	21	17	14	11
Age (Ma)	1076	1076.7	1078	1078	1078	1079	1081	1082	1082	1082
2σ error	12	14	9.4	12	14	21	29	21	13	9.3
Age Ma	1077.6	1084	1088.7	1077	1097	1076	1072	1075	1079	1081.2
Final207_206_Prop2SE	0.0013	0.0016	0.001	0.0013	0.0019	0.0026	0.0036	0.0022	0.0015	0.0011
Final207_206	0.07572	0.0764	0.07592	0.0748	0.0773	0.0753	0.076	0.0753	0.0752	0.07536
206_238:207_235 error	0.58746	0.37212	0.58963	0.46123	0.1	0.08049	0.1	0.36818	0.29495	0.37732
2σ error	0.0026	0.0024	0.002	0.0025	0.0027	0.0033	0.0038	0.0031	0.0025	0.0021
Pb206_U238	0.1817	0.1818	0.182	0.1821	0.1821	0.1823	0.1826	0.1829	0.1828	0.1828
2σ error	0.033	0.04	0.027	0.034	0.042	0.059	0.077	0.06	0.035	0.027
Pb207_U235	1.893	1.907	1.923	1.884	1.951	1.897	1.875	1.884	1.893	1.897
U/Th	2.22	2.76	2.241	1.907	3.764	2.666	1.801	2.829	1.891	3.315
[U] ppm	190.176	91.391	590.225	135.134	39.69125	26.9338	15.38365	36.4187	131.2885	286.1055
Grain #	101	44	149	223	303	162	186	73	161	296
Sample Name:	AJRL_101	AJRL_44	AJRL_149	AJRL_223	AJRL_303	AJRL_162	AJRL_186	AJRL_73	AJRL_161	AJRL_296

%error	5.3	2.2	2.7	3.7	4.4	2.9	8.3	2.8	5.2	2.7
% Discordance*	-2.7	0.3	-1.2	-3.6	3.3	3.4	-5	-1.7	-6.3	-1.8
2σ error	17	11	14	14	14	16	21	12	14	12
(Ma)	1083	1085.2	1086	1086	1086	1087	1088	1088.5	1089	1089.7
2σ error	53	29	33	42	50	35	78	32	52	33
Age (Ma)	1063	1093	1072	1052	1137	1128	1056	1082	1040	1073
2σ error	17	11	14	14	14	16	21	12	14	12
Age (Ma)	1083	1085.2	1086	1086	1086	1087	1088	1088.5	1089	1089.7
2σ error	17	9.3	12	15	16	15	28	10	18	11
Age Ma	1081	1087	1079.8	1075	1106	1103	1087	1090.6	1076	1085.4
Final207_206_Prop2SE	0.0019	0.0011	0.0012	0.0015	0.002	0.0013	0.0027	0.0012	0.0019	0.0012
Final207_206	0.0749	0.07604	0.07496	0.0746	0.0775	0.0773	0.0745	0.07557	0.0738	0.07513
206_238:207_235 error	0.27062	0.20012	0.55577	0.43813	0.1277	0.72466	0.50189	0.41071	0.28242	0.31358
2σ error	0.0031	0.0021	0.0025	0.0027	0.0025	0.003	0.0039	0.0023	0.0026	0.0022
Pb206_U238	0.183	0.1834	0.1834	0.1835	0.1835	0.1836	0.184	0.184	0.1841	0.1842
2σ error	0.05	0.027	0.034	0.041	0.048	0.045	0.074	0.03	0.05	0.031
Pb207_U235	1.905	1.918	1.899	1.883	1.978	1.964	1.908	1.929	1.888	1.912
U/Th	1.99	3.477	3.34	2.181	2.967	17.93	1.562	3.176	1.13	4
[U] ppm	78.2615	315.693	140.199	69.3415	61.6825	586.6845	32.083	136.4235	45.702	161.383
Grain #	301	289	181	224	283	210	128	245	59	270
Sample Name:	AJRL_301	AJRL_289	AJRL_181	AJRL_224	AJRL_283	AJRL_210	AJRL_128	AJRL_245	AJRL_59	AJRL_270

%error	4.6	3	4.4	2.7	4.5	2.3	5.5	4.3	6.8	3.8
% Discordance*	-5	0.6	-3.1	-1.9	-2.1	-1	-1.4	-3.4	0.6	-3.4
2σ error	14	12	15	11	14	13	16	17	18	14
(Ma)	1090	1091.1	1092	1094.2	1095	1096.2	1098	1098	1098	1099
2σ error	44	37	46	33	44	30	45	42	64	40
Age (Ma)	1062	1107	1087	1076	1104	1081	1122	1076	1120	1074
2σ error	14	12	15	11	14	13	16	17	18	14
Age (Ma)	1090	1091.1	1092	1094.2	1095	1096.2	1098	1098	1098	1099
2σ error	14	12	16	11	14	11	15	12	19	14
Age Ma	1081	1092.4	1096	1089.9	1093	1087.2	1103	1084	1108	1091
Final207_206_Prop2SE	0.0017	0.0014	0.0017	0.0012	0.0016	0.0011	0.0016	0.0016	0.0025	0.0014
Final207_206	0.0751	0.0762	0.0756	0.07546	0.0767	0.07558	0.0769	0.0753	0.0773	0.0751
206_238:207_235 error	0.12296	0.13864	0.28045	0.37194	0.15987	0.49457	0.29184	0.39749	0.1	0.35725
2σ error	0.0027	0.0022	0.0027	0.0021	0.0026	0.0023	0.003	0.0031	0.0032	0.0026
Pb206_U238	0.1843	0.1844	0.1846	0.185	0.1851	0.1854	0.1855	0.1857	0.1853	0.1858
2σ error	0.04	0.034	0.046	0.032	0.04	0.032	0.043	0.036	0.056	0.041
Pb207_U235	1.894	1.93	1.948	1.927	1.938	1.92	1.962	1.911	1.978	1.928
U/Th	2.67	1.801	2.295	3.383	2.048	2.819	2.101	2.84	3.083	2.951
[U] ppm	56.806	126.758	70.092	129.566	65.415	184.006	56.822	87.362	32.36645	83.204
Grain #	218	268	312	212	274	280	26	88	123	252
Sample Name:	AJRL_218	AJRL_268	AJRL_312	AJRL_212	AJRL_274	AJRL_280	AJRL_26	AJRL_88	AJRL_123	AJRL_252

%error	2.6	3.5	2.6	7.6	8.5	3.3	4.8	5.3	3.3	4
% Discordance*	-2.1	-5.4	0.5	-4.8	-7.1	-3.5	-4.2	-2.3	-0.4	-1.6
2σ error	12	14	12	18	18	15	14	16	13	14
(Ma)	1099.9	1102	1102.3	1103	1103	1106	1109	1110	1110.4	1111
2σ error	31	39	31	66	55	38	50	55	37	44
Age (Ma)	1086	1051	1100	1115	1115	1082	1077	1116	1122	1103
2σ error	12	14	12	18	18	15	14	16	13	14
Age (Ma)	1099.9	1102	1102.3	1103	1103	1106	1109	1110	1110.4	1111
2σ error	9.9	13	11	22	20	14	16	16	11	14
Age Ma	1090.8	1085	1102	1104	1100	1100	1095	1115	1112.5	1112
Final207_206_Prop2SE	0.0012	0.0014	0.0012	0.0026	0.0021	0.0014	0.0018	0.0021	0.0014	0.0017
Final207_206	0.07559	0.0744	0.07608	0.0769	0.0766	0.0755	0.0753	0.0772	0.0771	0.0763
206_238:207_235 error	0.34009	0.3616	0.23812	0.19173	0.32893	0.5257	0.2181	0.098199	0.048336	0.17932
2σ error	0.0022	0.0025	0.0023	0.0033	0.0033	0.0028	0.0026	0.003	0.0024	0.0026
Pb206_U238	0.1861	0.1865	0.1865	0.1866	0.1867	0.1872	0.1878	0.188	0.188	0.1881
2σ error	0.028	0.037	0.031	0.064	0.058	0.04	0.046	0.047	0.032	0.044
Pb207_U235	1.929	1.911	1.962	1.976	1.95	1.951	1.946	2.003	1.984	1.99
U/Th	2.363	1.725	2.94	2.179	2.65	3.63	2.532	2.933	2.346	4.25
[U] ppm	168.2635	95.7975	153.327	24.2359	48.4065	97.0745	56.95875	48.47905	107.3405	62.56885
Grain #	133	84	285	314	326	167	91	217	17	242
Sample Name:	AJRL_133	AJRL_84	AJRL_285	AJRL_314	AJRL_326	AJRL_167	AJRL_91	AJRL_217	AJRL_17	AJRL_242

%error	2.7	5.5	4.9	3.7	2.5	2.1	3.8	2.6	2.8	2.1
% Discordance*	-0.1	-3.2	-1.7	-0.1	0.7	0.5	1.9	-0.7	-1.3	-0.8
2σ error	12	16	15	13	12	11	14	12	13	11
(Ma)	1111.7	1112	1112	1112.1	1113.8	1114.7	1115	1115.4	1115.5	1115.6
2σ error	34	53	52	40	32	29	40	32	34	29
Age (Ma)	1120	1105	1115	1116	1126	1116	1146	1111	1121	1120
2σ error	12	16	15	13	12	11	14	12	13	11
Age (Ma)	1111.7	1112	1112	1112.1	1113.8	1114.7	1115	1115.4	1115.5	1115.6
2σ error	11	17	17	12	11	9.6	13	11	12	10
Age Ma	1111.5	1112	1115	1116.7	1117.7	1115.6	1117	1115.8	1119.8	1115.1
Final207_206_Prop2SE	0.0013	0.002	0.0021	0.0015	0.0013	0.0011	0.0015	0.0013	0.0014	0.0012
Final207_206	0.07667	0.0769	0.0767	0.0768	0.07712	0.0768	0.0781	0.07658	0.0767	0.07685
206_238:207_235 error	0.21973	0.051706	0.18478	-0.034714	0.29242	0.30794	0.26565	0.24611	0.37021	0.45161
2σ error	0.0021	0.0029	0.0028	0.0024	0.0023	0.0021	0.0025	0.0023	0.0023	0.0021
Pb206_U238	0.1881	0.1883	0.1883	0.1883	0.1886	0.1888	0.1889	0.1889	0.1889	0.1889
2σ error	0.03	0.049	0.05	0.036	0.031	0.028	0.039	0.032	0.034	0.03
Pb207_U235	1.984	1.997	2	1.999	2.005	2.002	2.004	2.003	2.009	2
U/Th	2.27	1.721	2.56	1.956	2.017	1.958	1.48	3.295	1.51	14.76
[U] ppm	116.4275	38.4	45.26235	69.473	109.674	174.565	66.671	141.647	169.525	322.982
Grain #	83	21	169	74	7	293	178	251	284	25
Sample Name:	AJRL_83	AJRL_21	AJRL_169	AJRL_74	AJRL_7	AJRL_293	AJRL_178	AJRL_251	AJRL_284	AJRL_25

%error	24	5.6	2.8	2.6	3.9	4.3	4	3.4	4.7	2
% Discordance*	-32	-3.7	-0.8	0	-4.3	-5.6	-3.5	-2.1	-3	-2.1
2σ error	24	16	13	12	16	17	16	14	16	17
(Ma)	1117	1117	1132.1	1135.2	1136	1142	1142	1143.6	1144	1146
2σ error	100	55	32	33	40	41	40	39	48	26
Age (Ma)	1020	1108	1130	1138	1117	1095	1117	1137	1127	1130
2σ error	24	16	13	12	16	17	16	14	16	17
Age (Ma)	1117	1117	1132.1	1135.2	1136	1142	1142	1143.6	1144	1146
2σ error	34	19	11	11	13	14	12	13	17	12
Age Ma	1090	1120	1126.3	1136.6	1129	1125	1128	1145	1134	1140
Final207_206_Prop2SE	0.0037	0.0022	0.0012	0.0012	0.0015	0.0016	0.0015	0.0015	0.0019	0.001
Final207_206	0.0747	0.0769	0.0775	0.07772	0.0768	0.0762	0.0771	0.0777	0.0774	0.07733
206_238:207_235 error	0.18115	0.21344	0.40685	0.32534	0.36898	0.37209	0.31081	0.34963	0.22456	0.83386
2σ error	0.0044	0.0029	0.0024	0.0023	0.003	0.0031	0.003	0.0025	0.0029	0.0031
Pb206_U238	0.1888	0.1892	0.1918	0.1926	0.1927	0.1939	0.1935	0.1941	0.1942	0.1946
2σ error	0.098	0.054	0.034	0.033	0.04	0.041	0.038	0.039	0.05	0.036
Pb207_U235	1.932	2.011	2.035	2.065	2.042	2.031	2.036	2.088	2.062	2.073
U/Th	2.73	1.756	3.81	5.332	2.137	2.445	2.878	2.477	4.84	1.731
[U] ppm	12.037	45.311	148.943	108.0825	112.527	67.8805	180.22	73.698	63.00695	307.1195
Grain #	54	313	103	11	247	140	307	136	150	180
Sample Name:	AJRL_54	AJRL_313	AJRL_103	AJRL_11	AJRL_247	AJRL_140	AJRL_307	AJRL_136	AJRL_150	AJRL_180

%error	2.6	6.1	3	3.8	2.2	2.7	3.8	3.8	2.7	3
% Discordance*	-1.9	-5.9	-2.2	-4.1	-2.7	-2.5	-2.2	-0.8	-1.3	-2.3
2σ error	18	18	18	16	13	26	15	15	15	16
(Ma)	1147	1148	1148	1149	1152.7	1162	1178	1206	1216	1249
2σ error	28	53	33	38	29	27	42	44	34	35
Age (Ma)	1125	1117	1132	1117	1126	1130	1169	1224	1196	1213
2σ error	18	18	18	16	13	26	15	15	15	16
Age (Ma)	1147	1148	1148	1149	1152.7	1162	1178	1206	1216	1249
2σ error	12	18	14	14	11	18	14	15	13	13
Age Ma	1141.5	1134	1144	1149	1142.3	1145	1179	1211	1209	1229
Final207_206_Prop2SE	0.0011	0.0022	0.0013	0.0014	0.0011	0.0011	0.0017	0.0018	0.0014	0.0014
Final207_206	0.07715	0.0765	0.0774	0.077	0.07728	0.07737	0.079	0.0812	0.0801	0.0808
206_238:207_235 error	0.74943	0.051269	0.66748	0.44459	0.52175	0.89266	0.14971	0.25144	0.50474	0.70601
2σ error	0.0033	0.0034	0.0033	0.003	0.0024	0.0048	0.0028	0.0029	0.0029	0.003
Pb206_U238	0.1948	0.195	0.195	0.1952	0.1956	0.1977	0.2005	0.2058	0.2077	0.2138
2σ error	0.037	0.053	0.041	0.043	0.032	0.054	0.043	0.05	0.043	0.045
Pb207_U235	2.076	2.061	2.083	2.103	2.076	2.093	2.196	2.303	2.292	2.352
U/Th	1.499	2.634	2.585	1.861	2.638	13.45	3.067	2.2	36	1.304
[U] ppm	291.655	44.313	309.38	134.275	210.2725	331.9706	164.844	69.2375	334.7185	127.6045
Grain #	290	27	134	90	55	191	239	209	182	129
Sample Name:	AJRL_290	AJRL_27	AJRL_134	AJRL_90	AJRL_55	AJRL_191	AJRL_239	AJRL_209	AJRL_182	AJRL_129

%error	3	4.3	1.4	2.7	2.1	2.3	3.3	3.9	4.4	1.7
% Discordance*	-1.6	-0.7	-1	0	1.5	0	-3.6	0.1	-2.6	1.1
2σ error	16	18	13	15	14	16	17	20	20	14
(Ma)	1258	1265	1329.2	1340	1343.5	1344	1349	1350	1353	1353.8
2σ error	37	52	26	36	31	32	40	49	47	27
Age (Ma)	1253	1251	1318	1341	1351	1342	1321	1369	1321	1369
2σ error	16	18	13	15	14	16	17	20	20	14
Age (Ma)	1258	1265	1329.2	1340	1343.5	1344	1349	1350	1353	1353.8
2σ error	14	22	9.9	13	11	11	16	20	21	10
Age Ma	1252	1257	1324	1343	1346.6	1342.5	1336	1355	1333	1361.6
Final207_206_Prop2SE	0.0016	0.0023	0.0011	0.0016	0.0014	0.0014	0.0018	0.0023	0.0021	0.0012
Final207_206	0.0825	0.0824	0.08517	0.0862	0.0866	0.0862	0.0853	0.0877	0.0851	0.08738
206_238:207_235 error	0.42825	0.51797	0.38516	0.096382	0.19044	0.38548	0.2737	0.41511	0.70203	0.38195
2σ error	0.003	0.0035	0.0025	0.003	0.0028	0.003	0.0032	0.0039	0.0039	0.0027
Pb206_U238	0.2155	0.2169	0.229	0.2311	0.2318	0.2318	0.2328	0.233	0.2336	0.2337
2σ error	0.048	0.076	0.036	0.048	0.041	0.042	0.059	0.076	0.076	0.039
Pb207_U235	2.432	2.459	2.685	2.753	2.766	2.754	2.73	2.806	2.732	2.822
U/Th	2.66	4.395	2.579	1.685	3.422	3.56	2.677	1.272	1.704	3.117
[U] ppm	51.4441	75.98455	214.6485	96.8675	122.996	102.4685	44.025	62.758	38.1282	199.23
Grain #	276	173	68	92	236	198	151	10	80	205
Sample Name:	AJRL_276	AJRL_173	AJRL_68	AJRL_92	AJRL_236	AJRL_198	AJRL_151	AJRL_10	AJRL_80	AJRL_205

%error	3.1	1.9	2.2	3.3	2.4	2.2	2	1.9	3.6	2.1
% Discordance*	0.4	-1	-0.1	1.7	0.6	1	0.6	0.3	0.2	-1.5
2σ error	18	14	14	23	17	15	17	14	20	15
(Ma)	1364	1366.8	1367.9	1368	1372	1372	1375	1377.8	1381	1382.7
2σ error	41	30	33	42	35	32	30	30	47	30
Age (Ma)	1389	1354	1380	1385	1381	1381	1380	1374	1369	1362
2σ error	18	14	14	23	17	15	17	14	20	15
Age (Ma)	1364	1366.8	1367.9	1368	1372	1372	1375	1377.8	1381	1382.7
2σ error	17	11	12	18	14	12	12	11	19	11
Age Ma	1373	1360.9	1378.8	1380	1376	1372.5	1382.5	1373.3	1368	1370.7
Final207_206_Prop2SE	0.0018	0.0013	0.0015	0.0019	0.0016	0.0015	0.0014	0.0013	0.0021	0.0014
Final207_206	0.0885	0.08674	0.088	0.0884	0.088	0.0879	0.088	0.08766	0.0872	0.0871
206_238:207_235 error	0.48291	0.36937	0.25008	0.57119	0.52405	0.21912	0.4412	0.18646	0.27682	0.28954
2σ error	0.0033	0.0028	0.0027	0.0041	0.0032	0.0029	0.0032	0.0028	0.0038	0.0029
Pb206_U238	0.2353	0.236	0.2364	0.2357	0.2372	0.2372	0.2377	0.2381	0.2386	0.2393
2σ error	0.065	0.042	0.046	0.073	0.053	0.046	0.046	0.04	0.072	0.043
Pb207_U235	2.873	2.819	2.878	2.888	2.876	2.868	2.901	2.866	2.858	2.86
U/Th	1.4	2.374	3.529	3.46	2.224	1.546	1.539	2.02	1.28	1.84
[U] ppm	69.664	148.342	104.7095	93.122	89.419	87.8205	165.56	163.92	48.22	124.094
Grain #	331	257	291	288	300	305	189	255	231	131
Sample Name:	AJRL_331	AJRL_257	AJRL_291	AJRL_288	AJRL_300	AJRL_305	AJRL_189	AJRL_255	AJRL_231	AJRL_131

%error	2	1.9	4	2.5	2.6	1.7	2.3	2.7	2.3	4.2
% Discordance*	-0.8	0.7	-0.9	-2.2	-1.6	0.8	2.3	-1.1	0.3	-1.3
2σ error	15	18	19	16	17	17	16	20	17	22
(Ma)	1395.1	1413	1416	1417	1420	1422	1424	1427	1427	1427
2σ error	31	28	52	36	36	27	34	37	33	49
Age (Ma)	1384	1426	1408	1399	1412	1432	1455	1419	1426	1445
2σ error	15	18	19	16	17	17	16	20	17	22
Age (Ma)	1395.1	1413	1416	1417	1420	1422	1424	1427	1427	1427
2σ error	12	12	19	14	14	11	13	14	13	17
Age Ma	1384.5	1418.1	1417	1411	1420	1426.9	1438	1425	1427	1435
Final207_206_Prop2SE	0.0014	0.0013	0.0023	0.0017	0.0017	0.0013	0.0017	0.0017	0.0016	0.0024
Final207_206	0.08796	0.08984	0.0896	0.0887	0.0897	0.09031	0.0911	0.0896	0.0902	0.0908
206_238:207_235 error	0.30748	0.60488	0.21065	0.025615	0.25783	0.46984	0.23748	0.42612	0.38391	0.14533
2σ error	0.0028	0.0035	0.0037	0.003	0.0032	0.0032	0.0031	0.0037	0.0033	0.0042
Pb206_U238	0.2416	0.245	0.2458	0.2458	0.2465	0.2468	0.2472	0.2471	0.2479	0.2478
2σ error	0.043	0.048	0.076	0.057	0.056	0.046	0.051	0.057	0.053	0.069
Pb207_U235	2.904	3.044	3.049	3.012	3.057	3.079	3.12	3.061	3.081	3.119
U/Th	1.305	3.9	2.071	2.317	3.948	5.05	1.904	3.913	1.95	3.174
[U] ppm	144.39	239.2775	30.3926	65.269	53.8939	179.7315	93.8225	64.63545	159.437	48.33935
Grain #	145	4	287	110	156	336	334	108	124	304
Sample Name:	AJRL_145	AJRL_4	AJRL_287	AJRL_110	AJRL_156	AJRL_336	AJRL_334	AJRL_108	AJRL_124	AJRL_304

%error	1.7	2.1	1.9	2	2.3	1.8	2.5	2.6	1.8	1.5
% Discordance*	1.4	-1.7	-0.2	0.6	0.7	1.4	-2.7	0.2	-1.1	-1.1
2σ error	17	15	16	17	16	15	15	16	15	14
(Ma)	1429	1433	1439	1440	1440	1440	1441.8	1443	1446.3	1447
2σ error	29	31	28	29	38	28	36	36	31	27
Age (Ma)	1449	1407	1436	1454	1433	1460	1421	1462	1432	1432
2σ error	17	15	16	17	16	15	15	16	15	14
Age (Ma)	1429	1433	1439	1440	1440	1440	1441.8	1443	1446.3	1447
2σ error	11	12	12	11	15	12	13	14	13	11
Age Ma	1442.1	1425.7	1443.5	1446	1436	1448.4	1430	1449	1442.9	1446.4
Final207_206_Prop2SE	0.0014	0.0014	0.0013	0.0014	0.0018	0.0013	0.0017	0.0017	0.0014	0.0013
Final207_206	0.091	0.0893	0.09061	0.09128	0.0905	0.09137	0.0898	0.0918	0.0904	0.0904
206_238:207_235 error	0.39208	0.19561	0.26467	0.3901	0.30656	0.41456	0.24607	0.33526	0.40012	0.39181
2σ error	0.0031	0.003	0.0032	0.0032	0.0031	0.003	0.003	0.0032	0.0029	0.0028
Pb206_U238	0.2479	0.2491	0.2501	0.2503	0.2503	0.2504	0.2505	0.2509	0.2516	0.2517
2σ error	0.045	0.045	0.046	0.046	0.059	0.048	0.053	0.06	0.051	0.045
Pb207_U235	3.14	3.071	3.142	3.157	3.118	3.167	3.089	3.165	3.14	3.151
U/Th	5.65	1.577	3.483	3.233	1.666	1.562	2.359	1.74	2.529	3.579
[U] ppm	247.7995	114.352	146.159	100.8351	98.7725	211.6125	93.9425	74.489	126.475	238.429
Grain #	126	40	107	192	215	329	229	266	102	302
Sample Name:	AJRL_126	AJRL_40	AJRL_107	AJRL_192	AJRL_215	AJRL_329	AJRL_229	AJRL_266	AJRL_102	AJRL_302

%error	2.2	2.4	1.6	4.4	1.5	1.7	2.3	2.4	2.1	2.2
% Discordance*	-1.3	-2.2	-0.4	-1.3	-0.6	-2.4	-0.8	-0.9	-1.8	-1.3
2σ error	17	17	16	27	15	15	17	20	18	22
(Ma)	1448	1448	1451	1456	1456.8	1457.7	1458	1461	1503	1629
2σ error	32	33	27	54	26	26	35	30	29	36
Age (Ma)	1429	1425	1439	1415	1445	1428	1449	1428	1481	1614
2σ error	17	17	16	27	15	15	17	20	18	22
Age (Ma)	1448	1448	1451	1456	1456.8	1457.7	1458	1461	1503	1629
2σ error	13	13	11	22	11	11	15	14	12	17
Age Ma	1439	1432	1448.1	1432	1449	1442.8	1455	1444	1489.9	1629
Final207_206_Prop2SE	0.0015	0.0016	0.0013	0.0025	0.0013	0.0012	0.0016	0.0014	0.0014	0.0019
Final207_206	0.0901	0.0898	0.09051	0.0897	0.09081	0.09017	0.0911	0.0903	0.0927	0.0996
206_238:207_235 error	0.4206	0.38395	0.45955	0.50271	0.41044	0.38877	0.33957	0.71957	0.55507	0.51941
2σ error	0.0033	0.0034	0.0031	0.0052	0.0029	0.003	0.0032	0.0038	0.0035	0.0043
Pb206_U238	0.2519	0.2519	0.2523	0.2528	0.2534	0.2538	0.2539	0.2544	0.2627	0.2876
2σ error	0.052	0.053	0.047	0.09	0.045	0.043	0.06	0.055	0.051	0.082
Pb207_U235	3.13	3.101	3.162	3.115	3.169	3.138	3.198	3.146	3.339	3.98
U/Th	5.054	1.437	1.997	2.065	3.217	2.259	5.83	2.473	2.006	1.509
[U] ppm	95.83	135.753	192.0925	23.65635	159.0925	224.491	93.2895	147.9015	263.636	114.8635
Grain #	46	81	226	339	298	60	141	127	338	214
Sample Name:	AJRL_46	AJRL_81	AJRL_226	AJRL_339	AJRL_298	AJRL_60	AJRL_141	AJRL_127	AJRL_338	AJRL_214

%error	1.7	1.5	1.8	1.2	1.6	2.5	1.7	1.6	2.2	2.2
% Discordance*	1.7	1.6	0.4	0.1	0.4	-1.1	0.2	0.9	-1.5	-1.7
2σ error	19	17	18	17	17	25	19	18	21	21
(Ma)	1674	1679	1681	1683.9	1690	1692	1692	1694	1697	1699
2σ error	30	27	30	25	29	34	28	28	34	30
Age (Ma)	1700	1705	1696	1687	1694	1667	1707	1706	1686	1671
2σ error	19	17	18	17	17	25	19	18	21	21
Age (Ma)	1674	1679	1681	1683.9	1690	1692	1692	1694	1697	1699
2σ error	14	12	13	10	13	15	12	13	16	14
Age Ma	1683	1685.4	1683.9	1687.8	1691	1678	1697.5	1699	1690	1688
Final207_206_Prop2SE	0.0017	0.0015	0.0017	0.0014	0.0016	0.0019	0.0016	0.0016	0.0018	0.0017
Final207_206	0.1038	0.1043	0.1039	0.10353	0.104	0.1023	0.1044	0.1045	0.1032	0.1027
206_238:207_235 error	0.42876	0.29241	0.17151	0.33626	0.3383	0.51742	0.45523	0.53033	0.53066	0.31717
2σ error	0.0039	0.0035	0.0037	0.0033	0.0035	0.0049	0.0038	0.0036	0.0043	0.0043
Pb206_U238	0.2965	0.2975	0.298	0.2985	0.2997	0.2996	0.3001	0.3005	0.3012	0.3016
2σ error	0.073	0.061	0.066	0.054	0.067	0.076	0.064	0.07	0.084	0.075
Pb207_U235	4.246	4.257	4.245	4.266	4.286	4.227	4.326	4.334	4.286	4.276
U/Th	3.281	2.277	4.032	3.676	2.238	2.701	2.467	3.665	4.803	2.147
[U] ppm	89.298	148.5535	78.9569	216.8545	76.438	62.4585	113.1175	185.5855	137.1732	110.122
Grain #	232	96	53	70	346	5	228	272	77	278
Sample Name:	AJRL_232	AJRL_96	AJRL_53	AJRL_70	AJRL_346	AJRL_5	AJRL_228	AJRL_272	AJRL_77	AJRL_278

%error	1.5	2.3	1.2	1	1.5	3	1.6	1.6	1.5	1.2
% Discordance*	-2.1	1.2	3	-0.9	-0.4	-2.8	-0.9	0.1	-1.7	1.6
2σ error	18	21	17	16	20	28	18	18	18	18
(Ma)	1711	1731	1731	1732.3	1733	1733	1741	1746	1764	1765
2σ error	27	39	26	24	26	38	28	29	26	24
Age (Ma)	1687	1754	1781	1722	1722	1694	1731	1756	1737	1789
2σ error	18	21	17	16	20	28	18	18	18	18
Age (Ma)	1711	1731	1731	1732.3	1733	1733	1741	1746	1764	1765
2σ error	12	19	12	11	12	17	12	12	12	12
Age Ma	1702	1747	1757.5	1724.1	1727.1	1718	1740.6	1751.7	1748.4	1773
Final207_206_Prop2SE	0.0015	0.0022	0.0016	0.0014	0.0015	0.0022	0.0016	0.0017	0.0016	0.0015
Final207_206	0.1035	0.1075	0.109	0.10543	0.1054	0.104	0.106	0.1073	0.1063	0.10941
206_238:207_235 error	0.38021	0.47903	0.35181	0.4631	0.48181	0.5121	0.36506	0.1983	0.54295	0.36012
2σ error	0.0037	0.0043	0.0034	0.0033	0.004	0.0058	0.0037	0.0036	0.0038	0.0036
Pb206_U238	0.304	0.3081	0.3081	0.3083	0.3084	0.3086	0.31	0.3108	0.3148	0.3145
2σ error	0.061	0.1	0.065	0.059	0.067	0.096	0.064	0.065	0.068	0.063
Pb207_U235	4.347	4.574	4.649	4.466	4.472	4.431	4.551	4.617	4.599	4.728
U/Th	1.606	2.976	4.576	2.623	3.81	3.751	2.764	2.139	3.209	7.26
[U] ppm	202.638	139.6695	150.1145	178.464	154.3895	36.53615	121.588	107.098	135.059	214.6482
Grain #	52	47	185	130	106	249	322	41	311	159
Sample Name:	AJRL_52	AJRL_47	AJRL_185	AJRL_130	AJRL_106	AJRL_249	AJRL_322	AJRL_41	AJRL_311	AJRL_159

%error	2	0.95	2.1	1.6	1.3	1.6	1.2	1.7	2	1.5
% Discordance*	2	0.28	-1.4	6.8	-1.2	3.4	3.2	-0.8	0.7	-1
2σ error	22	17	21	22	18	18	19	19	21	19
(Ma)	1772	1775.9	1778	1789	1790	1791	1792	1795	1797	1801
2σ error	36	24	33	32	27	30	25	30	31	27
Age (Ma)	1810	1778	1743	1931	1772	1864	1844	1778	1808	1791
2σ error	22	17	21	22	18	18	19	19	21	19
Age (Ma)	1772	1775.9	1778	1789	1790	1791	1792	1795	1797	1801
2σ error	15	11	15	18	13	12	13	12	14	12
Age Ma	1788	1778.3	1755	1853	1779	1821.7	1815.9	1788.8	1803	1797.7
Final207_206_Prop2SE	0.0022	0.0014	0.0019	0.0022	0.0016	0.0019	0.0016	0.0018	0.0019	0.0016
Final207_206	0.1108	0.10881	0.1068	0.1184	0.1083	0.1142	0.11282	0.1089	0.1106	0.1093
206_238:207_235 error	0.27357	0.42152	0.42123	0.40092	0.49641	0.22193	0.61594	0.2435	0.38217	0.47781
2σ error	0.0043	0.0035	0.0043	0.0045	0.0038	0.0037	0.0039	0.0039	0.0044	0.0039
Pb206_U238	0.3152	0.3172	0.3176	0.3199	0.3201	0.3203	0.3205	0.3211	0.3216	0.3223
2σ error	0.086	0.065	0.085	0.11	0.075	0.075	0.075	0.071	0.081	0.071
Pb207_U235	4.816	4.76	4.636	5.216	4.772	5.01	4.985	4.826	4.908	4.877
U/Th	2.271	2.024	2.785	1.194	2.48	1.584	3.032	3.842	1.801	3.381
[U] ppm	39.8989	210.855	60.3013	127.321	136.6205	164.1385	186.1835	92.8695	88.352	159.24
Grain #	179	342	327	244	152	196	144	18	116	202
Sample Name:	AJRL_179	AJRL_342	AJRL_327	AJRL_244	AJRL_152	AJRL_196	AJRL_144	AJRL_18	AJRL_116	AJRL_202

%error	1.3	1.5	2.3	1.2	1.2	1.6	1.4	1.5	1.7	1.5
% Discordance*	-1.1	-0.8	0.7	-1	-1.7	-1.4	-0.4	-0.3	0.1	-0.2
2σ error	22	19	23	18	18	19	18	18	22	20
(Ma)	1805	1806	1808	1814	1818	1819	1823	1827	1827	1828
2σ error	23	26	37	24	25	28	27	26	29	29
Age (Ma)	1784	1799	1824	1802	1793	1792	1827	1818	1822	1821
2σ error	22	19	23	18	18	19	18	18	22	20
Age (Ma)	1805	1806	1808	1814	1818	1819	1823	1827	1827	1828
2σ error	13	12	18	11	12	13	11	12	13	13
Age Ma	1798.6	1808.3	1826	1809.8	1804.6	1801	1830.3	1819.3	1820.7	1823.4
Final207_206_Prop2SE	0.0014	0.0016	0.0023	0.0014	0.0015	0.0017	0.0016	0.0016	0.0018	0.0017
Final207_206	0.10917	0.1101	0.1117	0.11014	0.10975	0.1096	0.1117	0.1113	0.1114	0.1113
206_238:207_235 error	0.79387	0.42048	0.31694	0.48318	0.42751	0.29102	0.2423	0.40384	0.54737	0.29512
2σ error	0.0046	0.0038	0.0047	0.0037	0.0036	0.0038	0.0036	0.0038	0.0046	0.0041
Pb206_U238	0.3233	0.3233	0.3238	0.3251	0.3259	0.326	0.3269	0.3277	0.3277	0.3278
2σ error	0.073	0.072	0.1	0.063	0.069	0.077	0.071	0.072	0.079	0.077
Pb207_U235	4.883	4.934	5.031	4.946	4.918	4.895	5.058	5.004	5.004	5.03
U/Th	6.36	2.796	0.6429	3.593	3.273	4.385	2.791	1.448	2.27	1.194
[U] ppm	322.374	146.0035	29.837	167.1875	126.56	103.1546	118.6945	102.9995	147.13	58.6585
Grain #	132	273	104	184	220	321	94	13	148	14
Sample Name:	AJRL_132	AJRL_273	AJRL_104	AJRL_184	AJRL_220	AJRL_321	AJRL_94	AJRL_13	AJRL_148	AJRL_14

%error	2	1.7	1.2	1.3	1.3	2	1.3	3.3	1.4	1.3
% Discordance*	0.3	-0.7	0.7	0.9	1.1	0.2	-0.9	-2.1	-0.5	0.5
2σ error	22	20	18	19	18	21	21	30	20	19
(Ma)	1829	1831	1833	1835	1835	1836	1837	1837	1839	1839
2σ error	32	30	24	26	24	31	25	48	27	28
Age (Ma)	1842	1821	1844	1852	1849	1833	1823	1815	1836	1849
2σ error	22	20	18	19	18	21	21	30	20	19
Age (Ma)	1829	1831	1833	1835	1835	1836	1837	1837	1839	1839
2σ error	15	13	11	12	11	14	13	23	14	14
Age Ma	1839	1831.8	1833	1839.5	1845.6	1839	1836	1828	1837	1844
Final207_206_Prop2SE	0.002	0.0018	0.0015	0.0016	0.0015	0.0019	0.0016	0.0028	0.0017	0.0017
Final207_206	0.1128	0.1111	0.11263	0.1132	0.113	0.1123	0.1114	0.1112	0.1122	0.1132
206_238:207_235 error	0.41653	0.26172	0.40267	0.4593	0.35796	0.27821	0.59043	0.38734	0.53494	0.46655
2σ error	0.0045	0.0041	0.0037	0.0039	0.0038	0.0043	0.0044	0.0061	0.0042	0.0039
Pb206_U238	0.3281	0.3286	0.3288	0.3292	0.3294	0.3296	0.3298	0.33	0.3302	0.3301
2σ error	0.091	0.077	0.067	0.07	0.068	0.086	0.081	0.14	0.083	0.085
Pb207_U235	5.125	5.078	5.084	5.117	5.161	5.128	5.099	5.04	5.112	5.158
U/Th	4.979	2.956	2.58	2.902	1.954	1.009	3.54	1.234	2.605	1.809
[U] ppm	78.41325	113.3895	155.178	147.6215	159.0975	48.2475	184.5675	26.17655	115.441	71.078
Grain #	320	36	56	28	281	168	63	318	76	147
Sample Name:	AJRL_320	AJRL_36	AJRL_56	AJRL_28	AJRL_281	AJRL_168	AJRL_63	AJRL_318	AJRL_76	AJRL_147

%error	1.1	2.2	1.5	1.4	1.4	1.1	1.2	1.4	1.6	1.4
% Discordance*	0.1	-1.8	-0.5	-0.7	0.2	0	0.1	-0.4	-1.7	-1.4
2σ error	18	21	19	18	19	18	18	18	22	19
(Ma)	1840	1842	1843	1843	1843	1844	1844	1845	1845	1848
2σ error	26	33	28	28	27	24	23	26	25	27
Age (Ma)	1847	1814	1841	1832	1843	1842	1845	1841	1812	1826
2σ error	18	21	19	18	19	18	18	18	22	19
Age (Ma)	1840	1842	1843	1843	1843	1844	1844	1845	1845	1848
2σ error	13	15	13	12	12	12	11	12	14	12
Age Ma	1842.1	1834	1839.8	1837.4	1845.1	1840.4	1841.8	1838.4	1829	1839
Final207_206_Prop2SE	0.0016	0.002	0.0017	0.0017	0.0016	0.0015	0.0015	0.0016	0.0016	0.0016
Final207_206	0.1129	0.1112	0.1123	0.1122	0.1125	0.11269	0.11278	0.1125	0.1107	0.1118
206_238:207_235 error	0.46844	0.2581	0.40315	0.24283	0.31725	0.47776	0.30242	0.28056	0.54816	0.31391
2σ error	0.0037	0.0044	0.004	0.0037	0.0039	0.0037	0.0038	0.0037	0.0046	0.0039
Pb206_U238	0.3303	0.3307	0.3311	0.3311	0.3311	0.3313	0.3312	0.3313	0.3315	0.332
2σ error	0.076	0.086	0.079	0.073	0.071	0.072	0.066	0.073	0.08	0.069
Pb207_U235	5.141	5.065	5.129	5.106	5.158	5.13	5.137	5.118	5.049	5.121
U/Th	3.02	1.478	2.693	2.126	1.763	1.47	0.923	1.566	1.72	1.997
[U] ppm	127.9321	48.227	66.3499	101.058	128.9925	134.7355	215.8335	103.683	130.758	110.5855
Grain #	50	187	75	109	306	39	343	197	221	138
Sample Name:	AJRL_50	AJRL_187	AJRL_75	AJRL_109	AJRL_306	AJRL_39	AJRL_343	AJRL_197	AJRL_221	AJRL_138

%error	1.2	1.3	2	1.3	1.3	2.6	1.9	1.4	2.4	1.8
% Discordance*	-0.2	-1	-1.6	-0.6	-0.2	-0.4	-3	-1.6	1.7	-1.2
2σ error	18	18	19	19	27	38	19	19	28	25
(Ma)	1848	1850	1850	1850	1853	1854	1855	1857	1858	1860
2σ error	23	26	35	25	22	31	32	25	42	28
Age (Ma)	1847	1831	1827	1847	1832	1840	1804	1839	1886	1844
2σ error	18	18	19	19	27	38	19	19	28	25
Age (Ma)	1848	1850	1850	1850	1853	1854	1855	1857	1858	1860
2σ error	11	11	16	12	16	22	14	11	23	17
Age Ma	1842	1842.3	1842	1853.2	1841	1848	1839	1852.8	1879	1855
Final207_206_Prop2SE	0.0015	0.0016	0.0021	0.0016	0.0014	0.0019	0.0019	0.0015	0.0027	0.0018
Final207_206	0.11288	0.112	0.1114	0.1129	0.11198	0.1125	0.1105	0.11257	0.1157	0.1129
206_238:207_235 error	0.31427	0.28999	0.12433	0.38113	0.86578	0.82051	0.14325	0.46653	0.52329	0.62533
2σ error	0.0037	0.0037	0.004	0.0038	0.0055	0.0078	0.004	0.0039	0.0058	0.0051
Pb206_U238	0.332	0.3325	0.3324	0.3324	0.3326	0.3335	0.3335	0.3338	0.3342	0.334
2σ error	0.065	0.069	0.095	0.071	0.096	0.13	0.083	0.068	0.15	0.1
Pb207_U235	5.138	5.14	5.146	5.202	5.14	5.16	5.116	5.2	5.38	5.213
U/Th	2.852	1.935	7.5	3.087	3.24	2.91	1.0554	1.634	1.196	1.722
[U] ppm	200.1575	222.858	31.8023	143.1755	215.5935	134.2695	103.8705	129.891	50.1545	126.575
Grain #	248	137	154	275	32	120	193	213	165	64
Sample Name:	AJRL_248	AJRL_137	AJRL_154	AJRL_275	AJRL_32	AJRL_120	AJRL_193	AJRL_213	AJRL_165	AJRL_64

%error	1.3	1.9	1.6	1.2	1	1.2	3	2.5	1.7	1.9
% Discordance*	-0.2	0.1	-0.6	0.3	-1.1	-1.3	-0.6	-1	-0.3	-0.3
2σ error	18	30	27	20	18	19	26	25	23	24
(Ma)	1860	1860	1864	1865	1867	1872	1874	1877	1879	1879
2σ error	26	25	24	24	23	24	45	41	28	32
Age (Ma)	1843	1861	1857	1859	1852	1853	1875	1856	1871	1876
2σ error	18	30	27	20	18	19	26	25	23	24
Age (Ma)	1860	1860	1864	1865	1867	1872	1874	1877	1879	1879
2σ error	11	15	14	12	10	12	17	18	14	16
Age Ma	1849.9	1864	1865	1858.5	1858.8	1861.1	1863	1871	1871	1879
Final207_206_Prop2SE	0.0016	0.0016	0.0015	0.0015	0.0014	0.0016	0.003	0.0025	0.0018	0.002
Final207_206	0.1127	0.1136	0.11364	0.11375	0.11323	0.11323	0.1148	0.1132	0.114	0.1148
206_238:207_235 error	0.23847	0.8302	0.79323	0.60971	0.52237	0.48431	0.18357	0.23281	0.51063	0.4542
2σ error	0.0038	0.0063	0.0055	0.0041	0.0038	0.004	0.0054	0.0052	0.0047	0.0049
Pb206_U238	0.3345	0.3339	0.3355	0.3351	0.3357	0.3371	0.3375	0.3376	0.3386	0.3386
2σ error	0.07	0.094	0.088	0.073	0.064	0.073	0.11	0.11	0.086	0.1
Pb207_U235	5.187	5.277	5.274	5.235	5.24	5.256	5.254	5.317	5.318	5.364
U/Th	1.525	3.951	0.9232	2.138	2.647	2.513	1.035	2.326	2.658	0.946
[U] ppm	129.749	199.139	268.99	234.9125	336.0955	184.5745	22.62775	27.3004	95.09625	34.7118
Grain #	188	259	332	319	333	143	260	345	237	241
Sample Name:	AJRL_188	AJRL_259	AJRL_332	AJRL_319	AJRL_333	AJRL_143	AJRL_260	AJRL_345	AJRL_237	AJRL_241

%error	2.1	1.1	1.6	2.3	1.1	1.4	0.92	1.4	1.2	1.8
% Discordance*	-2.2	-1	-1.6	-1	-1	-0.3	-1	0.1	-4.6	0.3
2σ error	21	18	19	31	18	20	18	21	18	23
(Ma)	1879	1883	1886	1886	1889	1891	1898	1899	1902	1905
2σ error	33	23	28	28	23	26	22	28	24	29
Age (Ma)	1849	1864	1860	1843	1873	1885	1877	1904	1830	1917
2σ error	21	18	19	31	18	20	18	21	18	23
Age (Ma)	1879	1883	1886	1886	1889	1891	1898	1899	1902	1905
2σ error	14	10	13	18	11	12	11	14	12	13
Age Ma	1869	1873.1	1872.3	1871	1881.8	1884.6	1885.7	1897	1866.4	1913
Final207_206_Prop2SE	0.0021	0.0014	0.0018	0.0017	0.0015	0.0017	0.0014	0.0018	0.0015	0.002
Final207_206	0.1134	0.11396	0.1137	0.1128	0.11464	0.1155	0.11488	0.1166	0.11189	0.1175
206_238:207_235 error	0.23608	0.37431	0.14969	0.90775	0.4853	0.48254	0.56423	0.42213	0.42226	0.40233
2σ error	0.0043	0.0037	0.004	0.0065	0.0038	0.0042	0.0038	0.0043	0.0038	0.0047
Pb206_U238	0.3384	0.3393	0.3398	0.34	0.3406	0.341	0.3424	0.3427	0.3431	0.344
2σ error	0.09	0.063	0.08	0.11	0.067	0.079	0.068	0.084	0.072	0.087
Pb207_U235	5.299	5.328	5.327	5.328	5.379	5.404	5.407	5.474	5.283	5.582
U/Th	0.8471	1.599	3.145	2.97	1.759	2.02	3.151	2.23	1.552	1.241
[U] ppm	66.135	357.59	71.49375	234.505	257.7145	113.197	356.816	74.8385	111.769	68.569
Grain #	323	264	155	263	233	31	112	177	105	211
Sample Name:	AJRL_323	AJRL_264	AJRL_155	AJRL_263	AJRL_233	AJRL_31	AJRL_112	AJRL_177	AJRL_105	AJRL_211

%error	1.5	1.6	1.7	1.3	1.1	1.2	1.1	2.2	1.3	2.5
% Discordance*	1.3	-0.8	1.1	-0.3	-0.9	-0.4	0.5	-1.5	0.2	-1.4
2σ error	21	21	21	21	20	19	18	23	19	24
(Ma)	1905	1909	1915	1919	1926	1926	1927	1927	1929	1931
2σ error	28	28	29	24	23	24	24	35	26	41
Age (Ma)	1926	1890	1936	1919	1908	1919	1929	1904	1935	1920
2σ error	21	21	21	21	20	19	18	23	19	24
Age (Ma)	1905	1909	1915	1919	1926	1926	1927	1927	1929	1931
2σ error	13	13	13	11	12	11	10	14	12	17
Age Ma	1915.2	1899.4	1921	1920.6	1916	1922.5	1927.7	1915	1928.5	1921
Final207_206_Prop2SE	0.0018	0.0018	0.0019	0.0016	0.0015	0.0016	0.0016	0.0023	0.0017	0.0026
Final207_206	0.1178	0.1159	0.1185	0.1174	0.11691	0.1175	0.11828	0.1167	0.1185	0.1173
206_238:207_235 error	0.42006	0.31866	0.26043	0.41468	0.67397	0.33658	0.2998	0.022005	0.34457	0.073262
2σ error	0.0044	0.0044	0.0043	0.0043	0.0042	0.0039	0.0038	0.0048	0.004	0.005
Pb206_U238	0.3438	0.3447	0.346	0.3469	0.3482	0.3482	0.3481	0.3484	0.3489	0.3494
2σ error	0.085	0.081	0.085	0.076	0.075	0.074	0.069	0.094	0.076	0.11
Pb207_U235	5.592	5.491	5.631	5.627	5.603	5.64	5.678	5.575	5.685	5.646
U/Th	2.245	1.983	0.813	1.691	3.795	2.767	2.205	0.5765	1.598	1.053
[U] ppm	98.2321	78.5075	77.025	108.0895	194.7401	204.557	284.307	51.0165	97.896	29.27445
Grain #	234	58	254	279	12	118	67	206	57	8
Sample Name:	AJRL_234	AJRL_58	AJRL_254	AJRL_279	AJRL_12	AJRL_118	AJRL_67	AJRL_206	AJRL_57	AJRL_8

%error	1.2	1.1	0.88	1.5	1.1	1.4	2.2	2.4	2.2	1.3
% Discordance*	-1.5	-0.4	-0.71	-0.6	-3.2	0.1	-5.6	-2.9	1.2	2.2
2σ error	20	19	18	23	18	20	28	28	28	20
(Ma)	1937	1942	1946	1949	1955	1983	2002	2003	2032	2035
2σ error	25	25	22	26	24	26	32	38	32	27
Age (Ma)	1921	1926	1934	1934	1897	1987	1906	1978	2048	2086
2σ error	20	19	18	23	18	20	28	28	28	20
Age (Ma)	1937	1942	1946	1949	1955	1983	2002	2003	2032	2035
2σ error	12	11	11	12	11	13	17	20	15	13
Age Ma	1926.8	1929.7	1938	1945.3	1925.8	1984.1	1953	1988	2042	2057.9
Final207_206_Prop2SE	0.0016	0.0016	0.0015	0.0017	0.0016	0.0018	0.0021	0.0027	0.0023	0.002
Final207_206	0.1176	0.11799	0.1185	0.1187	0.11618	0.1221	0.1163	0.1214	0.1263	0.1292
206_238:207_235 error	0.56168	0.36186	0.55825	0.54303	0.41242	0.43076	0.56996	0.5105	0.41642	0.27583
2σ error	0.0041	0.0041	0.0038	0.0048	0.0039	0.0043	0.0057	0.006	0.006	0.0043
Pb206_U238	0.3506	0.3517	0.3525	0.353	0.354	0.3603	0.3639	0.3646	0.3708	0.3712
2σ error	0.08	0.073	0.072	0.081	0.072	0.09	0.11	0.13	0.11	0.095
Pb207_U235	5.674	5.692	5.746	5.797	5.66	6.048	5.847	6.05	6.451	6.596
U/Th	1.542	1.513	1.975	16.3	1.315	3.542	1.711	0.74	3.21	1.211
[U] ppm	140.1475	137.33	313.37	135.3419	170.803	51.7101	62.608	28.9218	114.285	103.691
Grain #	71	341	100	324	190	119	297	153	203	111
Sample Name:	AJRL_71	AJRL_341	AJRL_100	AJRL_324	AJRL_190	AJRL_119	AJRL_297	AJRL_153	AJRL_203	AJRL_111

%error	1.7	1.6	2	2	2	1.3	0.81	0.97	0.71	1.2
% Discordance*	3.4	1.5	0.4	-0.2	-1.8	1.9	0.26	0.2	-0.08	-0.2
2σ error	25	22	26	24	26	26	24	24	23	27
(Ma)	2036	2044	2045	2057	2110	2328	2545	2561	2586	2695
2σ error	33	30	33	32	32	29	20	23	21	24
Age (Ma)	2107	2070	2072	2051	2080	2371	2548.3	2569	2578	2699
2σ error	25	22	26	24	26	26	24	24	23	27
Age (Ma)	2036	2044	2045	2057	2110	2328	2545	2561	2586	2695
2σ error	18	13	16	15	16	19	12	12	11	13
Age Ma	2070	2059.8	2065	2046	2097	2355	2546.4	2565.2	2582.1	2693.5
Final207_206_Prop2SE	0.0025	0.0021	0.0024	0.0023	0.0023	0.0026	0.002	0.0023	0.0021	0.0028
Final207_206	0.1305	0.1278	0.1277	0.1265	0.1288	0.1524	0.16913	0.1712	0.172	0.1851
206_238:207_235 error	0.41471	0.20968	0.40901	0.28887	0.41767	0.63408	0.67818	0.56062	0.46114	0.32144
2σ error	0.0054	0.0047	0.0056	0.0051	0.0057	0.0058	0.0056	0.0056	0.0053	0.0064
Pb206_U238	0.3715	0.3731	0.3735	0.3759	0.387	0.435	0.4842	0.4879	0.4937	0.5192
2σ error	0.13	0.098	0.12	0.11	0.12	0.19	0.14	0.15	0.14	0.18
Pb207_U235	6.67	6.61	6.63	6.515	6.863	9.18	11.274	11.515	11.723	13.19
U/Th	1.282	2.326	0.835	1.138	1.885	2.955	3.135	1.785	2.162	0.9465
[U] ppm	31.67915	69.345	36.3805	46.39	44.12455	104.3963	187.3245	106.849	198.8235	61.5375
Grain #	113	139	208	6	317	85	48	225	246	115
Sample Name:	AJRL_113	AJRL_139	AJRL_208	AJRL_6	AJRL_317	AJRL_85	AJRL_48	AJRL_225	AJRL_246	AJRL_115

%error	2	0.73	1	0.83	0.92	0.71	0.87	1.4	0.77	0.82
% Discordance*	-0.4	0.06	0.8	-0.91	-0.51	-0.35	0.9	-1.3	-0.39	-0.27
2σ error	56	24	27	24	26	24	24	37	28	28
(Ma)	2701	2706	2708	2711	2713	2730	2765	2779	2813	2955
2σ error	21	20	22	21	21	20	22	22	20	20
Age (Ma)	2686	2706.3	2728	2690	2689	2718.4	2784	2740	2801.8	2944
2σ error	56	24	27	24	26	24	24	37	28	28
Age (Ma)	2701	2706	2708	2711	2713	2730	2765	2779	2813	2955
2σ error	25	12	13	12	13	12	12	15	14	12
Age Ma	2693	2706.6	2718.5	2699.1	2698.6	2725.8	2775.5	2759	2801.2	2949.2
Final207_206_Prop2SE	0.0024	0.0022	0.0026	0.0024	0.0024	0.0023	0.0026	0.0025	0.0024	0.0027
Final207_206	0.1838	0.186	0.1877	0.1841	0.184	0.1874	0.1951	0.1899	0.197	0.2152
206_238:207_235 error	0.93827	0.52462	0.47583	0.41257	0.64743	0.50647	0.45267	0.7904	0.78348	0.61478
2σ error	0.013	0.0057	0.0065	0.0056	0.0062	0.0057	0.0058	0.0087	0.0067	0.0068
Pb206_U238	0.521	0.5218	0.5222	0.5228	0.5233	0.5274	0.5356	0.5383	0.5473	0.5816
2σ error	0.35	0.16	0.18	0.16	0.19	0.17	0.19	0.23	0.21	0.22
Pb207_U235	13.25	13.383	13.55	13.277	13.28	13.647	14.38	14.15	14.78	17.27
U/Th	1.796	6.5	1.938	1.001	1.584	2.279	1.746	1.0918	1.568	1.451
[U] ppm	169.598	129.8205	130.2295	132.2155	87.3625	174.4385	116.2535	115.0865	229.0805	157.1315
Grain #	33	258	330	250	43	114	309	347	183	72
Sample Name:	AJRL_33	AJRL_258	AJRL_330	AJRL_250	AJRL_43	AJRL_114	AJRL_309	AJRL_347	AJRL_183	AJRL_72

%error	1	0.8	0.93	0.77	NAN	NAN	NAN	NAN
% Discordance*	-0.5	-0.21	-0.77	-0.34	no value	no value	no value	no value
2σ error	31	29	32	30				
(Ma)	3017	3137	3142	3279	no value	no value	no value	no value
2σ error	22	21	21	18				
Age (Ma)	3003	3135	3121	3262.5	no value	no value	no value	no value
2σ error	31	29	32	30				
Age (Ma)	3017	3137	3142	3279	no value	no value	no value	no value
2σ error	15	12	13	13				
Age Ma	3007	3136.1	3132.6	3261.8	no value	no value	no value	no value
Final207_206_Prop2SE	0.0031	0.003	0.0032	0.0032				
Final207_206	0.2232	0.242	0.2403	0.2624	no value	no value	no value	no value
206_238:207_235 error	0.6207	0.55777	0.58148	0.60059	NaN	NaN	NaN	NaN
2σ error	0.0077	0.0072	0.0079	0.0079				
Pb206_U238	0.5968	0.6259	0.6283	0.6631	no value	no value	no value	no value
2σ error	0.28	0.27	0.28	0.32				
Pb207_U235	18.33	20.96	20.88	23.85	no value	no value	no value	no value
U/Th	3.384	1.725	1.21	1.839	no value	no value	no value	no value
[U] ppm	145.4705	92.398	165.3075	96.3275				
Grain #	160	337	262	230	65	207	243	271
Sample Name:	AJRL_160	AJRL_337	AJRL_262	AJRL_230	AJRL_65	AJRL_207	AJRL_243	AJRL_271
Concordia Age = 39.0 ±0.3 Ma					MSWD (of conc.&equiv.) = 0.74			

%disc	101.6	100.8	107	106.4	105.9	103.7	103.6	107.1	105.9
±2σ abs	1.7	0.82	0.74	0.73	0.79	1.2	0.64	0.7	0.74
best date	38.3	38.52	38.67	38.71	38.78	38.9	39.2	39.24	39.65
±2σ abs	1.7	0.82	0.74	0.73	0.79	1.2	0.64	0.7	0.74
Pb206_U238	38.3	38.52	38.67	38.71	38.78	38.9	39.2	39.24	39.65
±2σ abs	7.2	2	2.1	2.2	2	3.9	1.4	1.5	2
Pb207_U235	38.3	38.1	38.3	37.6	38.3	40.5	38.8	39.2	40
±2σ abs	0.0097	0.0028	0.0025	0.003	0.0025	0.0052	0.0016	0.0018	0.0024
Pb207_Pb206	0.0492	0.0471	0.0463	0.0457	0.046	0.05	0.0462	0.0473	0.0481
Corr.coef.	0.045436	0.018743	0.026814	0.03368	0.06932	0.078938	0.2854	0.19237	0.13639
±2σ %	0.00027	0.00013	0.00012	0.00011	0.00012	0.00019	0.0001	0.00011	0.00012
Pb206_U238	0.00596	0.00599	0.00602	0.00602	0.00603	0.00606	0.006099	0.006106	0.00617
±2σ %	0.0074	0.002	0.0021	0.0023	0.002	0.0041	0.0014	0.0015	0.0021
Pb207_U235	0.0388	0.0383	0.0385	0.0377	0.0384	0.0403	0.039	0.0394	0.0402
±2σ %	0.0097	0.0028	0.0025	0.003	0.0025	0.0052	0.0016	0.0018	0.0024
Pb207_Pb206	0.0492	0.0471	0.0463	0.0457	0.046	0.05	0.0462	0.0473	0.0481
Th/U	0.575269	0.175915	0.160753	0.199217	0.201381	0.47	0.209722	0.185973	0.170604
Th(ppm)	42.8	57.7	59.8	76.3	72.9	65.8	120.8	82.2	62.1
U(ppm)	74.4	328	372	383	362	140	576	442	364
Grain #	22	86	171	99	158	204	95	37	2
Sample Name:	AJRL_22	AJRL_86	AJRL_171	AJRL_99	AJRL_158	AJRL_204	AJRL_95	AJRL_37	AJRL_2

%disc	99.4	99.7	104.9	102.8	100	100.7	99.2	96	81	93
±2σ abs	0.69	0.7	0.9	0.82	1.1	1.1	1.5	1.1	2.3	1.7
best date	40.79	41.48	41.59	41.62	44	45.8	45.9	46.2	51.7	52
±2σ abs	0.69	0.7	0.9	0.82	1.1	1.1	1.5	1.1	2.3	1.7
Pb206_U238	40.79	41.48	41.59	41.62	44	45.8	45.9	46.2	51.7	52
±2σ abs	1.6	1.6	1.8	1.7	2.6	2.8	6.5	2.8	8	4.4
Pb207_U235	40	41.7	40.9	40.6	44.8	45.9	43.8	45.9	46.1	52.1
±2σ abs	0.0019	0.0019	0.002	0.002	0.0032	0.0032	0.007	0.0028	0.0076	0.0035
Pb207_Pb206	0.0461	0.0472	0.0461	0.0455	0.0488	0.0481	0.0448	0.045	0.0425	0.0492
Corr.coef.	0.031568	0.021523	0.29003	0.19411	0.16238	0.19032	0.1	0.12875	0.22637	0.56776
±2σ %	0.00011	0.00011	0.00014	0.00013	0.00017	0.00018	0.00024	0.00018	0.00036	0.00027
Pb206_U238	0.006348	0.006456	0.00647	0.00648	0.00684	0.00714	0.00714	0.00719	0.00805	0.0081
±2σ %	0.0016	0.0016	0.0018	0.0017	0.0026	0.0028	0.0066	0.0028	0.0083	0.0046
Pb207_U235	0.0402	0.042	0.0412	0.0408	0.0452	0.0463	0.0437	0.0463	0.0465	0.0528
±2σ %	0.0019	0.0019	0.002	0.002	0.0032	0.0032	0.007	0.0028	0.0076	0.0035
Pb207_Pb206	0.0461	0.0472	0.0461	0.0455	0.0488	0.0481	0.0448	0.045	0.0425	0.0492
Th/U	0.518694	0.5	0.209351	0.243358	0.536866	0.806878	0.506135	0.789474	0.428571	0.62963
Th(ppm)	208.1	222	109.7	131.9	233	305	33	180	87	340
U(ppm)	401.2	444	524	542	434	378	65.2	228	203	540
Grain #	49	1	176	82	15	194	78	135	23	16
Sample Name:	AJRL_49	AJRL_1	AJRL_176	AJRL_82	AJRL_15	AJRL_194	AJRL_78	AJRL_135	AJRL_23	AJRL_16

%disc	86	94	104	107	98	52	40	8	-2	-20
±2σ abs	1.5	3.2	2.8	2.4	3.9	3.8	2.5	3.6	7.5	8.3
best date	88.8	159.9	160.8	161.2	162	170.1	171.2	202.9	393.1	517.8
±2σ abs	1.5	3.2	2.8	2.4	3.9	3.8	2.5	3.6	7.5	8.3
Pb206_U238	88.8	159.9	160.8	161.2	162	170.1	171.2	202.9	393.1	517.8
±2σ abs	3.8	8.4	6.6	4.8	12	6	4.6	3.8	9.9	12
Pb207_U235	88.8	158.3	161.9	158.8	166	171.5	172.4	203.7	402.8	518
±2σ abs	0.0019	0.0028	0.0021	0.0016	0.0042	0.0016	0.0014	0.0009	0.0016	0.0016
Pb207_Pb206	0.0476	0.0475	0.0492	0.0483	0.0514	0.0506	0.0496	0.05063	0.0559	0.0579
Corr.coef.	0.30639	0.053479	0.24474	0.067445	0.1	0.55982	0.18844	0.59367	0.34144	0.34759
±2σ %	0.00024	0.00051	0.00045	0.00039	0.00061	0.0006	0.0004	0.00058	0.0012	0.0014
Pb206_U238	0.01386	0.02511	0.02526	0.02533	0.02545	0.02674	0.02691	0.03198	0.0629	0.0835
±2σ %	0.0041	0.0097	0.0076	0.0055	0.014	0.0071	0.0053	0.0046	0.015	0.019
Pb207_U235	0.0915	0.1694	0.1735	0.1695	0.179	0.1834	0.1846	0.2222	0.487	0.666
±2σ %	0.0019	0.0028	0.0021	0.0016	0.0042	0.0016	0.0014	0.0009	0.0016	0.0016
Pb207_Pb206	0.0476	0.0475	0.0492	0.0483	0.0514	0.0506	0.0496	0.05063	0.0559	0.0579
Th/U	0.301648	0.652174	0.385039	1.094588	0.659382	0.205993	0.552684	0.300607	0.288667	0.543563
Th(ppm)	95.2	58.5	48.9	224.5	27.76	110	278	297	86.6	41.8
U(ppm)	315.6	89.7	127	205.1	42.1	534	503	988	300	76.9
Grain #	9	79	175	219	24	66	282	170	166	328
Sample Name:	AJRL_9	AJRL_79	AJRL_175	AJRL_219	AJRL_24	AJRL_66	AJRL_282	AJRL_170	AJRL_166	AJRL_328

%disc	-15	0.9	0	-39	-1.2	-3	-3.2	-0.3	-6.7	2.2
±2σ abs	11	10	15	19	14	18	14	14	15	11
best date	702.8	990.3	991	999	1024	1031	1052	1054	1055	1060.4
±2σ abs	11	10	15	19	14	18	14	14	15	11
Pb206_U238	702.8	990.3	991	999	1024	1031	1052	1054	1055	1060.4
±2σ abs	17	9.9	11	24	11	20	17	14	17	8.8
Pb207_U235	703	996.3	991.6	998	1022.5	1039	1066	1055	1043	1068.6
±2σ abs	0.0022	0.0011	0.0015	0.0029	0.0012	0.0026	0.0021	0.0017	0.0018	0.001
Pb207_Pb206	0.0634	0.07284	0.073	0.0708	0.07318	0.0756	0.0759	0.0752	0.0738	0.07562
Corr.coef.	0.11708	0.43354	0.17684	0.068755	0.6368	0.23541	0.10908	0.26278	0.29513	0.52354
±2σ %	0.0019	0.0019	0.0027	0.0034	0.0025	0.0032	0.0026	0.0026	0.0026	0.0021
Pb206_U238	0.1152	0.1659	0.1661	0.1677	0.1722	0.1731	0.177	0.1777	0.1775	0.1788
±2σ %	0.035	0.026	0.029	0.065	0.031	0.056	0.049	0.041	0.047	0.025
Pb207_U235	0.996	1.665	1.657	1.677	1.738	1.79	1.857	1.828	1.796	1.865
±2σ %	0.0022	0.0011	0.0015	0.0029	0.0012	0.0026	0.0021	0.0017	0.0018	0.001
Pb207_Pb206	0.0634	0.07284	0.073	0.0708	0.07318	0.0756	0.0759	0.0752	0.0738	0.07562
Th/U	0.474636	0.196891	0.068047	0.367433	0.102703	0.4	0.570213	0.303571	0.558841	0.106935
Th(ppm)	16.28	38	12.16	7.83	38	11.88	26.8	15.3	19.28	77.1
U(ppm)	34.3	193	178.7	21.31	370	29.7	47	50.4	34.5	721
Grain #	157	240	294	222	238	142	299	121	122	256
Sample Name:	AJRL_157	AJRL_240	AJRL_294	AJRL_222	AJRL_238	AJRL_142	AJRL_299	AJRL_121	AJRL_122	AJRL_256

%disc	0.7	-11	2.1	-0.2	0.9	-16	-1.2	-34	2.6	2.9
±2σ abs	16	21	13	14	12	16	22	17	12	14
best date	1063	1063	1063.7	1065	1065.5	1066	1066	1067	1067.1	1069
±2σ abs	16	21	13	14	12	16	22	17	12	14
Pb206_U238	1063	1063	1063.7	1065	1065.5	1066	1066	1067	1067.1	1069
±2σ abs	14	24	11	19	11	23	17	25	12	13
Pb207_U235	1081	1043	1067	1069	1073.6	1061	1062	1060	1084	1079
±2σ abs	0.0019	0.0028	0.0012	0.0021	0.0012	0.0025	0.0014	0.0028	0.0013	0.0013
Pb207_Pb206	0.0753	0.0739	0.0754	0.0753	0.07558	0.0744	0.0747	0.0742	0.076	0.0761
Corr.coef.	0.31104	0.10447	0.48078	0.28616	0.43328	0.27488	0.71544	0.084016	0.28619	0.49514
±2σ %	0.0029	0.0039	0.0024	0.0026	0.0022	0.0029	0.0041	0.0031	0.0022	0.0025
Pb206_U238	0.1793	0.1793	0.1794	0.1796	0.1797	0.1799	0.18	0.18	0.18	0.1804
±2σ %	0.039	0.065	0.03	0.054	0.03	0.065	0.049	0.07	0.034	0.036
Pb207_U235	1.896	1.807	1.862	1.869	1.881	1.856	1.845	1.827	1.909	1.894
±2σ %	0.0019	0.0028	0.0012	0.0021	0.0012	0.0025	0.0014	0.0028	0.0013	0.0013
Pb207_Pb206	0.0753	0.0739	0.0754	0.0753	0.07558	0.0744	0.0747	0.0742	0.076	0.0761
Th/U	0.387912	0.370323	0.239554	0.41375	0.395509	0.458515	0.299298	0.360513	0.326185	0.400441
Th(ppm)	35.3	5.74	43	16.55	68.7	10.5	46.9	7.03	28.9	90.9
U(ppm)	91	15.5	179.5	40	173.7	22.9	156.7	19.5	88.6	227
Grain #	51	195	19	335	201	62	235	199	200	61
Sample Name:	AJRL_51	AJRL_195	AJRL_19	AJRL_335	AJRL_201	AJRL_62	AJRL_235	AJRL_199	AJRL_200	AJRL_61

%disc	-1.2	-9.7	0.4	-0.9	0.3	-1.1	1.5	0.1	1.2	0.1
±2σ abs	13	16	12	13	13	13	12	14	13	11
best date	1069.8	1071	1072.4	1072.5	1073.7	1074.3	1074.9	1076	1076.7	1078
±2σ abs	13	16	12	13	13	13	12	14	13	11
Pb206_U238	1069.8	1071	1072.4	1072.5	1073.7	1074.3	1074.9	1076	1076.7	1078
±2σ abs	13	20	9.6	11	9.5	11	11	12	14	9.4
Pb207_U235	1073	1057	1073	1068.9	1078.6	1070.6	1076.4	1077.6	1084	1088.7
±2σ abs	0.0015	0.002	0.0012	0.0013	0.0012	0.0013	0.0014	0.0013	0.0016	0.001
Pb207_Pb206	0.0754	0.0745	0.07548	0.0754	0.07556	0.075	0.0761	0.07572	0.0764	0.07592
Corr.coef.	0.036759	0.22648	0.19801	0.34497	0.34396	0.32157	0.18558	0.58746	0.37212	0.58963
±2σ %	0.0024	0.0029	0.0022	0.0024	0.0023	0.0023	0.0022	0.0026	0.0024	0.002
Pb206_U238	0.1805	0.1809	0.181	0.181	0.1813	0.1814	0.1815	0.1817	0.1818	0.182
±2σ %	0.036	0.053	0.027	0.032	0.027	0.032	0.031	0.033	0.04	0.027
Pb207_U235	1.881	1.828	1.878	1.865	1.894	1.872	1.889	1.893	1.907	1.923
±2σ %	0.0015	0.002	0.0012	0.0013	0.0012	0.0013	0.0014	0.0013	0.0016	0.001
Pb207_Pb206	0.0754	0.0745	0.07548	0.0754	0.07556	0.075	0.0761	0.07572	0.0764	0.07592
Th/U	0.296715	0.343643	0.28972	0.434014	0.335294	0.316946	0.47449	0.477193	0.36342	0.439252
Th(ppm)	28.9	10	62	63.8	57	30.3	93	81.6	30.6	235
U(ppm)	97.4	29.1	214	147	170	95.6	196	171	84.2	535
Grain #	93	34	35	87	286	3	164	101	44	149
Sample Name:	AJRL_93	AJRL_34	AJRL_35	AJRL_87	AJRL_286	AJRL_3	AJRL_164	AJRL_101	AJRL_44	AJRL_149

%disc	-2.8	1.6	-14.5	-14	-2.4	-1	-0.3	-2.7	0.3	-1.2
±2σ abs	14	15	18	21	17	14	11	17	11	14
best date	1078	1078	1079	1081	1082	1082	1082	1083	1085.2	1086
±2σ abs	14	15	18	21	17	14	11	17	11	14
Pb206_U238	1078	1078	1079	1081	1082	1082	1082	1083	1085.2	1086
±2σ abs	12	14	21	29	21	13	9.3	17	9.3	12
Pb207_U235	1077	1097	1076	1072	1075	1079	1081.2	1081	1087	1079.8
±2σ abs	0.0013	0.0019	0.0026	0.0036	0.0022	0.0015	0.0011	0.0019	0.0011	0.0012
Pb207_Pb206	0.0748	0.0773	0.0753	0.076	0.0753	0.0752	0.07536	0.0749	0.07604	0.07496
Corr.coef.	0.46123	0.1	0.08049	0.1	0.36818	0.29495	0.37732	0.27062	0.20012	0.55577
±2σ %	0.0025	0.0027	0.0033	0.0038	0.0031	0.0025	0.0021	0.0031	0.0021	0.0025
Pb206_U238	0.1821	0.1821	0.1823	0.1826	0.1829	0.1828	0.1828	0.183	0.1834	0.1834
±2σ %	0.034	0.042	0.059	0.077	0.06	0.035	0.027	0.05	0.027	0.034
Pb207_U235	1.884	1.951	1.897	1.875	1.884	1.893	1.897	1.905	1.918	1.899
±2σ %	0.0013	0.0019	0.0026	0.0036	0.0022	0.0015	0.0011	0.0019	0.0011	0.0012
Pb207_Pb206	0.0748	0.0773	0.0753	0.076	0.0753	0.0752	0.07536	0.0749	0.07604	0.07496
Th/U	0.536667	0.260695	0.366129	0.558088	0.370746	0.503407	0.304494	0.435211	0.283108	0.333846
Th(ppm)	64.4	9.75	9.08	7.59	12.42	59.1	81.3	30.9	83.8	43.4
U(ppm)	120	37.4	24.8	13.6	33.5	117.4	267	71	296	130
Grain #	223	303	162	186	73	161	296	301	289	181
Sample Name:	AJRL_223	AJRL_303	AJRL_162	AJRL_186	AJRL_73	AJRL_161	AJRL_296	AJRL_301	AJRL_289	AJRL_181

%disc	-3.6	3.3	3.4	-5	-1.7	-6.3	-1.8	-5	0.6	-3.1
±2σ abs	14	14	16	21	12	14	12	14	12	15
best date	1086	1086	1087	1088	1088.5	1089	1089.7	1090	1091.1	1092
±2σ abs	14	14	16	21	12	14	12	14	12	15
Pb206_U238	1086	1086	1087	1088	1088.5	1089	1089.7	1090	1091.1	1092
±2σ abs	15	16	15	28	10	18	11	14	12	16
Pb207_U235	1075	1106	1103	1087	1090.6	1076	1085.4	1081	1092.4	1096
±2σ abs	0.0015	0.002	0.0013	0.0027	0.0012	0.0019	0.0012	0.0017	0.0014	0.0017
Pb207_Pb206	0.0746	0.0775	0.0773	0.0745	0.07557	0.0738	0.07513	0.0751	0.0762	0.0756
Corr.coef.	0.43813	0.1277	0.72466	0.50189	0.41071	0.28242	0.31358	0.12296	0.13864	0.28045
±2σ %	0.0027	0.0025	0.003	0.0039	0.0023	0.0026	0.0022	0.0027	0.0022	0.0027
Pb206_U238	0.1835	0.1835	0.1836	0.184	0.184	0.1841	0.1842	0.1843	0.1844	0.1846
±2σ %	0.041	0.048	0.045	0.074	0.03	0.05	0.031	0.04	0.034	0.046
Pb207_U235	1.883	1.978	1.964	1.908	1.929	1.888	1.912	1.894	1.93	1.948
±2σ %	0.0015	0.002	0.0013	0.0027	0.0012	0.0019	0.0012	0.0017	0.0014	0.0017
Pb207_Pb206	0.0746	0.0775	0.0773	0.0745	0.07557	0.0738	0.07513	0.0751	0.0762	0.0756
Th/U	0.46203	0.341506	0.056477	0.637993	0.315748	0.875989	0.247869	0.375479	0.560714	0.427002
Th(ppm)	28.9	19.5	32.7	17.8	40.1	33.2	37.8	19.6	62.8	27.2
U(ppm)	62.55	57.1	579	27.9	127	37.9	152.5	52.2	112	63.7
Grain #	224	283	210	128	245	59	270	218	268	312
Sample Name:	AJRL_224	AJRL_283	AJRL_210	AJRL_128	AJRL_245	AJRL_59	AJRL_270	AJRL_218	AJRL_268	AJRL_312

%disc	-1.9	-2.1	-1	-1.4	-3.4	0.6	-3.4	-2.1	-5.4	0.5
±2σ abs	11	14	13	16	17	18	14	12	14	12
best date	1094.2	1095	1096.2	1098	1098	1098	1099	1099.9	1102	1102.3
±2σ abs	11	14	13	16	17	18	14	12	14	12
Pb206_U238	1094.2	1095	1096.2	1098	1098	1098	1099	1099.9	1102	1102.3
±2σ abs	11	14	11	15	12	19	14	9.9	13	11
Pb207_U235	1089.9	1093	1087.2	1103	1084	1108	1091	1090.8	1085	1102
±2σ abs	0.0012	0.0016	0.0011	0.0016	0.0016	0.0025	0.0014	0.0012	0.0014	0.0012
Pb207_Pb206	0.07546	0.0767	0.07558	0.0769	0.0753	0.0773	0.0751	0.07559	0.0744	0.07608
Corr.coef.	0.37194	0.15987	0.49457	0.29184	0.39749	0.1	0.35725	0.34009	0.3616	0.23812
±2σ %	0.0021	0.0026	0.0023	0.003	0.0031	0.0032	0.0026	0.0022	0.0025	0.0023
Pb206_U238	0.185	0.1851	0.1854	0.1855	0.1857	0.1853	0.1858	0.1861	0.1865	0.1865
±2σ %	0.032	0.04	0.032	0.043	0.036	0.056	0.041	0.028	0.037	0.031
Pb207_U235	1.927	1.938	1.92	1.962	1.911	1.978	1.928	1.929	1.911	1.962
±2σ %	0.0012	0.0016	0.0011	0.0016	0.0016	0.0025	0.0014	0.0012	0.0014	0.0012
Pb207_Pb206	0.07546	0.0767	0.07558	0.0769	0.0753	0.0773	0.0751	0.07559	0.0744	0.07608
Th/U	0.293729	0.494881	0.350588	0.495088	0.362733	0.335667	0.342857	0.418407	0.574645	0.339437
Th(ppm)	35.6	29	59.6	25.2	29.2	10.07	26.4	64.1	48.5	48.2
U(ppm)	121.2	58.6	170	50.9	80.5	30	77	153.2	84.4	142
Grain #	212	274	280	26	88	123	252	133	84	285
Sample Name:	AJRL_212	AJRL_274	AJRL_280	AJRL_26	AJRL_88	AJRL_123	AJRL_252	AJRL_133	AJRL_84	AJRL_285

%disc	-4.8	-7.1	-3.5	-4.2	-2.3	-0.4	-1.6	-0.1	-3.2	-1.7
±2σ abs	18	18	15	14	16	13	14	12	16	15
best date	1103	1103	1106	1109	1110	1110.4	1111	1111.7	1112	1112
±2σ abs	18	18	15	14	16	13	14	12	16	15
Pb206_U238	1103	1103	1106	1109	1110	1110.4	1111	1111.7	1112	1112
±2σ abs	22	20	14	16	16	11	14	11	17	17
Pb207_U235	1104	1100	1100	1095	1115	1112.5	1112	1111.5	1112	1115
±2σ abs	0.0026	0.0021	0.0014	0.0018	0.0021	0.0014	0.0017	0.0013	0.002	0.0021
Pb207_Pb206	0.0769	0.0766	0.0755	0.0753	0.0772	0.0771	0.0763	0.07667	0.0769	0.0767
Corr.coef.	0.19173	0.32893	0.5257	0.2181	0.098199	0.048336	0.17932	0.21973	0.051706	0.18478
±2σ %	0.0033	0.0033	0.0028	0.0026	0.003	0.0024	0.0026	0.0021	0.0029	0.0028
Pb206_U238	0.1866	0.1867	0.1872	0.1878	0.188	0.188	0.1881	0.1881	0.1883	0.1883
±2σ %	0.064	0.058	0.04	0.046	0.047	0.032	0.044	0.03	0.049	0.05
Pb207_U235	1.976	1.95	1.951	1.946	2.003	1.984	1.99	1.984	1.997	2
±2σ %	0.0026	0.0021	0.0014	0.0018	0.0021	0.0014	0.0017	0.0013	0.002	0.0021
Pb207_Pb206	0.0769	0.0766	0.0755	0.0753	0.0772	0.0771	0.0763	0.07667	0.0769	0.0767
Th/U	0.453881	0.404977	0.294053	0.387931	0.339198	0.434292	0.23457	0.440758	0.593472	0.385783
Th(ppm)	9.94	17.9	26.7	20.25	15.23	42.3	13.91	46.5	20	16.01
U(ppm)	21.9	44.2	90.8	52.2	44.9	97.4	59.3	105.5	33.7	41.5
Grain #	314	326	167	91	217	17	242	83	21	169
Sample Name:	AJRL_314	AJRL_326	AJRL_167	AJRL_91	AJRL_217	AJRL_17	AJRL_242	AJRL_83	AJRL_21	AJRL_169

%disc	-0.1	0.7	0.5	1.9	-0.7	-1.3	-0.8	-32	-3.7	-0.8
±2σ abs	13	12	11	14	12	13	11	24	16	13
best date	1112.1	1113.8	1114.7	1115	1115.4	1115.5	1115.6	1117	1117	1132.1
±2σ abs	13	12	11	14	12	13	11	24	16	13
Pb206_U238	1112.1	1113.8	1114.7	1115	1115.4	1115.5	1115.6	1117	1117	1132.1
±2σ abs	12	11	9.6	13	11	12	10	34	19	11
Pb207_U235	1116.7	1117.7	1115.6	1117	1115.8	1119.8	1115.1	1090	1120	1126.3
±2σ abs	0.0015	0.0013	0.0011	0.0015	0.0013	0.0014	0.0012	0.0037	0.0022	0.0012
Pb207_Pb206	0.0768	0.07712	0.0768	0.0781	0.07658	0.0767	0.07685	0.0747	0.0769	0.0775
Corr.coef.	-0.034714	0.29242	0.30794	0.26565	0.24611	0.37021	0.45161	0.18115	0.21344	0.40685
±2σ %	0.0024	0.0023	0.0021	0.0025	0.0023	0.0023	0.0021	0.0044	0.0029	0.0024
Pb206_U238	0.1883	0.1886	0.1888	0.1889	0.1889	0.1889	0.1889	0.1888	0.1892	0.1918
±2σ %	0.036	0.031	0.028	0.039	0.032	0.034	0.03	0.098	0.054	0.034
Pb207_U235	1.999	2.005	2.002	2.004	2.003	2.009	2	1.932	2.011	2.035
±2σ %	0.0015	0.0013	0.0011	0.0015	0.0013	0.0014	0.0012	0.0037	0.0022	0.0012
Pb207_Pb206	0.0768	0.07712	0.0768	0.0781	0.07658	0.0767	0.07685	0.0747	0.0769	0.0775
Th/U	0.512903	0.49237	0.50641	0.670139	0.304085	0.64538	0.066667	0.38009	0.565	0.239716
Th(ppm)	31.8	48.4	79	38.6	40.2	95	21.2	4.2	22.6	33.8
U(ppm)	62	98.3	156	57.6	132.2	147.2	318	11.05	40	141
Grain #	74	7	293	178	251	284	25	54	313	103
Sample Name:	AJRL_74	AJRL_7	AJRL_293	AJRL_178	AJRL_251	AJRL_284	AJRL_25	AJRL_54	AJRL_313	AJRL_103

%disc	0	-4.3	-5.6	-3.5	-2.1	-3	-2.1	-1.9	-5.9	-2.2
±2σ abs	12	16	17	16	14	16	17	18	18	18
best date	1135.2	1136	1142	1142	1143.6	1144	1146	1147	1148	1148
±2σ abs	12	16	17	16	14	16	17	18	18	18
Pb206_U238	1135.2	1136	1142	1142	1143.6	1144	1146	1147	1148	1148
±2σ abs	11	13	14	12	13	17	12	12	18	14
Pb207_U235	1136.6	1129	1125	1128	1145	1134	1140	1141.5	1134	1144
±2σ abs	0.0012	0.0015	0.0016	0.0015	0.0015	0.0019	0.001	0.0011	0.0022	0.0013
Pb207_Pb206	0.07772	0.0768	0.0762	0.0771	0.0777	0.0774	0.07733	0.07715	0.0765	0.0774
Corr.coef.	0.32534	0.36898	0.37209	0.31081	0.34963	0.22456	0.83386	0.74943	0.051269	0.66748
±2σ %	0.0023	0.003	0.0031	0.003	0.0025	0.0029	0.0031	0.0033	0.0034	0.0033
Pb206_U238	0.1926	0.1927	0.1939	0.1935	0.1941	0.1942	0.1946	0.1948	0.195	0.195
±2σ %	0.033	0.04	0.041	0.038	0.039	0.05	0.036	0.037	0.053	0.041
Pb207_U235	2.065	2.042	2.031	2.036	2.088	2.062	2.073	2.076	2.061	2.083
±2σ %	0.0012	0.0015	0.0016	0.0015	0.0015	0.0019	0.001	0.0011	0.0022	0.0013
Pb207_Pb206	0.07772	0.0768	0.0762	0.0771	0.0777	0.0774	0.07733	0.07715	0.0765	0.0774
Th/U	0.188406	0.476285	0.426256	0.309524	0.397626	0.205824	0.567159	0.689243	0.389163	0.380282
Th(ppm)	19.5	48.2	26.3	52	26.8	12.37	153.7	173	15.8	108
U(ppm)	103.5	101.2	61.7	168	67.4	60.1	271	251	40.6	284
Grain #	11	247	140	307	136	150	180	290	27	134
Sample Name:	AJRL_11	AJRL_247	AJRL_140	AJRL_307	AJRL_136	AJRL_150	AJRL_180	AJRL_290	AJRL_27	AJRL_134

%disc	-4.1	-2.7	-2.5	-2.2	-0.8	-1.3	-2.3	-1.6	-0.7	-1
±2σ abs	16	13	26	15	15	15	16	16	18	13
best date	1149	1152.7	1162	1178	1206	1216	1249	1258	1265	1329.2
±2σ abs	16	13	26	15	15	15	16	16	18	13
Pb206_U238	1149	1152.7	1162	1178	1206	1216	1249	1258	1265	1329.2
±2σ abs	14	11	18	14	15	13	13	14	22	9.9
Pb207_U235	1149	1142.3	1145	1179	1211	1209	1229	1252	1257	1324
±2σ abs	0.0014	0.0011	0.0011	0.0017	0.0018	0.0014	0.0014	0.0016	0.0023	0.0011
Pb207_Pb206	0.077	0.07728	0.07737	0.079	0.0812	0.0801	0.0808	0.0825	0.0824	0.08517
Corr.coef.	0.44459	0.52175	0.89266	0.14971	0.25144	0.50474	0.70601	0.42825	0.51797	0.38516
±2σ %	0.003	0.0024	0.0048	0.0028	0.0029	0.0029	0.003	0.003	0.0035	0.0025
Pb206_U238	0.1952	0.1956	0.1977	0.2005	0.2058	0.2077	0.2138	0.2155	0.2169	0.229
±2σ %	0.043	0.032	0.054	0.043	0.05	0.043	0.045	0.048	0.076	0.036
Pb207_U235	2.103	2.076	2.093	2.196	2.303	2.292	2.352	2.432	2.459	2.685
±2σ %	0.0014	0.0011	0.0011	0.0017	0.0018	0.0014	0.0014	0.0016	0.0023	0.0011
Pb207_Pb206	0.077	0.07728	0.07737	0.079	0.0812	0.0801	0.0808	0.0825	0.0824	0.08517
Th/U	0.546218	0.380829	0.07395	0.329412	0.527597	0.113804	0.786444	0.382627	0.229265	0.381218
Th(ppm)	65	73.5	24.13	50.4	32.5	37.1	84.7	18.06	16.53	75.1
U(ppm)	119	193	326.3	153	61.6	326	107.7	47.2	72.1	197
Grain #	90	55	191	239	209	182	129	276	173	68
Sample Name:	AJRL_90	AJRL_55	AJRL_191	AJRL_239	AJRL_209	AJRL_182	AJRL_129	AJRL_276	AJRL_173	AJRL_68

%disc	0	1.5	0	-3.6	0.1	-2.6	1.1	0.4	-1	-0.1
±2σ abs	15	14	16	17	20	20	14	18	14	14
best date	1340	1343.5	1344	1349	1350	1353	1353.8	1364	1366.8	1367.9
±2σ abs	15	14	16	17	20	20	14	18	14	14
Pb206_U238	1340	1343.5	1344	1349	1350	1353	1353.8	1364	1366.8	1367.9
±2σ abs	13	11	11	16	20	21	10	17	11	12
Pb207_U235	1343	1346.6	1342.5	1336	1355	1333	1361.6	1373	1360.9	1378.8
±2σ abs	0.0016	0.0014	0.0014	0.0018	0.0023	0.0021	0.0012	0.0018	0.0013	0.0015
Pb207_Pb206	0.0862	0.0866	0.0862	0.0853	0.0877	0.0851	0.08738	0.0885	0.08674	0.088
Corr.coef.	0.096382	0.19044	0.38548	0.2737	0.41511	0.70203	0.38195	0.48291	0.36937	0.25008
±2σ %	0.003	0.0028	0.003	0.0032	0.0039	0.0039	0.0027	0.0033	0.0028	0.0027
Pb206_U238	0.2311	0.2318	0.2318	0.2328	0.233	0.2336	0.2337	0.2353	0.236	0.2364
±2σ %	0.048	0.041	0.042	0.059	0.076	0.076	0.039	0.065	0.042	0.046
Pb207_U235	2.753	2.766	2.754	2.73	2.806	2.732	2.822	2.873	2.819	2.878
±2σ %	0.0016	0.0014	0.0014	0.0018	0.0023	0.0021	0.0012	0.0018	0.0013	0.0015
Pb207_Pb206	0.0862	0.0866	0.0862	0.0853	0.0877	0.0851	0.08738	0.0885	0.08674	0.088
Th/U	0.594118	0.29192	0.281998	0.37037	0.812144	0.602395	0.3125	0.710218	0.424018	0.282077
Th(ppm)	50.5	33.6	27.1	15	42.8	20.12	58	42.4	57.2	27.7
U(ppm)	85	115.1	96.1	40.5	52.7	33.4	185.6	59.7	134.9	98.2
Grain #	92	236	198	151	10	80	205	331	257	291
Sample Name:	AJRL_92	AJRL_236	AJRL_198	AJRL_151	AJRL_10	AJRL_80	AJRL_205	AJRL_331	AJRL_257	AJRL_291

%disc	1.7	0.6	1	0.6	0.3	0.2	-1.5	-0.8	0.7	-0.9
±2σ abs	23	17	15	17	14	20	15	15	18	19
best date	1368	1372	1372	1375	1377.8	1381	1382.7	1395.1	1413	1416
±2σ abs	23	17	15	17	14	20	15	15	18	19
Pb206_U238	1368	1372	1372	1375	1377.8	1381	1382.7	1395.1	1413	1416
±2σ abs	18	14	12	12	11	19	11	12	12	19
Pb207_U235	1380	1376	1372.5	1382.5	1373.3	1368	1370.7	1384.5	1418.1	1417
±2σ abs	0.0019	0.0016	0.0015	0.0014	0.0013	0.0021	0.0014	0.0014	0.0013	0.0023
Pb207_Pb206	0.0884	0.088	0.0879	0.088	0.08766	0.0872	0.0871	0.08796	0.08984	0.0896
Corr.coef.	0.57119	0.52405	0.21912	0.4412	0.18646	0.27682	0.28954	0.30748	0.60488	0.21065
±2σ %	0.0041	0.0032	0.0029	0.0032	0.0028	0.0038	0.0029	0.0028	0.0035	0.0037
Pb206_U238	0.2357	0.2372	0.2372	0.2377	0.2381	0.2386	0.2393	0.2416	0.245	0.2458
±2σ %	0.073	0.053	0.046	0.046	0.04	0.072	0.043	0.043	0.048	0.076
Pb207_U235	2.888	2.876	2.868	2.901	2.866	2.858	2.86	2.904	3.044	3.049
±2σ %	0.0019	0.0016	0.0015	0.0014	0.0013	0.0021	0.0014	0.0014	0.0013	0.0023
Pb207_Pb206	0.0884	0.088	0.0879	0.088	0.08766	0.0872	0.0871	0.08796	0.08984	0.0896
Th/U	0.288991	0.436498	0.661842	0.671329	0.489796	0.786241	0.549591	0.768602	0.25	0.482051
Th(ppm)	25.2	35.4	50.3	96	72	32	60.4	94	56.5	13.16
U(ppm)	87.2	81.1	76	143	147	40.7	109.9	122.3	226	27.3
Grain #	288	300	305	189	255	231	131	145	4	287
Sample Name:	AJRL_288	AJRL_300	AJRL_305	AJRL_189	AJRL_255	AJRL_231	AJRL_131	AJRL_145	AJRL_4	AJRL_287

%disc	-2.2	-1.6	0.8	2.3	-1.1	0.3	-1.3	1.4	-1.7	-0.2
±2σ abs	16	17	17	16	20	17	22	17	15	16
best date	1417	1420	1422	1424	1427	1427	1427	1429	1433	1439
±2σ abs	16	17	17	16	20	17	22	17	15	16
Pb206_U238	1417	1420	1422	1424	1427	1427	1427	1429	1433	1439
±2σ abs	14	14	11	13	14	13	17	11	12	12
Pb207_U235	1411	1420	1426.9	1438	1425	1427	1435	1442.1	1425.7	1443.5
±2σ abs	0.0017	0.0017	0.0013	0.0017	0.0017	0.0016	0.0024	0.0014	0.0014	0.0013
Pb207_Pb206	0.0887	0.0897	0.09031	0.0911	0.0896	0.0902	0.0908	0.091	0.0893	0.09061
Corr.coef.	0.025615	0.25783	0.46984	0.23748	0.42612	0.38391	0.14533	0.39208	0.19561	0.26467
±2σ %	0.003	0.0032	0.0032	0.0031	0.0037	0.0033	0.0042	0.0031	0.003	0.0032
Pb206_U238	0.2458	0.2465	0.2468	0.2472	0.2471	0.2479	0.2478	0.2479	0.2491	0.2501
±2σ %	0.057	0.056	0.046	0.051	0.057	0.053	0.069	0.045	0.045	0.046
Pb207_U235	3.012	3.057	3.079	3.12	3.061	3.081	3.119	3.14	3.071	3.142
±2σ %	0.0017	0.0017	0.0013	0.0017	0.0017	0.0016	0.0024	0.0014	0.0014	0.0013
Pb207_Pb206	0.0887	0.0897	0.09031	0.0911	0.0896	0.0902	0.0908	0.091	0.0893	0.09061
Th/U	0.428331	0.250295	0.191279	0.520335	0.253607	0.522535	0.315778	0.17521	0.635176	0.287801
Th(ppm)	25.4	12.74	32.9	43.5	15.47	74.2	14.21	41.7	63.2	39.4
U(ppm)	59.3	50.9	172	83.6	61	142	45	238	99.5	136.9
Grain #	110	156	336	334	108	124	304	126	40	107
Sample Name:	AJRL_110	AJRL_156	AJRL_336	AJRL_334	AJRL_108	AJRL_124	AJRL_304	AJRL_126	AJRL_40	AJRL_107

%disc	0.6	0.7	1.4	-2.7	0.2	-1.1	-1.1	-1.3	-2.2	-0.4
±2σ abs	17	16	15	15	16	15	14	17	17	16
best date	1440	1440	1440	1441.8	1443	1446.3	1447	1448	1448	1451
±2σ abs	17	16	15	15	16	15	14	17	17	16
Pb206_U238	1440	1440	1440	1441.8	1443	1446.3	1447	1448	1448	1451
±2σ abs	11	15	12	13	14	13	11	13	13	11
Pb207_U235	1446	1436	1448.4	1430	1449	1442.9	1446.4	1439	1432	1448.1
±2σ abs	0.0014	0.0018	0.0013	0.0017	0.0017	0.0014	0.0013	0.0015	0.0016	0.0013
Pb207_Pb206	0.09128	0.0905	0.09137	0.0898	0.0918	0.0904	0.0904	0.0901	0.0898	0.09051
Corr.coef.	0.3901	0.30656	0.41456	0.24607	0.33526	0.40012	0.39181	0.4206	0.38395	0.45955
±2σ %	0.0032	0.0031	0.003	0.003	0.0032	0.0029	0.0028	0.0033	0.0034	0.0031
Pb206_U238	0.2503	0.2503	0.2504	0.2505	0.2509	0.2516	0.2517	0.2519	0.2519	0.2523
±2σ %	0.046	0.059	0.048	0.053	0.06	0.051	0.045	0.052	0.053	0.047
Pb207_U235	3.157	3.118	3.167	3.089	3.165	3.14	3.151	3.13	3.101	3.162
±2σ %	0.0014	0.0018	0.0013	0.0017	0.0017	0.0014	0.0013	0.0015	0.0016	0.0013
Pb207_Pb206	0.09128	0.0905	0.09137	0.0898	0.0918	0.0904	0.0904	0.0901	0.0898	0.09051
Th/U	0.30457	0.62065	0.638587	0.41472	0.569254	0.388266	0.274107	0.196507	0.682051	0.497093
Th(ppm)	28.66	53.5	117.5	35.5	37.4	45	61.4	18	79.8	85.5
U(ppm)	94.1	86.2	184	85.6	65.7	115.9	224	91.6	117	172
Grain #	192	215	329	229	266	102	302	46	81	226
Sample Name:	AJRL_192	AJRL_215	AJRL_329	AJRL_229	AJRL_266	AJRL_102	AJRL_302	AJRL_46	AJRL_81	AJRL_226

%disc	-1.3	-0.6	-2.4	-0.8	-0.9	-1.8	-1.3	1.7	1.6	0.4
±2σ abs	27	15	15	17	20	18	22	19	17	18
best date	1456	1456.8	1457.7	1458	1461	1503	1629	1674	1679	1681
±2σ abs	27	15	15	17	20	18	22	19	17	18
Pb206_U238	1456	1456.8	1457.7	1458	1461	1503	1629	1674	1679	1681
±2σ abs	22	11	11	15	14	12	17	14	12	13
Pb207_U235	1432	1449	1442.8	1455	1444	1489.9	1629	1683	1685.4	1683.9
±2σ abs	0.0025	0.0013	0.0012	0.0016	0.0014	0.0014	0.0019	0.0017	0.0015	0.0017
Pb207_Pb206	0.0897	0.09081	0.09017	0.0911	0.0903	0.0927	0.0996	0.1038	0.1043	0.1039
Corr.coef.	0.50271	0.41044	0.38877	0.33957	0.71957	0.55507	0.51941	0.42876	0.29241	0.17151
±2σ %	0.0052	0.0029	0.003	0.0032	0.0038	0.0035	0.0043	0.0039	0.0035	0.0037
Pb206_U238	0.2528	0.2534	0.2538	0.2539	0.2544	0.2627	0.2876	0.2965	0.2975	0.298
±2σ %	0.09	0.045	0.043	0.06	0.055	0.051	0.082	0.073	0.061	0.066
Pb207_U235	3.115	3.169	3.138	3.198	3.146	3.339	3.98	4.246	4.257	4.245
±2σ %	0.0025	0.0013	0.0012	0.0016	0.0014	0.0014	0.0019	0.0017	0.0015	0.0017
Pb207_Pb206	0.0897	0.09081	0.09017	0.0911	0.0903	0.0927	0.0996	0.1038	0.1043	0.1039
Th/U	0.490806	0.306604	0.445866	0.175223	0.406667	0.498305	0.642285	0.322892	0.430689	0.248525
Th(ppm)	10.41	45.5	90.6	15.7	54.9	117.6	64.1	26.8	58.1	18.54
U(ppm)	21.21	148.4	203.2	89.6	135	236	99.8	83	134.9	74.6
Grain #	339	298	60	141	127	338	214	232	96	53
Sample Name:	AJRL_339	AJRL_298	AJRL_60	AJRL_141	AJRL_127	AJRL_338	AJRL_214	AJRL_232	AJRL_96	AJRL_53

%disc	0.1	0.4	-1.1	0.2	0.9	-1.5	-1.7	-2.1	1.2	3
±2σ abs	17	17	25	19	18	21	21	18	21	17
best date	1683.9	1690	1692	1692	1694	1697	1699	1711	1731	1731
±2σ abs	17	17	25	19	18	21	21	18	21	17
Pb206_U238	1683.9	1690	1692	1692	1694	1697	1699	1711	1731	1731
±2σ abs	10	13	15	12	13	16	14	12	19	12
Pb207_U235	1687.8	1691	1678	1697.5	1699	1690	1688	1702	1747	1757.5
±2σ abs	0.0014	0.0016	0.0019	0.0016	0.0016	0.0018	0.0017	0.0015	0.0022	0.0016
Pb207_Pb206	0.10353	0.104	0.1023	0.1044	0.1045	0.1032	0.1027	0.1035	0.1075	0.109
Corr.coef.	0.33626	0.3383	0.51742	0.45523	0.53033	0.53066	0.31717	0.38021	0.47903	0.35181
±2σ %	0.0033	0.0035	0.0049	0.0038	0.0036	0.0043	0.0043	0.0037	0.0043	0.0034
Pb206_U238	0.2985	0.2997	0.2996	0.3001	0.3005	0.3012	0.3016	0.304	0.3081	0.3081
±2σ %	0.054	0.067	0.076	0.064	0.07	0.084	0.075	0.061	0.1	0.065
Pb207_U235	4.266	4.286	4.227	4.326	4.334	4.286	4.276	4.347	4.574	4.649
±2σ %	0.0014	0.0016	0.0019	0.0016	0.0016	0.0018	0.0017	0.0015	0.0022	0.0016
Pb207_Pb206	0.10353	0.104	0.1023	0.1044	0.1045	0.1032	0.1027	0.1035	0.1075	0.109
Th/U	0.268137	0.445087	0.366957	0.390927	0.283333	0.207339	0.454271	0.627407	0.337713	0.214836
Th(ppm)	54.7	30.8	21.1	40.5	49.3	27.12	45.2	110.8	43.7	30.7
U(ppm)	204	69.2	57.5	103.6	174	130.8	99.5	176.6	129.4	142.9
Grain #	70	346	5	228	272	77	278	52	47	185
Sample Name:	AJRL_70	AJRL_346	AJRL_5	AJRL_228	AJRL_272	AJRL_77	AJRL_278	AJRL_52	AJRL_47	AJRL_185

%disc	-0.9	-0.4	-2.8	-0.9	0.1	-1.7	1.6	2	0.28	-1.4
±2σ abs	16	20	28	18	18	18	18	22	17	21
best date	1732.3	1733	1733	1741	1746	1764	1765	1772	1775.9	1778
±2σ abs	16	20	28	18	18	18	18	22	17	21
Pb206_U238	1732.3	1733	1733	1741	1746	1764	1765	1772	1775.9	1778
±2σ abs	11	12	17	12	12	12	12	15	11	15
Pb207_U235	1724.1	1727.1	1718	1740.6	1751.7	1748.4	1773	1788	1778.3	1755
±2σ abs	0.0014	0.0015	0.0022	0.0016	0.0017	0.0016	0.0015	0.0022	0.0014	0.0019
Pb207_Pb206	0.10543	0.1054	0.104	0.106	0.1073	0.1063	0.10941	0.1108	0.10881	0.1068
Corr.coef.	0.4631	0.48181	0.5121	0.36506	0.1983	0.54295	0.36012	0.27357	0.42152	0.42123
±2σ %	0.0033	0.004	0.0058	0.0037	0.0036	0.0038	0.0036	0.0043	0.0035	0.0043
Pb206_U238	0.3083	0.3084	0.3086	0.31	0.3108	0.3148	0.3145	0.3152	0.3172	0.3176
±2σ %	0.059	0.067	0.096	0.064	0.065	0.068	0.063	0.086	0.065	0.085
Pb207_U235	4.466	4.472	4.431	4.551	4.617	4.599	4.728	4.816	4.76	4.636
±2σ %	0.0014	0.0015	0.0022	0.0016	0.0017	0.0016	0.0015	0.0022	0.0014	0.0019
Pb207_Pb206	0.10543	0.1054	0.104	0.106	0.1073	0.1063	0.10941	0.1108	0.10881	0.1068
Th/U	0.380952	0.244521	0.264244	0.364286	0.486993	0.313196	0.13601	0.434807	0.492063	0.351526
Th(ppm)	62.4	35.7	9.09	40.8	46.8	39.4	28.29	15.74	93	19.58
U(ppm)	163.8	146	34.4	112	96.1	125.8	208	36.2	189	55.7
Grain #	130	106	249	322	41	311	159	179	342	327
Sample Name:	AJRL_130	AJRL_106	AJRL_249	AJRL_322	AJRL_41	AJRL_311	AJRL_159	AJRL_179	AJRL_342	AJRL_327

%disc	6.8	-1.2	3.4	3.2	-0.8	0.7	-1	-1.1	-0.8	0.7
±2σ abs	22	18	18	19	19	21	19	22	19	23
best date	1789	1790	1791	1792	1795	1797	1801	1805	1806	1808
±2σ abs	22	18	18	19	19	21	19	22	19	23
Pb206_U238	1789	1790	1791	1792	1795	1797	1801	1805	1806	1808
±2σ abs	18	13	12	13	12	14	12	13	12	18
Pb207_U235	1853	1779	1821.7	1815.9	1788.8	1803	1797.7	1798.6	1808.3	1826
±2σ abs	0.0022	0.0016	0.0019	0.0016	0.0018	0.0019	0.0016	0.0014	0.0016	0.0023
Pb207_Pb206	0.1184	0.1083	0.1142	0.11282	0.1089	0.1106	0.1093	0.10917	0.1101	0.1117
Corr.coef.	0.40092	0.49641	0.22193	0.61594	0.2435	0.38217	0.47781	0.79387	0.42048	0.31694
±2σ %	0.0045	0.0038	0.0037	0.0039	0.0039	0.0044	0.0039	0.0046	0.0038	0.0047
Pb206_U238	0.3199	0.3201	0.3203	0.3205	0.3211	0.3216	0.3223	0.3233	0.3233	0.3238
±2σ %	0.11	0.075	0.075	0.075	0.071	0.081	0.071	0.073	0.072	0.1
Pb207_U235	5.216	4.772	5.01	4.985	4.826	4.908	4.877	4.883	4.934	5.031
±2σ %	0.0022	0.0016	0.0019	0.0016	0.0018	0.0019	0.0016	0.0014	0.0016	0.0023
Pb207_Pb206	0.1184	0.1083	0.1142	0.11282	0.1089	0.1106	0.1093	0.10917	0.1101	0.1117
Th/U	0.831925	0.403045	0.622207	0.324277	0.271478	0.55243	0.2955	0.155627	0.35709	1.568807
Th(ppm)	88.6	50.3	89.1	56.1	23.7	43.2	44	48.4	48.1	34.2
U(ppm)	106.5	124.8	143.2	173	87.3	78.2	148.9	311	134.7	21.8
Grain #	244	152	196	144	18	116	202	132	273	104
Sample Name:	AJRL_244	AJRL_152	AJRL_196	AJRL_144	AJRL_18	AJRL_116	AJRL_202	AJRL_132	AJRL_273	AJRL_104

%disc	-1	-1.7	-1.4	-0.4	-0.3	0.1	-0.2	0.3	-0.7	0.7
±2σ abs	18	18	19	18	18	22	20	22	20	18
best date	1814	1818	1819	1823	1827	1827	1828	1829	1831	1833
±2σ abs	18	18	19	18	18	22	20	22	20	18
Pb206_U238	1814	1818	1819	1823	1827	1827	1828	1829	1831	1833
±2σ abs	11	12	13	11	12	13	13	15	13	11
Pb207_U235	1809.8	1804.6	1801	1830.3	1819.3	1820.7	1823.4	1839	1831.8	1833
±2σ abs	0.0014	0.0015	0.0017	0.0016	0.0016	0.0018	0.0017	0.002	0.0018	0.0015
Pb207_Pb206	0.11014	0.10975	0.1096	0.1117	0.1113	0.1114	0.1113	0.1128	0.1111	0.11263
Corr.coef.	0.48318	0.42751	0.29102	0.2423	0.40384	0.54737	0.29512	0.41653	0.26172	0.40267
±2σ %	0.0037	0.0036	0.0038	0.0036	0.0038	0.0046	0.0041	0.0045	0.0041	0.0037
Pb206_U238	0.3251	0.3259	0.326	0.3269	0.3277	0.3277	0.3278	0.3281	0.3286	0.3288
±2σ %	0.063	0.069	0.077	0.071	0.072	0.079	0.077	0.091	0.077	0.067
Pb207_U235	4.946	4.918	4.895	5.058	5.004	5.004	5.03	5.125	5.078	5.084
±2σ %	0.0014	0.0015	0.0017	0.0016	0.0016	0.0018	0.0017	0.002	0.0018	0.0015
Pb207_Pb206	0.11014	0.10975	0.1096	0.1117	0.1113	0.1114	0.1113	0.1128	0.1111	0.11263
Th/U	0.270356	0.304826	0.228396	0.353102	0.697175	0.434457	0.838776	0.199599	0.34	0.385102
Th(ppm)	42.5	36	22.36	38.7	61.7	58	41.1	14.95	35.7	54.8
U(ppm)	157.2	118.1	97.9	109.6	88.5	133.5	49	74.9	105	142.3
Grain #	184	220	321	94	13	148	14	320	36	56
Sample Name:	AJRL_184	AJRL_220	AJRL_321	AJRL_94	AJRL_13	AJRL_148	AJRL_14	AJRL_320	AJRL_36	AJRL_56

%disc	0.9	1.1	0.2	-0.9	-2.1	-0.5	0.5	0.1	-1.8	-0.5
±2σ abs	19	18	21	21	30	20	19	18	21	19
best date	1835	1835	1836	1837	1837	1839	1839	1840	1842	1843
±2σ abs	19	18	21	21	30	20	19	18	21	19
Pb206_U238	1835	1835	1836	1837	1837	1839	1839	1840	1842	1843
±2σ abs	12	11	14	13	23	14	14	13	15	13
Pb207_U235	1839.5	1845.6	1839	1836	1828	1837	1844	1842.1	1834	1839.8
±2σ abs	0.0016	0.0015	0.0019	0.0016	0.0028	0.0017	0.0017	0.0016	0.002	0.0017
Pb207_Pb206	0.1132	0.113	0.1123	0.1114	0.1112	0.1122	0.1132	0.1129	0.1112	0.1123
Corr.coef.	0.4593	0.35796	0.27821	0.59043	0.38734	0.53494	0.46655	0.46844	0.2581	0.40315
±2σ %	0.0039	0.0038	0.0043	0.0044	0.0061	0.0042	0.0039	0.0037	0.0044	0.004
Pb206_U238	0.3292	0.3294	0.3296	0.3298	0.33	0.3302	0.3301	0.3303	0.3307	0.3311
±2σ %	0.07	0.068	0.086	0.081	0.14	0.083	0.085	0.076	0.086	0.079
Pb207_U235	5.117	5.161	5.128	5.099	5.04	5.112	5.158	5.141	5.065	5.129
±2σ %	0.0016	0.0015	0.0019	0.0016	0.0028	0.0017	0.0017	0.0016	0.002	0.0017
Pb207_Pb206	0.1132	0.113	0.1123	0.1114	0.1112	0.1122	0.1132	0.1129	0.1112	0.1123
Th/U	0.343338	0.479021	0.982143	0.419643	0.805543	0.383381	0.553259	0.327104	0.677885	0.36563
Th(ppm)	46.9	68.5	38.5	70.5	17.73	40.6	34.8	38.86	28.2	22.34
U(ppm)	136.6	143	39.2	168	22.01	105.9	62.9	118.8	41.6	61.1
Grain #	28	281	168	63	318	76	147	50	187	75
Sample Name:	AJRL_28	AJRL_281	AJRL_168	AJRL_63	AJRL_318	AJRL_76	AJRL_147	AJRL_50	AJRL_187	AJRL_75

%disc	-0.7	0.2	0	0.1	-0.4	-1.7	-1.4	-0.2	-1	-1.6
±2σ abs	18	19	18	18	18	22	19	18	18	19
best date	1843	1843	1844	1844	1845	1845	1848	1848	1850	1850
±2σ abs	18	19	18	18	18	22	19	18	18	19
Pb206_U238	1843	1843	1844	1844	1845	1845	1848	1848	1850	1850
±2σ abs	12	12	12	11	12	14	12	11	11	16
Pb207_U235	1837.4	1845.1	1840.4	1841.8	1838.4	1829	1839	1842	1842.3	1842
±2σ abs	0.0017	0.0016	0.0015	0.0015	0.0016	0.0016	0.0016	0.0015	0.0016	0.0021
Pb207_Pb206	0.1122	0.1125	0.11269	0.11278	0.1125	0.1107	0.1118	0.11288	0.112	0.1114
Corr.coef.	0.24283	0.31725	0.47776	0.30242	0.28056	0.54816	0.31391	0.31427	0.28999	0.12433
±2σ %	0.0037	0.0039	0.0037	0.0038	0.0037	0.0046	0.0039	0.0037	0.0037	0.004
Pb206_U238	0.3311	0.3311	0.3313	0.3312	0.3313	0.3315	0.332	0.332	0.3325	0.3324
±2σ %	0.073	0.071	0.072	0.066	0.073	0.08	0.069	0.065	0.069	0.095
Pb207_U235	5.106	5.158	5.13	5.137	5.118	5.049	5.121	5.138	5.14	5.146
±2σ %	0.0017	0.0016	0.0015	0.0015	0.0016	0.0016	0.0016	0.0015	0.0016	0.0021
Pb207_Pb206	0.1122	0.1125	0.11269	0.11278	0.1125	0.1107	0.1118	0.11288	0.112	0.1114
Th/U	0.47033	0.576585	0.683032	1.081348	0.641509	0.541379	0.49798	0.348649	0.517363	0.135626
Th(ppm)	42.8	65.5	79.3	186.1	57.8	62.8	49.3	64.5	102.8	4.18
U(ppm)	91	113.6	116.1	172.1	90.1	116	99	185	198.7	30.82
Grain #	109	306	39	343	197	221	138	248	137	154
Sample Name:	AJRL_109	AJRL_306	AJRL_39	AJRL_343	AJRL_197	AJRL_221	AJRL_138	AJRL_248	AJRL_137	AJRL_154

%disc	-0.6	-0.2	-0.4	-3	-1.6	1.7	-1.2	-0.2	0.1	-0.6
±2σ abs	19	27	38	19	19	28	25	18	30	27
best date	1850	1853	1854	1855	1857	1858	1860	1860	1860	1864
±2σ abs	19	27	38	19	19	28	25	18	30	27
Pb206_U238	1850	1853	1854	1855	1857	1858	1860	1860	1860	1864
±2σ abs	12	16	22	14	11	23	17	11	15	14
Pb207_U235	1853.2	1841	1848	1839	1852.8	1879	1855	1849.9	1864	1865
±2σ abs	0.0016	0.0014	0.0019	0.0019	0.0015	0.0027	0.0018	0.0016	0.0016	0.0015
Pb207_Pb206	0.1129	0.11198	0.1125	0.1105	0.11257	0.1157	0.1129	0.1127	0.1136	0.11364
Corr.coef.	0.38113	0.86578	0.82051	0.14325	0.46653	0.52329	0.62533	0.23847	0.8302	0.79323
±2σ %	0.0038	0.0055	0.0078	0.004	0.0039	0.0058	0.0051	0.0038	0.0063	0.0055
Pb206_U238	0.3324	0.3326	0.3335	0.3335	0.3338	0.3342	0.334	0.3345	0.3339	0.3355
±2σ %	0.071	0.096	0.13	0.083	0.068	0.15	0.1	0.07	0.094	0.088
Pb207_U235	5.202	5.14	5.16	5.116	5.2	5.38	5.213	5.187	5.277	5.274
±2σ %	0.0016	0.0014	0.0019	0.0019	0.0015	0.0027	0.0018	0.0016	0.0016	0.0015
Pb207_Pb206	0.1129	0.11198	0.1125	0.1105	0.11257	0.1157	0.1129	0.1127	0.1136	0.11364
Th/U	0.325564	0.308955	0.352419	0.944706	0.623124	0.82619	0.584007	0.652444	0.252128	1.093458
Th(ppm)	43.3	62.1	43.7	80.3	70.6	34.7	65	73.4	47.4	234
U(ppm)	133	201	124	85	113.3	42	111.3	112.5	188	214
Grain #	275	32	120	193	213	165	64	188	259	332
Sample Name:	AJRL_275	AJRL_32	AJRL_120	AJRL_193	AJRL_213	AJRL_165	AJRL_64	AJRL_188	AJRL_259	AJRL_332

%disc	0.3	-1.1	-1.3	-0.6	-1	-0.3	-0.3	-2.2	-1	-1.6
±2σ abs	20	18	19	26	25	23	24	21	18	19
best date	1865	1867	1872	1874	1877	1879	1879	1879	1883	1886
±2σ abs	20	18	19	26	25	23	24	21	18	19
Pb206_U238	1865	1867	1872	1874	1877	1879	1879	1879	1883	1886
±2σ abs	12	10	12	17	18	14	16	14	10	13
Pb207_U235	1858.5	1858.8	1861.1	1863	1871	1871	1879	1869	1873.1	1872.3
±2σ abs	0.0015	0.0014	0.0016	0.003	0.0025	0.0018	0.002	0.0021	0.0014	0.0018
Pb207_Pb206	0.11375	0.11323	0.11323	0.1148	0.1132	0.114	0.1148	0.1134	0.11396	0.1137
Corr.coef.	0.60971	0.52237	0.48431	0.18357	0.23281	0.51063	0.4542	0.23608	0.37431	0.14969
±2σ %	0.0041	0.0038	0.004	0.0054	0.0052	0.0047	0.0049	0.0043	0.0037	0.004
Pb206_U238	0.3351	0.3357	0.3371	0.3375	0.3376	0.3386	0.3386	0.3384	0.3393	0.3398
±2σ %	0.073	0.064	0.073	0.11	0.11	0.086	0.1	0.09	0.063	0.08
Pb207_U235	5.235	5.24	5.256	5.254	5.317	5.318	5.364	5.299	5.328	5.327
±2σ %	0.0015	0.0014	0.0016	0.003	0.0025	0.0018	0.002	0.0021	0.0014	0.0018
Pb207_Pb206	0.11375	0.11323	0.11323	0.1148	0.1132	0.114	0.1148	0.1134	0.11396	0.1137
Th/U	0.459906	0.373139	0.394908	0.955087	0.429032	0.374714	1.07909	1.177606	0.621795	0.319549
Th(ppm)	97.5	115.3	66.7	17.65	10.64	32.75	29.88	61	194	21.25
U(ppm)	212	309	168.9	18.48	24.8	87.4	27.69	51.8	312	66.5
Grain #	319	333	143	260	345	237	241	323	264	155
Sample Name:	AJRL_319	AJRL_333	AJRL_143	AJRL_260	AJRL_345	AJRL_237	AJRL_241	AJRL_323	AJRL_264	AJRL_155

%disc	-1	-1	-0.3	-1	0.1	-4.6	0.3	1.3	-0.8	1.1
±2σ abs	31	18	20	18	21	18	23	21	21	21
best date	1886	1889	1891	1898	1899	1902	1905	1905	1909	1915
±2σ abs	31	18	20	18	21	18	23	21	21	21
Pb206_U238	1886	1889	1891	1898	1899	1902	1905	1905	1909	1915
±2σ abs	18	11	12	11	14	12	13	13	13	13
Pb207_U235	1871	1881.8	1884.6	1885.7	1897	1866.4	1913	1915.2	1899.4	1921
±2σ abs	0.0017	0.0015	0.0017	0.0014	0.0018	0.0015	0.002	0.0018	0.0018	0.0019
Pb207_Pb206	0.1128	0.11464	0.1155	0.11488	0.1166	0.11189	0.1175	0.1178	0.1159	0.1185
Corr.coef.	0.90775	0.4853	0.48254	0.56423	0.42213	0.42226	0.40233	0.42006	0.31866	0.26043
±2σ %	0.0065	0.0038	0.0042	0.0038	0.0043	0.0038	0.0047	0.0044	0.0044	0.0043
Pb206_U238	0.34	0.3406	0.341	0.3424	0.3427	0.3431	0.344	0.3438	0.3447	0.346
±2σ %	0.11	0.067	0.079	0.068	0.084	0.072	0.087	0.085	0.081	0.085
Pb207_U235	5.328	5.379	5.404	5.407	5.474	5.283	5.582	5.592	5.491	5.631
±2σ %	0.0017	0.0015	0.0017	0.0014	0.0018	0.0015	0.002	0.0018	0.0018	0.0019
Pb207_Pb206	0.1128	0.11464	0.1155	0.11488	0.1166	0.11189	0.1175	0.1178	0.1159	0.1185
Th/U	0.386047	0.575771	0.495069	0.318072	0.427941	0.678423	0.784111	0.436139	0.490057	1.262626
Th(ppm)	83	130.7	50.2	105.6	29.1	65.4	45.4	38.86	34.5	75
U(ppm)	215	227	101.4	332	68	96.4	57.9	89.1	70.4	59.4
Grain #	263	233	31	112	177	105	211	234	58	254
Sample Name:	AJRL_263	AJRL_233	AJRL_31	AJRL_112	AJRL_177	AJRL_105	AJRL_211	AJRL_234	AJRL_58	AJRL_254

%disc	-0.3	-0.9	-0.4	0.5	-1.5	0.2	-1.4	-1.5	-0.4	-0.71
±2σ abs	21	20	19	18	23	19	24	20	19	18
best date	1919	1926	1926	1927	1927	1929	1931	1937	1942	1946
±2σ abs	21	20	19	18	23	19	24	20	19	18
Pb206_U238	1919	1926	1926	1927	1927	1929	1931	1937	1942	1946
±2σ abs	11	12	11	10	14	12	17	12	11	11
Pb207_U235	1920.6	1916	1922.5	1927.7	1915	1928.5	1921	1926.8	1929.7	1938
±2σ abs	0.0016	0.0015	0.0016	0.0016	0.0023	0.0017	0.0026	0.0016	0.0016	0.0015
Pb207_Pb206	0.1174	0.11691	0.1175	0.11828	0.1167	0.1185	0.1173	0.1176	0.11799	0.1185
Corr.coef.	0.41468	0.67397	0.33658	0.2998	0.022005	0.34457	0.073262	0.56168	0.36186	0.55825
±2σ %	0.0043	0.0042	0.0039	0.0038	0.0048	0.004	0.005	0.0041	0.0041	0.0038
Pb206_U238	0.3469	0.3482	0.3482	0.3481	0.3484	0.3489	0.3494	0.3506	0.3517	0.3525
±2σ %	0.076	0.075	0.074	0.069	0.094	0.076	0.11	0.08	0.073	0.072
Pb207_U235	5.627	5.603	5.64	5.678	5.575	5.685	5.646	5.674	5.692	5.746
±2σ %	0.0016	0.0015	0.0016	0.0016	0.0023	0.0017	0.0026	0.0016	0.0016	0.0015
Pb207_Pb206	0.1174	0.11691	0.1175	0.11828	0.1167	0.1185	0.1173	0.1176	0.11799	0.1185
Th/U	0.586316	0.260654	0.350265	0.45214	1.775	0.62837	0.956904	0.645029	0.655462	0.507143
Th(ppm)	55.7	47.83	66.2	116.2	63.9	53.6	22.87	78.5	78	142
U(ppm)	95	183.5	189	257	36	85.3	23.9	121.7	119	280
Grain #	279	12	118	67	206	57	8	71	341	100
Sample Name:	AJRL_279	AJRL_12	AJRL_118	AJRL_67	AJRL_206	AJRL_57	AJRL_8	AJRL_71	AJRL_341	AJRL_100

%disc	-0.6	-3.2	0.1	-5.6	-2.9	1.2	2.2	3.4	1.5	0.4
±2σ abs	23	18	20	28	28	28	20	25	22	26
best date	1949	1955	1983	2002	2003	2032	2035	2036	2044	2045
±2σ abs	23	18	20	28	28	28	20	25	22	26
Pb206_U238	1949	1955	1983	2002	2003	2032	2035	2036	2044	2045
±2σ abs	12	11	13	17	20	15	13	18	13	16
Pb207_U235	1945.3	1925.8	1984.1	1953	1988	2042	2057.9	2070	2059.8	2065
±2σ abs	0.0017	0.0016	0.0018	0.0021	0.0027	0.0023	0.002	0.0025	0.0021	0.0024
Pb207_Pb206	0.1187	0.11618	0.1221	0.1163	0.1214	0.1263	0.1292	0.1305	0.1278	0.1277
Corr.coef.	0.54303	0.41242	0.43076	0.56996	0.5105	0.41642	0.27583	0.41471	0.20968	0.40901
±2σ %	0.0048	0.0039	0.0043	0.0057	0.006	0.006	0.0043	0.0054	0.0047	0.0056
Pb206_U238	0.353	0.354	0.3603	0.3639	0.3646	0.3708	0.3712	0.3715	0.3731	0.3735
±2σ %	0.081	0.072	0.09	0.11	0.13	0.11	0.095	0.13	0.098	0.12
Pb207_U235	5.797	5.66	6.048	5.847	6.05	6.451	6.596	6.67	6.61	6.63
±2σ %	0.0017	0.0016	0.0018	0.0021	0.0027	0.0023	0.002	0.0025	0.0021	0.0024
Pb207_Pb206	0.1187	0.11618	0.1221	0.1163	0.1214	0.1263	0.1292	0.1305	0.1278	0.1277
Th/U	0.071675	0.757241	0.281649	0.59745	1.364384	0.28972	0.810563	0.780351	0.428571	1.211158
Th(ppm)	9.54	109.8	13.66	32.8	29.88	31	70.6	20.89	27	34.3
U(ppm)	133.1	145	48.5	54.9	21.9	107	87.1	26.77	63	28.32
Grain #	324	190	119	297	153	203	111	113	139	208
Sample Name:	AJRL_324	AJRL_190	AJRL_119	AJRL_297	AJRL_153	AJRL_203	AJRL_111	AJRL_113	AJRL_139	AJRL_208

%disc	-0.2	-1.8	1.9	0.26	0.2	-0.08	-0.2	-0.4	0.06	0.8
±2σ abs	24	26	26	24	24	23	27	56	24	27
best date	2057	2110	2328	2545	2561	2586	2695	2701	2706	2708
±2σ abs	24	26	26	24	24	23	27	56	24	27
Pb206_U238	2057	2110	2328	2545	2561	2586	2695	2701	2706	2708
±2σ abs	15	16	19	12	12	11	13	25	12	13
Pb207_U235	2046	2097	2355	2546.4	2565.2	2582.1	2693.5	2693	2706.6	2718.5
±2σ abs	0.0023	0.0023	0.0026	0.002	0.0023	0.0021	0.0028	0.0024	0.0022	0.0026
Pb207_Pb206	0.1265	0.1288	0.1524	0.16913	0.1712	0.172	0.1851	0.1838	0.186	0.1877
Corr.coef.	0.28887	0.41767	0.63408	0.67818	0.56062	0.46114	0.32144	0.93827	0.52462	0.47583
±2σ %	0.0051	0.0057	0.0058	0.0056	0.0056	0.0053	0.0064	0.013	0.0057	0.0065
Pb206_U238	0.3759	0.387	0.435	0.4842	0.4879	0.4937	0.5192	0.521	0.5218	0.5222
±2σ %	0.11	0.12	0.19	0.14	0.15	0.14	0.18	0.35	0.16	0.18
Pb207_U235	6.515	6.863	9.18	11.274	11.515	11.723	13.19	13.25	13.383	13.55
±2σ %	0.0023	0.0023	0.0026	0.002	0.0023	0.0021	0.0028	0.0024	0.0022	0.0026
Pb207_Pb206	0.1265	0.1288	0.1524	0.16913	0.1712	0.172	0.1851	0.1838	0.186	0.1877
Th/U	0.885417	0.522392	0.338676	0.325862	0.566278	0.445	1.067073	0.581769	0.246944	0.513769
Th(ppm)	34	20.53	32.75	56.7	53.4	80.1	52.5	86.8	30.3	59.7
U(ppm)	38.4	39.3	96.7	174	94.3	180	49.2	149.2	122.7	116.2
Grain #	6	317	85	48	225	246	115	33	258	330
Sample Name:	AJRL_6	AJRL_317	AJRL_85	AJRL_48	AJRL_225	AJRL_246	AJRL_115	AJRL_33	AJRL_258	AJRL_330

%disc	-0.91	-0.51	-0.35	0.9	-1.3	-0.39	-0.27	-0.5	-0.21	-0.77
±2σ abs	24	26	24	24	37	28	28	31	29	32
best date	2711	2713	2730	2765	2779	2813	2955	3017	3137	3142
±2σ abs	24	26	24	24	37	28	28	31	29	32
Pb206_U238	2711	2713	2730	2765	2779	2813	2955	3017	3137	3142
±2σ abs	12	13	12	12	15	14	12	15	12	13
Pb207_U235	2699.1	2698.6	2725.8	2775.5	2759	2801.2	2949.2	3007	3136.1	3132.6
±2σ abs	0.0024	0.0024	0.0023	0.0026	0.0025	0.0024	0.0027	0.0031	0.003	0.0032
Pb207_Pb206	0.1841	0.184	0.1874	0.1951	0.1899	0.197	0.2152	0.2232	0.242	0.2403
Corr.coef.	0.41257	0.64743	0.50647	0.45267	0.7904	0.78348	0.61478	0.6207	0.55777	0.58148
±2σ %	0.0056	0.0062	0.0057	0.0058	0.0087	0.0067	0.0068	0.0077	0.0072	0.0079
Pb206_U238	0.5228	0.5233	0.5274	0.5356	0.5383	0.5473	0.5816	0.5968	0.6259	0.6283
±2σ %	0.16	0.19	0.17	0.19	0.23	0.21	0.22	0.28	0.27	0.28
Pb207_U235	13.277	13.28	13.647	14.38	14.15	14.78	17.27	18.33	20.96	20.88
±2σ %	0.0024	0.0024	0.0023	0.0026	0.0025	0.0024	0.0027	0.0031	0.003	0.0032
Pb207_Pb206	0.1841	0.184	0.1874	0.1951	0.1899	0.197	0.2152	0.2232	0.242	0.2403
Th/U	1.002804	0.62336	0.436789	0.566277	0.905163	0.6334	0.686622	0.296324	0.574939	0.827312
Th(ppm)	107.3	47.5	69.1	58.1	85.9	126.3	92.9	40.3	46.8	114.5
U(ppm)	107	76.2	158.2	102.6	94.9	199.4	135.3	136	81.4	138.4
Grain #	250	43	114	309	347	183	72	160	337	262
Sample Name:	AJRL_250	AJRL_43	AJRL_114	AJRL_309	AJRL_347	AJRL_183	AJRL_72	AJRL_160	AJRL_337	AJRL_262

Sample Name:	Grain #	U(ppm)	Th(ppm)	Th/U	Pb207_Pb206	±2σ %	Pb207_U235	±2σ %	Pb206_U238	±2σ %	Corr.coef.	±2σ abs	Pb207_Pb206	±2σ abs	Pb207_U235	±2σ abs	Pb206_U238	±2σ abs	best date	±2σ abs	%disc
AJRL_230	230	85.4	46.5	0.544496	0.2624	0.0032	23.85	0.32	0.6631	0.0079	0.60059	0.0032	0.2624	0.0032	3261.8	13	3279	30	3279	30	-0.34
AJRL_65	65	0.0111	-5E-07		no value		no value		no value		NaN		no value		no value		no value		no value		no value
AJRL_207	207	0.0071	0.0014		no value		no value		no value		NaN		no value		no value		no value		no value		no value
AJRL_243	243	-7.00E-06	-3E-06		no value		no value		no value		NaN		no value		no value		no value		no value		no value
AJRL_271	271	-8.00E-06	0.00024		no value		no value		no value		NaN		no value		no value		no value		no value		no value
Concordia Age = 39.0 ±0.3 Ma											MSWD (of conc.&equiv.) = 0.74										

Appendix D: Field Measurements

OBJECTID	OrientationDataPoints_ID	Type	PlotAtScale	Azimuth	Inclination	Dip_Direction	Latitude	Longitude
1	d4ca6b5754a708f5aec4c6e8f833106a	Bedding	48000	67	15	102	37.05325996	-114.7931037
2	418929f19cfd7f4fd341b7f60466719d	Bedding	48000	99	17	189	37.023752	-114.907346
3	d37d0a8317943e334c52f0d0e9b69924	Bedding	18429	78	12	168	37.024853	-114.908273
4	6c2d863cad8fe0e9b9ca3b131f7d0dc5	Bedding	48000	79	25	169	37.02751	-114.907698
5	8dfcede96cde76bc7fb74d08fb887f4b	Bedding	34325	132	12	222	37.029982	-114.907566
6	6c2b85a8ecff19e3670998a2bfec20fb	Bedding	13993	100	6	190	37.030927	-114.907126
7	2ffe0d65baf525da81b6031abe115c8b	Fault	2270	85	76	175	37.031043	-114.906982
8	dc53fd3a4b2bb2af423dac92eb0f46f0	Bedding	4591	93	13	183	37.031139	-114.907443
9	0e2859e1d3dade4521eed4c64a05a764	Bedding	26089	174	20	264	37.031804	-114.908147
10	f9381d36d586e780be7ae85543aff9f0	Bedding	21758	77	23	167	37.033277	-114.907475
11	6f4b5d7ea15a8b59a19f0c602ff64cd1	Bedding	1	180	36	270	37.035922	-114.907117
12	dbbea276991cf95ace6f0b2e1eb853f0	Bedding	1748	185	45	275	37.035829	-114.907011

13	a02d805a90696993a9776483486f2780	Bedding	15154	131	18	221	37.035645	-114.905799
14	a22f1debbef175334da42411ad3efdb7	Bedding	26913	133	15	223	37.037531	-114.905765
15	66c5f3d6aed704284aeda173c64a2bb3	Bedding	13287	62	12	152	37.037799	-114.904618
16	4a1fcf0f6d2fb6f1427bec7fa5f13129	Bedding	6779	105	6	195	37.038008	-114.904067
17	ecbcf52a62eaad592c781ea84e5af3c1	Bedding	13098	35	25	125	37.038472	-114.903792
18	53100c539c8781f5c9ff8d8d568883ba	Bedding	7350	14	26	104	37.038798	-114.903271
19	db4997730ff190aefeb55921cfb4f97e	Bedding	348	359	33	89	37.038822	-114.90328
20	0232f74fb34ed2b7123a914dde10f622	Bedding	1	29	24	119	37.040215	-114.902359
21	43fb8a7efc8f7621a252d4b68e1ebd02	Bedding	14208	2	19	92	37.041223	-114.902585
22	79735a350705c00dfdd21419338a9676	Bedding	48000	277	27	7	37.043935	-114.90656
23	3973095e65230911acbe081e3b9c3896	Bedding	1	278	20	8	37.044392	-114.905056
24	404bd36420428e3dcf0c5fa3c9a53f88	Bedding	24085	257	34	347	37.04266	-114.90509
25	36a1095fd5f2e470a238d2638bc0e2b5	Bedding	10972	254	29	344	37.042791	-114.904117

26	df80aae8ba0b3d3ab1e06a09e7176193	Bedding	10154	354	10	84	37.042133	-114.903717
27	bdef72f91129b9cc19c40071afc8bc43	Bedding	692	21	4	111	37.042113	-114.903774
28	7a92940cc61e37d117a3a3f3fa149784	Bedding	1	311	13	41	37.041312	-114.903929
29	107a978638c379d679cff0c611f04192	Bedding	1	262	7	352	37.040869	-114.904981
30	451ed561acf5c82f8e457db10de32daf	Bedding	39624	209	34	299	37.04021	-114.905922
31	d9b5ab4dcb1311e08af320c1576e355a	Bedding	6031	217	28	307	37.040449	-114.906375
32	f33d65bd2348ee46dc5412398882e17b	Bedding	2652	194	20	284	37.040292	-114.906239
33	941b4886872042c265d8395f28d92557	Bedding	1	131	10	221	37.03847	-114.906189
34	4de976d7c0b73a596d07af91dd2f066a	Bedding	8994	140	22	230	37.037815	-114.906492
35	814c10ab4b656c152e7d475241468920	Bedding	1	247	18	337	37.037643	-114.908033
36	0ff3370108dfec291ff1fff074b4ada6	Bedding	16399	194	25	284	37.036603	-114.908734
37	7a9eba4c4fa4a0a6687a7869407eac1d	Bedding	543	227	25	317	37.036566	-114.908718
38	ef929ccd268a70b61c52f235d281893a	Bedding	9900	173	28	263	37.035992	-114.909194

39	f8ccc02f58e4c85385b4aaf8bf947966	Bedding	7961	197	18	287	37.036033	-114.90848
40	4afb254f1e9661321d1be52f321f6dc9	Bedding	11627	176	27	266	37.035363	-114.907896
41	9fc043e6a9be1f4ea6d33eaf9c610386	Bedding	16926	172	15	262	37.034418	-114.908014
42	a6796dd4ab19785f47106fbe4b933d18	Bedding	1	190	34	280	37.033683	-114.90874
43	d445c83de88e33e93d773221169aa97a	Bedding	25408	174	20	264	37.032834	-114.910036
44	ebc7dad9e4e2fb15a4897baf2911310a	Bedding	1	174	14	264	37.031922	-114.910777
45	b80b5677038221d106175375366d4415	Bedding	5902	254	5	344	37.031648	-114.910371
46	f32f409defe3824bb221b9bfd74db6eb	Bedding	4914	218	8	308	37.031376	-114.910654
47	78c1a22476de3ca5c939e4eb67c6630a	Bedding	1	191	12	281	37.030075	-114.911462
48	9fd10693067811ac5a3188d2e0e4f6d7	Bedding	1	174	12	264	37.028968	-114.911617
49	8f581854bba481cbbb63ab34f0ca059e	Bedding	1	122	11	212	37.027565	-114.911473
50	66ea39e78479aa28af893dc7313fc799	Bedding	9902	145	3	235	37.026895	-114.91178
51	da25107568ddd084beb000daae5f5e16	Bedding	156	142	7	232	37.026894	-114.911794

52	4852a88a9b8b7ecfc7bab2650f90fa24	Bedding	31562	113	12	203	37.021562	-114.908115
53	72105c73b44794f545448b3e71f29dda	Bedding	8161	98	15	188	37.021326	-114.907443
54	0a4342e4471075a3bb8b85222683078f	Bedding	1	206	20	296	37.037918	-114.893689
55	eba2888abc427273bc286d754931f20c	Bedding	7820	189	33	279	37.037838	-114.894385
56	5e3b0d2192d3be851835a062f60b0193	Bedding	14081	4	60	94	37.038358	-114.89483
57	0c7a289004ae6e352215a57fcb1f388b	Bedding	48000	336	23	66	37.041444	-114.896957
58	ddf9710544c1b8b75667c08de5e7be32	Bedding	19601	17	44	107	37.042851	-114.897118
59	deb4e9f3e6f5e7f5bc5e1e507aad31c2	Bedding	9213	338	17	68	37.043504	-114.897269
60	4f672f9ffe7cecfd0829f6eba3995ceb	Bedding	48000	30	36	120	37.045853	-114.896293
61	08ff5090002f7cbcc7baeaf1a715e6ec	Bedding	1	319	6	49	37.046606	-114.897413
62	a6f294cf970368a55a9ba73fd1adb281	Fault	1	4	42	94	37.045899	-114.898396
63	7323d8d3e5c90c2284f8f2a8baae60ce	Bedding	47534	349	21	79	37.047729	-114.89987
64	b65eb53ff657a4c04703d2dab3ac994d	Bedding	24793	298	14	28	37.04951	-114.899685

65	ebe90b734705202494a522ff0b979229	Fault	7030	199	69	289	37.049575	-114.899058
66	c0efe2e2112ed30b88033a46f8adba8b	Bedding	3291	339	31	69	37.049548	-114.898764
67	65cc45c82ef879c72b58a3811a7503a5	Bedding	16023	320	17	50	37.04945	-114.898246
68	6fb82343c95f283a9613e285b1708574	Bedding	13690	336	13	66	37.04868	-114.897476
69	69f1d33ad349b699bb77f1f036b26a30	Bedding	29243	7	31	97	37.047068	-114.894144
70	b8aa98b37ab1e52ccf2da670df2e114c	Fault	2204	264	86	354	37.047032	-114.894337
71	d514e56d6e4a0296a299a0c51e0a94ed	Bedding	3815	349	35	79	37.047272	-114.894374
72	1ac218691a14435beb23ef804a598679	Bedding	48000	224	22	314	37.036496	-114.867663
73	df970875b9824b11653530dd46964537	Bedding	48000	325	31	55	37.019654	-114.883812
74	f8382463564c54a0c86466a5e25c76d5	Bedding	48000	236	18	326	37.023887	-114.884081
75	7e00ca222cea7e8ad5a88cf4e172a030	Bedding	29394	31	11	121	37.025993	-114.883791
76	36fa828933a4b130ea41b606ccb607bb	Bedding	2968	233	3	323	37.026189	-114.883898
77	97374ec27cbfe540a05394823187b2ab	Bedding	11004	180	32	270	37.025491	-114.884557

78	c43a8ba9b97941fd624c52b3a01cfa7f	Bedding	15204	218	23	308	37.024572	-114.885148
79	622798076c7aecf18b396ad533aea322	Bedding	9131	201	4	291	37.024873	-114.885878
80	c191fc9214cfaaf4d0592ddb99963a8b	Bedding	47135	233	22	323	37.025457	-114.887839
81	b348642767e225e8e2c8d3ac5192c93d	Bedding	10291	236	33	326	37.026143	-114.888191
82	77928ded0e89515dc7105339144a9ace	Bedding	2237	221	30	311	37.026005	-114.888087
83	95cb8ab04fb1984b4f240fc369f170c5	Bedding	19386	338	29	68	37.027375	-114.884049
84	fe67f27d710b4ba8b1a7a753961d969c	Bedding	5462	301	16	31	37.0276	-114.883646
85	c431a9d2340e86b873e17fb0c997d854	Bedding	17611	251	9	341	37.028393	-114.883103
86	7a1fccdeb30b79df8f7555cbd46ed62a	Bedding	48000	341	70	71	37.02757	-114.880751
87	bc8b73751dcf9fac701454c01b394175	Bedding	11300	156	78	246	37.026908	-114.881343
88	fbf1484dc89c9f407490395f10cd8dd3	Bedding	4005	156	85	246	37.026669	-114.881545
89	d8562c656081f18b7653240ad07c003f	Bedding	27550	177	59	267	37.024519	-114.881733
90	13d7f2d5b79e95cc20c8a4eddeed5406	Bedding	38403	182	40	272	37.022593	-114.881029

91	0c362bb02e4e79ebffed8d29269c83f7	Bedding	6506	178	68	268	37.022135	-114.880903
92	0f505b825bc134b20382b8b47b10e972	Bedding	35481	318	28	48	37.020941	-114.878594
93	7a82722a07b7dadbfe4b48116e43c5da	Bedding	48000	41	42	131	37.104903	-114.726359
94	93f582eec1684139cabf3d1cb2e570e4	Bedding	1521	28	31	118	37.105003	-114.726415
95	864669c06d56e294f28e2fc00c5dda7e	Bedding	8670	45	49	135	37.104496	-114.726951
96	399e063bab85a16ded54576d5cd1bf21	Bedding	1180	357	65	87	37.104443	-114.726868
97	fc12d98fb88dfc966afe514f7c32581e	Bedding	46651	340	30	70	37.101748	-114.727811
98	0a6cc579aa8d8f492fa6ee81ccfd53f7	Bedding	48000	11	46	101	37.096119	-114.729141
99	7800d2f0d482551a0df68578214ce9d4	Bedding	14596	340	42	70	37.095111	-114.729517
100	87677ea27a36620f572e5f1cfc5fe13f	Compaction Foliation	1	351	55	81	37.093967	-114.728697
101	a70b3f681557182bf658586a958891d5	Bedding	48000	3	52	93	37.092782	-114.728739
102	fe516ca904049fb3561b1df863d9ec1c	Bedding	1	29	28	119	37.090512	-114.730443
103	f4a604cfef0627c3f3bc1b27e585c36f	Bedding	48000	42	20	132	37.089758	-114.731461

104	bda41b1c78f0b73eb2fb4596e4d998b2	Bedding	32507	354	37	84	37.092721	-114.731418
105	dcc571bea795848bcf84f2e2be12db5e	Bedding	26493	11	42	101	37.095708	-114.731469
106	6855415a82989b61da8768b657b6ad55	Bedding	25589	5	47	95	37.097872	-114.728425
107	4f8c01018af5d44ddde73635f42d2f98	Bedding	12255	9	47	99	37.098712	-114.728084
108	61889dcbe9578c2b29e07e7357ecaa37	Compaction Foliation	48000	56	28	146	37.098271	-114.725364
109	d6d3547a18e0479fd93819f326238594	Compaction Foliation	1	0	32	90	37.097717	-114.724353
110	18bf766db3e511587373061b59ec6841	Compaction Foliation	3576	81	34	171	37.09769	-114.724033
111	df1ad416720f0105831288e7f3fdb3b5	Bedding	33860	40	23	130	37.098327	-114.722318
112	5b504d6d08f781f0d911eabe310f1451	Compaction Foliation	23669	27	20	117	37.099927	-114.721579
113	7682ac8b1b6927dcc2745e73f480d7df	Bedding	15402	41	32	131	37.100537	-114.720421
114	588cab8867cfa6c854d14851253bcc57	Compaction Foliation	6104	21	30	111	37.100787	-114.720873
115	8b3a5b32648cefef77b00b8dd6fe1652	Bedding	48000	17	33	107	37.101822	-114.722071
116	02119bdb7ae2c24a70d4dcc0347b2a7a	Bedding	1	344	44	74	37.102516	-114.72278

117	0dd85c547787e633c42008a0ca41f612	Bedding	48000	231	50	321	37.011864	-114.869839
118	3c640db3266510a8fb5ad4e7487b57ea	Fault	1	190	89	280	37.009074	-114.871432
119	a13b29163c44dd300a4907053eb04a48	Bedding	5978	350	22	80	37.008701	-114.871163
120	587724e643abd030b75b01aef4f44897	Bedding	1121	38	43	128	37.008668	-114.871255
121	f971eb7a4cc8f67e635ef49c4eedc60a	Bedding	5058	52	25	142	37.008343	-114.871077
122	24f6ba8a7e1308976111194042c1dfa4	Bedding	4061	36	26	126	37.008074	-114.870933
123	5973d94f83b6b1ddff9f11e01ac6cdb5	Fault	1055	179	85	269	37.007998	-114.870929
124	ca32b0cf657c90d16b0efa16187b0011	Bedding	35047	277	17	7	37.006919	-114.869788
125	150b02691c467194e6b58d61e6f0044f	Bedding	16344	255	23	345	37.006694	-114.868346
126	57510115699c1829d351373ce8b4c074	Bedding	33377	236	25	326	37.009046	-114.868386
127	109863ae4f2d95f6e2bdcc8bea03d7ec	Bedding	9542	243	32	333	37.009323	-114.867601
128	005eda61b30c5589a2aee6f7f0e561d4	Bedding	48000	214	33	304	37.012772	-114.864686
129	12ffb651a593ca203ea9589695efe901	Fault	3922	83	73	173	37.013052	-114.864735

130	994b05d36b1d6389694f477470190be3	Bedding	10651	231	29	321	37.013393	-114.864123
131	cb881dcfa597065a6c55e8db5c13fe9f	Bedding	46278	255	28	345	37.014234	-114.860947
132	af8a77c3018e4c8b8f49aa58c8b9d975	Bedding	9228	223	23	313	37.014721	-114.860382
133	9d914fa38dbb51441c080eb776f62b8d	Bedding	22748	210	48	300	37.015643	-114.859901
134	f28e38c532f970321f58fd131a880926	Bedding	21032	240	36	330	37.017159	-114.859881
135	61d97c0bdeaf8ccd0862f99112910eed	Bedding	4049	230	40	320	37.017122	-114.85952
136	f1a894b89ceaa71851cd39c550ad7ae1	Bedding	17575	210	60	300	37.018167	-114.858924
137	89647d510d3acbd9fda824e99eea6920	Bedding	10177	223	58	313	37.018893	-114.858793
138	c97a4e128d53fe3af993609c178bdbf9	Bedding	1	222	65	312	37.019542	-114.860294
139	83ff62929aa1eea8b5f007e562c90dfb	Bedding	40951	357	27	87	37.10506	-114.722679
140	06a6d831da67ba2f6f38a0ead30e1a11	Bedding	3843	357	31	87	37.104928	-114.722375
141	97c7db66be6b4db7e042ddef261db248	Bedding	3078	351	44	81	37.104856	-114.722113
142	88604e015ea338c3660e6ed7a2633841	Bedding	18703	8	44	98	37.104886	-114.72101

143	ab68ee036a7b97b66b9271212835ba8c	Bedding	1054	49	68	139	37.104939	-114.721078
144	0815a154c36dea80174d9635ad3f7a78	Bedding	5785	355	54	85	37.105164	-114.720622
145	051e48c16ee40bc1812b33310e03d7c0	Bedding	8482	3	44	93	37.105326	-114.72154
146	4b3670b5fb3a99bbb85656bba809b58b	Bedding	5744	347	38	77	37.105448	-114.722034
147	ada87a854e21d73db1515b66b3cb8192	Bedding	48000	323	37	53	37.109125	-114.729313
148	62eaa0da88ec0939ca874ef988783c7f	Bedding	14401	11	39	101	37.108202	-114.72872
149	54776c38c2d61199e82bcc7fabb5fee6	Bedding	1826	357	34	87	37.108108	-114.728605
150	c3618f122dc6e43114d98554671408f9	Bedding	1	10	25	100	37.114206	-114.733248
151	a9d1334c9e47ef3917a53aaf0eb61104	Bedding	33367	334	38	64	37.111931	-114.734222
152	dc13f98499c6da2a836af7299a5317fa	Bedding	1	339	46	69	37.110915	-114.733261
153	aa7153932481564f5a57ae8861997dca	Bedding	3451	348	36	78	37.110883	-114.733569
154	6ef14b02c1568891d72ef600d79fd992	Bedding	7198	336	43	66	37.110791	-114.73389
155	7a2b3562169c96835073b50f1d47a31f	Bedding	15680	332	35	62	37.110145	-114.734294

156	f8c3cc0c09eed93805f3dbcb663fa5b0	Bedding	3390	338	29	68	37.109901	-114.734311
157	cc809893705bd2ffcd9eec95a7e89fcb	Bedding	9685	350	32	80	37.109447	-114.734279
158	c42ed4a142e05151b22bea0442f953d7	Bedding	7128	345	47	75	37.108978	-114.734541
159	0c554658ae71158e4cfc63cac29503a8	Bedding	3450	350	20	80	37.108941	-114.734234
160	6c2974256e787722d0b05533f54c8ea7	Bedding	28617	347	37	77	37.110885	-114.730656
161	9850f2f996bed753cc44a8a588cd2800	Bedding	11889	319	20	49	37.111504	-114.731396
162	ded48b39fa07d78576662a45addf1007	Bedding	14261	321	36	51	37.113513	-114.7323
163	02b95667eaa0ccf11dd1635e2e6ae152	Bedding	20891	331	25	61	37.1151	-114.731735
164	83aa84be939cc1cecd8c4f745fb939ff	Bedding	1	345	25	75	37.075811	-114.770087
165	6274b2fe15e57359d1038a76e5ac8d41	Bedding	1	322	38	52	37.075649	-114.767079
166	f597796d79bee491308951eba375743b6	Bedding	1	327	37	57	37.076	-114.76711
167	4b317d0efab0ffb4182aea2bd5b93297	Bedding	1	358	21	88	37.075736	-114.767484
168	0b7eb6ec9f0da0e6d45b3684c44ca038	Bedding	1	337	22	67	37.07571	-114.767887

169	cd24a762639378e64a1d3a90ebf61b61	Bedding	19953	356	49	86	37.074391	-114.767949
170	1c02fc6d7ce51371d614bc8f6be5d34a	Bedding	9400	344	45	74	37.073802	-114.767531
171	2af4412a3adcbb18f107acda0ae60d3a	Bedding	709	347	43	77	37.073765	-114.767487
172	575302b9edf0cdd1d77e85fc1b824a94	Bedding	48000	108	22	198	37.0804	-114.747578
173	795d12eff382b3def6b7fa8d9defa011	Compaction Foliation	48000	52	5	142	37.07667	-114.751499
174	693f44eae64ec7dc730991fed67a2a66	Compaction Foliation	1	200	42	290	37.073932	-114.755972
175	1987f41b399699227ca3b059d8a896fa	Compaction Foliation	18622	2	24	92	37.074891	-114.757144
176	18e26f54f0fd756830367509a1d9dbcd	Bedding	1	132	4	222	37.073882	-114.757131
177	51d8b3d907f0f487b80db3b0ad7d4793	Bedding	1	142	9	232	37.073874	-114.757132
178	873e0521cd68c8fa7a8384ab211393db	Compaction Foliation	48000	29	19	299	37.066981	-114.753152
179	fc396446a9c8ed4839b9c198c367d513	Compaction Foliation	9534	1	9	263	37.066437	-114.753676
180	9a3bbb20ddf20ff2d62703d88b1ffdbe	Compaction Foliation	45829	188	77	278	37.063704	-114.753671
181	22e814e294befaca3a89b155fd44b784	Compaction Foliation	1	108	4	198	37.064584	-114.753605

182	eac0cd150413e766c5cdfb3c67673e35	Compaction Foliation	4571	48000	4	185	37.066368	-114.754078
183	ff26cb55ce0de549172b0bca6d3cd54b	Compaction Foliation	48000	99	10	189	37.066289	-114.757876
184	cbbf67eb4579ed7904e6c66894dbf40c	Compaction Foliation	16042	83	7	173	37.066807	-114.759166
185	b11088fdc0f2b7e0d6540237587becfb	Compaction Foliation	48000	3	34	93	37.067559	-114.765182
186	fef13cf0d9a20ac0f1229e02caf03dab	Bedding	48000	246	14	336	37.031259	-114.843207
187	6deea5df3c2a07ed8d2a6314ce4a99a9	Bedding	6900	227	4	317	37.030843	-114.842867
188	a1bec93b85a11473d21be07acf8fd712	Bedding	12678	18	6	108	37.031077	-114.84209
189	c18b1366a64d82447d9c8f385c3b6af6	Bedding	22761	162	10	252	37.031982	-114.84137
190	3f3d9d6d765fc0a63ba843ae96f8a09b	Bedding	47881	24	21	114	37.112404	-114.727969
191	5749363ffb314486e6e02468ce1a62e8	Bedding	7954	30	47	120	37.111892	-114.727647
192	320745158f015302fec3f521661f54de	Bedding	1	13	37	103	37.111767	-114.724636
193	c2083d3f28ba42dfafc120286b2945cb	Bedding	6755	1	33	91	37.111285	-114.72455
194	e3d5437d7feda9de5e929086ed8ebd35	Bedding	15395	336	16	66	37.111938	-114.723267

195	d6eca0f84bf2ec0a15a67f262d200c14	Bedding	29322	343	20	73	37.113049	-114.722538
196	8364e6093ba8934e3afcf13bed904153	Bedding	10037	352	17	82	37.11376	-114.722371
197	622d2b1b4fb4ca9475cfada901a11505	Bedding	4341	8	28	98	37.113853	-114.721998
198	3ba032226e608e4e9bc51491c931518d	Bedding	26160	28	23	118	37.114	-114.724571
199	60d78ae54933a8e9e7511a66276b2690	Bedding	2543	358	19	88	37.11382	-114.724614
200	61ad9ca19883f1d4f04b1a01920b416f	Bedding	5696	354	31	84	37.113692	-114.72491
201	bf751226f307387a450b37dcf49c5b5d	Bedding	11344	348	23	78	37.11277	-114.727056
202	aa3ecda6aa21c009ecfdcaff63a452fb	Bedding	7246	10	12	100	37.112889	-114.727691
203	5d3ec2e17e15dee23cd8bcae25a5bb8b	Bedding	3102	13	18	103	37.113049	-114.727886
204	a538b054cfa227ffc263688a4db3d6a5	Bedding	2117	23	11	113	37.113121	-114.728054
205	84758d2e308dd07351ca672953418d42	Bedding	2795	353	19	83	37.11325	-114.727903
206	fbbd5b8ec74f6b3698f43ad7623efc65	Fault	729	197	78	287	37.113291	-114.727862
207	21961848acd2469c9218c7ff69355982	Bedding	2458	0	23	90	37.112963	-114.72749

208	32ea4bc330a690c2690a244efab842b7	Bedding	1	327	22	57	37.112652	-114.729224
209	402c1635c7cb8bf6a0a01d7f8c94746c	Bedding	591	321	23	51	37.112664	-114.729275
210	c99c12ca992f5e7ad48e6a08c56c8694	Bedding	7729	15	29	105	37.113049	-114.728736
211	05c40a0deeab56547be609d3a0ee7873	Bedding	13956	299	33	29	37.113652	-114.729088
212	5582a70a33c69eef62f1021f953c9426	Bedding	1166	352	26	82	37.113725	-114.72914
213	f5a1d77e90ff3495b12a4a324bc81848	Bedding	4586	316	32	46	37.113837	-114.72943
214	9f69afd33d9c8288aa392b6f09f81d30	Bedding	6613	297	31	27	37.114122	-114.728989
215	1a59fbf75e2e9587495a4fcfb6f202cc	Bedding	1002	310	19	40	37.114127	-114.728899
216	a37d26dbdc96d5f9c38a9a9da2340d97	Bedding	43128	285	24	15	37.115511	-114.729725
217	ef6751acaacfdc540167cf0cc0eeb4cc	Bedding	1692	257	11	347	37.115625	-114.729779
218	e235b2c6ff8044ed81adc7ee08513849	Bedding	1	318	20	48	37.116575	-114.729744
219	0da2d6c01e1aa840d293fd8ce818d0c9	Bedding	5104	228	15	318	37.116333	-114.73009
220	911b11d21b2612481777b29ffe382da8	Bedding	4059	266	9	356	37.116047	-114.730013

221	a3ff237b2cca6c06fa7d52a60ba7fd30	Bedding	6742	316	12	46	37.115961	-114.729496
222	47a12aba42e511f593f2d699ba74d6e8	Bedding	3311	322	10	52	37.115732	-114.729412
223	6f3e318de9303ae9155fb1572722e29e	Bedding	2011	104	17	194	37.115731	-114.729593
224	aa0f28a2e1487c0293f81787e76b108d	Bedding	4784	317	19	47	37.115911	-114.72907
225	3ae7199acff5d594833b6dc70fb935c9	Compaction Foliation	32376	173	74	263	37.115616	-114.726814
226	f6ef0e42a85722e7fd41a5b653f54210	Compaction Foliation	1	76	89	166	37.114214	-114.726699
227	187bcc9ac35440399983ba1c56478705	Compaction Foliation	5044	49	8	139	37.114538	-114.726493
228	7884868d050d6f14644ee7a689187eb4	Bedding	1	322	38	52	37.114879	-114.728085
229	535b37b7b5d79148bee18af0eeb20be9	Bedding	5554	339	28	69	37.115101	-114.728501
230	7d33175d140c8f5f3002ff18c519b187	Bedding	7816	299	29	29	37.115123	-114.729215
231	09d9c81fd9ec657f9b349f97b1bd839e	Bedding	2692	289	18	19	37.115305	-114.729299
232	4930085900cec3bb35bc5374f7078866	Bedding	1643	293	20	23	37.115461	-114.729591
233	967737e44c459c0a6917e44996032af7	Bedding	48000	118	34	208	37.003356	-114.872661

234	7daebf1be90eeb82a3e0969ed80cb613	Bedding	5604	219	55	309	37.003701	-114.872923
235	6a3c1d2938bc5355b9fc8c17460c4c6b	Bedding	1569	190	17	280	37.0037	-114.873064
236	59a5fb7652cf2ef4a9dda9e305765727	Bedding	11493	180	24	270	37.003419	-114.873691
237	9c78cc472f3fb1b600f8e781b4153576	Bedding	4128	191	28	281	37.0033	-114.874031
238	cdbe7613cf7b5bcc7f2314221bed8cf9	Bedding	3533	204	19	294	37.003198	-114.874322
239	a77bf2fdaa7769f12b0ad6e10c53e50f	Bedding	9064	182	14	272	37.003687	-114.874434
240	cf06d4bfa06db66c736df3eb0d20594d	Bedding	36592	297	12	27	37.005066	-114.875165
241	6e084fdb08db07a3194d06c15f3da203	Bedding	3618	185	21	275	37.004811	-114.875097
242	7dbce8a73177e7836cd04986b86ae2b0	Bedding	11181	217	36	307	37.00426	-114.875164
243	d7e01212391b5698057ebeb1460f7fae	Bedding	2762	208	22	298	37.004067	-114.875225
244	dc3badc95949f2e4073d25c980f8674e	Bedding	7396	217	23	307	37.003739	-114.875305
245	43daf6b80fdbe9bb030ec5d6d84865c1	Bedding	6536	334	25	64	37.00397	-114.875817
246	0bc74b4e0899dafb9413adedd8685ef0	Bedding	2413	211	19	301	37.003899	-114.876015

247	c56d98d0ef2fc79daf6d5fb17c2e7551	Bedding	1930	3	51	93	37.003818	-114.875874
248	640bd4c9d229efa0f6b87c7485a3f035	Bedding	769	256	14	346	37.003844	-114.875935
249	54ae1e161a52bdc9cb52455fbe96ee29	Bedding	436	179	24	269	37.003841	-114.875974
250	eb3db6bad38a52749877375b0e6ea8da	Bedding	5973	198	29	288	37.003567	-114.876006
251	6e6b1d02043e4fc563d604fa179a70b2	Bedding	35101	197	43	287	37.002731	-114.87638
252	c9ded5a3b6f81bbd4f463715489e6465	Bedding	1042	219	23	309	37.002682	-114.876451
253	920ffa59929ef7af532b85b1bad77ea5	Bedding	17971	217	37	307	37.00165	-114.87727
254	facfbea84fa5efb598fc2cff0a9d11a0	Bedding	34398	169	16	259	37.000276	-114.876814
255	4b913a2d4d80c55c60dbddcee7e6a064	Bedding	9750	210	42	300	37.000087	-114.877658
256	53ae9cdaf8455486ce2fe50e7aa16a85	Bedding	4106	149	18	239	36.999797	-114.877732
257	7ce3c2e225f900011682d62152685b36	Bedding	26916	196	17	286	36.999061	-114.8787
258	b6b61d987260c4a1296059d62be98abe	Bedding	2416	201	29	291	36.998904	-114.878794
259	01f062cd2fe1f4cd023a3e64bd6f7c53	Bedding	48000	180	78	270	36.995366	-114.881738

260	c8533266fb48223ffd27541f2ea9ddab	Bedding	22007	198	76	288	36.996752	-114.880776
261	6894b00df28a5d196f4df83ee8dae37b	Bedding	10273	355	75	85	36.997429	-114.880402
262	7647d427b253b9a8446a0a26d1f25f42	Bedding	8477	195	61	285	36.999496	-114.879235
263	e6d895c8bcf6443da7b1ff19e6f44633	Bedding	5309	185	48	275	36.99944	-114.879707
264	edb4e65b2c72f592736963485ffe7923	Bedding	20536	245	34	335	37.000043	-114.880081
265	c9c772ec33a2e828ba274047826f99ac	Bedding	3269	248	44	338	37.000128	-114.879807
266	354a03629e6bdbc46bc03c8bd55b36a6	Bedding	6899	290	18	20	37.000038	-114.879461
267	0a7879e4ad0f20327281d400f5f1a6e4	Bedding	9825	184	75	274	36.996938	-114.881628
268	bf89915d4b77140f9dcf09ebbd10ea71	Bedding	1888	197	76	287	36.996818	-114.881708
269	4ca8d1c7437412ca57d2be739ade66f1	Bedding	1273	176	76	266	36.995358	-114.881852
270	faefa32788e72dcc211b2d52efd32c9a	Bedding	10656	209	50	299	36.995582	-114.882657
271	16c027b2e6f4061fda3270596104fe91	Bedding	1316	229	49	319	36.99549	-114.882628
272	8214106e61eb241d4f0b0fffacd14ab5	Bedding	2695	208	43	298	36.995776	-114.88267

273	62a91a59b0c81e1fe73e681418b4fbf2	Bedding	2429	220	76	310	36.995911	-114.882531
274	e7ee907a7782315630d5946e25608793	Bedding	1792	226	57	316	36.995787	-114.882486
275	079c06735c1ee71cc79c708b497eef64	Bedding	1	73	31	163	37.132222	-114.709578
276	dba5be1b97a078abfca9846a33145ab7	Bedding	850	132	48	222	37.13221	-114.709503
277	2594f7eda387657bdf7be0e179c98ded	Bedding	817	134	34	224	37.132157	-114.709471
278	cca2e8e4f4e343b44b2f2609dc84f99f	Bedding	2485	120	30	210	37.132044	-114.709603
279	c6db0d3f48ee5098d7d658d0d570915c	Bedding	5017	130	34	220	37.131887	-114.709408
280	6c5cba34b5d2e1b70525abea1e66cfc2	Bedding	1064	100	30	190	37.131911	-114.709317
281	ff4d7c4f52b6d55a4db99a1b478ab7b4	Bedding	2269	43	31	133	37.131998	-114.709258
282	1992d802e49bce5a7c28f92c9d12b814	Bedding	3724	31	38	121	37.132163	-114.709251
283	733030927de23790400f2775234b350c	Bedding	2480	25	36	115	37.13231	-114.709124
284	4a8d923baf833f4547fba861a54ce0b0	Bedding	12790	44	18	134	37.131775	-114.708571
285	07ca692bb0ad2a4cd266dc4b88c28b74	Bedding	853	325	28	55	37.131723	-114.70853

286	10979dbbed3f516993834c9f3f04c17c	Bedding	17637	64	16	154	37.131099	-114.710322
287	a706dfe818926eece9965789e9a32181	Bedding	1	257	13	347	37.131338	-114.711511
288	b3fea21871cdae75eb49830368e0c0dc	Bedding	29091	324	22	54	37.132625	-114.712148
289	ea568d7f4f1d782b28ca505c86c6541f	Bedding	1060	312	12	42	37.113912	-114.729448
290	73cfe5d5f5e4445785982548de4a4a39	Bedding	48000	300	23	30	37.081957	-114.767276
291	dd19bbc3387f14d8416d014c78169360	Bedding	32817	354	35	84	37.080539	-114.764913
292	d31c7fab07a9c617b5b97538a164c0a0	Bedding	1	28	44	118	37.081237	-114.766559
293	e1bd76c5c7121aaa15ea43fbf7248c4a	Bedding	3	71	78	161	37.081022	-114.76675
294	d18c02de7344d3eb3710c7bb75bb0299	Bedding	33124	215	49	305	37.079592	-114.767685
295	573eac2bdd4abd90e1930af81923ab4d	Bedding	7926	287	20	17	37.079723	-114.768379
296	541f74c407baff3d21a05a90044f5650	Fault	3125	204	36	294	37.079598	-114.767966
297	4adf494c49df216c72d31a1678388e9e	Fault Maybe LANF	1	254	27	344	37.079029	-114.770762
298	203a0c851d16e9c967e120a364f69520	Fault	1	230	80	320	37.079034	-114.770709

299	78bf346d1dd8a788fbdf96634163d7f1	Bedding	12630	12	46	102	37.078168	-114.770393
300	ded212413fe24917777757edccbd627f	Bedding	16265	343	32	73	37.076976	-114.770251
301	00339fd7ee140c5fd50c01a9ea205937	Bedding	1	42	21	132	37.076178	-114.773161
302	3d5696046aaeacf6676855d36d357156	Bedding	48000	28	27	118	37.076187	-114.773298
303	8e184a6d26800c55f04423e7ab9a40be	Bedding	1	21	44	111	37.076295	-114.773519
304	a89bd02745107a74afd6ab725d885582	Bedding	600	23	28	113	37.076295	-114.773465
305	1ee463a14905c92344440df8c6a88ea9	Bedding	22065	244	22	334	37.077286	-114.774585
306	7cb969a01d6c35b1f0217e4b6adaaacd	Bedding	1	277	24	7	37.077789	-114.773884
307	18e3d026c7e09d0c2cb21fb1425b474b	Bedding	48000	302	12	32	37.077727	-114.773796
308	8e203afed3ff49d759c4cd4bad7a9ae0	Bedding	48000	42	8	132	37.035314	-114.851486
309	7bb43be6109c363215c8d896a1e81745	Bedding	1089	342	4	72	37.035247	-114.851537
310	ddba8001a0040070f2df7e954d1cbd5e	Bedding	2937	130	7	220	37.035173	-114.851683
311	51fa11db8577c50f30ec61b139e215fb	Compaction Foliation	48000	67	2	157	37.034862	-114.85578

312	867a990c2d3b0a5113970dba7e078fe3	Compaction Foliation	6266	55	23	145	37.034736	-114.855239
313	8334f9a22968ccb87236e41b09faa60a	Bedding	26696	187	29	277	37.022175	-114.885177
314	8592372d0b9cd9299881808f736ecb35	Bedding	1	211	16	301	37.022392	-114.88627
315	127e311db02bdb97fd0c7ad0aad008c0	Bedding	9963	192	45	282	37.021809	-114.886793
316	40b2011ba572c7c55f0ba00bfdc42034	Bedding	5751	267	19	357	37.021872	-114.887304
317	13bac217f2784535daa7c994510fdd65	Bedding	46289	234	27	324	37.021125	-114.887547
318	70ffb4d826cd4458bdfb04982571ac3a	Bedding	242	235	20	325	37.021142	-114.887552
319	b457afeec0a7f548c8601c679da4d733	Bedding	4346	36	27	126	37.020889	-114.887804
320	a1a06771a0c2ce5f1f94a3f43986947d	Bedding	233	274	21	4	37.020894	-114.887784
321	74f0d8caaa97ee4e6ef01e641ddcc3e6	Bedding	2374	297	35	27	37.020816	-114.887997
322	bd4a8b07fd00c245e3e856c23a9abb74	Bedding	11955	258	38	348	37.020463	-114.888235
323	6c05fb96bb1f11188be43a9fdea2b98c	Bedding	7763	326	12	56	37.020712	-114.88886
324	dbe4ba2d90560592a151c2cfbee9d2b7	Bedding	3276	359	17	89	37.020544	-114.889067

325	398707670ee84fa54cbe9ced9a837c5d	Bedding	2990	262	2	352	37.02039	-114.889255
326	39952115541e0d6c477686b3d568d180	Bedding	418	260	25	350	37.020418	-114.889269
327	7b6134e9c00d08508beec25e1420db2b	Bedding	394	287	23	17	37.020426	-114.889235
328	f14ef42fe49401f7995ed0e20c2aa09e	Bedding	29774	357	14	87	37.020086	-114.889889
329	a7e8664c7b587b8b279a35ebceb78284	Bedding	5701	162	18	252	37.019679	-114.88996
330	54aede2f0f444fc5d0a70f3d4e52a3be	Bedding	15253	350	35	80	37.01902	-114.890225
331	c6ff638c87aec14834b79eba07cced0d	Bedding	1712	337	45	67	37.018903	-114.890274
332	35d051539c4d86fabe08ee6d5c0e04c1	Bedding	48000	47	6	137	37.011019	-114.890183
333	b438461950ca93164b5f20f1e2c46657	Bedding	48000	241	25	331	37.081063	-114.85222
334	10211d3fc4dff4d45eb4ae21c5a965df	Bedding	1	227	15	317	37.080689	-114.850831
335	cdcbbcbc240fde40197f07aa38b8daea	Bedding	44282	218	14	308	37.081276	-114.848245
336	0d8df816ea673310f280c784ea584ada	Bedding	125	260	25	350	37.081274	-114.848256
337	17bea3b550c010247b009fa8b7e0ef05	Bedding	36735	199	21	289	37.082411	-114.845259

338	9a31b5190f315ab35c04e8afcccd6c5f	Bedding	26547	223	29	313	37.084102	-114.844141
339	38694e5418cd9184b18734e9ca5d5368	Bedding	1556	231	58	321	37.019444	-114.860226
340	69d83e62779ec108db37038587fcc265	Fault	60	220	82	310	37.01944	-114.860228
341	48bb757090a09452db2b3e18d54f7635	Fault	2376	267	86	357	37.019484	-114.860093
342	06045e8544715ad66804fa049567c135	Bedding	17977	267	36	357	37.018519	-114.861286
343	c56859a4fcf6a80555eda415cde4cdc2	Bedding	4999	330	34	60	37.018698	-114.861676
344	472081599264762adf0e9166e925640e	Bedding	70	197	71	287	37.018693	-114.861675
345	effb5cd4b266aab3bb8216e5f4ab35fa	Bedding	1	205	33	295	37.015003	-114.863952
346	51180fdcc9b1b7c7d2e50ba54255df32	Bedding	10086	227	57	317	37.014422	-114.864497
347	df34d803b8094dacfbcc5fcab0172527	Bedding	15152	218	37	308	37.015004	-114.865314
348	92c9cab250a9d5af61de5b70e22c3bf7	Bedding	1892	85	71	175	37.015007	-114.865484
349	65aa546abc4f6f5ec72fa21aac849942	Bedding	7510	257	50	347	37.011358	-114.870079
350	28e70e32d68b7ca8e8397e970264d550	Bedding	1	243	60	333	37.010912	-114.870486

351	d233175153548023314d368ef1ecdefc	Bedding	3237	231	43	321	37.010687	-114.870409
352	18c39c011333b1c367abae16797e120d	Bedding	6822	352	25	82	37.010477	-114.870772
353	0447c345098c40a4c5b893df24dade7d	Bedding	505	205	20	295	37.010505	-114.870743
354	ee9ce3d854be82405181403cab531d12	Bedding	6337	229	28	319	37.010838	-114.871121
355	08570c9d131ab2d8799730717fd38a38	Bedding	48000	145	63	235	37.006253	-114.881825
356	b706c5c4d3db2c36077385a9f93210ad	Bedding	10696	193	51	283	37.005648	-114.882421
357	56dbdc7e3035591b74b7ff224d2892b7	Bedding	5101	183	55	273	37.005603	-114.882876
358	290dbd3ab4432c8e22377d4dc27ec6de	Bedding	21473	181	54	271	37.005334	-114.883378
359	a753fc60c993350934636950 74f2fa94	Bedding	2843	207	60	297	37.005507	-114.883515
360	fbde08c6aadd518a38c3ee483c39756b	Bedding	2444	160	49	250	37.005654	-114.883636
361	ee75a33b6229c3f3a43cefcb147659fb	Bedding	1704	176	45	266	37.005736	-114.88375
362	e19ea6b489cb0bfd95563f509240455e	Bedding	8723	218	56	308	37.005921	-114.883659
363	541169f9ff08febac6ccf546e1ccfd71	Bedding	3383	156	45	246	37.006112	-114.883848

364	85ef86b007dfe64a7ed69c17fbf934bd	Bedding	3383	200	32	290	37.006303	-114.884037
365	740a735a7ddf263fb5e524df1f6a3aaf	Bedding	48000	185	57	275	37.062958	-114.871956
366	1d6b5ce21d185a04b304d7d887d20c01	Bedding	48000	154	64	244	37.069171	-114.868999
367	274c7dc2d8d7d055843ed2a31c6340da	Bedding	5987	137	56	227	37.069531	-114.868702
368	c8b6557d43784dd6b39759c3835921cf	Bedding	65	136	55	226	37.069527	-114.868705
369	8aef8a3e115b4e4af711adbc4670546e	Bedding	69	139	56	229	37.069534	-114.868697
370	193b4756c3053189624bc81019f152a2	Bedding	14866	171	73	261	37.070063	-114.868258
371	3daa8583961a39257c2db4528b84cb0e	Bedding	11368	210	54	300	37.07077	-114.868775
372	029c871504c44c7d921e9cd6749ae74c	Fault	48000	219	48	309	37.073788	-114.868526
373	c077a75e7414a5b077b7d73b81c51756	Bedding	636	130	42	220	37.073823	-114.868563
374	f72014c3db39f5526c4762f4aad62195	Fault	206	191	62	281	37.073836	-114.868554
375	1768b3e3f3b13e062750224bb5643e92	Bedding	5558	115	51	205	37.074186	-114.868583
376	89255bfbbae378e53e03bdb8259f731f	Fault	48000	208	46	298	37.078279	-114.868066

377	6d41de2eb1cd4b54419368aa37a4be18	Foliation	2240	191	23	281	37.078411	-114.86795
378	22cbdf96936e540dbda5be6c8c69e988	Bedding	501	148	41	238	37.078446	-114.867939
379	d657791e65e075f0f4b32a1e52b6e816	Bedding	767	168	29	258	37.078362	-114.867918
380	8c4b3e4b924ac073a2fc9b01ca8813e8	Bedding	34372	206	35	296	37.078826	-114.86505
381	e2c0f0b33f7d07adf2072dcfe0e7233c	Bedding	822	136	50	226	37.078768	-114.865065
382	3012a0ca15b280d596a882f6b026f660	Cleavage	6752	47	84	137	37.078885	-114.865653
383	03ed840a01b00287320640d86446424b	Bedding	111	174	24	264	37.078885	-114.865663
384	3ff82d2e606072ed066db09a59e810f0	Bedding	13188	131	44	221	37.078486	-114.866158
385	4b1065d4f4f909e98f52166aede54959	Bedding	4912	197	55	287	37.078832	-114.866252
386	ef86a5bdc7abc86dc4eccf72cb04acd4	Bedding	33067	186	45	276	37.08113	-114.865812
387	e83fdd94b119e71a0c84feda60c88ee8	Bedding	14527	183	15	273	37.081475	-114.867046
388	c5d37debe0cb2d9f284dbaf952fd5958	Bedding	27479	181	85	271	37.08262	-114.864183
389	3d5ac5e0a94da2e2b77fc635c922e1f6	Bedding	5777	172	53	262	37.082378	-114.864606

390	6fb8192fe070e5fe043e8114df67e44f	Bedding	15056	171	88	261	37.083664	-114.864553
391	36faaea2de5ee06c57044cb14c2e167e	Bedding	48000	119	32	209	37.085225	-114.865178
392	d906b7d6ffee6133286f3a33342e32f6	Bedding	11562	168	75	258	37.085592	-114.864244
393	5c4e43707dcf290e95b9c8717d6eceda	Bedding	25298	169	54	259	37.086593	-114.863673
394	40940d21cd19dda8291e1b9dd1db3237	Bedding	4416	194	55	284	37.086552	-114.863279
395	63cb972e3143cbc99437b8f879e88eed	Bedding	2729	178	47	268	37.08649	-114.863046
396	bcef035f042668ccabb89e490fe6b13f	Bedding	10217	235	48	325	37.087224	-114.863199
397	cb89dfe70da8b3e69793fabd6e70f215	Bedding	8823	259	37	349	37.087696	-114.862667
398	bf2deab7e170b203468d2dbabd6c5dc1	Bedding	7490	234	24	324	37.087595	-114.862005
399	c9412164e3072a7b7bd2febb64306dec	Bedding	3191	318	5	48	37.087589	-114.862292
400	4989de37e5af0aa7cbbcfe167a4d1936	Bedding	3023	191	32	281	37.087389	-114.8624
401	e47097d2746abea6e98c6d97f1ab4ed3	Bedding	2817	177	62	267	37.087317	-114.862637
402	96b4fb3f6da1ff710bb57d8f70849d67	Bedding	3041	240	44	330	37.087176	-114.862932

403	4c6b55b7a6e44d0567e49fe96b2cf341	Fault	1863	251	49	341	37.08711	-114.862786
404	07cb34377e56224d075b376594d8d5e9	Fault	4670	243	40	333	37.086946	-114.862962
405	a36bc9ed040378563e1a0fac44786d80	Bedding	1781	208	69	298	37.087126	-114.862627
406	393552105e411bda2a5bc9b4dedf6010	Bedding	4361	199	64	289	37.086932	-114.86257
407	c0aefef26ce4a6eb07d814af13506fb3	Bedding	1000	261	39	351	37.087191	-114.863279
408	e1050b3a8bb4c74b5c7ef988969ba887	Bedding	1428	218	41	308	37.087672	-114.862368
409	e12d35142bcc3b6ee9d861a20cb5c493	Bedding	1090	256	36	346	37.087767	-114.862709
410	a6dbc72267eb527b4e21e5402a4c331e	Bedding	2373	253	50	343	37.087864	-114.862627
411	96c6d3dceefd8a89577f009e43bbc036	Bedding	802	272	54	2	37.087813	-114.862661
412	d1660f51566f836d236009522f0e3dd0	Bedding	5385	219	45	309	37.088029	-114.862418
413	075751c71e15380087a85c7de514a058	Bedding	48000	23	27	113	37.089055	-114.86076
414	81b30ad726e0202fd447e3251b55d306	Bedding	1542	11	30	101	37.088956	-114.860697
415	27e0d45d0991e2c5cf6c111570d041d9	Bedding	4110	309	24	39	37.088786	-114.860605

416	53deddabfc4ec5d7b485f4250d4d581a	Bedding	273	275	51	5	37.088768	-114.860595
417	6ada3753581f598a38c91f70e51dad76	Bedding	546	321	22	51	37.088767	-114.860648
418	12e7cde28fbc6e00181a23bbb1b2bd67	Bedding	8198	161	89	251	37.088465	-114.860801
419	52ae3bb5ff5ba31a20cb031741dccfc6	Bedding	2473	184	26	274	37.088294	-114.860864
420	0b8a85a8d05ddb638509e3c604006d09	Bedding	1308	179	14	269	37.088284	-114.860981
421	898a23b08303b168d4db7623a026d7e4	Bedding	20831	163	87	253	37.087584	-114.860384
422	d739c2ba412da6e25df9250e8e7ab405	Bedding	45122	216	74	306	37.085815	-114.861116
423	05a276a6b5aaa6b2c93d980e761502b5	Bedding	1	23	81	113	37.086626	-114.859961
424	9c1f14bef7e61d5d9e68cfdd736f1d10	Bedding	10661	167	90	257	37.085901	-114.859643
425	9dc7763e5a60772f21d9ba3f52e7c2dd	Bedding	400	162	84	252	37.085876	-114.859661
426	e46f5429bf4e289afc9d3504e1d3e9ef	Bedding	34938	354	88	84	37.08636	-114.858047
427	c90d3e617822ba332b33970dea649570	Compaction Foliation	6089	331	15	61	37.086447	-114.85751
428	1a87ab5ab03df8f71572d1ae354470cd	Compaction Foliation	3183	177	79	267	37.086219	-114.857542

429	6edab1db67be4b1592c42fabe8b2b502	Compaction Foliation	1266	20	19	110	37.08619	-114.857434
430	bc30a2a361f05743b2fbe18e95e1b27c	Bedding	10605	178	68	268	37.086034	-114.857184
431	c88ae7c674ccb4e95fb05f964ec4b60c	Compaction Foliation	2804	11	25	101	37.086146	-114.856974
432	fd6763a2efc2db0652c31370cc9fce9e	Bedding	33004	298	17	28	37.085185	-114.855465
433	a9bbe3e135af6e7383cbc3d551bcadab	Bedding	1124	281	4	11	37.085116	-114.855412
434	fd6b103bbceef96955d1f16fa9d7a6e3	Bedding	1	267	3	357	37.084467	-114.854728
435	a7ae70fb88e05490b7041e1c6d049f31	Bedding	24439	233	10	323	37.082553	-114.853393
436	3ad8711e0265823505cbcd37a1ea0ca0	Bedding	6310	333	31	63	37.082123	-114.853578
437	70b831f6bd6fef9d121a91039a08e8be	Bedding	2004	180	19	270	37.082106	-114.853399
438	57ace7429547b3deea108438637cbaf5	Bedding	18	152	15	242	37.082105	-114.853398
439	a0fdf3a2edd6a27aeaedcf7d9a678734	Bedding	5141	334	41	64	37.081775	-114.853419
440	595b5e5f7eeab5ecefadab4701dfcdfd	Bedding	1541	336	44	66	37.081673	-114.853364
441	3aff131fb063037c4699a53e8142574a	Bedding	11192	264	5	354	37.081856	-114.852405

442	22743704bd05a5b9191b7b81ede06a80	Bedding	7981	256	14	346	37.082185	-114.851816
443	d4cb9d784d32f739e2cec89764ea43fb	Bedding	1864	260	14	350	37.082282	-114.8517
444	0df04032c68177f25d9294a4b9013431	Fault	927	148	88	238	37.082246	-114.851782
445	9a1bbfa9fa4a2f2db1a674c9ca20c0e7	Bedding	312	256	18	346	37.082247	-114.85181
446	fb10292cd42b955c7a647bd8cb0499a6	Bedding	1	242	18	332	37.082378	-114.84879
447	01e0e811f415c5539f5dc1a405442346	Bedding	33463	223	14	313	37.083622	-114.848945
448	8968ff53a4dce34027e5f92a331958ee	Bedding	3917	214	28	304	37.083589	-114.848595
449	c68588da3692e556a695c9711e63701d	Bedding	3368	247	17	337	37.083594	-114.848292
450	897a79a41c0dcc0bef30f2b1b1ec270c	Bedding	22552	212	10	302	37.084	-114.846166
451	097de274b66186edeefb6492e46c107e	Bedding	11741	171	11	261	37.083249	-114.845407
452	b527addd9964e56083a9d2827ef78f42	Bedding	7433	222	17	312	37.083734	-114.844627
453	e898de87675ff17d1d320a912618f301	Fault	1139	332	54	62	37.084149	-114.844225
454	8c4f34b7d02a8b61307e72d29630451d	Bedding	878	220	30	310	37.08405	-114.844186

455	1c60a4f7dd72d20519e97016b928f214	Bedding	48000	257	7	347	37.049047	-114.822233
456	dc87f57ffe9177e42fa15cb0e7e2d748	Bedding	782	287	2	17	37.04908	-114.82229
457	8117fe06c2dbcbf7438e7df64757d3d4	Bedding	638	279	8	9	37.049092	-114.822221
458	53cdb7ec4341249edb3b428958292da9	Bedding	24313	186	6	276	37.048507	-114.824313
459	760bbf3f4ed1abd6bfece702a34ca745	Bedding	10232	196	6	286	37.048144	-114.823512
460	bb45eaef2b835e57ac8f6e7cef4ac320	Bedding	48000	233	9	323	37.040951	-114.822471
461	17dd295b2b24eb44bc46ca02fa89791e	Bedding	13686	232	12	322	37.040186	-114.821694
462	5c999f2609a9603661b1facd2d43616f	Bedding	48000	250	7	340	37.03758	-114.821174
463	dadf52840e2a066ccc19d74e67834e9a	Bedding	32500	235	8	325	37.03747	-114.824093
464	a619e4a832ce954b545082cfb1f2d30d	Bedding	31273	174	7	264	37.035703	-114.825839
465	cb157f8d681199d09f5879b429920f1b	Bedding	24669	202	3	292	37.036384	-114.827888
466	072305fb6b2c751a0f1df81dc7564d6f	Bedding	1988	210	9	300	37.036314	-114.828044
467	f73df1c18c9fcae02413eb6b7449b8f7	Bedding	512	237	12	327	37.03635	-114.828054

468	83104f90c104ab9ec92b3555809ce08c	Bedding	48000	259	5	349	37.038941	-114.828705
469	49dad4859a4c178bc948832b937ecfb9	Bedding	12313	188	8	278	37.039578	-114.829476
470	7fb13b742cb3e7a951966799d3161261	Bedding	8642	249	4	339	37.040178	-114.829685
471	fd91158077609bf8f310282d21705707	Bedding	2817	203	3	293	37.040032	-114.829861
472	b2159585d7b97e3ad16e740c69ebb6b2	Bedding	45729	204	3	294	37.041575	-114.831177
473	237f037a1b8a75b4e9e888a06db73dc9	Bedding	40497	313	5	43	37.043331	-114.834086
474	a754ca9b1650be3585ed6f9f8f957eee	Bedding	11688	216	4	306	37.042712	-114.833373
475	8e16535ca64ee394c01e8a8b2f6ed94c	Bedding	9554	217	10	307	37.042135	-114.832904
476	9b91994e81bcd5901414bd2965f57395	Bedding	2746	234	5	324	37.04202	-114.832703
477	efdba7e50e1743f8f3c8e429dd8cdbf6	Bedding	8251	262	3	352	37.04159	-114.832607
478	dff17b2a307ca014afbc6940c87255ef	Bedding	48000	44	25	134	37.028557	-114.901329
479	ac877f184fd76aa6b6a17b16f0124c18	Bedding	3131	44	20	134	37.028356	-114.901457
480	234377096c3e0c784fa9303d1f8113fd	Bedding	2996	50	17	140	37.028153	-114.901549

481	09b06f19bc6081f29f6f747c3c7092b9	Bedding	9825	55	28	145	37.027937	-114.901756
482	2519bb6ffba3d88d9b25bec587b86f2e	Bedding	5036	96	18	186	37.027668	-114.901452
483	c55ae9397d61b3154bb665c39237c1b5	Bedding	2417	120	10	210	37.027659	-114.901235
484	9b09502e9fc09a5756a6d716777565ee	Bedding	3585	187	6	277	37.027412	-114.901408
485	0409a000ba9d21a703440e9737c1ed4b	Bedding	6835	30	17	120	37.02757	-114.902166
486	13c9e5fd5257fa065b980b2b5421f7e1	Bedding	16651	36	20	126	37.028958	-114.90274
487	ac9f25d15a1e857fd88eb4411a3d1b98	Bedding	8727	56	18	146	37.029507	-114.902357
488	67a0d5ca7e9876eb49d0f47472cf5bec	Bedding	31774	35	20	125	37.030759	-114.902115
489	6d4a53b989513124b443dd8d82ed9c2a	Bedding	23324	27	4	117	37.032271	-114.903032
490	385bfd5239589b83e4710adb4216be1c	Bedding	14693	1	16	91	37.033139	-114.902275
491	b14b1ca139103a64a1f1079b25557bcb	Bedding	11273	70	9	160	37.03361	-114.903101
492	00e4754495a8ae9bb35313e1fc392b1d	Bedding	3864	68	14	158	37.033883	-114.90317
493	55ea6b45bb2e4a0c0e0708d29cfa82c8	Bedding	48000	26	14	116	37.034542	-114.90254

494	b5216a8f43f05af0dfd568bf7094fe0a	Bedding	3915	34	23	124	37.034612	-114.902199
495	b417d06d381a4ef75cb3309c37a77eff	Bedding	19446	274	37	4	37.034132	-114.900868
496	f7739791c262c3279607809946f1918	Bedding	4106	345	49	75	37.034074	-114.900506
497	3e86f8c3145fa664adb93a842c7a3950	Bedding	2233	333	24	63	37.034022	-114.900696
498	91b31f226b568595770b5ea23870a7d1	Bedding	3463	0	28	90	37.033839	-114.900611
499	c609809b9820a632b4eea95118e2baa9	Bedding	361	33	15	123	37.033849	-114.900641
500	b654e1f766b5ccde11952bbfd5cf0f9f	Bedding	6219	359	15	89	37.033291	-114.901749
501	a6bec7b8feb533ed29c348e5df3908d6	Fault	3334	257	76	347	37.033033	-114.902006
502	3eaccd3985dbcc6be737a9c64af97389	Bedding	1148	16	5	106	37.033007	-114.902104
503	3ee1f2cc1d41b745c25ff23254d4694d	Bedding	17963	335	21	65	37.031853	-114.901251
504	ee3fd5d1cb88cba2be31ba702b1469d8	Bedding	8865	68	9	158	37.032078	-114.900505
505	233a94f10e985d09ab96fde798fc9079	Bedding	1	76	25	166	37.030986	-114.900261
506	057f32be1a81184b37cb2af4faa13443	Bedding	6154	102	13	192	37.030919	-114.899714

507	4302a483d0b98ad3c4a2fff5239655ca	Bedding	1	148	9	238	37.030855	-114.899031
508	d0ebad4b982843458b5d934d487e21f6	Bedding	5960	163	8	253	37.031001	-114.898527
509	ea8bb374cf7e0e7d116df40605fc6f14	Bedding	1850	186	12	276	37.030913	-114.898402
510	37e815cc77cb399a66eab440e1acadc5	Bedding	48000	138	11	228	37.030832	-114.897219
511	a044bde6ad0a9134affb7288c97bba95	Bedding	3794	184	19	274	37.030907	-114.897547
512	79d01cf5ab3454231850932d61377b08	Bedding	10151	167	15	257	37.030667	-114.898149
513	09e4d1716ad40081229ef31fdb8e7d84	Bedding	566	150	10	240	37.030627	-114.898159
514	ee287d55ded54eb53eb812cbefd43fee	Bedding	2421	172	23	262	37.030515	-114.898256
515	2a15e2bd2ef31964a379bcb88493e47d	Bedding	5695	144	5	234	37.030259	-114.898092
516	051fdf3a95b6ebc1b5722118e8b34f22	Bedding	10683	120	14	210	37.03008	-114.897012
517	b55bb5a6985b31256823e219a8712a98	Bedding	5910	103	9	193	37.029672	-114.897165
518	6b014ad29daa10bb13f110382534332d	Bedding	1	105	7	195	37.029286	-114.896848
519	ebee9681933f2fbd2b3aa37a72fe9c42	Bedding	11536	125	3	215	37.028526	-114.896427

520	c48fdba48b63067afaa54eea4e9e6fcd	Bedding	4897	169	6	259	37.028331	-114.89606
521	2e29fdda2830508fe34aa295bbea0287	Bedding	1459	188	3	278	37.028494	-114.896302
522	1764b22eeab77ad558ec578fa2bc5e5b	Bedding	10528	206	31	296	37.028912	-114.895612
523	e871610c176bf5827b7eb6122e8808c3	Bedding	5436	187	16	277	37.029035	-114.895148
524	372c5d4548c52205f73dd25515ebb099	Bedding	7868	214	38	304	37.028451	-114.8952
525	5bffd9b25e3875baf09d8b4aae0bdf7a	Bedding	3160	250	6	340	37.028265	-114.895364
526	171b31a2ef94a09c2cdede6483ba0b3b	Bedding	89	199	21	289	37.02827	-114.895369
527	99b4dcea175b01fbe87b8b8d5e916a53	Bedding	3153	215	57	305	37.028288	-114.895646
528	aca9f918c634f7ca9e0649dda227e3f0	Bedding	1	24	34	114	37.027766	-114.895709
529	ce73ad70c3b1695e82dde3f60ad20f9e	Bedding	2586	243	13	333	37.027589	-114.895782
530	cf01b3f233f9ec0fc691b92317774702	Bedding	0	66	9	156	37.027589	-114.895782
531	1a5238893aa9651c8693b595324f8ba3	Bedding	0	328	5	58	37.027589	-114.895782
532	543b8c554aa9709380cedd68977dd029	Bedding	436	231	25	321	37.027563	-114.895804

533	11bc3dc70c7cfc5a791e14276679b833	Bedding	229	191	39	281	37.027559	-114.895824
534	639a11df03d801bfcfee65364ac209e4	Bedding	5386	7	12	97	37.027438	-114.89545
535	51c54881f7d3776910cb2197f5212229	Bedding	204	226	9	316	37.027435	-114.895468
536	bd200a3f9a898d63637de4c987a6c84e	Bedding	1957	76	13	166	37.027644	-114.89562
537	f4db01801083790d0aacfe19a5967c67	Bedding	3589	159	6	249	37.027697	-114.895398
538	a1ca457c26cecffefed9f639dcbcce27	Bedding	1967	177	9	267	37.027815	-114.8953
539	3f70d183e11e1f93a8db339ec0711d0b	Bedding	5832	214	16	304	37.027979	-114.895257
540	7686f5a2d066f5193e93df51f54c28a5	Bedding	2072	212	36	302	37.028106	-114.895159
541	cc296853916be4edb5d7cf5caa9d5311	Bedding	1295	203	43	293	37.028176	-114.895082
542	28553db249632cc2e4599e6645459847	Bedding	1320	198	51	288	37.028195	-114.895201
543	8df4e657d211194171d55ab75222c153	Bedding	958	169	13	259	37.028264	-114.895204
544	a9b85be7f1143657c46b681a4561c490	Bedding	581	178	19	268	37.028256	-114.895415
545	8bed0b4ff843db698acfa7e21beee422	Bedding	2375	19	20	109	37.027937	-114.895698

546	a7bb56774807f5ddd4e83995f70a3bb5	Bedding	1360	254	20	344	37.027855	-114.895765
547	0b63dffda960a7be97657a20f23e1155	Bedding	227	210	33	300	37.027846	-114.895748
548	2b728501c8473cdf1f61db3be5e5899e	Bedding	1030	214	65	304	37.027622	-114.895865
549	df3fe323caac046ae97f0222acb54d8e	Bedding	4436	183	74	273	37.02756	-114.896014
550	e67a01eefe2399daf59e8412425c24e0	Bedding	48000	203	11	293	37.02454	-114.896859
551	395a1a8e1bbb3233f78e4a663433e6e4	Bedding	2970	168	9	258	37.024364	-114.896707
552	b1b00ccd588cf6146087fd3dac7f8988	Bedding	925	183	6	273	37.024391	-114.896783
553	c98ba018e0350b42259c164da02f05e4	Bedding	48000	54	3	144	37.02016	-114.894982
554	1236867f6dcf92cbda922a7ce2bc7367	Bedding	3905	50	17	140	37.020039	-114.895299
555	e7dc8134e40c4ead0c1a5f00ae6771d6	Bedding	1450	25	13	115	37.019935	-114.895312
556	dc80ddca61685d674d44c84e490fcf88	Bedding	213	85	5	175	37.019923	-114.895324
557	02007444035b3e37fb913857761ff7da	Bedding	490	230	3	320	37.01997	-114.895318
558	f91b76c7beb96b15ef27ad6d7e2c1a44	Bedding	8611	353	18	83	37.020322	-114.890605

559	effd1c87b68ed4aa413b1d7a22ba82b3	Bedding	6384	263	19	353	37.020779	-114.890672
560	c23b8ce96926ee4e47dad259c6d457a4	Bedding	6034	232	22	322	37.021144	-114.890377
561	e50fb06480f0bfa8bde4c9daebad4de6	Bedding	24656	265	29	355	37.02172	-114.890761
562	680fcf1e51663d4c11a03059a4a0ce4a	Bedding	34697	200	48	290	37.033174	-114.896124
563	a32791450ea5dcfd71dfda17fa4f130c	Bedding	8630	206	68	296	37.033669	-114.895654
564	3356f1d110032be22183f31e6b3b470b	Bedding	808	225	9	315	37.033724	-114.89563
565	b422b1f77c424c6ac01bb5ebf8135756	Bedding	4561	180	78	270	37.033956	-114.895454
566	0d514bc60702cf36c36eb5fc99568968	Bedding	2063	13	71	103	37.034068	-114.895576
567	397e76ed295ab11201cb931ddb978dee	Bedding	0	210	6	300	37.034068	-114.895576
568	ae9f7aacda361740ee3ac6e59a6a112b	Bedding	179	237	16	327	37.03408	-114.89557
569	3e21497ed32e2d4de1f4dfbc488929cb	Bedding	1490	206	8	296	37.034173	-114.895548
570	2125490097f9b3c86af9f5d01cf8e4e9	Bedding	1	353	90	83	37.034305	-114.89548
571	20a37a924db85ddea63ed6ef68b3bd42	Bedding	625	177	69	267	37.034309	-114.895536

572	28c20be358b0f4e1af8ebce6e2b1ea8b	Bedding	1305	259	21	349	37.034 35	-114.895 583
573	062f27497a348a3f235587c51bb7f8f2	Bedding	5263	314	18	44	37.034 664	-114.895 327
574	b20b9cd1568f299c161a274ba199cf62	Bedding	2042	238	14	328	37.034 548	-114.895 44
575	53d9bff3395649e234b56587e5fc352c	Bedding	399	242	11	332	37.034 535	-114.895 472
576	b1cda741a7822e8b3ad4243855c4b631	Bedding	1476	3	77	93	37.034 442	-114.895 429
577	e629ae2a3ee61da4b597eb6201b28578	Bedding	316	200	69	290	37.034 446	-114.895 401
578	d5e5be70edbf423e5978fcc69e1232f6	Bedding	73	186	75	276	37.034 441	-114.895 399
579	07b48a6e3d64a969889aff928c49cefd	Bedding	757	206	63	296	37.034 44	-114.895 361
580	dc6ef5d9baa07aa3712832f5feb0ba8a	Bedding	11654	27	88	117	37.034 885	-114.894 722
581	a6e858c57b908f5e3324553e824f79f9	Bedding	2835	358	79	88	37.034 466	-114.895 264
582	0df9bdbef632dcea3cee0a2247e8a9c9	Bedding	5344	141	18	231	37.035 096	-114.895 124
583	a62780ca3895b61b5bcb38ed04ef4ea9	Bedding	1401	41	82	131	37.035 02	-114.895 041
584	ceb5fc1bd4b27df053d4741c6395fe75	Bedding	423	8	43	98	37.035 05	-114.895 048

585	363e029ffe70122716fd53dc59d1d7ba	Bedding	2682	261	22	351	37.034979	-114.895316
586	05611c46a9803c9bd90f26c8ffecf662	Bedding	2262	359	62	89	37.034851	-114.89519
587	31509a5cecad707163a6664fd94187d8	Bedding	913	238	75	328	37.034609	-114.895282
588	e52222ad074a71164c289cb30b23ee0f	Bedding	1988	250	28	340	37.034781	-114.895034
589	38d00bc25c8e26acd7bc00da6ade1ec3	Bedding	9907	6	13	96	37.035215	-114.893932
590	25d750428354484aec3b79acf5fac794	Bedding	31086	277	20	7	37.035722	-114.893133
591	adab4ec086db1660af8e29c3ccad1fe2	Bedding	17883	204	32	294	37.037477	-114.892178
592	db53fd0df7071ca4780d034ca036c485	Bedding	5473	200	30	290	37.03736	-114.891708
593	b64125ac679ed8612e90029428170119	Bedding	4061	257	13	347	37.037545	-114.891425
594	127084c9773fd763f563bf82bb41e6a3	Bedding	547	238	22	328	37.037583	-114.891438
595	be98374ab5a8dec42c1fb8e39d03cca1	Bedding	478	231	14	321	37.037544	-114.891382
596	1c7405a5e311399781ea52f58bbb231f	Bedding	11	241	19	331	37.037544	-114.891383
597	9c7fe428ab87a0cfd74474dad0ecbd5e	Bedding	2447	277	41	7	37.037468	-114.891227

598	0f5b8a1f3654f3e3f8d9e3286c237339	Bedding	12399	331	17	61	37.037305	-114.891084
599	47054944e7880228d67c817756cefe38	Bedding	8353	344	6	74	37.036808	-114.89066
600	e092da4b7c0e64ffcd35e7a3b8f5d250	Bedding	1485	218	16	308	37.037592	-114.891305
601	2e9d98ad2e23e7e84c51784c5da72c4a	Bedding	2572	327	21	57	37.03773	-114.89144
602	7a456c41f9a679063a74cec4159b1ea6	Bedding	2989	347	6	77	37.037162	-114.891285
603	3290fd68299468d62c465469119ab83d	Bedding	500	329	8	59	37.037196	-114.8913
604	3a8c1d2c154bae344229ef12f6c0c1b6	Bedding	4910	265	24	355	37.037028	-114.891555
605	4cafe0d090555a796bb429f7be9341bf	Bedding	4593	211	20	301	37.036704	-114.89164
606	83f34e4d51ef7d6e489872b0d1ec4237	Bedding	1210	221	28	311	37.036644	-114.891561
607	ab1fb3d1f51a3e5f0b84e879be4424fb	Bedding	4582	210	8	300	37.036418	-114.891434
608	d2a892ad70327492d2390b9e43d70bc6	Bedding	1647	250	9	340	37.0363	-114.89145
609	881487957e0c226b2c352c4bd9e2c738	Bedding	4849	223	35	313	37.025801	-114.888281
610	d6cf8d916bba2058b9f0a31cc4a61ac1	Bedding	2314	230	30	320	37.025688	-114.888434

611	e870701937819089c8049dc9c376483b	Bedding	936	241	35	331	37.025749	-114.888398
612	ef389cbf50e26c8e91ca91586e565106	Bedding	19188	246	25	336	37.024074	-114.887814
613	403c5e115cbac4f0b33923e9f2554b5d	Bedding	123	263	22	353	37.024075	-114.887825
614	4cafa970d4195f627934c0f1efcafddb	Bedding	3689	274	18	4	37.02381	-114.887854
615	46775fc96d1427a08654169af57a8deb	Bedding	1229	311	15	41	37.023859	-114.887762
616	fcf824bfc7ae96a098b6e62aae8ed7d5	Bedding	18747	321	11	51	37.023392	-114.886359
617	d24e1050bb590d28d502c1ae0e8b49eb	Bedding	1217	331	27	61	37.02347	-114.886409
618	4b045fb9b0e7c818de81c99a6f544d02	Bedding	430	323	24	53	37.023496	-114.886388
619	fd863e34993f9c02949272c1c91ca90a	Bedding	7225	203	5	293	37.02288	-114.886043
620	ac2347e5c839d4f43281ac667e282e8c	Bedding	1027	226	21	316	37.022386	-114.886362
621	954188969b72eeecd26abd6cb3be3c5e	Bedding	1580	226	28	316	37.02228	-114.886296
622	9c85c445230fa0b7604e56810fbf151a	Bedding	3639	191	37	281	37.022133	-114.886322
623	c291ad910dabb178bfd00831fdc41197	Bedding	1678	230	31	320	37.022022	-114.886382

624	fac8647f1717eeac16db30849f110faf	Bedding	3274	243	31	333	37.022005	-114.886629
625	33af6e6a11b2ff94fa5e34343f4ce469	Bedding	2231	226	33	316	37.021663	-114.886709
626	e9cc5807a48888eb4804841fd7737407	Bedding	1	256	31	346	37.020952	-114.886188
627	2325d089595ec0a7ac88af9c2116bc6b	Bedding	2160	234	29	324	37.020826	-114.886074
628	0647ded9175fc7caf7e22ed25a5044f6	Bedding	787	193	37	283	37.020818	-114.886004
629	9454d0bb74a7d74ff06c8d18ebb2c098	Bedding	11396	259	41	349	37.020146	-114.886386
630	04954092ae7dd10482e93925bdbead5e	Bedding	18	252	36	342	37.020147	-114.886387
631	1e5f9ba689c59cec7947706759643473	Compaction Foliation	48000	5	13	95	37.095563	-114.854828
632	eae89a0f56fc26b1f9173e93fed138e8	Compaction Foliation	28821	110	22	200	37.093496	-114.854568
633	ab60af38d0c26271f52f8cf9e72ddee2	Bedding	8513	184	11	274	37.093527	-114.853803
634	79678b186515417f22c011b99edcfd2a	Bedding	20439	270	2	0	37.09412	-114.852902
635	0b59da40c6c1a48e265a106909969559	Bedding	48000	73	8	163	37.092314	-114.849232
636	b4b088aa3f2bb3dc7115b8736f77c864	Bedding	353	77	7	167	37.092293	-114.84925

637	efc19df4d511364b1c6853d66b720b04	Bedding	48000	337	24	67	37.089405	-114.845645
638	58ec3e92e1dde96a4698073d47783e40	Bedding	40055	201	17	291	37.023016	-114.903864
639	41778a3ba63493db583f0111bc191128	Bedding	279	193	16	283	37.023005	-114.903843
640	0faee907d7f39b9c4ad367919ccc2da4	Bedding	20809	46	24	136	37.02685	-114.906018
641	2b35e8c59eece40d61b66736b062b34d	Bedding	1088	27	27	117	37.026772	-114.906028
642	567c6fbfff16afe0a1c7e37889787cba	Bedding	17305	40	19	130	37.028188	-114.906392
643	4841d7e3e6ba1cb5bd8179715410b543	Bedding	1038	50	7	140	37.028258	-114.906359
644	f59db3b6f35558106e3c827bef70ccf1	Bedding	13360	126	12	216	37.029068	-114.90688
645	f4599f6ff59c69ca929abc466a82fca1	Bedding	25100	83	10	173	37.02941	-114.905425
646	6d984e399fc1bcf778eec572ac8e4c85	Bedding	2878	94	12	184	37.029565	-114.905253
647	0c685935a48441e08d0671dae4dda916	Bedding	727	248	21	338	37.027951	-114.901819
648	7db8e50dfb3505acb1e99fa409676056	Bedding	521	244	25	334	37.027972	-114.901773
649	1c10f7caaae2e2a4b36d0059923d1de9	Bedding	2278	89	8	179	37.027807	-114.901343

650	0faed5a0a443fdd643fdca458d0f16ff	Bedding	1402	73	14	163	37.027804	-114.901469
651	4649f358b8027489add5fc4c39653658	Bedding	1	204	28	294	37.026717	-114.901163
652	e024e7d7d545b3cfce7edd0694c6c143	Bedding	3182	200	24	290	37.026495	-114.901235
653	a7c3a05f81f927705d1da008b76a8cc2	Bedding	4929	196	32	286	37.027048	-114.901002
654	b90d287ab77f18f74e4652e972383242	Bedding	7341	190	20	280	37.026273	-114.900804
655	ed4778c05b054a23c3003d09f0794a02	Bedding	223	172	25	262	37.026266	-114.900786
656	ca3f4c685f71bb8ed2ac6d605ffc5cfa	Bedding	1624	238	17	328	37.026275	-114.900658
657	ced1b5c7ffa45e62e2f5bfceff2d0f5b	Bedding	404	220	19	310	37.026302	-114.900807
658	432c6ab903df9a17107d6633a5132c09	Bedding	16426	201	11	291	37.027292	-114.899872
659	dc2330df99ca7b61e9c3d677fdcf7b82	Bedding	2908	174	17	264	37.027427	-114.899672
660	d6f80952fa7d3ef5d802a63f471e11c4	Bedding	494	230	18	320	37.027265	-114.899843
661	2723a20ba1641fc6ea615d41062a27ec	Bedding	696	210	15	300	37.027377	-114.899667
662	e563fb5d5ba35242a03f9497473375a9	Bedding	1	165	19	255	37.027922	-114.898657

663	09ddd5dbcb294ab965b80d1c7a0f87c0	Bedding	0	163	17	253	37.027922	-114.898657
664	0c25d90286a28f86a2596b4b6fbd5166	Bedding	4981	158	19	248	37.027567	-114.89859
665	2bb35d199e7181a17679f7cbd537df6b	Bedding	11851	167	14	257	37.028593	-114.897471
666	e0ae727e56c3e287d8e54925deb3309f	Bedding	1658	172	15	262	37.028562	-114.897327
667	2cb14abf8016e9e4a916fce6e802fc60	Bedding	571	198	9	288	37.028602	-114.897315
668	a4e7d724013b3f559d453e9a61e95405	Bedding	15794	172	18	262	37.027521	-114.897328
669	be69737547f8f200dfad4f85f72732ce	Bedding	361	160	28	250	37.027546	-114.897319
670	736119fac00288bae5286a74c2d13a00	Bedding	1347	151	6	241	37.027618	-114.897322
671	74e70fc476df99dc20d24f8176665c9e	Bedding	1706	152	9	242	37.027585	-114.897197
672	0f829c24a8d2560620ffcca015092613	Bedding	463	186	25	276	37.027618	-114.897203
673	13ebe7c9a3d99b06ce12f1e3df2b45c5	Bedding	13806	191	25	281	37.026771	-114.895684
674	956630402a23481528d1d09729dc9e3a	Bedding	10003	175	27	265	37.026065	-114.895867
675	6ab4a5240a09696c313ecbf8d64e11bf	Bedding	737	189	18	279	37.026118	-114.895862

676	27176c43a063d25c5b55accf73a84ecc	Bedding	1	200	59	290	37.013135	-114.892792
677	fa739d5a48b1de48feb9b150855da616	Bedding	1387	208	49	298	37.013035	-114.892793
678	eb13b21511123a9dd358817c009a827f	Compaction Foliation	48000	348	11	258	37.077032	-114.76311
679	96765cfed0d87057a1776fb51075fd0b	Dyke	1	320	72	50	37.076902	-114.762988
680	f6027db4d6fa73614c7a258c455aabf7	Compaction Foliation	13444	35	24	125	37.076063	-114.763117
681	d47a8fc4aaedd5eb4a814f9c87fbed3b	Compaction Foliation	42972	15	36	105	37.074015	-114.763985
682	c009926d3294d9f0f144377990c22712	Compaction Foliation	1	142	85	232	37.074008	-114.764143
683	4d96fe397fd3d2a5a05a007ea7e6d196	Compaction Foliation	13207	48000	19	94	37.074238	-114.76514
684	7f20c452abb04f901360db335b5b3353	Bedding	1	118	15	208	37.094885	-114.85028
685	497831994d0e2d6b0974443d2009e2ac	Compaction Foliation	1	209	15	299	37.100693	-114.851302
686	0e4ea34231c98b5148609397d02e77bb	Compaction Foliation	8601	160	73	250	37.101313	-114.851298
687	186e8f8967c4ac0616bc1665a3eb5b13	Compaction Foliation	15238	323	11	53	37.10078	-114.849935
688	85b71cb089a7ace7cbfeddb472fa53a4	Compaction Foliation	48000	350	22	80	37.099408	-114.845993

689	e657462441f4b6740ea092e0162c186d	Compaction Foliation	20819	294	24	24	37.09791	-114.845881
690	32ceec1c6f781301ad1bc372e0c094b5	Compaction Foliation	38923	309	13	39	37.093775	-114.846242
691	930a00143690b6b143d816e67a4780cf	Bedding	28761	99	8	189	37.091702	-114.84627
692	710f1a839227646f7d318027bd88a284	Bedding	15799	325	23	55	37.090482	-114.845183
693	aa7cae8e5580004e5c7141d42d138876	Bedding	1	332	27	62	37.089255	-114.844205
694	748de861c312142f68c14b7730a042ad	Compaction Foliation	2461	350	18	80	37.089322	-114.844
695	53979f9b4852a9b82182ffcb91ccd251	Compaction Foliation	33960	317	9	47	37.090052	-114.842698
696	c1eb512fd87838b23c58cdb8ddf5a23a	Bedding	5002	359	37	89	37.111918	-114.727198
697	96b0b177d0cc766c52e41a15bf03b770	Bedding	6135	29	32	119	37.111478	-114.727453
698	621b05577046a7a7abbd9d6988ae7844	Bedding	83	22	42	112	37.11148	-114.72746
699	b6f824ab0a164439c821acc90bdf9616	Bedding	1162	289	34	19	37.111425	-114.727372
700	b7a31f679413e0dd0150f2c1f01a5597	Bedding	2672	327	40	57	37.109113	-114.729073
701	31c5fac446dd50cad6b506374cb5768c	Bedding	1	17	55	107	37.107512	-114.727968

702	32569d8a7bb4c1b14ff20a960239d52f	Bedding	24740	45	31	135	37.107347	-114.729483
703	3ca180d7d7f14d93b4a45ef7b7a4594e	Bedding	752	110	58	200	37.107398	-114.72946
704	d2a12ab6e50d62fd6eac376537329a79	Bedding	4633	13	37	103	37.107325	-114.729067
705	9aae37ee3397d860932074d7a8e74ede	Bedding	8935	12	41	102	37.106868	-114.727978
706	d8ed07e8a2cee6df6456143149a727f1	Bedding	5431	5	39	95	37.106643	-114.727578
707	19cf81d2640fe64fe7f8449e4cc69341	Bedding	29855	2	42	92	37.106958	-114.725562
708	d2bd538bc090df2e8592bdf58c4a88ad	Fault	3533	224	49	314	37.132868	-114.712243
709	8f92770f397642767218f130bf17ad84	Fault	700	248	25	338	37.132917	-114.712258
710	cc7a45ff444b3c49acdd19cec528e3c6	Bedding	825	20	40	110	37.13263	-114.712222
711	199d8222ba03e62c75043308fb55396f	Bedding	2233	280	23	10	37.13295	-114.71207
712	e117b2fa7b62680736c2a0ac0ad22a36	Bedding	1294	25	47	115	37.132965	-114.712185
713	dea7fd73dcb5287d16969 8de144319d1	Bedding	8624	209	10	299	37.13288	-114.71144
714	4b00f73f80fbc779b81ef1d8e1535b07	Bedding	1249	134	29	224	37.132053	-114.709347

715	b5d3e34a4cc3d49046db9e528a9aa3ea	Bedding	1536	120	31	210	37.13198	-114.709483
716	d899a31c0664d0f7a231775e1d6a4c72	Bedding	9117	345	40	75	37.132462	-114.710342
717	26f6f41808600abe291c074cc3ef7bda	Bedding	0	62	33	152	37.132462	-114.710342
718	b48457267e10069fd339f8b8978a08e4	Bedding	373	328	39	58	37.13218	-114.709277
719	a0f85f712da28b1870ebe8fc5b981930	Bedding	616	29	39	119	37.132167	-114.709417
720	fac087c1c81d4ed0ac55967b47f083f6	Bedding	278	49	45	139	37.132187	-114.709415
721	7e4b17fec67d50e17c4bd73a67fb3051	Bedding	1683	50	45	140	37.132277	-114.709443
722	ecffa0b3d923c39a316bdcaf2f2d3bc7	Bedding	372	358	22	88	37.132218	-114.709535
723	2ed77aef9110e3a074b7b62e1a42cfea	Bedding	558	345	25	75	37.1322	-114.70962
724	ccdb1bee488c9427dc895aec043e9d45	Bedding	647	5	27	95	37.13202	-114.709513
725	7b3a52a85c3d6e4b83eddee7bcd3ac46	Fault	48000	9	80	99	37.03064466	-114.8164844
726	aa99b074d697b45e0e5d66dd39692e22	Bedding	1	107	6	197	37.02995786	-114.8178185
727	18b33ee3a00749080c90ac50fa142a59	Bedding	12132	318	28	48	37.02933943	-114.8185896

728	63956e7a70610bba7f56bb19709ec655	Bedding	48000	40	11	130	37.02886292	-114.8206269
729	47b18aa5c389532cf670bcbc42573405	Bedding	28461	40	22	130	37.02945696	-114.823076
730	294f0ad4c0ac4527408a3fad551e4aeb	Bedding	27816	9	28	99	37.02768408	-114.8242441
731	e5cdbf1cf1c83d2a9b2d14b8f337ae89	Bedding	1	300	11	30	37.02687969	-114.8249475
732	38b9199da5efa9bc71b3733a761aed6f	Bedding	1	271	13	1	37.0249282	-114.8255076
733	da5001e292a4dfa9aa75998494c1996c	Bedding	4530	246	14	336	37.02466696	-114.8257519
734	d91e2120a5f07a0fcfba70629f648c56	Bedding	11227	236	20	326	37.02450216	-114.8263658
735	cae1bceb43d7f4336b808909e8cb0d12	Bedding	1	322	1	52	37.05625941	-114.78988
736	3c14fe69b47b877f75389cf184af3e48	Bedding	13577	123	9	213	37.05610712	-114.7886739
737	63a1c6c0f8751af001bbb2a807d499f8	Bedding	11111	131	14	221	37.05544896	-114.7881045
738	02880dcee6c5f62dda95dfab131bf40f	Bedding	9824	154	7	244	37.05477139	-114.7883611
739	60cbf2c0a65359a7fe6d61e1a1b582a9	Bedding	7482	152	18	242	37.05508278	-114.7889104
740	a0dad27f57d5968d2ad07d2cab40f35d	Bedding	3210	161	18	251	37.05513452	-114.7891918

741	072968dde568fd2d8db547e92a160e2d	Bedding	823	145	21	235	37.055 19375	-114.789 187
742	68ba69d8c526442cf1729f3c3273562e	Bedding	7041	122	16	212	37.055 21027	-114.789 5233
743	0454fb84927276dda5b9476f9806cb7a	Bedding	5239	77	22	167	37.055 2745	-114.789 9877
744	42741cc1dcb116d0c99fa33dcd02e00e	Bedding	24537	13	30	103	37.054 74656	-114.791 9082
745	81193d438543ef1868b42405a6f47822	Bedding	1	76	15	166	37.052 6149	-114.790 9464
746	3c4ffc0b04780add5e42f9bb72535c4b	Bedding	1	97	9	187	37.052 89953	-114.791 6681
747	d4ca6b5754a708f5aec4c6e8f833106a	Bedding	50000	67	15	157	37.053 25996	-114.793 1037
1267		Bedding	6	9	80		37.030 645	-114.816 484
1268		Bedding	5	107	6		37.029 958	-114.817 818
1269		Bedding	7	318	28		37.029 339	-114.818 59
1270		Bedding	1	40	11		37.028 863	-114.820 627
1271		Bedding	1	40	22		37.029 457	-114.823 076
1272		Bedding	2	9	28		37.027 684	-114.824 244

1273		Bedding	7	300	11		37.026 88	-114.824 947
1274		Bedding	5	271	13		37.024 928	-114.825 508
1275		Bedding	1	246	14		37.024 667	-114.825 752
1276		Bedding	3	236	20		37.024 502	-114.826 366
1277		Bedding	6	322	1		37.056 259	-114.789 88
1278		Bedding	2	123	9		37.056 107	-114.788 674
1279		Bedding	5	131	14		37.055 449	-114.788 104
1280		Bedding	6	154	7		37.054 771	-114.788 361
1281		Bedding	6	152	18		37.055 083	-114.788 91
1282		Bedding	7	161	18		37.055 135	-114.789 192
1283		Bedding	3	145	21		37.055 194	-114.789 187
1284		Bedding	5	122	16		37.055 21	-114.789 523
1285		Bedding	8	77	22		37.055 275	-114.789 988

1286		Bedding	6	13	30		37.054747	-114.791908
1287		Bedding	1	76	15		37.052615	-114.790946
1288		Bedding	1	97	9		37.0529	-114.791668
1289		Bedding	1	67	15		37.05326	-114.793104
1290		Bedding	753	60	2		37.056134	-114.788615
1291		Bedding	48000	195	3		37.054781	-114.785381
1292		Bedding	28358	178	15		37.056808	-114.78571
1293		Bedding	21088	189	12		37.056901	-114.787603
1294		Bedding	48000	3	46		37.138652	-114.702605
1295		Bedding	6085	344	12		37.138305	-114.70227
1296		Compaction Foliation	48000	23	18		37.134433	-114.699039
1297		Bedding	48000	45	17		37.135106	-114.703296
1298		Bedding	41173	27	65		37.135461	-114.706976

1299		Compaction Foliation	44423	41	39		37.135135	-114.711238
1300		Bedding	37129	15	27		37.12968	-114.708533
1301		Bedding	9271	13	23		37.129035	-114.708751
1302		Bedding	29694	12	39		37.127616	-114.70924
1303		Bedding	9696	37	47		37.127951	-114.710006
1304		Bedding	1	183	35		37.126038	-114.711825
1305		Bedding	11417	345	83		37.125485	-114.711064
1306		Compaction Foliation	29933	0	39		37.124382	-114.710098
1307		Bedding	21671	21	36		37.122956	-114.710894
1308		Bedding	20636	187	23		37.123276	-114.712708
1309		Bedding	1	15	48		37.123301	-114.71379
1310		Bedding	6425	30	64		37.123763	-114.71375
1311		Bedding	37385	174	48		37.124346	-114.714444

1312		Bedding	14	186	43		37.124345	-114.714444
1313		Bedding	0	157	39		37.124345	-114.714444
1314		Bedding	14	74	10		37.124344	-114.714444
1315		Bedding	0	28	22		37.124344	-114.714444
1316		Bedding	611	29	38		37.124306	-114.714421
1317		Bedding	1423	37	30		37.124264	-114.714367
1318		Bedding	3987	65	66		37.124294	-114.714091
1319		Bedding	14094	9	44		37.124949	-114.713423
1320		Bedding	1	124	25		37.125823	-114.713
1321		Bedding	1675	146	35		37.125856	-114.712855
1322		Bedding	13697	321	84		37.127	-114.711548
1323		Bedding	4967	329	10		37.127261	-114.711242
1324		Bedding	2719	234	19		37.12743	-114.711366
1325		Bedding	46169	51	16		37.129554	-114.712062

1326		Bedding	1219	22	20		37.129481	-114.712123
1327		Bedding	1	19	23		37.142556	-114.707959
1328		Bedding	14905	8	19		37.141926	-114.706872
1329		Bedding	4431	24	65		37.141658	-114.706655
1330		Bedding	357	223	16		37.141676	-114.706632
1331		Bedding	3408	31	21		37.141585	-114.706362
1332		Bedding	125	19	16		37.141587	-114.706373
1333		Bedding	11269	3	27		37.141587	-114.70595
1334		Bedding	9546	340	41		37.142254	-114.705739
1335		Bedding	44592	5	32		37.141972	-114.704011
1336		Bedding	18020	11	33		37.141414	-114.702546
1337		Bedding	783	17	28		37.141367	-114.702585
1338		Bedding	10636	358	44		37.141173	-114.701637

1339		Bedding	6463	16	32		37.141092	-114.701064
1340		Compaction Foliation	48000	11	32		37.139567	-114.696504
1341		Bedding	48000	3	32		37.145103	-114.699292
1342		Bedding	37989	177	19		37.067574	-114.768599
1343		Bedding	48000	47	19		37.063878	-114.770186
1344		Bedding	15630	278	17		37.064299	-114.77149
1345		Bedding	4012	248	13		37.064175	-114.771816
1346		Bedding	40552	49	23		37.063585	-114.773815
1347		Bedding	48000	182	7		37.064827	-114.78089
1348		Bedding	15969	204	8		37.065843	-114.781565
1349		Bedding	6678	295	14		37.066288	-114.781336
1350		Bedding	48000	239	14		37.068545	-114.780629
1351		Bedding	24644	189	4		37.068892	-114.778455

1352		Bedding	17845	76	3		37.069642	-114.777151
1353		Bedding	13168	194	16		37.069024	-114.776252
1354		Bedding	8349	25	26		37.069612	-114.776092
1355		Bedding	48000	234	12		37.069499	-114.774854
1356		Bedding	12730	22	11		37.06909	-114.773829
1357		Bedding	36753	50	19		37.068266	-114.771928
1358		Bedding	9151	170	10		37.067616	-114.771788
1359		Bedding	4816	21	16		37.067926	-114.771593
1360		Bedding	34287	5	11		37.070553	-114.770759
1361		Bedding	17950	40	18		37.071835	-114.770977
1362		Bedding	30829	325	18		37.073615	-114.770511
1363		Bedding	2501	277	30		37.073774	-114.770617
1364		Bedding	7870	9	23		37.074123	-114.770196

1365		Bedding	7615	352	13		37.074577	-114.769811
1366		Bedding	7515	1	46		37.07434	-114.768622
1367		Bedding	9211	186	27		37.026066	-114.884971
1368		Bedding	32619	358	34		37.039032	-114.896272
1369		Bedding	17200	48	28		37.040548	-114.898026
1370		Bedding	8151	349	21		37.041052	-114.897503
1371		Bedding	1	1	25		37.042024	-114.898704
1372		Bedding	48000	5	34		37.043543	-114.900547
1373		Bedding	17950	331	16		37.044638	-114.901407
1374		Bedding	1033	347	18		37.044685	-114.901335
1375		Bedding	11573	38	24		37.045367	-114.901913
1376		Bedding	6666	16	20		37.045116	-114.901346
1377		Bedding	8173	349	29		37.042996	-114.900274

1378		Bedding	1	13	17		37.042094	-114.900653
1379		Bedding	9956	43	9		37.042024	-114.901544
1380		Bedding	9333	200	61		37.041381	-114.901297
1381		Bedding	20778	22	28		37.040357	-114.900499
1382		Bedding	6888	27	28		37.040002	-114.900066
1383		Bedding	16200	10	31		37.039198	-114.900677
1384		Bedding	9282	349	15		37.038694	-114.900128
1385		Bedding	2595	9	14		37.03851	-114.900086
1386		Bedding	2446	42	33		37.038351	-114.900181
1387		Bedding	25342	354	20		37.036027	-114.901213
1388		Bedding	8190	17	24		37.035443	-114.901105
1389		Bedding	39120	340	35		37.033106	-114.899299
1390		Bedding	6660	342	22		37.032792	-114.898846

1391		Bedding	4289	177	13		37.032744	-114.898465
1392		Bedding	2137	198	19		37.032739	-114.898273
1393		Bedding	1	238	35		37.032708	-114.897628
1394		Bedding	4610	239	13		37.032724	-114.897214
1395		Bedding	1	237	29		37.032143	-114.896807
1396		Bedding	28807	208	18		37.031341	-114.894708
1397		Bedding	1	191	10		37.031209	-114.893474
1398		Bedding	48000	226	54		37.030563	-114.886352
1399		Bedding	13407	190	11		37.030309	-114.885189
1400		Bedding	4310	216	20		37.030127	-114.885503
1401		Bedding	23716	206	18		37.028955	-114.885628
1402		Bedding	29657	357	27		37.030002	-114.883779
1403		Bedding	1	252	9		37.027224	-114.882757

1404		Bedding	6289	8	89		37.027453	-114.882269
1405		Bedding	4391	246	32		37.027476	-114.880374
1406		Bedding	14011	353	22		37.026755	-114.880007
1407		Bedding	5014	216	23		37.026412	-114.879865
1408		Bedding	1	171	90		37.026019	-114.88112
1409		Bedding	4166	167	62		37.024744	-114.881485
1410		Bedding	2274	143	89		37.024774	-114.881284
1411		Bedding	2338	169	82		37.022048	-114.881083
1412		Bedding	6763	303	18		37.02014	-114.88386
1413		Compaction Foliation	48000	43	13		37.093296	-114.750313
1414		Slickenside	1	341	0		37.090736	-114.746754
1415		Fault	1	158	57		37.090741	-114.746742
1416		Bedding	48000	1	51		37.086692	-114.735294

1417		Bedding	35842	68	7		37.085819	-114.738329
1418		Bedding	32746	75	25		37.086212	-114.741234
1419		Bedding	23549	57	16		37.086539	-114.743313
1420		Bedding	1	238	36		37.089864	-114.746565
1421		Fault	1	240	54		37.090157	-114.7468
1422		Slickenline	1	5	2		37.090568	-114.746768
1423		Fault	1	188	88		37.09059	-114.746734
1424		Bedding	1	48	50		37.08387	-114.759224
1425		Bedding	48000	42	42		37.083741	-114.759353
1426		Bedding	37969	18	20		37.086468	-114.760298
1427		Compaction Foliation	1	26	78		37.08588	-114.763219
1428		Fault	1	213	53		37.08493	-114.761383
1429		Bedding	11120	12	7		37.023606	-114.906363

1430		Bedding	989	188	1		37.018642	-114.861621
1431		Bedding	1383	207	2		37.014984	-114.864074
1432		Bedding	649	36	0		37.015013	-114.864009
1433		Bedding	475	211	1		37.005688	-114.883641

References

Abdelhaleem, S. A., 2022, Fault development and interaction by compaction, tectonism, and linkage: Examples from Quaternary fault development in southern Nevada; PhD Dissertation, University of Nevada, Las Vegas: Nevada, USA.

Abdelhaleem, S. A., Barba, W. K., Reed, N. G., Reid, A. J., and Taylor, W. J., 2020, Transverse faults in rifting: Timpahute Lineament, East-Central Nevada. Geological Society of America Abstracts with Programs. v. 52, No. 4, doi: 10.1130/abs/2020CD-347211.

Abdelhaleem, S.A., 2022, Fault development and interaction by compaction, tectonism, and linkage: Examples from Quaternary fault development in southern Nevada, Ph.D. Dissertation, University of Nevada, Las Vegas: Nevada, USA.

Anderson, R.E., compiler, 1999, Fault number 1123, Kane Springs Wash fault, in Quaternary fault and fold database of the United States: U.S. Geological Survey website, https://earthquakes.usgs.gov/hazards/qfaults, accessed April, 19, 2022

Andersen, T., 2005. Detrital zircons as tracers of sedimentary provenance: limiting conditions from statistics and numerical simulation: Chemical Geology, v. 216, p. 249-270.

Arehart, G.B., DeYoung, S., Poulson, S.R., Heaton, J.S., and Weiss, S., 2013, Sulfur isotopes in Plutonic Rocks of the Great Basin as Indicators of Crustal Architecture: The Journal of Geology, v. 121, p. 355–369, doi:10.1086/670651.

Armstrong, R.L., 1968, Sevier orogenic belt in Nevada and Utah: Bulletin of the Geological Society of America, v. 79, p. 429–458, doi:10.1130/0016-7606(1968)79[429:SOBINA]2.0.CO;2.

Atwater, T., and Stock, J., 1998, Pacific-North America plate tectonics of the Neogene southwestern United States: An update: International Geology Review, v. 40, p. 375–402, doi:10.1080/00206819809465216.

Axen, G.J., Wernicke, B.P., Skelly, M.F., and Taylor, W.J., 1990, Mesozoic and Cenozoic tectonics of the Sevier thrust belt in the Virgin River Valley area, southern Nevada, in Wernicke, B.P. ed., Memoir of the Geological Society of America, v. 176, p. 123–153, doi:10.1130/MEM176-p123.

Axen, G.J., Taylor, W.J., and Bartley, J.M., 1993, Space-time patterns and tectonic controls of Tertiary extension and magmatism in the Great Basin of the western United States: Geological Society of America Bulletin, v. 105, p. 56–76, doi:10.1130/0016-7606(1993)105<0056:STPATC>2.3.CO;2.

Axen, G.J., 1998, The Caliente-Enterprise Zone, southeastern Nevada and southwestern Utah, in Faults, J.E. and Stewart, J.H. eds., Geological Society of America, Special Paper, v. 323, p. 181–194, doi: 10.1130/0-8137-2323-X.181.

Beard, L.S. et al., 2007, Preliminary geologic map of the Lake Mead 30'x60' quadrangle, Clark County, Nevada and Mohave County, Arizona: U.S. Geological Survey OF-2007-1010, p. 109, https://pubs.usgs.gov/of/2007/1010/

Best, M.G., Barr, D.L., Christiansen, E.H., Gromme, S., Deino, A.L., and Tingey, D.G., 2009, The Great Basin Altiplano during the middle Cenozoic ignimbrite flareup: Insights from volcanic rocks: International Geology Review, v. 51, p. 589–633, doi:10.1080/00206810902867690.

Best, M.G., Christiansen, E.H., Deino, A.L., Gromme, S., Hart, G.L., and Tingey, D.G., 2013a, The 36–18 Ma Indian Peak–Caliente ignimbrite field and calderas, southeastern Great

Basin, USA: Multicyclic super-eruptions: Geosphere, v. 9, p. 864–950, doi: 10.1130/GES00902.1.

Best, M.G., Christiansen, E.H., de Silva, S., and Lipman, P.W., 2016, Slab-rollback ignimbrite flareups in the southern Great Basin and other Cenozoic American arcs: A distinct style of arc volcanism: Geosphere, v. 12, p. 1097–1135, doi:10.1130/GES01285.1.

Best, M.G., Gromme, S., Deino, A.L., Christiansen, E.H., Hart, G.L., and Tingey, D.G., 2013b, The 36-18 Ma central Nevada ignimbrite field and calderas, Great Basin, USA: Multicyclic super-eruptions: Geosphere, v. 9, p. 1562–1636, doi: 10.1130/GES00945.1.

Bidgoli, T.S., 2005, The role of transverse faults in Great Basin extension: Transfer faults or N-S extension? MS Thesis, University of Nevada, Las Vegas: Nevada, USA, ProQuest Dissertations Publishing, https://search.proquest.com/docview/305388608.

Bowers, W.E., 1972, The Canaan Peak, Pine Hollow, and Wasatch Formations in the Table Cliff Region, Garfield County, Utah: USGS Bulletin, v. 1331-B, p. 1–39.

Burchfiel, B.C., Wernicke, B., Willemin, J.H., Axen, G.J., and Cameron, C.S., 1982, A new type of decollement thrusting: Nature, v. 300, p. 513–515, doi: 10.1038/300513a0.

Busby, C.J., and Putirka, K., 2009, Miocene evolution of the western edge of the Nevadaplano in the central and northern Sierra Nevada: Palaeocanyons, magmatism, and structure: International Geology Review, v. 51, p. 670–701, doi: 10.1080/00206810902978265.

Camp, V.E., Pierce, K.L., and Morgan, L.A., 2015, Yellowstone plume trigger for Basin and Range extension, and coeval emplacement of the Nevada-Columbia Basin magmatic belt: Geosphere, v. 11, p. 203–225, doi:10.1130/GES01051.1.

Campbell, I.H., Reiners, P.W., Allen, C.M., Nicolescu, S., and Upadhyay, R., 2005, He-Pb double dating of detrital zircons from the Ganges and Indus Rivers: Implication for

quantifying sediment recycling and provenance studies: Earth and Planetary Science Letters, v. 237, p. 402-432.

Canada, A.S., Cassel, E.J., McGrew, A.J., Smith, M.E., Stockli, D.F., Foland, K.A., Jicha, B.R., and Singer, B.S., 2019, Eocene exhumation and extensional basin formation in the Copper Mountains, Nevada, USA: Geosphere, v. 15, p. 1577–1597, doi:10.1130/GES02101.1.

Cashman, P.H., and Fontaine, S.A., 2000, Strain partitioning in the northern Walker Lane, western Nevada and northeastern California: Tectonophysics, v. 326, p. 111–130, doi:10.1016/S0040-1951(00)00149-9.

Cashman, P.H., and Sturmer, D.M., 2021, Paleogeographic reconstruction of Mississippian to Middle Pennsylvanian basins in Nevada, southwestern Laurentia: Palaeogeography, Palaeoclimatology, Palaeoecology, v. 584, p. 110666, doi:10.1016/j.palaeo.2021.110666.

Cassel, E.J., Breecker, D.O., Henry, C.D., Larson, T.E., and Stockli, D.F., 2014, Profile of a paleo-orogen: High topography across the present-day Basin and Range from 40 to 23 Ma: Geology, v. 42, p. 1007–1010, doi:10.1130/G35924.1.

Cassel, E.J., Smith, M.E., and Jicha, B.R., 2018, The impact of slab rollback on Earth's surface: Uplift and extension in the hinterland of the North American Cordillera: Geophysical Research Letters, v. 45, p. 10,996-11,004, doi:10.1029/2018GL079887.

Colgan, J.P., Dumitru, T.A., Reiners, P.W., Wooden, J.L., and Miller, E.L., 2006, Cenozoic tectonic evolution of the Basin and Range province in northwestern Nevada: American Journal of Science, v. 306, p. 616–654, doi:10.2475/08.2006.02.

Collanega, L., Corti, G., Breda, A., Massironi, M., and Keir, D., 2020, 3D Extension at plate boundaries accommodated by interacting fault systems: Scientific Reports, v. 10, doi:10.1038/s41598-020-65599-5.

Davis, S.J., Dickinson, W.R., Gehrels, G.E., Spencer, J.E., Lawton, T.F., and Carroll, A.R., 2010, The Paleogene California River: Evidence of Mojave-Uinta paleodrainage from U-Pb ages of detrital zircons: Geology, v. 38, p. 931–934, doi:10.1130/G31250.1.

DeCelles, P.G., 2004, Late Jurassic to Eocene evolution of the Cordilleran thrust belt and foreland basin system, western U.S.A: American Journal of Science, v. 304, p. 105–168, doi: 10.2475/ajs.304.2.105.

DeCelles, P.G., and Coogan, J.C., 2006, Regional structure and kinematic history of the Sevier fold-and-thrust belt, central Utah: Bulletin of the Geological Society of America, v. 118, p. 841–864, doi:10.1130/B25759.1.

DeCelles, P.G., and Graham, S.A., 2015, Cyclical processes in the North American Cordilleran orogenic system: Geology, v. 43, p. 499–502, doi: 10.1130/G36482.1.

dePolo, C.M., 1998, A reconnaissance technique for estimating the slip rates of normal-slip faults in the Great Basin, and application to faults in Nevada, United States of America: University of Nevada, Reno, ProQuest Dissertations Publishing, https://search.proquest.com/docview/304438753.

dePolo, D.M., and dePolo, C.M., 2012, Earthquakes in Nevada: 1840s to 2010, Nevada Bureau of Mines and Geology Map 179, https://pubs.nbmg.unr.edu/Earthquakes-in-NV-1840s-to-2010-p/m179.htm.

Dickinson, W.R., 2004, Evolution of the North American Cordillera: Annual Review of Earth and Planetary Sciences, v. 32, p. 13–45, doi:10.1146/annurev.earth.32.101802.120257.

Dickinson, W.R., 2006, Geotectonic evolution of the Great Basin: Geosphere, v. 2, p. 353, doi: 10.1130/GES00054.1.

Dickinson, W.R. and Gehrels, G.E., 2009, Use of U-Pb ages of detrital zircons to infer maximum depositional ages of strata: A test against a Colorado Plateau Mesozoic database: Earth and Planetary Science Letters, v. 288, p. 115-125, doi: 10.1016/j.epsl.2009.09.013.

Dickinson, W.R., and Gehrels, G.E., 2010, Insights into North American paleogeography and paleotectonics from U-Pb ages of detrital zircons in Mesozoic strata of the Colorado Plateau, USA: International Journal of Earth Sciences, v. 99, p. 1247–1265, doi:10.1007/s00531-009-0462-0.

Dohrenwend, J.C., Schell, B.A., Menges, C.M., Moring, B.C., and McKittrick, M.A., 1996, Reconnaissance photogeologic map of young (Quaternary and late Tertiary) faults in Nevada, in Singer, D.A., ed., Analysis of Nevada's metal-bearing mineral resources: Nevada Bureau of Mines and Geology Open-File Report 96-2, 1 pl., scale 1:1,000,000

Druschke, P., Hanson, A. D., Wells, M. L., Gehrels, G. E., and Stockli, D.,2011, Paleogeographic isolation of the cretaceous to Eocene Sevier hinterland, east-central Nevada: Insights from U-Pb and (U-Th)/He detrital zircon ages of hinterland strata. Bulletin of the Geological Society of America, v. 123(5), p. 1141–1160. https://doi.org/10.1130/B30029.1.

Eaton, J.G., Korth, W.W., and Brinkman, D.B., 2018, Vertebrate fossils from the Claron Formation, Sweetwater Creek Area, Garfield County, Utah, U.S.A.: Rocky Mountain Geology, v. 53, p. 113–127, doi:10.24872/rmgjournal.53.2.113.

Ekren, E. B., Bucknam, R C., Carr, W. J, Dixon, G. L., and Quinlivan, W. D., 1976, East-trending structural lineaments in central Nevada: U.S. Geological Survey Professional Paper 986, 16 p.

Ellis, M.A., Barnes, J.B., and Colgan, J.P., 2015, Geomorphic evidence for enhanced Pliocene–Quaternary faulting in the northwestern Basin and Range: Lithosphere, v. 7, p. 59–72, doi:10.1130/L401.1.

Ely, R.M., and Taylor, W. J., 2018, Termination of the eastern Buckhorn fault and triaxial strain along the fault: implications for the development of the Pahranagat shear zone and the development of the boundary zone between the central and northern Basin and Range: Geological Society of America Annual Conference, Geological Society of America Abstracts with Programs, v. 50, no. 6, ISSN 0016-7592, doi: 10.1130/abs/2018AM-322953.

Erdman, M.E., Lee, C.T.A., Levander, A., and Jiang, H., 2016, Role of arc magmatism and lower crustal foundering in controlling elevation history of the Nevadaplano and Colorado Plateau: A case study of pyroxenitic lower crust from central Arizona, USA: Earth and Planetary Science Letters, v. 439, p. 48–57, doi:10.1016/j.epsl.2016.01.032.

EROS, 2018, USGS EROS Archive–- Aerial Photography–- National Agriculture Imagery Program (NAIP):, https://www.usgs.gov/centers/eros/science/usgs-eros-archive-aerial-photography-national-agriculture-imagery-program-naip?qt-science_center_objects=0#overview (accessed July 2022).

Evans, M. D., 2018, Structural evolution and regional implications of the Arrowhead Mine fault within the Pahranagat Shear Zone, Nevada, USA. MS Thesis, University of Nevada, Las Vegas: Nevada, USA. https://digitalscholarship.unlv.edu/thesesdissertations/3248.

Elison, M.W., Speed, R.C., and Kistler, R.W., 1990, Geologic and isotopic constraints on the crustal structure of the northern Great Basin: Geological Society of America Bulletin, v. 102, p. 1077–1092, doi:10.1130/0016-7606(1990)102<1077:GAICOT>2.3.CO;2.

Faulds, J.E., and Varga, R.J., 1998, The role of accommodation zones and transfer zones in the regional segmentation of extended terranes, in Faulds, J.E. and Stewart, J.H. eds., Accommodation zones and transfer zones; the regional segmentation of the Basin and Range Province, Geological Society of America Special Paper 323, p. 1–45, doi: 10.1130/0-8137-2323-X.1.

Fedo, C.M., Sicrombe, K.N., and Rainbird, R.H., 2003, Detrital zircon analysis of the sedimentary record: Reviews in Mineralogy & Geochemistry, v. 53, p. 277-303.

Felger, T.J., and Beard, L.S., 2010, Geologic map of Lake Mead and surrounding regions, southern Nevada, southwestern Utah, and northwestern Arizona, in Umhoefer, P.J., Beard, L.S., and Lamb, M.A. eds., Miocene Tectonics of the Lake Mead Region, Central Basin and Range, Geological Society of America, v. 463, p. 0, doi:10.1130/2010.2463(02).

French, D.E., Trexler, J.H., Cashman, P.H., Walker, J.P., and Wylie, A.S., 2020, Mississippian mud rocks of the eastern Great Basin: Stratigraphy, tectonic significance, and hydrocarbon potential: AAPG Bulletin, v. 104, p. 387–410, doi:10.1306/05091918190.

Friedrich, A.M., and Bartley, J.M., 2003, Three-dimensional structural reconstruction of a thrust system overprinted by postorogenic extension, Wah Wah thrust zone, southwestern Utah: GSA Bulletin, v. 115, p. 1473–1491, doi:10.1130/B25148.1.

Garrity, C.P., and Soller, D.R., 2009, Database of the Geologic Map of North America; adapted from the map by J.C. Reed, Jr. and others (2005): U.S. Geological Survey Data Series 424 [https://pubs.usgs.gov/ds/424/].

Giallorenzo, M.A., Wells, M.L., Yonkee, W.A., Stockli, D.F., and Wernicke, B.P., 2018, Timing of exhumation, Wheeler Pass thrust sheet, southern Nevada and California: Late Jurassic to

middle Cretaceous evolution of the southern Sevier fold-and-thrust belt: Bulletin of the Geological Society of America, v. 130, p. 558–579, doi:10.1130/B31777.1.

Greene, D.C., 2014, The Confusion Range, west-central Utah: Fold-thrust deformation and a western Utah thrust belt in the Sevier hinterland: Geosphere, v. 10, p. 148-169, doi:10.1130/GES00972.1.

Goldstrand, P.M., 1994, Tectonic development of Upper Cretaceous to Eocene strata of southwestern Utah: Geological Society of America Bulletin, v. 106, p. 145–154, doi:10.1130/0016-7606(1994)106<0145:TDOUCT>2.3.CO;2.

Hammond, W.C., and Thatcher, W., 2004, Contemporary Tectonic Deformation of the Basin and Range Province, Western United States: 10 years of Observation with the Global Positioning System: Journal of Geophysical Research: Solid Earth, v. 109, doi:10.1029/2003jb002746.

Harding, A.E., Scott, R.B., Mehnert, H.H., and Pampeyan, E.H., 1991, Kane Springs Wash caldera, Southeast Nevada – the other half of the story: Geological Society of America Abstracts with Programs, v. 23, no. 4, p. 30.

Harding, A.E., Scott, R.B., Mehnert, H.H., and Snee, L.W., 1992, Evidence of the Kane Springs Wash caldera in the Meadow Valley Mountains, southeastern Nevada, in Scott, R.B. and Swadley, W.C., eds., Geologic Studies in the Basin and Range – Colorado Plateau Transition in Southeastern Nevada, Southwestern Utah and Northwestern Arizona, 1995: U.S. Geological Survey Bulletin 2056-A, p. 135-179.

Henry, C.D., 2008, Ash-flow tuffs and paleovalleys in northeastern Nevada: Implications for Eocene paleogeography and extension in the Sevier hinterland, northern Great Basin: Geosphere, v. 4, p. 1–35, doi:10.1130/GES00122.1.

Henry, C.D., and Faulds, J.E., 2010, Ash-flow tuffs in the Nine Hill, Nevada, paleovalley and implications for tectonism and volcanism of the western Great Basin, USA: Geosphere, v. 6, p. 339–369, doi: 10.1130/GES00548.1.

Henry, C.D., Hinz, N.H., Faulds, J.E., Colgan, J.P., John, D.A., Brooks, E.R., Cassel, E.J., Garside, L.J., Davis, D.A., and Castor, S.B., 2012, Eocene-Early Miocene paleotopography of the Sierra Nevada-Great Basin-Nevadaplano based on widespread ash-flow tuffs and paleovalleys: Geosphere, v. 8, p. 1–27, doi: 10.1130/GES00727.1.

Henza, A.A., Withjack, M.O., and Schlische, R.W., 2010, Normal-fault development during two phases of non-coaxial extension: An experimental study: Journal of Structural Geology, v. 32, p. 1656–1667, doi:10.1016/j.jsg.2009.07.007.

Hudson, M.R., Rosenbaum, J.G., Gromme, C.S., Scott, R.B., and Rowley, P.D., 1998, Paleomagnetic evidence for counterclockwise rotation in a broad sinistral shear zone, Basin and Range Province, southeastern Nevada and southwestern Utah, in Faulds, J.E. and Stewart, J.H. eds., Accommodation zones and transfer zones; the regional segmentation of the Basin and Range Province, Geological Society of America Special Paper 323, p. 149–180, doi: 10.1130/0-8137-2323-X.149.

Jackson, S.E., Pearson, N.J., Griffin, W.L., and Belousova, E.A., 2004, The application of laser ablationinductively coupled plasma-mass spectrometry to in situ U-Pb zircon geochronology: Chemical Geology, v. 211, p. 47-69.

Jayko, A. S., 1990, Shallow crustal deformation in the Pahranagat area, southern Nevada: Geological Society of America Memoir 176, p. 213-236.

Jayko, A. S., 2007, Geologic map of the Pahranagat Range Quadrangle, Lincoln and Nye Counties, Nevada: U.S. Geologic Survey, scale 1:100,000.

Krantz, R.W., 1989, Orthorhombic fault patterns: The odd axis model and slip vector orientations: Tectonics, v. 8, p. 483–495, doi:10.1029/TC008I003P00483.

Kreemer, C., Blewitt, G., and Hammond, W.C., 2010, Evidence for an active shear zone in southern Nevada linking the Wasatch fault to the Eastern California shear zone: Geology, v. 38, p. 475–478, doi: 10.1130/G30477.1.

Kucks, Robert P., 1999, Bouguer gravity anomaly data grid for the conterminous US: https://mrdata.usgs.gov/services/gravity?request=getcapabilities&service=WMS&version=1.3.0

Kucks, R.P., Hill, P.L., and Ponce, D.A., 2006, Nevada magnetic and gravity maps and data: A website for the distribution of data: doi:10.3133/DS234.

Lawton, T.F., Cashman, P.H., Trexler, J.H., and Taylor, W.J., 2017, The late Paleozoic southwestern Laurentian borderland: Geology, v. 45, p. 675–678, doi:10.1130/G39071.1.

Long, S.P., 2012, Magnitudes and spatial patterns of erosional exhumation in the Sevier hinterland, eastern Nevada and western Utah, USA: Insights from a Paleogene paleogeologic map: Geosphere, v. 8, p. 881–901, doi:10.1130/GES00783.1.

Long, S.P., Thomson, S.N., Reiners, P.W., and Di Fiori, R. V., 2015, Synorogenic extension localized by upper-crustal thickening: An example from the Late Cretaceous Nevadaplano: Geology, v. 43, p. 351–354, doi:10.1130/G36431.1.

Long, S.P., 2019, Geometry and magnitude of extension in the Basin and Range Province (39°N), Utah, Nevada, and California, USA: Constraints from a province-scale cross section: Bulletin of the Geological Society of America, v. 131, p. 99–119, doi:10.1130/B31974.1.

Longwell, B.C.R., Pampeyan, E.H., Bowyer, B., Roberts, R.J., and Longwell, C.R., 1965, Geology and Mineral Deposits of Clark County, Nevada: Nevada Bureau of Mines and Geology: Bulletin 62, https://pubs.nbmg.unr.edu/Geol-mineral-of-Clark-Co-p/b062.htm.

Lundstrom, S.C., Page, W.R., Langenheim, V.E., Young, O.D., Mahan, S.A., and Dixon, G.L., 1998, Preliminary Geologic Map of the Valley Quadrangle, Clark County, Nevada: Open-File Report, doi:10.3133/OFR98508.

Miller, J.M.L., Nelson, E.P., Hitzman, M., Muccilli, P., and Hall, W.D.M., 2007, Orthorhombic fault-fracture patterns and non-plane strain in a synthetic transfer zone during rifting: Lennard shelf, Canning basin, Western Australia: Journal of Structural Geology, v. 29, p. 1002–1021, doi:10.1016/j.jsg.2007.01.004.

Moore, K., Bidgoli, T. ~S., Taylor, W. ~J., Sturmer, D., and Stockli, D. ~F., 2020, Late Cretaceous to Eocene exhumation history of the Sevier hinterland plateau in east-central and southern Nevada., in AGU Fall Meeting Abstracts, v. 2020, p. T049- 0002.

Muhlbauer, J.G., Fedo, C.M., and Farmer, G.L., 2017, Influence of textural parameters on detrital-zircon age spectra with application to provenance and paleogeography during the Ediacaran−Terreneuvian of southwestern Laurentia: Geological Society of America Bulletin, v. 129, p. B31611.1, doi:10.1130/b31611.1.

Page, W.R., Swadley, W.C., and Scott, R.B., 1990, Preliminary geologic map of the Delamar 3 SW Quadrangle, Lincoln County, Nevada: U.S. Geological Survey Open-File Report 90–336, doi: 10.3133/ofr90336.

Page, W.R., and Pampeyan, E.H., 1996, Preliminary geologic map of the Paleozoic rocks in the Wildcat Wash SE and Wildcat Wash SW quadrangles, Lincoln and Clark counties, Nevada: U.S. Geological Survey Open-File Report 96-26, doi: 10.3133/ofr9626.

Page, W.R., Dixon, G.L., Rowley, P.D, and Brickey, D.W., 2005a, Geologic map of parts of the Colorado, White River, and Death Valley groundwater flow systems, Nevada, Utah, and Arizona: Nevada Bureau of Mines and Geology Map 150, scale 1:250,000.

Page, W.R., Lundstrom, S.C., Harris, A.G., Langenheim, V.E., Workman, J.B., Mahan, S.A., Paces, J.B., Rowley, P.D., Dixon, G.L., Burchfiel, B.C., Bell, J.W., and Smith, E.I., 2005b, Geologic and geophysical maps of the Las Vegas 30' x 60' Quadrangle, Clark and Nye Counties, Nevada, and Inyo County, California: U.S. Geological Survey Scientific Investigations Map 2814, scale 1:100,000.

Pampeyan, E.H., 1993, Geologic map of the Meadow Valley Mountains, Lincoln and Clark counties, Nevada: U.S. Geological Survey, Miscellaneous Investigations Series Map I-2173, doi: 10.3133/i2173.

Pavlis, T.L., Rutkofske, J., Guerrero, F., and Serpa, L.F., 2014, Structural overprinting of Mesozoic thrust systems in eastern California and its importance to reconstruction of Neogene extension in the Southern Basin and Range: Geosphere, v. 10, p. 732–756, doi:10.1130/GES00993.1.

Peacock, D.C.P., Nixon, C.W., Rotevatn, A., Sanderson, D.J., and Zuluaga, L.F., 2016, Glossary of fault and other fracture networks: Journal of Structural Geology, v. 92, p. 12–29, doi:10.1016/j.jsg.2016.09.008.

Peck, A., 2018, Miocene-Quaternary deformation along the central Maynard Lake fault, Pahranagat shear zone, Nevada, doi:10.34917/13568651. MS Thesis, University of Nevada, Las Vegas: Nevada, USA.

Pérouse, E., and Wernicke, B.P., 2017, Spatiotemporal evolution of fault slip rates in deforming continents: The case of the Great Basin region, northern Basin and Range province: Geosphere, v. 13, p. 112–135, doi: 10.1130/GES01295.1.

Price, T., and Taylor, W.J., 2017, Miocene-Pliocene(?) Folds and the left-lateral Buckhorn fault with regional implications, Pahranagat shear zone, Nevada: Geological Society of America Abstracts with Programs, v. 49, doi:10.1130/abs/2017am-305503.

Pullen, A., Ibáñez-Mejía, M., Gehrels, G. E., Ibáñez-Mejía, J. C., and Pecha, M., 2014, What happens when n= 1000? Creating large-n geochronological datasets with LA-ICP-MS for geologic investigations: Journal of Analytical Atomic Spectrometry, v. 29, p. 971-980, doi:10.1039/c4ja00024b.

Reches, Z., 1983, Faulting of rocks in three-dimensional strain fields II. Theoretical analysis: Tectonophysics, v. 95, p. 133–156, doi:10.1016/0040-1951(83)90264-0.

Reed, N.G., and Taylor, W.J. (2019). Kane Springs Wash Fault, NV Quaternary Faults. Proceedings of the Annual Geosymposium. University of Nevada, Las Vegas: Nevada, USA.

Reid, A. J., Taylor, W., and Reed, N.G. (2020). Heterogeneous extension along the northern boundary of the central Basin and Range sub-province: The Kane Springs Wash fault, southern Nevada. Geological Society of America Abstracts with Programs, v. 52(4), 1-1. http://dx.doi.org/10.1130/abs/2020CD-347498.

Reiners, P.W., Campbell, I.H., Nicolescu, S., Allen, C.M., Hourigan, J.K., Garver, J.I., Mattinson, J.M., and Cowan, D.S., 2005, (U-Th)/(He-Pb) Double dating of detrital zircons, American Journal of Science, v. 305, p. 259-311.

Rowley, P.D., 1998, Cenozoic transverse zones and igneous belts in the Great Basin, Western United States: Their tectonic and economic implications, in Faulds, J.E. and Stewart, J.H. eds., Accommodation zones and transfer zones; the regional segmentation of the Basin and Range Province, Geological Society of America, p. 195–228, doi: 10.1130/0-8137-2323-X.195.

Ryan, W.B.F. et al., 2009, Global multi-resolution topography synthesis: Geochemistry, Geophysics, Geosystems, v. 10, doi:10.1029/2008GC002332.

Sanjuan, J., Vicente, A., and Eaton, J.G., 2020, New charophyte flora from the Pine Hollow and Claron formations (southwestern Utah). Taxonomic, biostratigraphic, and paleobiogeographic implications: Review of Palaeobotany and Palynology, v. 282, p. 104289, doi:10.1016/j.revpalbo.2020.104289.

Saylor, J.E. and Sundell, K.E., 2016, Quantifying comparison of large detrital geochronology data sets: Geosphere, v. 12, p. 203-220.

Saylor, J.E., Stockli, D.F., Horton, B.K., Nie, J., and Mora, A., 2012, Discriminating rapid exhumation from syndepostional volcanism using detrital zircon double dating: Implications for the tectonic history of the Eastern Cordillera, Colombia: Geological Society of America Bulletin, v. 124, p. 762779.

Schoenborn, W.A., Fedo, C.M., and Farmer, G.L., 2012, Provenance of the Neoproterozoic Johnnie Formation and Stirling Quartzite, southeastern California, determined by detrital zircon geochronology and Nd isotope geochemistry: Precambrian Research, v. 206–207, p. 182–199, doi:10.1016/j.precamres.2012.02.017.

Scott, R.B., Page, W.R., and Swadley, W.C., 1990, Preliminary geologic map of the Delamar 3 NW Quadrangle, Lincoln County, Nevada: U.S. Geological Survey, doi: 10.3133/ofr90405.

Scott, R.B., and Swadley, W.C., 1995, Geologic studies in the Basin and Range-Colorado Plateau transition in southeastern Nevada, southwestern Utah, and northwestern Arizona, 1992: U.S. G.P.O., Open-File Report 90-336, doi: 10.3133/b2056.

Scott, R.B., Swadley, W.C., and Novak, S.W., 1993, Geologic map of the Delamar Lake Quadrangle, Lincoln County, Nevada: U.S. Geological Survey Geologic Quadrangle 1730, doi:10.3133/gq1730.

Scott, R.B., Unruh, D.M., Snee, L.W., Harding, A.E., Nealey, L.D., Blank, H.R., Budahn, J.R., and Mehnert, H.H., 1995, Relation of peralkaline magmatism to heterogeneous extension during the middle Miocene, southeastern Nevada: Journal of Geophysical Research: Solid Earth, v. 100, p. 10381–10401, doi: 10.1029/94JB03217.

Sircombe, K.N., 2000, Reading the bumpy barcode: Quantification and interpretation of detrital geochronology data with provenance study examples from modern beach sands and Archean metasedimentary rocks: Geological Society of America Abstracts with Programs, v. 32, no. 6, p. 68.

Smith, M.E., Carroll, A.R., Jicha, B.R., Cassel, E.J., and Scott, J.J., 2014, Paleogeographic record of Eocene Farallon slab rollback beneath western North America: Geology, v. 42, p. 1039–1042, doi:10.1130/G36025.1.

Smith, M.E., Cassel, E.J., Jicha, B.R., Singer, B.S., and Canada, A.S., 2017, Hinterland drainage closure and lake formation in response to middle Eocene Farallon slab removal, Nevada, U.S.A.: Earth and Planetary Science Letters, v. 479, p. 156–169, doi:10.1016/j.epsl.2017.09.023.

Snell, K.E., Koch, P.L., Druschke, P., Foreman, B.Z., and Eiler, J.M., 2014, High elevation of the “Nevadaplano” during the Late Cretaceous: Earth and Planetary Science Letters, v. 386, p. 52–63, doi:10.1016/j.epsl.2013.10.046.

Snow, J.K., and Wernicke, B.P., 2000, Cenozoic tectonism in the central basin and range: Magnitude, rate, and distribution of upper crustal strain: American Journal of Science, v. 300, p. 659–719, doi:10.2475/ajs.300.9.659.

Stockli, D.F., Surpless, B.E., Dumitru, T.A., and Farley, K.A., 2002, Thermochronological constraints on the timing and magnitude of Miocene and Pliocene extension in the central Wassuk Range, western Nevada: Tectonics, v. 21, p. 10-1-10–19, doi:10.1029/2001TC001295.

Sturmer, D.M., Trexler, J.H., and Cashman, P.H., 2018, Tectonic analysis of the Pennsylvanian Ely-Bird Spring Basin: Late Paleozoic tectonism on the southwestern Laurentia Margin and the distal limit of the Ancestral Rocky Mountains: Tectonics, v. 37, p. 604–620, doi:10.1002/2017TC004769.

Surpless, B.E., Stockli, D.F., Dumitru, T.A., and Miller, E.L., 2002, Two-phase westward encroachment of Basin and range extension into the northern Sierra Nevada: Tectonics, v. 21, p. 2-1-2–10, doi:10.1029/2000tc001257.

Swadley, W.C., Page, W.R., Scott, R.B., and Pampeyan, E.H., 1994, Geologic map of the Delamar 3 SE Quadrangle, Lincoln County, Nevada: U.S. Geological Survey Geologic Quadrangle 1754, doi: 10.3133/gq1754

Swanson, E., and Wernicke, B.P., 2017, Geologic map of the east-central Meadow Valley Mountains, and implications for reconstruction of the Mormon Peak detachment, Nevada: Geosphere, v. 13, p. 1234–1253, doi: 10.1130/GES01148.1.

Taylor, W.J., Abdelhaleem, S.A., Ely, R.M., Evans, M., Muhammad, M.M., Peck, A., Price, T., Reed, N.G., and Reid, A.J., 2022, The boundary zone between the northern and central Basin & Range subprovinces: A developing rift segment boundary. Geological Society of America Abstracts with Programs, v. 54, No. 2, abstract 27-1, doi: 10.1130/abs/2022CD-374351.

Taylor, W.J., Bartley, J.M., Lux, D.R., and Axen, G.J., 1989, Timing of Tertiary extension in the Railroad Valley-Pioche Transect, Nevada: Constraints from 40Ar/39Ar ages of volcanic rocks: Journal of Geophysical Research, v. 94, p. 7757-7774.

Taylor, W.J., and Bartley, J.M., 1992, Prevolcanic extensional Seaman breakaway fault and its geologic implications for eastern Nevada and western Utah: doi:10.1130/0016-7606(1992)104<0255:PESBFA>2.3.CO;2.

Taylor, W.J., 1993, Stratigraphic and lithologic analysis of the Claron Formation in southwestern Utah: Stratigraphic and lithologic analysis of the Claron Formation in southwestern Utah: Utah Geological Survey Miscellaneous Publication 93-1, doi:10.34191/mp-93-1.

Taylor, W.J., Bartley, J.M., Martin, M.W., Geissman, J.W., Walker, J.D., Armstrong, P.A., and Fryxell, J.E., 2000, Relations between hinterland and foreland shortening: Sevier orogeny central North American Cordillera: Tectonics, v. 19, p. 1124–1143, doi:10.1029/1999TC001141.

Taylor, W.J., and Switzer, D.D., 2001, Temporal changes in fault strike (to 90°) and extension directions during multiple episodes of extension: An example from Eastern Nevada: Bulletin of the Geological Society of America, v. 113, p. 743–759, doi:10.1130/0016-7606(2001)113<0743:TCIFST>2.0.CO;2.

Thenhaus, P.C., and Barnhard, T.P., 1998, Insights from Quaternary relations for segmentation of the Great Basin by regional, transverse accommodation zones, in Accommodation zones and transfer zones; the regional segmentation of the Basin and Range Province, Geological Society of America Special Paper 323, p. 229–239, doi: 10.1130/0-8137-2323-X.229.

Tschanz, C.M., and Pampeyan, E.H., 1970, Geology and mineral deposits of Lincoln County, Nevada.: Nevada Bureau of Mines and Geology Bulletin 73, 188 pp.

Vermeesch, P., 2004, How many grains are needed for a provenance study?: Earth and Planetary Science Letters, v. 224, p. 441–451

Wernicke, B., Spencer, J.E., Burchfiel, B.C., and Guth, P.L., 1982, Magnitude of crustal extension in the southern Great Basin (USA).: Geology, v. 10, p. 499–502, doi:10.1130/0091-7613(1982)10<499:MOCEIT>2.0.CO;2.

Wernicke, B., Walker, J.D., and Beaufait, M.S., 1985, Structural discordance between neogene detachments and frontal Sevier thrusts, central Mormon Mountains, southern Nevada: Tectonics, v. 4, p. 213–246, doi:10.1029/TC004i002p00213.

Wernicke, B., Axen, G.J., and Snow, J.K., 1988, Basin and Range extensional tectonics at the latitude of Las Vegas, Nevada: Bulletin of the Geological Society of America, v. 100, p. 1738–1757, doi:10.1130/0016-7606(1988)100<1738:BARETA>2.3.CO;2.

Wernicke, B., 1985, Uniform-sense normal simple shear of the continental lithosphere.: Canadian Journal of Earth Sciences, v. 22, p. 108–125, doi:10.1139/e85-009.

Wernicke, B., Axen, G.J., and Snow, J.K., 1990, Basin and Range extensional tectonics at the latitude of Las Vegas, Nevada: Special Paper of the Geological Society of America, v. 253, p. 243–262, doi:10.1130/SPE253-p243.

Wernicke, B., 1992, Cenozoic extensional tectonics of the U.S. Cordillera: The Cordilleran Orogen, p. 553–17, doi:10.1130/DNAG-GNA-G3.553.

Wilkins, S.J., and Schultz, R.A., 2003, Cross faults in extensional settings: Stress triggering, displacement localization, and implications for the origin of blunt troughs at Valles Marineris, Mars: Journal of Geophysical Research E: Planets, v. 108, p. 5056, doi:10.1029/2002je001968.

Workman, B.D., 2012, Sequence stratigraphy and detrital zircon provenance of the Eureka Quartzite in south-central Nevada and eastern California: 107 p., https://www.semanticscholar.org/paper/Sequence-Stratigraphy-and-Detrital-Zircon-of-the-in-Workman/08ed65843045a15ea42bb76b00d6f71e57db39a3 (accessed June 2022).

Wright, J.E., and Wooden, J.L., 1991, New Sr, Nd, and Pb isotopic data from plutons in the northern Great Basin: implications for crustal structure and granite petrogenesis in the hinterland of the Sevier thrust belt: Geology, v. 19, p. 457–460, doi:10.1130/0091-7613(1991)019<0457:NSNAPI>2.3.CO;2.

Yonkee, W.A., Dehler, C.D., Link, P.K., Balgord, E.A., Keeley, J.A., Hayes, D.S., Wells, M.L., Fanning, C.M., and Johnston, S.M., 2014, Tectono-stratigraphic framework of Neoproterozoic to Cambrian strata, west-central U.S.: Protracted rifting, glaciation, and evolution of the North American Cordilleran margin: Earth-Science Reviews, v. 136, p. 59–95, doi:10.1016/j.earscirev.2014.05.004.

Yonkee, W.A., and Weil, A.B., 2015, Tectonic evolution of the Sevier and Laramide belts within the North American Cordillera orogenic system: Earth Science Reviews, v. 150, p. 531-593, doi: 10.1016/j.earscirev.2015.08.001.

Curriculum Vitae:

Andrew Reid

702-720-4467 (Google Voice) | andrew.reid27@gmail.com

Education

M.S., Geology, University of Nevada – Las Vegas, (Current)
Area of Focus: Structural Geology and Tectonics
Thesis: *Mesozoic Sevier Thrusts Overprinted by Miocene-Quaternary Left-Lateral Deformation: Structures and Tectonism of The Kane Springs Wash Region, Nevada*, Advisor: Wanda J. Taylor (Approved Proposal Available)

B.S., Geology, University of Nevada - Las Vegas, August 2018.
Research: *Prospectivity of Carbonatites in the Great Basin*, Advisor: Simon Jowitt, *Modified Slab Deformation of Tiger's Eye Quartz*, Advisor: Pamela Burnley

B.S., Psychology, University of Nevada - Las Vegas, August 2013.

Areas of Focus

Structural Geology, specifically structural field methods and analysis. Geospatial analysis and prospectivity modeling using geophysical, geochemical, aeroradiometric data and spectral imagery. High-pressure and high-temperature rock deformation experimentation.

Positions

March 2022 – Present **Geologist 1 – Underground Mine Geologist**
Barrick Gold – Nevada Gold Mines

Responsibilities: My work focuses first, and foremost, on workplace safety to carry out daily underground geological work with technical expertise. Daily work includes lithological mapping, structural mapping, inspecting stopes, collecting muck samples and chip sampling, drill core logging, geological interpretation and modelling. This work is in collaboration with technical and operational teams to ensure timely and effective ore control activities and meet monthly production and development plans while adding value to overall mining operations. Commonly required to carry out special projects including geological reviews, preparation of reports.

May 2021 – March 2022 **Staff Geologist**
Southwest Geotechnical

Responsibilities: My work focused on special inspections of soil stability of foundations in new and old construction sites. Reports are directly sent to Project Manager, typically a geotechnical engineer, and are used to provide third-party inspections of grading sites. Sample collection and use of field instruments required. Driving to new sites and developments in vehicle.

Aug. 2018 – May 2021 **Graduate Teaching Assistant**
University of Nevada, Las Vegas
Department of Geoscience

Responsibilities: My research focused on developing map products and other field data to better understand the tectonic development of the

Basin and Range province in the western US, emphasizing overprinted deformation. My duties include teaching laboratory courses and methods in structural geology, and advanced field geology with an emphasis on tectonics and field methodology.

Jun. 2019 – Aug. 2019 **Contract Geologist**
Barrick Gold Exploration

Responsibilities: My work focused on the management and QA of legacy geologic data including drill log information, geochemical and metallurgical assays. My primary duty was to determine the viability and duplication of legacy data obtained from purchased junior exploration companies.

Feb. 2018 – Aug. 2018 **Geospatial Information Systems Technician**
Desert Research Institute
Division of Earth and Ecosystem Sciences with Lynn Fenstermaker

Responsibilities: My work focused on the remote sensing of vegetation, soils, rocks, to monitor ecosystems, perform habitat studies, and land coverage dissemination using multispectral and hyperspectral imagery from aerial and satellite platforms for clientele. Other projects included the generation of free-standing databases with important land use and agricultural information to disseminate to clients to enhance their analytic capabilities. I created workflows to accomplish the goals of the given study and so methodology is repeatable in future work. Software includes QGIS, ArcGIS, and ENVI.

Jul. 2017- Aug. 2018 **Research Assistant**
Nevada Rock Deformation Laboratory
University of Nevada – Las Vegas
Laboratory of Dr. Burnley

Responsibilities: My work focused on performing experiments in the Single Piston Griggs Apparatus. I performed high-pressure high-temperature experiments, sample preparation, machining sample assemblies, creating thin-sections for post-deformation analysis, mineral synthesis, powdered XRD analysis of synthesized minerals, Laboratory equipment and facilities maintenance.

Aug. 2015 – Jul. 2016 **Registrar Analyst**
University of Nevada, Las Vegas
Office of the Registrar

Responsibilities: My duties included the construction and maintenance of the curriculum and course database with operative conditional SQL statements, garnering compliance from academic departments to adhere to academic calendar deadlines, troubleshooting curriculum and scheduling changes to meet academic department goals while adhering to academic standards set by the Nevada System of Higher Education. Maintenance of social media and website data for the Office of the Registrar. Generating new efficient workflows that ensure a timely and effective processing of all incoming space management requests by academic departments and intraoffice needs.

Aug. 2013 – Aug. 2015 **Enrollment Counselor**

University of Nevada – Las Vegas
Enrollment Services Center

Responsibilities: I was responsible for assisting students with the navigation and compliance of university policy, the evaluation of applications for in-state residency, troubleshooting international student procedures, creation and operation of social media outreach initiative, updating the outward facing MyUNLV system in compliance with UNLV reprographic, creating new workflows that and procedural manuals for modernizing incoming requests that allow for transparency and approachability of office procedures.

Awards

Fall 2019	Bernada French Scholarship Recipient
April 2017	3rd Place Undergraduate GIS Poster, UNLV 2017 Geosymposium
May 2013	Millennium Scholar Nevada GEAR UP Scholar EPSCoR Nevada Discoveries Magazine Student Highlight

Scientific Presentations

1. Taylor, W.J., Abdelhaleem, S.A., Ely, R.M., Evans, M., Muhammad, M.M., Peck, A., Price, T., Reed, N.G., and Reid, A.J., 2022, *The boundary zone between the northern and central Basin & Range subprovinces: A developing rift segment boundary*. Geological Society of America Abstracts with Programs, v. 54, No. 2, abstract 27-1, doi: 10.1130/abs/2022CD-374351.
2. Reid, A. J., Reed N.G., Taylor, W.J., *Heterogeneous Extension Along the Northern Boundary of the Central Basin and Range Sub-Province: The Kane Springs Wash Fault, Southern Nevada.* Geological Society of America Cordilleran Section Meeting. 2020.
3. Abdelhaleem, S.A., Barba, W.K., Reed, N.G., Reid, A.J., Taylor, W.J., *Transverse Faults in Rifting: Timpahute Lineament, East-Central Nevada.* Geological Society of America Cordilleran Section Meeting. 2020.
4. Reid, A. J., Reed N.G., Taylor, W.J., *Distinctive West Vergence in the Late Paleozoic of North-Central Nevada: Kinematics and Timing.* Geological Society of America Cordilleran Section Meeting. 2020.
5. Reid, A. J., *Cretaceous Sevier thrust faults and Neogene left-lateral deformation: Structures and tectonism in Kane Springs Wash, Nevada.* Geosymposium. University of Nevada, Las Vegas, 2019.
6. Reid, A.J., *Preliminary Prospectivity of Carbonatites in The Great Basin: Geophysical and Aeroradiometric Modeling Using Spatial Data Modeler Weights of Evidence*. Geosymposium. University of Nevada, Las Vegas, 2018.
7. Reid, A.J., *Viability of Modified Single Piston Slab Deformation Assembly.* Geosymposium. University of Nevada, Las Vegas, 2018.
8. Bryce, T., Momchev, P., Rivera, P., Reid, A.J., *Environmental Impact of Dams, an Index of Dams in the Great Basin. Geosymposium*. University of Nevada, Las Vegas, 2017.

Professional Organizations

1. American Association of Petroleum Geologists | Former President and Treasurer of the UNLV Student Chapter (no longer an active member)
2. Geological Society of America

Personal References

Wanda Taylor, Professor
Department of Geoscience
University of Nevada Las Vegas
Box 454010
4505 S Maryland Parkway
Las Vegas, Nevada, 89154-4010
702-895-4615
wanda.taylor@unlv.edu

Rodney Metcalf, Professor
Department of Geoscience
University of Nevada, Las Vegas
Box 454010
4505 S Maryland Parkway
Las Vegas, Nevada, 89154-4010
702-895-4442
rod.metcalf@unlv.edu

Simon Jowitt, Professor
Department of Geoscience
University of Nevada Las Vegas

Box 454010
4505 S Maryland Parkway
Las Vegas, Nevada, 89154-4010
702-895-2447
simon.jowitt@unlv.edu

Lynn Fenstermaker, Research Professor and Director
Division of Earth and Ecosystem Sciences
Desert Research Institute
755 E Flamingo Road
Las Vegas, Nevada, 89119
702-862-5412
lynn.fenstermaker@dri.edu

Michael Clifford, Assistant Research Professor
Division of Earth and Ecosystem Sciences
Desert Research Institute
755 E Flamingo Road
Las Vegas, Nevada, 89119
702-862-5436
michael.clifford@dri.edu